AN ABSTRACT OF THE THESIS OF

Ram Ravichandran for the degree of Doctor of Philosophy in

Electrical and Computer Engineering presented on May 22, 2014.

Title: Development of High Efficiency Solar Absorbers .

Abstract approved: _____

John F. Wager

Current cadmium telluride and copper indium gallium diselenide thin-film solar cells (TFSCs) utilize thick absorbers (2 - 4 $\mu$m). For efficient carrier extraction in these TFSCs, the absorber layer requires high carrier mobilities and a long minority carrier lifetime, which necessitates the use of a high purity, defect-free thin film. Developing new materials with absorption strengths stronger than those of current materials allows an ultra-thin ($<$1 $\mu$m) absorber to be incorporated in a drift-based TFSC. Device simulation indicates that a built-in drift field aids carrier extraction, reducing mobility and lifetime requirements.

Iron- and copper-based materials are investigated within the context of ultra-thin absorbers. $FeS_2$ is unstable due to the formation of deleterious, low band-gap phases while $Fe_2GeS_4$ and $CuSbS_2$ exhibit a sluggish, non-abrupt onset of absorption, limiting their application in an ultra-thin drift-based TFSC. $Cu_3SbS_4$ exhibits desirable optical and electrical properties with a simulated TSFC efficiency of 19% for a 750 nm thick absorber layer. A new tetrahedrite-based absorber, $Cu_{10}Zn_2Sb_4Se_{13}$ demonstrates exceptionally strong absorption, with a simulated TSFC efficiency of 21% for a 250 nm thick absorber, indicating that $Cu_3SbS_4$ and $Cu_{10}Zn_2Sb_4Se_{13}$ have potential for high efficiency drift-based TFSC applications.

# Development of High Efficiency Solar Absorbers

by

Ram Ravichandran

A THESIS

submitted to

Oregon State University

in partial fulfillment of
the requirements for the
degree of

Doctor of Philosophy

Presented May 22, 2014
Commencement June 2014

Doctor of Philosophy thesis of Ram Ravichandran presented on May 22, 2014

APPROVED:

---

Major Professor, representing Electrical and Computer Engineering

---

Director of the School of Electrical Engineering and Computer Science

---

Dean of the Graduate School

I understand that my thesis will become part of the permanent collection of Oregon State University libraries. My signature below authorizes release of my thesis to any reader upon request.

---

Ram Ravichandran, Author

## ACKNOWLEDGMENTS

The work presented herein would not have been possible without the support and motivation of my advisors, Dr. John Wager and Dr. Doug Keszler. I owe thanks to Dr. Tom Plant for guiding me towards my graduate career, and my committee members, Dr. Ted Brekken and Dr. Bill Warnes.

I cannot thank my family enough for all the help and support over the years. Thank you for being there, at every step of all my endeavors, sharing my successes and helping me overcome my fears and failures.

I am very thankful to Chris Tasker, Rick Presley, and Manfred Dittirich who help maintain the cleanroom, and provide a learning environment even for those who are not mechanically inclined! The absorber group, including Dr. Robert Kokenyesi, Dr. Jaeseok Heo, Dr. Brian Pelatt, and Greg Angelos, has been crucial to the work presented herein. I'm looking forward to our continued friendship.

I owe thanks to many people in Corvallis who have helped me make OSU home, especially Dr. William Cowell, Ira Jewell, John McGlone, and Pratim Chowdhury. Thanks for being partners in crime and giving me reasons to step away from the lab. Dr. Jaeseok Heo and Dr. Liping Yu contributed to the theoretical calculations presented in this work.

This work was funded by the U.S. Department of Energy, Office of Science, Office of Basic Energy Sciences under Contract No. DE-AC36-08GO28308 to NREL.

TABLE OF CONTENTS

TABLE OF CONTENTS (Continued)

TABLE OF CONTENTS (Continued)

LIST OF FIGURES

# DEVELOPMENT OF HIGH EFFICIENCY SOLAR ABSORBERS

## 1. MOTIVATION - A PATHWAY TOWARDS SUSTAINABLE SOLAR ENERGY

Photovoltaics (PV) has come a long way since April 25th, 1954, when Bell laboratories demonstrated the first operational silicon solar cell capable of generating 1 watt of power [1]. Over the next sixty years, the cumulative globally installed PV capacity has grown dramatically, reaching 102 GW in 2012 [2]. More recently, the US installed a total of 4751 MW of new PV capacity accounting for 29% of new electricity generation capability in 2013, making solar energy the second largest source of new electricity generation behind natural gas [3]. While these statistics indicate an impressive growth over the past years, PV contributes a mere 0.3% of the overall energy generated by the US in 2013 [4]. The reason for this low contribution is that photovoltaics is currently too expensive to implement on a large scale.

The most mature PV technology, based on crystalline silicon has the highest module efficiencies (14 - 18%) and currently dominates the PV market with over 80% of the market share. However, manufacturing of silicon-based solar modules is inherently expensive and energy intensive. Thin-film solar cells (TFSCs) utilizing Cu(In,Ga)$Se_2$ and CdTe as the absorber layer require significantly less material (2 - 4 $\mu$m compared to $>$100 $\mu$m for silicon) and can be manufactured over large areas, reducing manufacturing costs. Of these two, only CdTe has proven large-scale manfacturability, with module efficiencies recently reaching 17% by FirstSolar. However, the drawback of CdTe is that it relies on toxic (Cd) and non Earth-abundant (Te) elements, limiting the large-scale implementation of CdTe-based TFSCs.

The fundamental material property that defines performance of a solar cell is how well the absorber layer in the solar cell absorbs sunlight. Developing materials that exhibit high absorption across the solar spectrum compared to CIGS or CdTe potentially not only improves the overall TFSC efficiency, but also reduces the absorber layer thickness. Thus, the motivation of this thesis is to develop new Earth-abundant materials exhibiting significantly higher optical absorption than those of current solar absorbers.

To achieve this objective, the structure of this thesis is laid out as follows. Chapter 2 contains a literature review beginning with a discussion of optical absorption in semiconductors, followed by TFSC device physics, and a survey of current TFSC technologies. Chapter 3 provides details regarding fabrication techniques, characterization methodologies, and TFSC simulations utilized in this study. Chapter 4 presents a simulation study on the necessary absorber layer properties required to provide a TFSC with an efficiency $\eta > 20\%$. Chapter 5 begins material exploration with iron pyrite ($FeS_2$) and $Fe_2GeS_4$ as entry points into iron-based absorbers. Material development, thin-film fabrication, characterization, and device simulation results are presented. Chapter 6 investigates copper-based absorbers. Beginning with design paradigms for high optical absorption, thin-film fabrication, characterization, and device simulation results for two families of copper-based absorbers (Cu-Sb-S and tetrahedrites) are presented. Lastly, Chapter 7 summarizes conclusions from this research and presents proposed directions for further investigations.

# 2. SUNLIGHT, SOLAR ABSORBERS, AND SOLAR CELLS

A solar cell has two functionalities. First is **generation**, or efficient absorption of the solar spectrum to generate a large number of photogenerated electron-hole pairs. Second is effective **transport** of photogenerated carriers towards their respective contacts with minimal recombination to generate electrical power. This chapter presents a review of fundamental concepts and existing literature pertaining to thin-film solar cells (TFSCs) by addressing the above two device functionalities. Since the absorber is the heart of a solar cell, emphasis is placed on the necessary properties and behavior of this layer. Beginning with a brief description of sunlight, the interaction of light with the absorber is emphasized. Device configurations of TFSCs and properties are described next. Finally, common solar absorber materials such as CdTe, Cu(In,Ga)$Se_2$, amorphous Si and alternate absorbers such as $FeS_2$ are reviewed.

## 2.1 Sunlight and Semiconductors

### 2.1.1 Solar Spectrum

The incident radiation spectrum from the sun can be described using Planck's black body radiation expression at a temperature of 5800 K [5]. The intensity, spectral distribution and radiant power per unit area of sunlight arriving on the Earth's surface is significantly altered by atmospheric scattering and absorption via gases. In the infrared region, absorption is caused by water vapor, carbon monoxide, methane and fluorinated hydrocarbons, while in the ultraviolet region, absorption is primarily caused by oxygen and ozone gases [6]. The modification of the solar spectrum due to this absorption is termed air mass (AM) intensity

and is used to denote the ratio of the optical path of light to a normal path at sea level on a cloudless day. It is defined as,

$$AMx = \frac{1}{cos\theta} \tag{2.1}$$

where $\theta = 0^\circ$ corresponds to the perpendicular incidence of the beam. AM0 refers to the solar spectrum outside the atmosphere for space-based applications, and AM1.5 global corresponds to an incident solar spectrum at $48.2^\circ$ and is used for terrestrial flat plane modules [7]. Figure 2.1 shows the AM0, AM1.5 solar spectrum along with the black body radiation curve at T = 5800 K. The integrated area under the curve for AM1.5 spectrum equals 1000 W/m$^2$ and is the standardized intensity value used to test solar cells and modules.

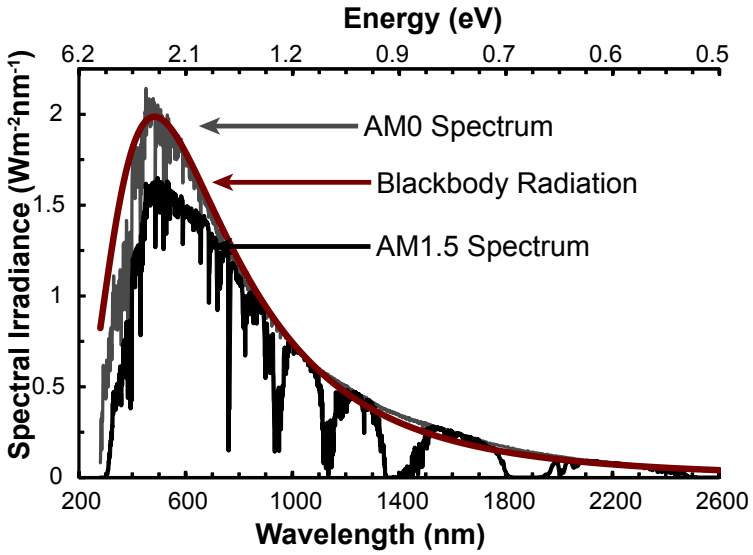


Figure 2.1: The spectral power density of sunlight outside the atmosphere (AM0), at the Earth's surface (AM1.5), and a blackbody radiation at 5800 K.

### 2.1.2 Absorption in Semiconductors

The fundamental operation of a solar cell relies on the interaction between light and a semiconductor, experimentally described using the absorption coefficient ($\alpha$) [$cm^{-1}$]. Figure 2.2(a) shows a simplified energy band diagram for a p-type semiconductor illuminated with above-band gap light. Absorption of photons results in interband transitions, where an electron is promoted from the valence band across the band gap to the conduction band. This results in a free electron in the conduction band along with a hole in the valence band, or a photogenerated electron-hole pair. An excited electron thermalizes to a position near the conduction band minimum, $E_C$ and subsequently relaxes to the top of the valence band, $E_V$, by recombining with a hole. Recombination occurs within a characteristic lifetime, and in the process a photon is emitted (for a direct band-gap semiconductor) with energy equal to the band gap, $E_G$. Although counterintuitive, a strong optical absorber should correspondingly also be a strong light-emitting material [8].

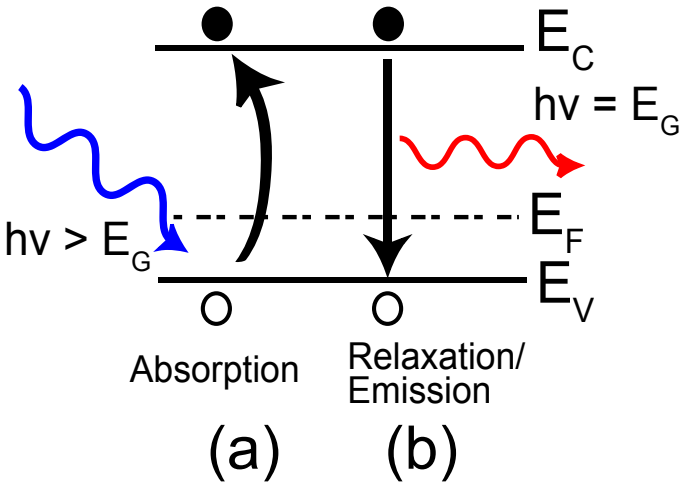


Figure 2.2: (a) Absorption of above-band gap light in a semiconductor results in a photogenerated electron-hole pair due to interband transitions. (b) Relaxation of the excited electron results in the emission of light with energy equal to the band gap.

Optically-induced interband transitions occur due to the perturbation of a material from equilibrium, described using the quantum mechanical transition rate ($W_{i\to f}$) [9], for an electron from an initially filled state ($i$) in the valence band to a final empty state ($j$) in the conduction band. This transition rate is calculated using Fermi's Golden Rule [10],

$$W_{i\to f} = \frac{2\pi}{\hbar} |H|^2 \, \delta(E_i - E_j \pm \hbar\omega), \tag{2.2}$$

where $H$ refers to the transition matrix element and $\delta(E_i - E_j \pm \hbar\omega)$ is an energy-conserving delta function. This energy-conserving delta function is valid only for discrete energy levels [10]. Since solids contain a distribution of energy states [9], the delta function is replaced by the joint density of states, $g(\hbar\omega)$ [cm$^{-3}$] [11]. The joint density of states (JDOS) refers to a convolution of occupied states at the valence band and unoccupied states in the conduction band participating in the interband transition. As a consequence of Fermi's Golden Rule, the JDOS and transition matrix element can be assessed independently to determine how each parameter affects absorption.

### Joint Density of States (JDOS)

The density of states (DOS) represents the distribution of electronic states in a solid within a given energy range of a band [11]. For a semiconductor with parabolic bands, the DOS can be expressed mathematically as [12],

$$D(E) = \frac{1}{2\pi^2} \left( \frac{2m^*}{\hbar^2} \right)^{3/2} E^{1/2}. \tag{2.3}$$

where $D(E)$ refers to the density of states [cm$^{-3}$] at a particular energy level (E) [eV] , $m^*$ refers to the effective mass [kg] for electrons in the conduction band, or holes in the valence band, and $\hbar$ is the reduced Planck constant. Near the valence band maxima (VBM) or conduction band minima (CBM), the DOS is strongly dependent on the carrier effective mass

($m^*$), which, in turn, is related to the curvature (second derivative [12]) of an energy band in reciprocal-($k$) space. This physics-based $k$-space perspective requires that the dispersion relation, i.e., E($\vec{k}$), be specified near the VBM and CBM to assess the relevant DOS. Alternatively, if atomic orbitals giving rise to the near-VBM and near-CBM portions of the energy bands are specified, insight into the magnitude of the DOS can be obtained from chemical considerations. This is accomplished by recognizing that a narrow energy band has a large DOS and a large effective mass, while a wide band has a dispersed DOS, and a smaller effective mass. As shown in Fig. 2.3, s-orbital derived bands have 2 electrons occupying a wide band dispersed in energy, p-orbital derived bands have 6 electrons occupying a band less dispersed in energy, while d-orbital derived bands have 10 electrons within a narrow band, highly localized in energy. Thus, $m_d^* > m_p^* > m_s^*$.

The effective mass $m^*$, plays an important role in determining transport properties. Carrier mobility ($\mu$) [cm$^2$ V$^{-1}$ s$^{-1}$] is given as [12],

$$\mu = \frac{q\,\langle\tau\rangle}{m^*}, \tag{2.4}$$

where $q$ is the charge of an electron [C], $\langle\tau\rangle$ [s] is the average time between scattering events, or more precisely, the average momentum relaxation time [13]. Equation 2.4 indicates that $m^*$ is inversely proportional to carrier mobility. As a result, an s-orbital derived band near the VBM (CBM) will result in a material with a large hole (electron) mobility, while a d-orbital derived band near the VBM (CBM) will result in a small hole (electron) mobility. While s-orbital derived bands at the VBM/ CBM are attractive for high mobility materials, interband transitions require narrow bands near the VBM/ CBM to provide a large JDOS near the band gap for strong optical absorption. As a result, transition metals such as manganese (d$^5$), iron (d$^6$). and copper (d$^{10}$) are attractive in solar absorber materials from a JDOS perspective.

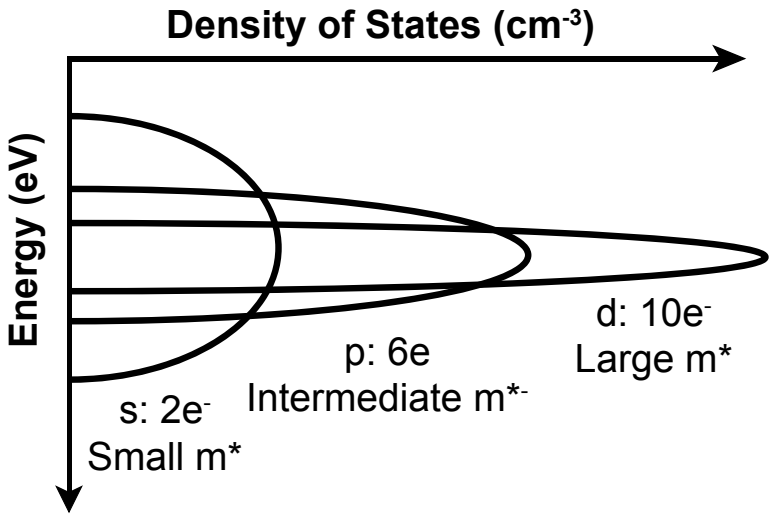


Figure 2.3: Density of states trends for s-, p-, and d-orbital derived bands, specifying the maximum electronic occupancy and expected effective mass trends for each band.

Thus, in a compound semiconductor, appropriately selecting elements which contribute to conduction and valence band edges to give rise to a large JDOS is a key aspect of designing a strong absorber for TFSC applications.

### Transition matrix element

The interaction between light modeled as an electromagnetic field and an electronic material is expressed through the magnetic vector potential, expressed mathematically as [14],

$$H = -\frac{q}{m_0}\mathbf{A}\cdot\mathbf{p}, \tag{2.5}$$

where $H$ is the perturbation associated by the interaction between the incident light wave ($A$) and a material described by the electronic dipole moment ($p$). The incident light, expressed as a plane wave ($A$) is given as [15],

$$\vec{A} = A_0\,\varepsilon\,\left(e^{\pm i(\mathbf{k}\cdot\mathbf{r}\,-\,\omega t)}\right)\,\hat{k}, \tag{2.6a}$$

with

$$A_0 = 2c \left(\frac{2\pi\hbar N}{\omega V}\right)^{1/2}. \tag{2.6b}$$

The perturbation, H, can be described by substituting Eqn. 2.6a into Eqn. 2.5 to give,

$$H = \frac{-q}{m_0}\, 2\varepsilon c \left(\frac{2\pi\hbar N}{\omega V}\right)^{1/2} \left(e^{\pm i(\mathbf{k}\cdot\mathbf{r} - \omega t)}\right) \hat{k}\cdot\mathbf{p}, \tag{2.7}$$

where $m_0$ is the rest mass of an electron [kg], $c$ is the speed of light [cm $s^{-1}$], $\mathbf{k}$ is the wave-vector [$cm^{-1}$], $\mathbf{r}$ is a radial distance [$cm$], $\omega$ is the angular frequency [$rad$], $t$ is time [$s$], $\varepsilon$ is the dielectric constant [F $cm^{-1}$], and $A_0$ is a constant related to the number of photons per unit volume ($NV^{-1}$) [# $cm^{-3}$]. For interband absorption, the interaction between this external perturbation field along with the initial ($i$) and final state ($j$) in a solid is described via the transition matrix element ($H_{ij}$) as [16],

$$H_{ij}(\mathbf{k}) = \langle i|H|j\rangle\,, \tag{2.8a}$$

$$= \frac{-qA_0}{2m_0 c}\left\langle i|e^{\pm\, i\mathbf{k}\cdot\mathbf{r}}\,\varepsilon\cdot\mathbf{p}|j\right\rangle. \tag{2.8b}$$

Equation 2.8b can be simplified using the *long wavelength approximation*, which states that for visible light and atomic dimentions, $e^{i\mathbf{k}\cdot\mathbf{r}} \sim 1$ [15]. For example, with $r$ = *50* Å, λ = 500 nm, k · r = 0.06 and $e^{0.06i}$ = 0.998 + 0.06i $\sim$ 1. As a result, for an isotropic material, Eqn. 2.8b can be re-written as,

$$H_{ij}(\mathbf{k}) = \frac{-qA_0\varepsilon}{2m_0 c}\left\langle i|\mathbf{p}|j\right\rangle. \tag{2.9}$$

Equation 2.9 is a Hamiltonian describing the transition matrix for an electron from an initial state in the VBM to the final state in the CBM. The square of the braket in Eqn. 2.9 represents the transition probability, and is zero if the transition between $i \rightarrow j$ is forbidden,

or has non-zero values if the transition between $i \rightarrow j$ is allowed. Parity selection rules govern allowed and forbidden transitions between orbital-derived bands in solids [17], based on the shape of an orbital, which is related to the distribution of charges [18]. *s* and *d* orbitals have a centro-symmetric charge distribution, and are referred to as even orbitals [19]. *p* and *f* orbitals, on the other hand, have a non-centro-symmetric charge distribution and are called odd orbitals [19]. Transitions between even-even or odd-odd orbitals are parity forbidden, while even-odd transitions are parity allowed [19]. In other words, the parity selection rule specifies that a transition is allowed if,

$$\Delta l = \pm 1 \tag{2.10}$$

where $\Delta l$ is the change in orbital angular momentum quantum number for an electron going from an initial state to a final state. Equation 2.10 implies that allowed transitions occur between s$\leftrightarrow$ p$\leftrightarrow$ d-orbital derived bands [20] since $\Delta l = \pm 1$, but transitions between s$\leftrightarrow$s; p$\leftrightarrow$p ; d$\leftrightarrow$d are forbidden since $\Delta l = 0$. s$\leftrightarrow$d transitions are also forbidden since $\Delta l = 2$. In solids however, the forbidden d-d transitions can be parity allowed due to mixing of *d* and *p* orbitals, resulting in allowed transitions [19]. Thus, based on Fermi's Golden Rule, maximizing absorption in a material not only requires the suitable elemental combination to provide a large JDOS near the VBM and CBM, but appropriate selection rules have to be considered to ensure allowed transitions between orbital-derived bands.

In addition to Fermi's Golden Rule, the nature of the band gap (direct or indirect) has to be taken into account. Figure 2.4(a) shows a *k*-space representation of an interband transition in a direct band gap material with parabolic energy bands. An interband transition in a direct band gap material is a two-particle interaction (photon - electron) and a key feature for such a material is that the top of the VBM coincides with the bottom of the CBM at the

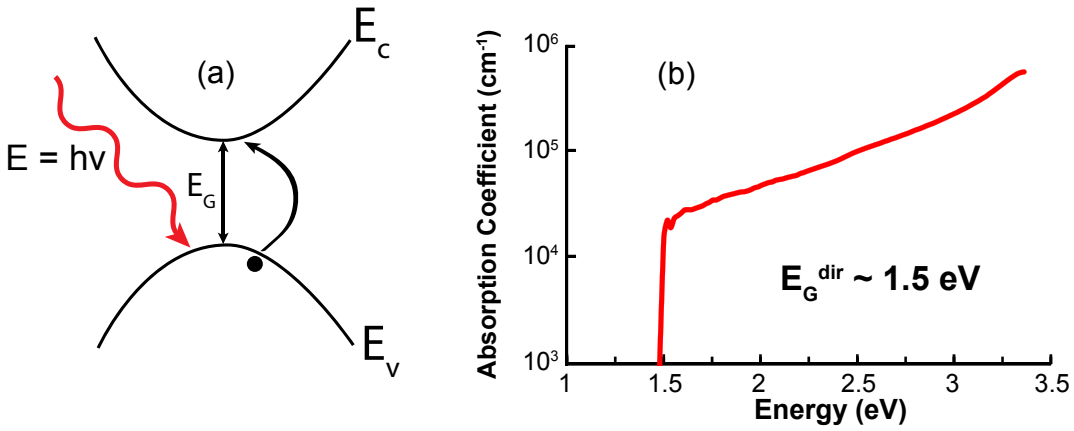


Figure 2.4: (a) *k*-space representation of an energy band diagram for a direct band gap material, and (b) absorption coefficient of CdTe. A direct band gap is characterized by a strong onset of absorption just above the band gap.

same value in *k*-space. As a result, an interband transition from the VBM to CBM in a direct band gap material translates into an abrupt onset of absorption at the band gap, as indicated by the absorption coefficient of CdTe shown in Fig. 2.4(b).

The absorption coefficient for a direct band gap material is modeled as [21],

$$\alpha^{dir}(E) = A \times (E - E_G)^{1/2}, \tag{2.11}$$

where $A$ is a constant dependent on material parameters such as the dielectric constant and effective mass (refer to the prefactor in Eqn. 2.9), $E$ is energy [eV] and $E_G$ is the direct band gap [eV].

In contrast to a direct band gap material, an interband transition in an indirect band gap semiconductor is a three-particle interaction (photon - electron - phonon) and a representative *k*-space energy band diagram is shown in Fig. 2.5(a). Here, the VBM and CBM are located at different values of *k*. As a result, a photoexcited electron requires an additional interaction with a phonon to make a transition from a filled band in the VBM to an empty band in the CBM. The corresponding absorption coefficient plot, using Si as a representative indirect

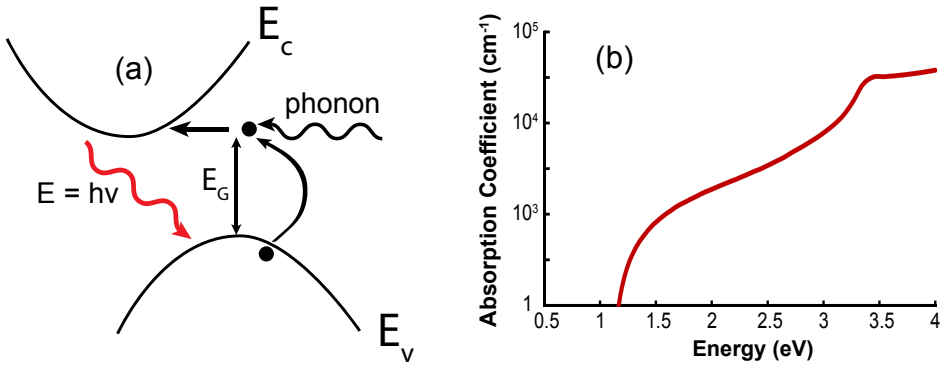


Figure 2.5: (a) Reciprocal space representation of an energy band diagram for an indirect band gap material, and (b) absorption coefficient of silicon. An indirect band gap material is characterized by a non-abrupt, gradual onset of absorption above the band gap.

band gap material is shown in Fig. 2.5(b). The absorption coefficient for an indirect band gap material is characterized by a non-abrupt, sluggish onset of absorption instead of an abrupt onset just above the band-gap for a direct band gap semiconductor. Absorption for an indirect band gap semiconductor can be expressed as [22],

$$\alpha^{indir}(E) = B \times (E - E_G \pm E_{ph})^2, \tag{2.12}$$

where $B$ is a constant that is dependent on material parameters such as the dielectric constant and effective mass (refer to the prefactor in Eqn. 2.9), $E$ is energy [eV], $E_G$ is the indirect band gap [eV], and $E_{ph}$ is the phonon energy [eV].

An estimate of the optical band gap can be extracted from a measured absorption coefficient using Eqns. 2.11 and 2.12. Using silicon as an example, the absorption coefficient plot in Fig. 2.5(b) is used to assess the indirect and direct band gap, as shown in Fig. 2.6. To estimate an indirect band gap for silicon, Eqn. 2.12 is linearized. Plotting the measured absorption coefficient as $(\alpha \times E)^{1/2}$ versus energy, the x-axis intercept provides an estimate of the indirect band, as shown in Fig. 2.6(a). The extrapolated indirect band gap is $E_G^{indr} \sim 1.1$

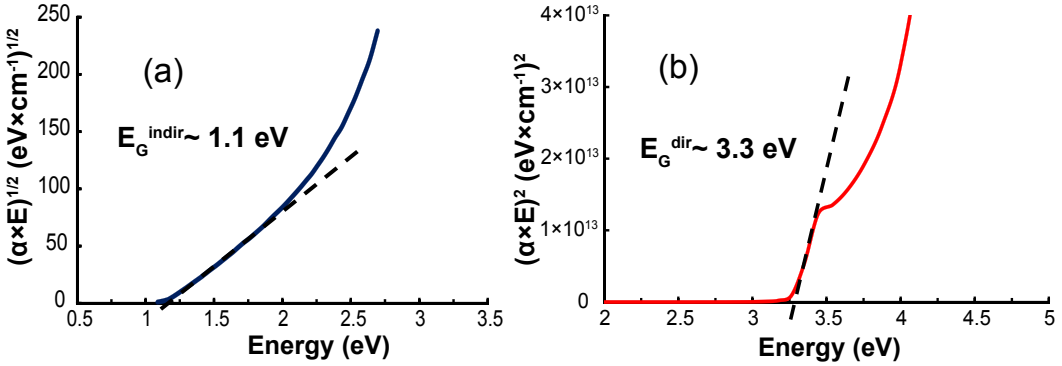


Figure 2.6: Estimation of the (a) indirect band gap, and (b) direct band gap of silicon. An indirect band gap of $E_G^{indr} \sim 1.1$ eV can be extracted, while a direct band gap $E_G^{dr} \sim 3.3$ eV is also observed.

eV, consistent with the known band gap of crystalline silicon [12]. By linearizing Eqn. 2.11, the direct band gap for silicon can be extracted. Plotting the measured absorption coefficient as $(\alpha \times E)^2$ versus energy, the x-axis intercept constitutes an estimate of the direct band, as shown in Fig. 2.6(b). Silicon has a direct band gap at $E_G^{dir} \sim 3.3$ eV.

The nature of the band gap has an important consequence with respect to the thickness requirement for an absorber layer in a solar cell. The indirect band gap nature of crystalline silicon implies that the minimum thickness required to fully absorb the solar spectrum is $\sim$ 200 $\mu$m [23]. This thickness corresponds to an absorption coefficient, $\alpha \sim 50$ cm$^{-1}$. TFSCs commonly utilize CIGS and CdTe as absorber layers which are both direct band gap materials. As a result of the abrupt onset of absorption in a direct band gap material, the minimum thickness required to completely absorb the solar spectrum is reduced to $<5$ $\mu$m [24]. This thickness corresponds to an absorption coefficient $> 2 \times 10^3$ cm$^{-1}$.

While the absorption coefficient shown in Figs. 2.4 and 2.5 do not show the presence of any sub-band gap absorption, absorption coefficient plots of non-optimized materials can show a rather large amount of sub-band gap absorption. This is predominately due to the

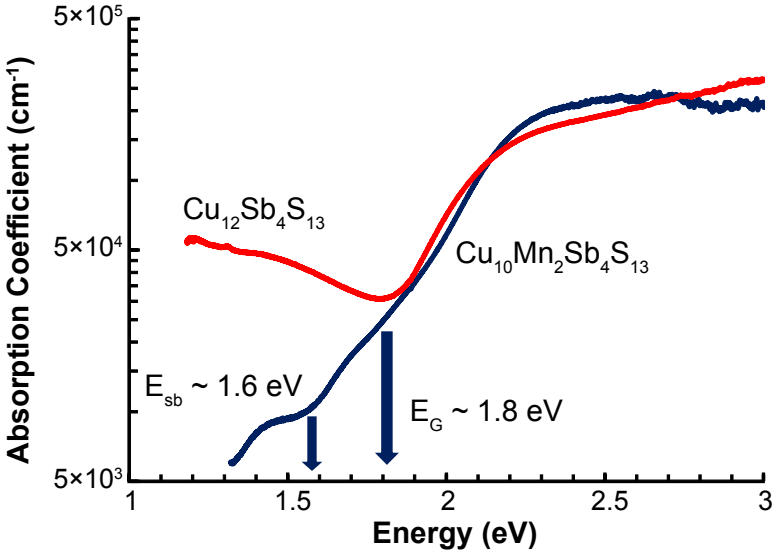


Figure 2.7: Absorption coefficient versus photon energy for a $Cu_{10}Mn_2Sb_4S_{13}$ and a $Cu_{12}Sb_4S_{13}$ thin film which have a band gap, $E_G \sim 1.8$ eV. However, an additional absorption feature can be seen in the $Cu_{10}Mn_2Sb_4S_{13}$ thin-film at $E_{sb} \sim 1.6$ eV, indicating the presence of an additional sub-band gap phase in the thin-film. $Cu_{12}Sb_4S_{13}$, on the other hand does not exhibit sub-band gap phases, but has a characteristic feature below the band gap indicating free-carrier absorption.

presence of additional lower band gap phases present in the material, and/or a large carrier concentration.

Figure 2.7 shows the absorption coefficients for $Cu_{10}Mn_2Sb_4S_{13}$ and $Cu_{12}Sb_4S_{13}$ thin films, both of which have a band gap, $E_G \sim 1.8$ eV. However, the absorption coefficient for the $Cu_{10}Mn_2Sb_4S_{13}$ thin-film also indicates the presence of another absorption event at $E_{sb} = 1.6$ eV, suggesting the presence of an sub-band gap phase in the thin film. $Sb_2S_3$ has a band gap, $E_G = 1.6$ eV [25] which gives rise to the absorption feature seen at $E_{sb} = 1.6$ eV. The absorption coefficient plot for the $Cu_{12}Sb_4S_{13}$ thin film, on the other hand, does not show evidence of any additional sub-band gap phases, but exhibits a steep, upward curvature for energies below the band-gap. This is a characteristic feature of free-carrier absorption in a degenerate semiconductor [11], where the presence of a large concentration of carriers gives

rise to a plasma resonance frequency, and the observed upward curvature in an absorption coefficient plot. The presence of a large carrier concentration results in a strong sub-band gap absorption value. This can be due to an inherent property of the material under consideration (i.e., it always has a large carrier concentration which cannot be controlled), or due to a non-optimized deposition process.

### 2.1.3 Recombination

When a semiconductor is perturbed from thermal equilibrium by above-band gap light, it seeks to restore itself back to equilibrium once the perturbation is removed. A photogenerated electron in the conduction band recombines with a corresponding hole in a characteristic *lifetime*, $\tau$ [s]. In a TFSC, this is an important parameter which can limit the overall device efficiency. While a long minority carrier lifetime ($\tau > 100\,\mu s$) is typical for a crystalline silicon solar cell [12], a TFSC typically short has lifetimes $<$100 ns [26] [24] due to the direct nature of the band gap (usually) and presence of an increased number of defects and grain boundaries compared to crystalline silicon [27].

The three possible recombination mechanisms are shown in Fig. 2.8. The first mechanism (Fig. 2.8a) is radiative recombination, where a photogenerated electron near the conduction band minimum recombines with a hole near the valence band maximum, emitting a photon in the process. The second recombination type (Fig. 2.8b) is Shockley-Reed-Hall (SRH), or trap-assisted recombination. The third process (Fig. 2.8c) is Auger recombination. Auger recombination is only significant for high doping concentrations ($n, p \geq 10^{18}\,cm^{-3}$), or high-level injection [12]. Since the carrier concentration for a solar absorber is less than $10^{18}\,cm^{-3}$, only radiative and SRH are relevant recombination mechanisms. Each recombination mechanism may be expressed as a lifetime, and the overall effective lifetime is the

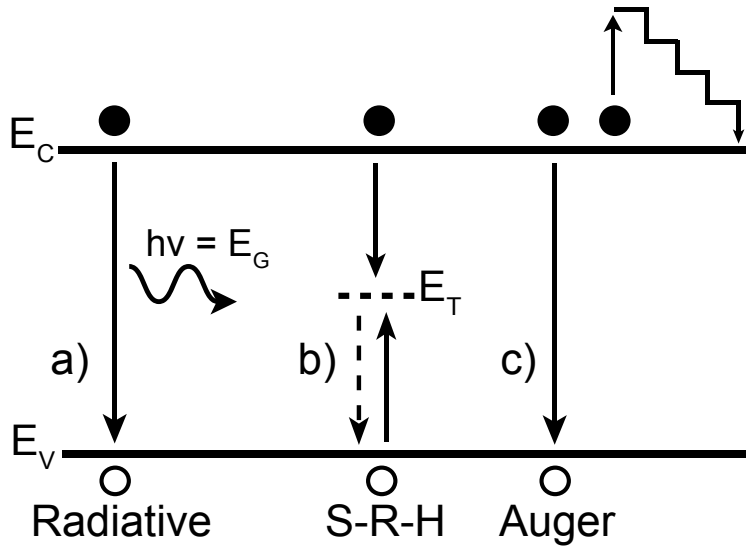


Figure 2.8: Recombination mechanisms in a semiconductor. (a) Radiative recombination, accompanied with the emission of a photon with energy equal to the band-gap. (b) SRH, or trap-mediated recombination, and (c) Auger recombination.

reciprocal sum of the two relevant lifetimes as [12],

$$\frac{1}{\tau_{eff}} = \frac{1}{\tau_{rad}} + \frac{1}{\tau_{SRH}}, \tag{2.13}$$

where $\tau_{rad}$ and $\tau_{SRH}$ are the minority carrier lifetimes [s] for radiative and SRH recombination. Equation. 2.13 indicates that the shorter recombination lifetime plays the dominant role in establishing the effective minority carrier lifetime.

### Radiative Recombination

Radiative recombination is the inverse process of interband absorption, and is of importance in a direct band gap semiconductor [16]. The net radiative recombination rate, $U_{rad}$ [$\mathrm{cm}^3\, s^{-1}$] can be written as [12],

$$U_{rad} = \frac{\Delta n}{\tau_{rad}}, \tag{2.14a}$$

with

$$\tau_{rad} = \frac{1}{R_{ec}(p_0 + n_0 + \Delta p)}, \tag{2.14b}$$

and

$$R_{ec} = \frac{G_{th}}{n_i^2}. \tag{2.14c}$$

where $G_{th}$ is the generation rate [$cm^3 s^{-1}$], $R_{ec}$ is the radiative recombination coefficient [$cm^3 s^{-1}$], $n_i$ is the intrinsic carrier concentration [$cm^{-3}$], $\Delta n$ ($\Delta p$) refers to the concentration of photogenerated (excess) electrons (holes) [$cm^{-3}$], and $n_0$ ($p_0$) refers to the equilibrium concentration of electrons (holes) [$cm^{-3}$]. For a p-type material ($p_0 \gg n_0$), under low-level injection ($p_0 \gg \Delta n = \Delta p$) and assuming full ionization ($p_0 \rightarrow N_A$), Eqn. 2.14b can be re-written as,

$$\tau_{rad} = \frac{1}{R_{ec} N_A}. \tag{2.15}$$

The recombination coefficient, $R_{ec}$ is larger ($\sim 10^{-10}$ $cm^3 s^{-1}$) for a direct band gap semiconductor than an indirect band gap semiconductor ($R_{ec} \sim 10^{-15}$ $cm^3 s^{-1}$) [28]. Assuming an absorber with a direct band gap and $N_A = 10^{16}$ $cm^{-3}$, $\tau_{rad} = 1\,\mu s$. With $N_A = 10^{14}$ $cm^{-3}$, the radiative lifetime $\tau_{rad} = 100\,\mu s$, indicating a long minority carrier lifetime value if the hole concentration can be precisely controlled (which may not be the case in polycrystalline semiconductors).

### SRH Recombination

For an indirect band gap semiconductor, recombination via trap states is usually the dominant recombination mechanism [12]. Recombination via a single trap state consists of two processes: electron capture and hole capture, described using Shockley-Read-Hall

(SRH) statistics as [29],

$$U_{SRH} = \frac{\sigma_n \sigma_p \, v_{th} \, N_{th} \, \left(np - n_i^2\right)}{\sigma_n \left[n + n_i \, exp\left(\frac{E_t - E_i}{k_B T}\right)\right] + \sigma_p \left[p + p_i \, exp\left(\frac{E_i - E_t}{k_B T}\right)\right]}, \tag{2.16}$$

where $U_{SRH}$ is the net SRH recombination rate [cm$^3$ s$^{-1}$], $\sigma_n$ ($\sigma_p$) refer to the capture cross-section for electrons (holes) [cm$^2$], $v_{th}$ is the thermal velocity [$cm\,s^{-1}$], $n$ ($p$) are the excess photogenerated electrons (holes) [cm$^{-3}$], $n_i$ is the intrinsic carrier concentration [cm$^{-3}$], with the intrinsic level corresponding to $E_i$ [eV] and $E_t$ [eV] is the energy position of the trap within the band gap. Equation 2.16 indicates that $U_{SRH}$ is maximum when $E_t = E_i$, or that near mid-gap states are the most effective recombination centers. As a result, Eqn. 2.16 can be solved for a p-type semiconductor with mid-gap trap states to give [12],

$$U_{SRH} = \frac{\sigma_n \sigma_p \, v_{th} \, N_t \left[\Delta n \, (n_0 + p_0) + \Delta n)\right]}{\sigma_p \left[p_0 + \Delta p + n_i\right]}. \tag{2.17}$$

Equation 2.17 can be further simplified by introducing the SRH lifetime, $\tau_{SRH}$ [s], as [30],

$$U_{SRH} = \frac{\Delta n}{\tau_{SRH}}, \tag{2.18a}$$

where

$$\tau_{SRH} = \frac{\tau_n \left(p_0 + \Delta p + n_i\right)}{\left(n_0 + p_0 + \Delta n\right)}, \tag{2.18b}$$

and

$$\tau_n = \frac{1}{\sigma_n \, v_{th} \, N_t}, \tag{2.18c}$$

where $\tau_n$ is referred to as the *minority carrier lifetime*, $\sigma_n$ is the capture cross-section for electrons [cm$^{-2}$], $v_{th}$ is the electron thermal velocity [cm$^2\,s^{-1}$] and $N_t$ is the concentration

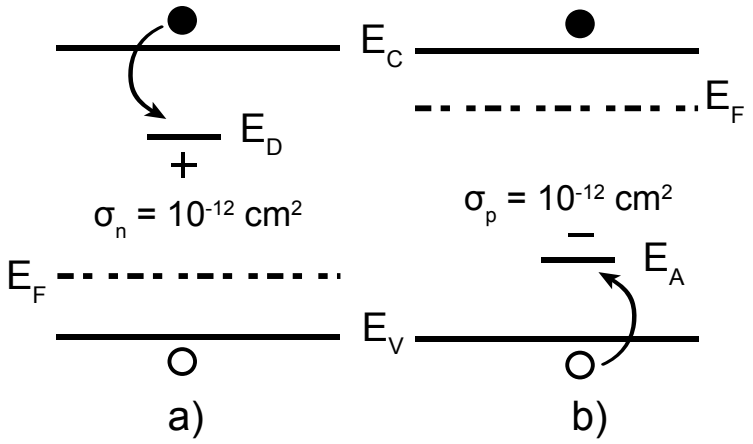


Figure 2.9: (a) Electron capture by an ionized donor trap in a p-type semiconductor, and (b) hole capture by an ionized acceptor trap in an n-type semiconductor.

of mid-gap traps [cm$^{-3}$]. For low level injection ($p_0 \gg \Delta n$) in a p-type material, Eqn. 2.18b can be written as,

$$\tau_{SRH} \approx \tau_n = \frac{1}{\sigma_n \, v_{th} \, N_t}. \tag{2.19}$$

Trap states can be classified as donor- or acceptor-like [29]. A donor-like (acceptor-like) trap state is likely to give away (accept) an electron. To serve as an effective recombination center, the traps have to be ionized, i.e., an ionized donor trap is positively charged, while an ionized acceptor defect is negatively charged. Recombination at a trap is characterized by a capture cross-section for electrons ($\sigma_n$) and holes ($\sigma_p$) with typical values for an attractive, neutral and, repulsive trap of: $10^{-12}$, $10^{-15}$ and, $10^{-18}$ cm$^{-2}$ [30], respectively. Figure 2.9(a) shows a p-type semiconductor with a positively charged ionized donor trap. Since the defect is positively charged, a photogenerated (minority carrier) free electron in the conduction band will be coulomb-attracted to the trap [31]. The capture cross-section for this case is $\sigma_n$ = $10^{-12}$ cm$^{-2}$. An ionized acceptor defect in a p-type material is negatively charged, and a

| Mid-gap defect concentration [$cm^{-3}$] | Minority carrier lifetime [ns] |
|---|---|
| $10^{12}$ | 100 |
| $10^{13}$ | 10 |
| $10^{14}$ | 1 |
| $10^{15}$ | 0.1 |
| $10^{16}$ | 0.01 |

Table 2.1: Calculated minority carrier lifetimes based on mid-gap defect densities. These values are used for subsequent device simulations in this study.

photogenerated minority carrier electron is repelled from this trap [31]. Conversely, a negatively charged acceptor trap in an n-type semiconductor, as shown in Fig. 2.9(b), primarily captures minority carrier holes. The capture cross-section for a minority carrier hole is $\sigma_p$ = $10^{-12}$ $cm^{-2}$.

Equation 2.19 can be assessed for a p-type absorber with donor-like traps ($\sigma_n = 10^{-12}$ $cm^{-2}$) and $v_{th} = 10^7$ $cm^2 s^{-1}$ to relate the minority carrier lifetime to the concentration of mid-gap defects in a material listed in Table 2.1. Comparing values in Table 2.1 along with calculated values for radiative recombination lifetime ($N_A$ = $10^{16}$ $cm^{-3}$, $\tau$ = 1 $\mu$s; $N_A$ = $10^{14}$ $cm^{-3}$, $\tau$ = 100 $\mu$s) and Eqn. 2.13 indicates that SRH recombination is the dominant recombination mechanism in a TFSC.

## 2.2 Solar Cell Device Primer

A TFSC is typically a *p-n* heterojunction diode, where the mechanism for charge separation involves a gradient in excess carriers diffusing to the edge of a depletion region, or a

*p-i-n* heterojunction diode, where carriers are influenced by a built-in electric field, resulting in a drift field transport. This section focuses on a device description of a TFSC. Beginning with a discussion of device configuration types, current-voltage characteristics for both a diffusion and drift-based TFSC are described. Finally, solar cell efficiency limits are discussed.

### 2.2.1 Solar Cell Device Configurations

Designing a high efficiency TFSC not only requires optimal photogeneration, but also requires a mechanism for efficient extraction of carriers. To produce power, photogenerated electron-hole pairs have to be efficiently extracted from the absorber at the appropriate contact. This requires a *built-in asymmetry* in the solar cell structure [32], such that electrons preferentially leave the TFSC at the n-type contact and holes at the p-type contact. Figure 2.10 shows two device geometries under three different conditions: equilibrium (dark), illumination, and illumination with a forward bias.

#### p-n Heterojunction TFSCs: Diffusion cells

Figure 2.10a shows a simulated energy-band diagram for a p-n heterojunction TFSC with an $n^+$ window layer ($N_D = 10^{18}$ cm$^{-3}$, $t = 50$ nm) and a p-type absorber layer ($N_A = 10^{16}$ cm$^{-3}$, $t = 600$ nm). Since $N_D \gg N_A$, a TFSC p-n heterojunction is a one-sided step junction, and as a result, this doping asymmetry causes most of the electric field drop across the p-type absorber, giving rise to a space charge region. However, the band bending due to the electric field in Fig. 2.10a is restricted to a portion of the absorber thickness, while the absorber bulk has negligible band bending or electric field drop to enhance carrier extraction. In this configuration, carrier transport is governed by diffusion of carriers towards the space charge region, and the structure is a *diffusion cell*.

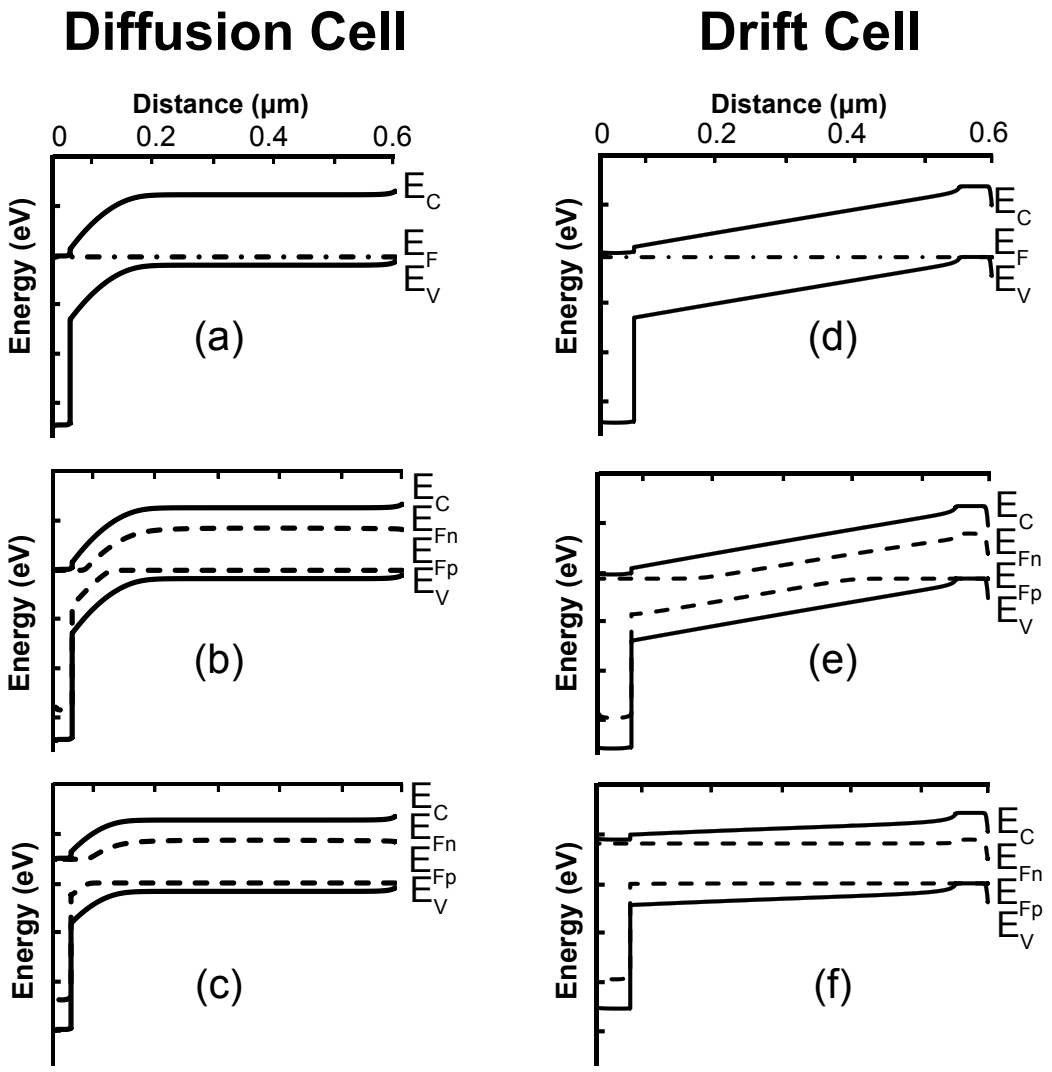


Figure 2.10: Device configurations for a TFSC. P-n junction (diffusion cell) at (a) equilibrium, (b) under illumination, (c) and illumination with a forward bias. P-i-n junction (drift cell) at (d) equilibrium, (e) under illumination, and (f) illumination with a forward bias.

Illumination results in the generation of excess carriers (Fig. 2.10b), so that the equilibrium Fermi level ($E_F$) splits into quasi-Fermi levels ($E_{Fp}$ and $E_{Fn}$), whose separation in energy from $E_F$ is related to excess carrier generation. The separation ($E_{Fn}$ - $E_{Fp}$), is known as quasi-Fermi level (QFL) splitting and the maximum QFL under illumination is equivalent to the open-circuit voltage ($V_{OC}$) in a TFSC. Thus, illumination of a solar cell generates a potential which forward biases the device. The resulting energy band diagram is shown in Fig. 2.10c. As a consequence of this forward bias, the electric field near the $n^+$-p interface is reduced. Solar cells based on crystalline silicon and Cu(In,Ga)$Se_2$ are examples of this type.

In this diffusion cell configuration shown in Fig. 2.10a-c, a large valence band discontinuity at the $n^+$-p heterojunction interface provides a valence band energy barrier reflecting holes and preventing them from recombining with electrons at the front contact. However, at the back contact in Figs. 2.10a-c, this device configuration does not have a corresponding conduction band energy barrier to prevent undesirable electron recombination.

p-i-n Heterojunction TFSCs: Drift cells

A p-i-n heterojunction configuration energy band diagram is shown in Fig. 2.10d. The energy band diagram for this configuration is simulated by sandwiching a low-doped p-type absorber ($N_A = 10^{14}$ cm$^{-3}$, $t = 600$ nm) between two highly doped asymmetric layers ($n^+$: $N_D = 10^{18}$ cm$^{-3}$, $t = 10$ nm and $p^+$: $N_A = 10^{18}$ cm$^{-3}$, $t = 10$ nm). These thin, highly doped layers cause an internal electric field to drop across the entire absorber, resulting in photogenerated carriers experiencing drift-aided transport. CdTe and amorphous silicon solar cells are examples of this configuration.

In a p-i-n heterojunction, or a *drift cell*, in addition to the valence band discontinuity providing a hole reflector at the $n^+$-p interface, a small conduction band offset at the p-

$p^+$ interface provides a built-in electron reflector. This barrier makes it more difficult for electrons to recombine at the back surface. Sites and Pan [33] show that a barrier height of 0.1 - 0.3 eV is sufficient to appreciably reduce back-surface recombination.

The quasi-Fermi level splitting under illumination is indicated in Fig. 2.10e and the effect of forward bias due to illumination is shown in Fig. 2.10f. A key feature of a drift cell compared to a diffusion cell is the existence of an internal electric field to enhance carrier transport even in a low mobility and low minority carrier lifetime semiconductor, such as amorphous silicon [5]. Under bias (Fig. 2.10f), the electric field decreases in magnitude. As a result, the photocurrent can be bias dependent [34]. The variation of TFSC material parameters such as the thickness, carrier concentration, minority carrier lifetime, and carrier mobilities for a diffusion and a drift-based TFSC is explored further in Chapter 4.

### 2.2.2 Current-Voltage Characteristics of TFSCs

In the dark, the current density-voltage (J-V) characteristics of a p-n junction-based (diffusion configuration) TFSC can be modeled using the Shockley diode equation [29],

$$J(V) = J_0 \left[ exp\left(\frac{qV}{nk_BT}\right) - 1 \right], \tag{2.20}$$

where $k_B$ is Boltzmann's constant [eV $K^{-1}$], $T$ is temperature [K], $n$ is the ideality factor, $q$ is electron charge [C], $V$ is the potential developed across the terminals of the cell [V] and $J_0$ is the reverse saturation current density [mA $cm^{-2}$]. Illumination results in the generation of a photocurrent, $J_{ph}$ [mA $cm^{-2}$], related to the number of photons absorbed as determined by the absorption coefficient. As a result, the J-V characteristics for an illuminated solar cell can be written as,

$$J(V) = J_{ph} - J_0 \left[ exp\left(\frac{qV}{nk_BT}\right) - 1 \right], \tag{2.21a}$$

with

$$J_{ph} = q \int_{E_G}^{\infty} (1-R)\, \Phi_b\, exp(-\alpha x_a) dE. \tag{2.21b}$$

where $\Phi_b$ is the incident solar flux [W m$^{-2}$ $\mu$m$^{-1}$], $R$ represents the reflection losses from the front surface [unitless], $\alpha$ is the absorption coefficient [cm$^{-1}$], and $x_a$ is the thickness of the absorber layer [nm or $\mu$m] [7].

The J-V characteristics corresponding to Eqn. 2.21a in the dark and under illumination are shown in Fig. 2.11a and are described using the following parameters:

- *Short-circuit current density* ($J_{sc}$): The short-circuit current density is obtained under zero load resistance when no voltage is applied. According to Eqn. 2.21a, $J_{sc} = J(V = 0) = J_{ph} - J_0$.

- *Open-circuit voltage* ($V_{oc}$): The open-circuit voltage is the voltage produced by the solar cell, under an infinite load resistance, when no current flows. Rewriting Eqn. 2.21a, for $J = 0$, the open circuit voltage is equal to,

$$V_{oc} = \frac{nk_BT}{q} ln\left(1 + \frac{J_{ph}}{J_0}\right). \tag{2.22}$$

- *Fill factor* ($FF$): The maximum power $P_{max}$ generated by a solar cell occurs at a voltage ($V_{max}$) and current density ($J_{max}$) maximum represented via the fill factor as,

$$FF = \frac{J_{max}V_{max}}{J_{sc}V_{oc}} = \frac{P_{max}}{J_{sc}V_{oc}}. \tag{2.23}$$

  The FF is equal to the largest rectangular area that fits the fourth quadrant of an illuminated J-V curve, indicated by the shaded region in Fig. 2.11a. Typical solar cells have FF between 0.6 - 0.8.

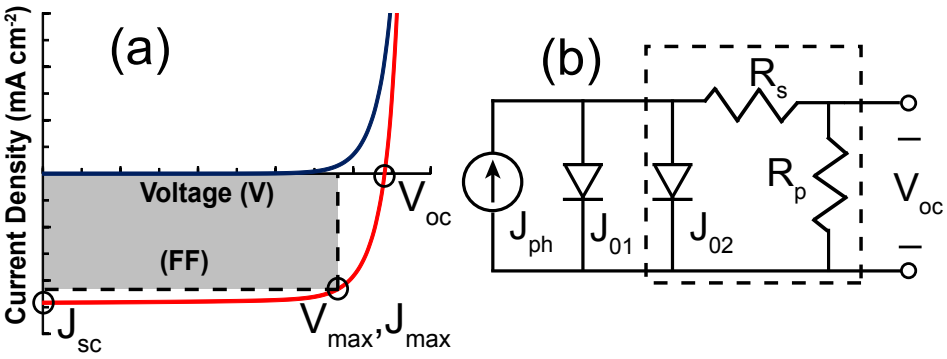


Figure 2.11: (a) J-V characteristics, and (b) equivalent circuit of a solar cell. The dashed box in (b) represents non-ideal components of the model.

- *Efficiency* ($\eta$): The efficiency of a solar cell is defined as the ratio of the output power density and the incident power density, $P_s$ as,

$$\eta = \frac{J_{max}V_{max}}{P_s} = \frac{J_{sc}V_{oc}FF}{P_s}. \tag{2.24}$$

The four quantities: $J_{sc}$, $V_{oc}$, $FF$, and $\eta$ represent key performance characteristics of a solar cell, defined for a particular illumination condition, typically the AM1.5 spectrum. These characteristic parameters for solar cells with different absorbers are listed in Table 2.2.

Recombination in the depletion region along with parasitic resistances have to be included in Eqn. 2.21a to fully describe solar cell behavior. During operation, the efficiency of a solar cell can be reduced due to power dissipated through contact resistance and leakage currents around the side of the device [40]. These effects are represented electrically as parasitic series ($R_s$) and parallel ($R_{sh}$) resistances [$\Omega$]. The series resistance arises from the bulk absorber material and metallic contacts to the solar cell along with interconnects. The parallel resistance is a shunt resistance associated with pinholes or other types of shunting defects in the absorber or other layers [41]. The variation in J-V characteristics for a hypo-

| Absorber | Band Gap [eV] | $V_{oc}$ [V] | $J_{sc}$ [mA $cm^{-2}$] | FF [unitless] | $\eta$ [%] | Ref. |
|---|---|---|---|---|---|---|
| Crystalline Si | 1.1 | 0.71 | 42.2 | 82.8 | 24.7 | [35] |
| GaAs | 1.4 | 1.02 | 28.2 | 87.1 | 25.1 | [36] |
| Amorphous Si | 1.6 | 0.89 | 16.7 | 67.8 | 10.1 | [37] |
| $Cu(In,Ga)Se_2$ | 1.1 | 0.67 | 35.7 | 77.0 | 19.4 | [26] |
| $Cu_2(Zn,Sn)SSe_4$ | 1.15 | 0.46 | 34.5 | 69.8 | 11.1 | [38] |
| CdTe | 1.4 | 0.85 | 25.9 | 74.5 | 18.3 | [39] |

Table 2.2: Electrical performance parameters of solar cells with different absorber materials.

thetical TFSC with different values for $R_s$ and $R_{sh}$ is shown in Figure. 2.12. Increasing $R_s$ from 0 $\Omega$ $cm^2$ to 20 $\Omega$ $cm^2$ in Fig. 2.12a shows a decrease in the FF. Decreasing $R_{sh}$ from 1 k$\Omega$ $cm^2$ to 25 $\Omega$ $cm^2$ in Fig.2.12b shows a significant change in the J-V characteristics. Not only does the FF reduce, but the $V_{oc}$ also decreases with decreasing $R_{sh}$. Thus, to reduce parasitic losses, an optimal solar cell requires a high parallel ($R_{sh}$) resistance and a low series ($R_s$) resistance. This result can be understood using the equivalent circuit shown in Fig. 2.11. A low value of $R_s$ is preferred since there would be no voltage drop before the output and a large value for $R_{sh}$ is necessary to prevent an additional current path.

If the diode equation given in Eqn. 2.20 is assumed to involve only diffusion current, the ideality factor, $n$, is equal to 1. Generation-recombination can also occur in the space charge region, resulting in an ideality factor of 2 [5]. A more complete description of a solar cell includes the parasitic resistances and involves a two diode model - $J_{01}$ accounting for diffusion current, and $J_{02}$ accounting for generation-recombination current in the depletion

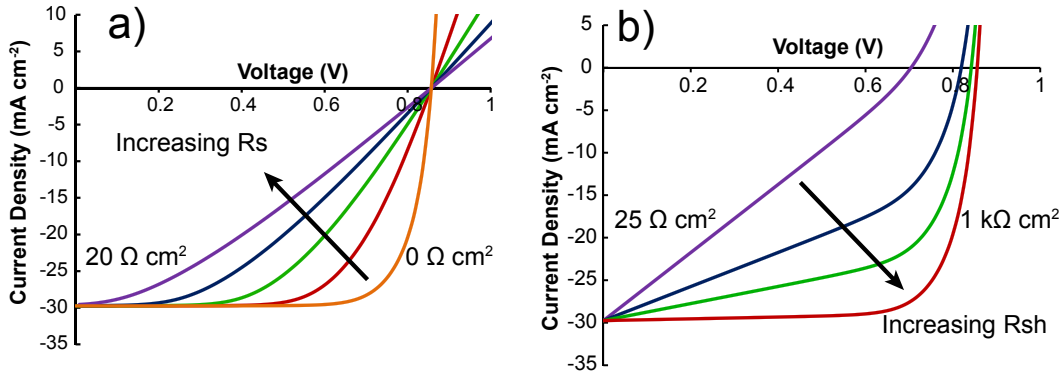


Figure 2.12: Variation in J-V characteristics for a hypothetical TFSC with different simulated values for parasitic a) series resistance ($R_s$), and b) parallel ($R_{sh}$) resistance. In both cases, a decrease in the FF can be observed, however a low value for ($R_{sh}$) also decreases $V_{oc}$.

region. J-V characteristics for this solar cell model is represented as [5],

$$J(V) = J_{ph} - J_{01}\left[exp\left(\frac{V+IR_s}{k_BT}\right)-1\right] - J_{02}\left[exp\left(\frac{V+IR_s}{2k_BT}\right)-1\right] - \left(\frac{V+IR_s}{R_p}\right). \quad (2.25)$$

The reverse saturation current density, $J_0$, for a diffusion cell is often formulated using the following empirical expression by Green [42],

$$J_0 = J_{00}\, exp\left(\frac{-E_G}{k_BT}\right), \quad (2.26a)$$

where

$$J_{00}^{Green} = 1.5\times 10^8 \ \ [\text{mA cm}^{-2}]\,. \quad (2.26b)$$

Equation. 2.26a can be derived from the reverse saturation current density for a p-n junction assuming only diffusion current is relevant [12],

$$J_0 = \left[\frac{qD_n n_i^2}{L_n N_A} + \frac{qD_p n_i^2}{L_p N_D}\right], \quad (2.27)$$

where $D_n$ ($D_p$) is the diffusion constant for minority carrier electrons (holes) [cm$^2$ s$^{-1}$], $L_n$ ($L_p$) is the diffusion length for electron (holes) [cm or $\mu$m], and $N_A$ ($N_D$) refers to the acceptor

(donor) density [$cm^{-3}$]. A TFSC is typically a one-sided step junction, with the n-type region higher doped than the p-type region. As a result, Eqn. 2.27 can be simplified to only account for minority carrier electrons in the p-type region. In addition, an expression for the intrinsic carrier concentration can be substituted into Eqn. 2.27 to give,

$$J_0 = \left[\frac{qD_n n_i^2}{L_n N_A}\right] = \left[\frac{qD_n N_C N_V}{L_n N_A}\right] \times exp\left(\frac{-E_G}{k_B T}\right) \tag{2.28}$$

where $N_C$ and $N_V$ refer to the effective density of states in the conduction band and valence band [$cm^{-3}$], respectively. Comparing Eqns. 2.26a and 2.28, $J_{00}$ is equivalent to a constant related to material properties of the absorber. For silicon, using material properties from [12] as listed in Table 2.3, $J_{00} = 2.11 \times 10^8$ mA $cm^{-2}$ for $N_A = 10^{17}$ $cm^{-3}$, providing a close match to Eqn. 2.26b. An estimation of $J_{00}$ for a CIGS-based TFSC using material parameters from [31] as listed in Table. 2.3 provides $J_{00} = 1.02 \times 10^{10}$ mA $cm^{-2}$ for $N_A = 10^{16}$ $cm^{-3}$. The calculated reverse saturation current density prefactor for a CIGS-based TFSC is nearly two orders of magnitude higher than that of a silicon solar cell. Comparing values shown in Table 2.3, while the electron mobility is lower in CIGS compared to silicon, the biggest differentiator is that the minority carrier lifetime in CIGS is five orders of magnitude lower than that of silicon, and as a result, the diffusion length is significantly reduced. This suggests that a diffusion-based TFSC would have an increased reverse saturation current density compared to that estimated using Green's empirical equation. In turn, this would lead to a reduced output current and a lower efficiency than expected from the extrapolated performance of a crystalline silicon-based solar cell.

In the dark, the electrical characteristics of a p-i-n diode (drift configuration) is modeled as [41],

$$J(V) = J_0 \left[exp\left(\frac{qV}{2k_B T}\right) - 1\right]. \tag{2.29}$$

| Parameter | Silicon | CIGS |
|---|---|---|
| $\mu_n$ [$cm^2 V^{-1} s^{-1}$] | 1450 | 100 |
| $\tau_n$ [s] | $10^{-3}$ | $10^{-8}$ |
| $N_C$ [$cm^{-3}$] | $2.8 \times 10^{19}$ | $2.2 \times 10^{18}$ |
| $N_V$ [$cm^{-3}$] | $2.65 \times 10^{19}$ | $1.8 \times 10^{19}$ |
| $N_A$ [$cm^{-3}$] | $10^{17}$ | $10^{16}$ |
| $J_{00}$ [mA $cm^{-2}$] | $1.5 \times 10^{8}$ | $1.02 \times 10^{10}$ |

Table 2.3: Material properties for silicon [12] and CIGS [31] used to calculate the reverse saturation current density prefactor, $J_{00}$.

Under illumination, photogenerated carriers are generated throughout the low-doped absorber, resulting in an additional recombination term since the space charge region extends across the entire absorber layer. For simplicity, it is assumed that the $p^+$ and $n^+$ regions on either side of the absorber are thin compared to the absorber thickness so that diffusion of carriers from these layers towards the absorber is not taken into account. Assuming that transport is purely governed by drift, the total current density for an illuminated p-i-n diode is [41],

$$J_{illum} = J_{ph} - J_0 - J_{recomb}, \tag{2.30}$$

where $J_{recomb}$ [mA $cm^{-2}$] refers to the recombination current density across the entire absorber layer. For a simple case where the electric field is uniform across the entire absorber, $J_{recomb}$ can be given as [41],

$$J_{recomb} = J_{ph} \times \frac{d_i}{l_{drift}}, \tag{2.31a}$$

and

$$l_{drift} = \mu\tau E_0 = \mu\tau \left( \frac{V_{bi} - V}{d_i} \right), \tag{2.31b}$$

where $l_{drift}$ is the drift length [cm] of minority carrier electrons and $d_i$ is the thickness of the absorber. In Eqn. 2.31b, the maximum $V_{bi}$ is $E_G/q$. Under no applied bias, Eqn. 2.31b can be simplified to,

$$l_{drift} = \mu\tau \frac{E_G}{q d_i}. \tag{2.32}$$

Representative TFSC absorber material parameters can be substituted into Eqn. 2.32 to estimate the drift length for a 1 $\mu$m thick absorber layer,

$$l_{drift} = 100\ \mathrm{cm^2 V^{-1} s^{-1}} \times 1\,ns \times \frac{1.5\,eV}{q \times 1\mu m}, \tag{2.33a}$$

or

$$\frac{d_i}{l_{drift}} = \frac{1 \times 10^{-4}\ \mathrm{cm}}{1.5 \times 10^{-3}\ \mathrm{cm}} = 0.067. \tag{2.33b}$$

Thus, for an absorber with a moderate lifetime and a high mobility, substituting Eqn. 2.33b into Eqn. 2.31a, it is evident that $J_{recomb}$ is of negligible importance in Eqn. 2.30. However, if the mobility or lifetime is significantly decreased, as is the case in amorphous silicon-based TFSCs, $J_{recomb}$ can be as high as $0.8 J_{ph}$ [43]. To first order, it can be assumed that an illuminated drift cell has similar J-V characteristics as a diffusion cell, and the reverse saturation current density has the same form as Eqn. 2.26a. Since the transport mechanism is no longer governed by diffusion, the current density prefactor in Eqn. 2.26a can be modeled using the generation-recombination current density in the depletion region [12],

$$J_{00}^{Drift} = \frac{1}{\tau} \times q\, d_i\, N_t, \tag{2.34}$$

where $N_t$ refers to the concentration of traps [$cm^{-3}$] and $\tau$ is the minority carrier lifetime [ns]. Using this simple model, it is evident that the reverse saturation density prefactor in a drift cell is dependent on the thickness of the absorber layer and the density of traps. For a hypothetical absorber with $d_i = 1\,\mu$m and a lifetime of 1 ns ($N_t = 10^{14}$ $cm^{-3}$), $J_{00}^{Drift}$ can be estimated as $1.6 \times 10^5$ mA $cm^{-2}$. While this estimate for $J_{00}^{Drift}$ is three orders of magnitude smaller than $J_{00}^{Green}$ (Eqn. 2.26b), the ideality factor for a drift cell is $n = 2$, effectively increasing the reverse saturation current density compared to that of a diffusion-based TFSC.

### 2.2.3 Efficiency Limits for a Single-Junction Solar Cell

The Shockley-Queisser (S-Q) limit has long been recognized as the theoretical upper limit estimate of the efficiency for a p-n junction solar cell. The S-Q model relates the efficiency of a solar cell to the optical band gap using a detailed balance assessment between generation of carriers and radiative recombination [44]. Using expressions for $J_{sc}$, $V_{oc}$, $FF$, and $\eta$ from the previous section, an empirical estimate for the ideal efficiency of a single junction solar cell can be plotted.

The upper maximum limit for $J_{sc}$ can be calculated using Eqn. 2.21b with the AM1.5 spectrum. To simplify the analysis, all photons above the band gap are assumed to be absorbed contributing to the photocurrent without any recombination and no reflection losses. Including the absorption coefficient, reflection losses, and recombination effects would correspondingly reduce these ideal estimates. A plot of $J_{sc}$ as a function of band gap is shown in Fig. 2.13a. $J_{sc}$ decreases with increasing band gap since a smaller portion of the incident spectrum is absorbed, resulting in a reduced density of photogenerated carriers.

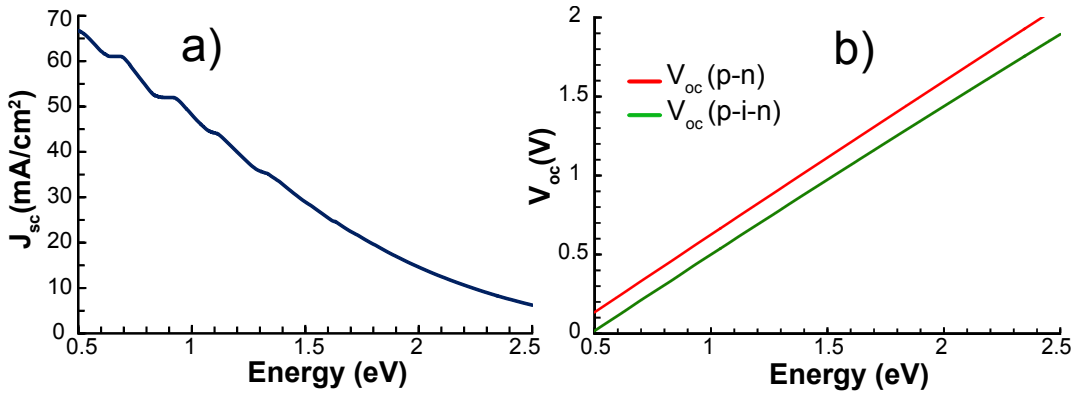


Figure 2.13: (a) $J_{sc}$, and (b) $V_{oc}$ as a function of band gap. The expression for the reverse saturation current density prefactor for a diffusion-based TFSC (Eqn. 2.26b) and a drift-based TFSC (Eqn. 2.34) is substituted in Eqn. 2.35d to estimate $V_{oc}$ for each configuration. An absorber layer thickness of $d_i = 1\,\mu$m and a lifetime of 1 ns ($N_t = 10^{14}$ cm$^{-3}$) is used to estimate $J_{00}^{Drift}$.

Equation 2.22 can be rewritten to describe the $V_{oc}$ as a function of band gap as [42],

$$V_{oc} = \frac{nk_BT}{q}\, ln\left(1+\frac{J_{ph}}{J_0}\right), \tag{2.35a}$$

$$= \frac{nk_BT}{q}\, ln\left(1+\frac{J_{ph}}{J_{00}\, exp\left(\frac{-E_G}{nk_BT}\right)}\right), \tag{2.35b}$$

$$= \frac{nk_BT}{q}\left[\left(\frac{J_{ph}}{J_{00}}\right)+\frac{E_G}{nk_BT}\right], \tag{2.35c}$$

or

$$qV_{oc} = nk_BT\left(\frac{J_{ph}}{J_{00}}\right)+E_G. \tag{2.35d}$$

The variation in $V_{oc}$ as a function of the band gap is is shown in Fig. 2.13b, calculated for the two different TFSC configurations using Eqn. 2.35d. The expression for $J_{00}^{Green}$ (Eqn. 2.26b) is used for a diffusion cell, and $J_{00}^{Drift}$ (Eqn. 2.34) for a drift cell.

To plot the variation in efficiency as a function of band gap, the fill factor (FF) has to be evaluated. While Eqn. 2.23 implies that the maximum current density and voltage need to

be measured, Green provides an empirical relation for the FF as [42],

$$FF = \frac{v_{oc} - ln\,(v_{oc} + 0.72)}{v_{oc} + 1}, \tag{2.36}$$

where $v_{oc} = \frac{qV_{oc}}{nk_BT}$ is the *normalized open-circuit voltage*. Finally, the efficiency, calculated as the product of $(V_{oc} \times J_{sc} \times FF)$ for both cell configurations is plotted in Fig. 2.14. It is seen that the maximum efficiency occurs for a range of band gaps from 1 - 1.5 eV for a single junction solar absorber with a maximum of $\sim 30\%$ at $E_G = 1.37$ eV. To boost the efficiency above this S-Q limit, multi-junction tandem cells based on III-V semiconductors have been explored for concentrator and space-based solar cell applications, achieving a maximum efficiency of 44% [39]. In addition, it is seen that a drift-based TFSC leads to a lower efficiency compared to that of a diffusion cell, due to increased recombination in the absorber layer. However, at $E_G = 1.37$ eV, the two configurations only have a 2% difference in efficiency.

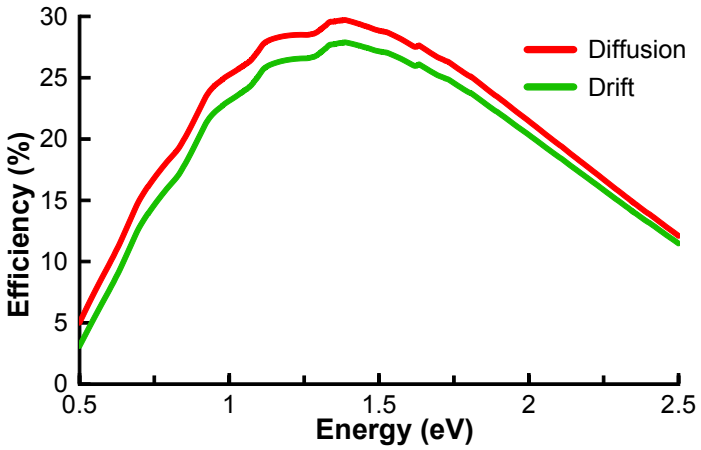


Figure 2.14: Solar cell efficiency for a single-junction cell as a function of energy band gap. The optimum band gap is between 1.1-1.5 eV, providing a theoretical efficiency as high as 30%. It is seen that a drift-type TFSC has a slightly lower predicted efficiency compared to a diffusion-based TFSC.

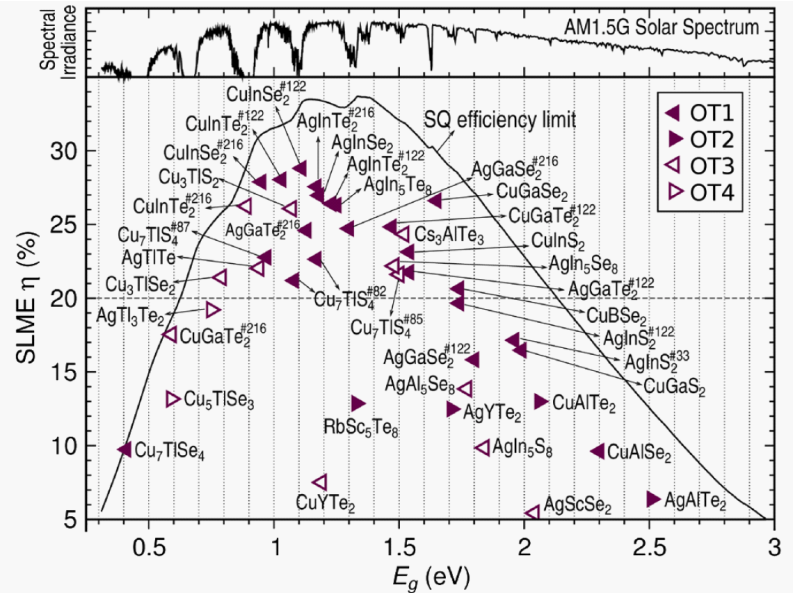


Figure 2.15: SLME efficiency as a function of band gap for various I-III-VI materials. [45]

The S-Q limit implies that any semiconductor material with a band gap between 1 - 1.5 eV should result in a high efficiency TFSC. The model does not take into account absorption characteristics or non-radiative recombination. To account for these, the spectroscopic limited maximum efficiency (SLME) was developed by Lu and Zunger, as shown in Fig. 2.15, and incorporates calculated theoretical absorption and band gap types, helping to resolve a spread of different efficiencies for materials having the same band gap value [45]. SLME can be used to screen a large subset of potential new solar absorbers and identify best-of-class materials prior to experimental synthesis.

## 2.3 Thin-Film Absorber Materials

### 2.3.1 Cadmium Telluride - CdTe

CdTe is a high-performance TFSC absorber material since its optical energy band gap, $E_G$ = 1.45 eV [46] at 300 K is in an optimal range for maximum photovoltaic energy conver-

sion, as shown in Fig. 2.14. The absorption coefficient for CdTe, plotted in Fig. 2.16, shows a direct band gap with a strong onset of absorption, reaching $1.5\times\ 10^4$ cm$^{-1}$ abruptly near the band gap energy. Absorption in CdTe is accomplished by exciting electrons from filled Te p-orbital derived valence band states to empty Cd s-orbital derived states in the conduction band. The strong onset of absorption arises as a consequence of the direct band gap nature of CdTe and allows the absorber layer to be 2 $\mu$m thick [5] (in contrast to 200 $\mu$m, which is the required thickness for a crystalline silicon solar cell [24]) and still provide high efficiency cells. Since the conduction band minimum is derived from Cd-s orbital derived bands which have low dispersion, CdTe has electron mobilities as high as 320 cm$^2$/V-s and hole mobilities of 40 cm$^2$/V-s [31]. First principle calculations have shown that CdTe has a strong tendency to self compensate with increasing p-type doping [47] [48]. With increasing acceptor-type doping, as the Fermi level shifts towards the valence band maxima, the formation energy to create compensating donor-type defects decreases [5]. This neutralizes (or compensates) further acceptor doping, limiting the maximum hole concentration in CdTe to $\sim 10^{15}$ cm$^{-3}$.

Closed-space sublimation (CSS) is the most common deposition technique employed for CdTe thin-films. Solid CdTe is heated in medium vacuum ($P_{base} \sim$ 5 mTorr) at T $>$ 500°C where the source material evaporates congruently and condenses onto a heated substrate maintained at a temperature between 400 - 600° C [50]. A small separation distance is maintained between the source and substrate, resulting in a high deposition rate ($>$ 10 $\mu$m/min) even in a continuous inline manufacturing process [51].

In the construction of a CdTe-based TFSC, (see inset of Fig. 2.16) an n-type buffer layer, CdS, is deposited using a solution-based chemical bath deposition (CBD) technique. In this process, the substrate is inserted into a solution heated to 80°C containing $Cd^{2+}$ and

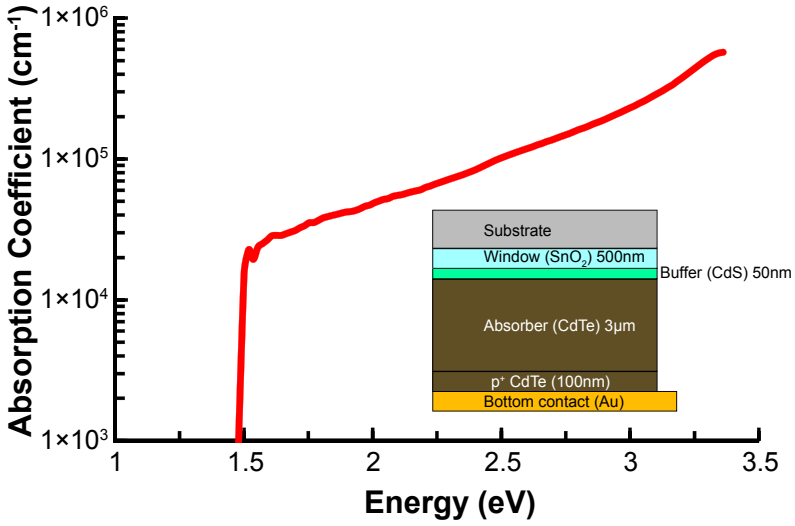


Figure 2.16: Absorption coefficient plot for CdTe [49]. (Inset) CdTe TFSC device structure. The TFSC is illuminated through the glass substrate, known as *superstrate* configuration.

$S^-$ ions, leading to the spontaneous formation of CdS thin films on the substrate [40]. The CdS buffer layer is subsequently covered by $SnO_2$, a transparent conductive oxide (TCO). This layer is typically deposited using a spray-on process by dissolving $SnCl_4$ in water and spraying onto a heated substrate exposed to air. Alternatively reactive oxide sputtering using a metallic Sn target is sometimes used. The complete cell structure is shown in the inset of Fig. 2.16. The difference in lattice constants between CdS (a = 4.135 Å [25]) and CdTe (a = 6.46 Å [25]) leads to a significant density of interface states which act as recombination centers. As-deposited devices show low charge collection and result in low efficiencies [52]. However, dramatic improvement in device efficiency is achieved using a $CdCl_2$ post-deposition *activation* step [24]. While there is no consensus on the role of this step, several improvements have been attributed to it. This step not only promotes recrystallization and grain growth [52], but also facilitates intermixing between CdS and CdTe [40], reducing the effects of the lattice mismatch and recombination centers. This activation treatment also pas-

sivates grain boundaries, leading to an increase in the minority carrier lifetime of electrons [24] in the CdTe absorber.

Device simulations [33] [53] indicate that CdTe is indeed a high-performance TFSC absorber. Efficiencies as high as 22% have been predicted based on numerical simulation by Sites and Pan [33] provided that the CdTe layer has a carrier concentation of $N_A = 10^{13}$ cm$^{-3}$ with a minority carrier lifetime of 2 ns and an electron reflector providing an energy barrier of 0.2 eV at the back contact. However, laboratory scale devices have not reached these high efficiencies for several reasons. The work function of CdTe is estimated to be $\sim$ 5.51 eV [54]. As a result, forming an ohmic contact is difficult even when a high work function material such as Au ($\Phi$ = 5.1 eV [55]) is used. Spies et al. use non-ideal Schottky barrier theory to show that the metal work function value required to form an ohmic contact with CdTe is significantly larger than commonly used contact materials [54]. Besides a simple metal-semiconductor ohmic contact, tunneling contacts are also difficult to realize due to self-compensation of CdTe, as discussed previously in this subsection. As a result, developing an effective back contact strategy for a CdTe solar cell is an art form and various solutions have been proposed. Cu/Te double layer thin films have been explored, which form $Cu_2Te$ upon annealing. This has the dual advantage of *(i)* forming a Te-rich $p^+$ back contact ($Cu_2Te$: $E_G^{ind}$ $\sim$ 0.5 eV, p $\sim$ $10^{20}$ cm$^{-3}$ [25]) at the backside and *(ii)* Cu migrating into the CdTe layer [5], potentially increasing the hole concentration of the doped or alloyed interfacial layer. In addition, during device processing, it is common to chemically etch the CdTe layer after the $CdCl_2$ treatment and prior to back (bottom) contact processing, resulting in the formation of a Te-rich layer back surface [56]. Thus, the lower carrier concentration of the CdTe film, in

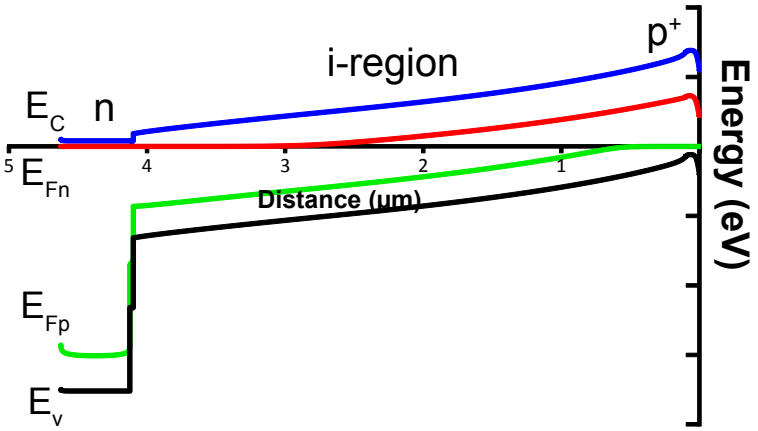


Figure 2.17: Energy band diagram of a CdTe TFSC. The internal electric field drops across the entire CdTe absorber, resulting in an $n^+$-p-$p^+$ configuration, where carrier transport is governed by drift.

addition to the $p^+$ back contact results in a device configuration resembling that of a $p^+$-i-n junction [57], as shown in Fig. 2.17, where carrier transport is governed by drift.

Wu [58] at NREL, developed a variety of strategies to fabricate a 16.5% efficient CdTe-based TFSC including use of an alternative window material, $Cd_2SnO_4$ (CTO), to replace $SnO_2$, use of a high resistivity ZTO buffer layer between CTO and CdS, increasing the thickness of CdTe to 10 $\mu$m and forming a back contact comprised of a HgTe:CuTe-doped graphite paste and a layer of Ag paste. Module efficiencies from First Solar are currently as high as 11.5%. Recently, GE Research reported an 18.3% efficient laboratory scale [39] device, indicating that CdTe is becoming a leading TFSC player. However, the toxicity of Cd along with the questionable elemental abundance of Te may possibly limit large scale implementation of CdTe-based thin-film photovoltaics.

### 2.3.2 Cu(In,Ga)$Se_2$ - CIGS

Cu(In, Ga)$Se_2$ (CIGS)-based TFSCs currently have the highest efficiency among TFSCs, with laboratory scale devices reaching 20% in 2009 fabricated by NREL [26] and module efficiency greater than 13% developed by MiaSolè [39]. This sucess is built on early work developing $CuInSe_2$ (CISe)-based solar cells by Wagner *et al.* at Bell labs, who reported a 5% efficient solar cell by evaporating n-type CdS onto a p-type CISe single crystal in 1975 [59]. Kazmerski *et al.* fabricated the first CISe-based TFSC in 1976 [60], following which, Boeing and ARCO pioneered development of CIGS-based TFSCs leading to a 14.1% efficient TFSC as early as 1988 [61].

The copper chalcopyrite system, Cu(In, Ga, Al)(S, $Se)_2$ includes a wide range of band gap energies ranging from 1.04 eV for CISe to 2.7 eV for $CuAlSe_2$ [25], spanning the entire solar spectrum. In addition, all compounds within this family exhibit a direct band gap [46]. The VBM in CISe is comprised of Cu-d orbital and Se-p orbital derived bands, while the CBM is composed of In-s orbital and Se-p orbital derived bands [62]. The direct band gap nature, coupled with narrow Cu-d orbital derived bands in the VBM and allowed transitions between Cu-d $\rightarrow$ Se-p as well as Se-p $\rightarrow$ In-s orbital derived bands result in the strong onset of absorption for CIGS, shown in Fig. 2.18. CISe typically has a band gap between 0.9 - 1.05 eV [25], slightly lower than the optimal value for a solar absorber based on the S-Q limit [44]. As a result, CISe is commonly alloyed with $CuGaSe_2$ ($E_G = 1.66$ eV [25]) to increase the optical band gap value and match the S-Q limit peak. The ratio of Ga:In = 30:70 provides an optimal band gap of 1.1 eV [27]. Since the CBM is comprised of In-s orbital derived bands, CISe has mobility values as high as 100 and 25 $cm^2\,V^{-1}s^{-1}$ for electrons and holes, respectively [31]. Typical minority carrier lifetimes are between 1 - 10 ns for laboratory-scale

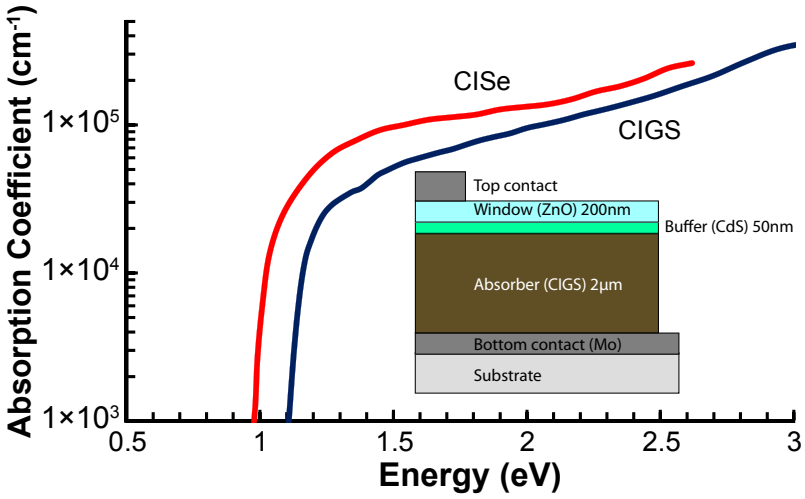


Figure 2.18: Absorption coefficient plot for CISe and CIGS. (Inset) CIGS TFSC device configuration.

devices, however the highest efficiency CIGS-based TFSC had a minority lifetime of 100 ns [26], indicating a high quality absorber layer.

CIGS is typically deposited under Cu-deficient conditions [5] resulting in a carrier concentration of $N_A \sim 10^{16}$ cm$^{-3}$ [31]. The main acceptor-type defect in CIGS is typically Cu vacancies ($V_{Cu}$) which have a low defect formation energy ($\Delta H_f$ = - 2 eV) [63]. However, the neutral defect pair ($2V_{Cu}$ + $In_{Cu}$), i.e., 2 copper vacancies and an indium antisite, has a lower formation energy ($\Delta H_f$ = - 1.4 eV) but is electrically inactive [48]. This low defect formation energy results in ordered defect compounds (ODCs) in CIGS [64] [65]. Under Cu-deficient growth conditions, the surface layer can form ODCs with a stoichiometry of $CuIn_5Se_8$, $CuIn_3Se_5$, $Cu_2In_4Se_7$, and/or $Cu_3In_5Se_9$ [63] which are all n-type [66] [67]. The presence of this ODC layer on the surface of a CIGS thin-film facilitates formation of a p-n homojunction and reduces interfacial recombination at the CdS-CIGS interface [68], thereby increasing the efficiency of a CIGS-based TFSC.

The two most common CIGS deposition techniques are *co-evaporation* and *selenization*. In the co-evaporation process, the four elements (Cu, In, Ga and Se) are thermally co-evaporated onto a heated substrate maintained at $\sim 500\ ^{\circ}$C [5] where Cu(In,Ga)$Se_2$ spontaneously forms due to intermixing. Each of the sources can be individually controlled, allowing for tunable composition during film growth. Since selenium has the highest vapor pressure among the elements [69], it is typically evaporated in excess [5]. In the 1980s, Boeing pioneered the bilayer process, where deposition begins in a Cu-rich condition which provides a large grain size [32], following which, the Cu/(In+Ga) ratio is reduced such that a Cu-deficient composition is achieved [70]. A three-stage co-evaporation process was also developed, where In, Ga and Se elemental sources are initially evaporated onto a substrate maintained at 300 $^{\circ}$C [32]. In the second stage, Cu and Se are evaporated at temperatures higher than 500 $^{\circ}$C to form a Cu-rich composition. Finally, in the third step, In, Ga and Se are evaporated to ensure that the overall In-rich, Cu-deficient composition is achieved. Films grown using this approach have an increased Ga/(In+Ga) ratio (larger band gap) towards the back of the film, giving rise to a band gap gradient between the bottom of the film and the top. In the selenization process, the deposition and compound formation occur in two different steps. A common approach is to deposit the metal precursors (Cu, In and Ga) using DC sputtering and then anneal the film in a $H_2Se$ environment at elevated temperatures [71]. Alternatively, all four elements can be deposited sequentially and subjected to a rapid thermal anneal in a Se environment [72]. While devices based on the selenization process have a lower efficiency than films deposited using the co-evaporation process (16% [73] in comparison to 20% [74]), the selenization process is favored by industrial manufacturers, since sputtering can be used to deposit the precursors over large areas. The device configuration for

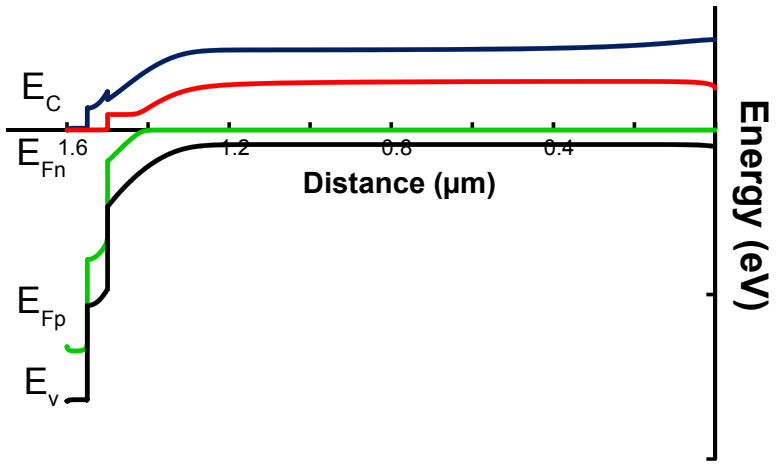


Figure 2.19: Representative energy band diagram for a CIGS-based TFSC. A wider band gap corresponding to CGS ($E_G$ = 1.6 eV) is included to show the effects of band-gap grading towards the back contact. The band-gap grading provides a back-surface field and reduces recombination at the back contact.

a CIGS-based TFSC, known as a substrate configuration, is shown in the inset of Fig. 2.18, and a corresponding energy band diagram is shown in Fig. 2.19. Here, molybdenum (Mo) is used as the bottom contact above which the CIGS layer is deposited using techniques outlined above. A thin (50 nm) CdS layer is deposited above the absorber as an n-type buffer layer, above which indium tin oxide (ITO) or Al-doped ZnO forms the top transparent contact.

Several salient aspects provide for a high efficiency CIGS-based TFSC. The addition of Ga during CIGS deposition results in a band gap gradient across the absorber layer, such that the bottom of the film has a higher band gap than the top [75]. Figure. 2.19 shows a representative energy band diagram with band gap grading towards the back contact. While not as pronounced as the back contact barrier in a CdTe-based TFSC (refer to Fig. 2.17), band gap grading provides a back-surface field to reflect stray electrons towards the n-type contact, thereby reducing recombination at the back surface. Similar to CdTe, the work function of CISe and CGS ranges between 5.3 [76] - 5.4 eV [77], and as a result, common

metals would not provide an ohmic contact [54]. During the absorber deposition process, a thin $MoSe_2$ layer ($\sim$ 10 nm) typically forms between the CIGS absorber and the Mo back contact [78]. $MoSe_2$ is a p-type semiconductor with a band gap of 1.3 eV [79]. The larger band gap of $MoSe_2$ compared to CIGS provides an electron mirror at the absorber back surface (in addition to band-gap grading) to mitigate minority carrier recombination at the back contact. In addition, Kohara *et al.* show that the presence of a $MoSe_2$ at the CIGS/Mo contact facilitates the formation of an ohmic contact [80]. The choice of glass substrate (fused silica, borosilicate glass or soda-lime glass) can also affect the device efficiency in a CIGS-based TFSC. During growth of the absorber layer, sodium (Na) can be unintentionally introduced into the CIGS layer by diffusion from a soda-lime glass substrate through the Mo back contact. Several models have been proposed to understand the role of Na on device performance. Na incorporation is believed to passivate CIGS grain boundaries and promote grain growth [81] [82]. Contreras *et al.* incorporated 20 nm of NaF between the absorber and Mo back contact and observed a higher device efficiency when compared to a control sample with no Na incorporation. These authors observed an enhancement of the grain-size along with an increase in the $V_{oc}$ and FF, and measured an increased carrier concentration for CIGS with Na incorporation. Thus, the presence of $MoSe_2$ and Na incorporation at the back surface aids in the formation of an effective back contact.

CIGS-based TFSCs currently have the highest laboratory scale efficiencies, reaching 20% in 2003 [26]. However, maintaning the appropriate CIGS composition reproducibly over large areas has made scaling-up challenging, along with the high production costs to manufacture a CIGS-based TFSC [83]. In addition, the rising costs and questionable ele-

mental abundance of In can possibly limit the large scale implementation of CIGS-based TFSCs.

### 2.3.3 Amorphous Silicon

The first amorphous silicon (a-Si)-based TFSC was fabricated by Carlson and Wronski in 1976 [84] with a photo-conversion efficiency of 2.4%. Subsequently, solar cells fabricated in the 1980s were widely used in low power consumer applications such as hand-held calculators [41]. Unlike CdTe or CIGS which are polycrystalline and exhibit long-range order, a-Si is amorphous, characterized by short-range structural order but long-range disorder resulting in opto-electronic properties that are significantly different than those of crystalline silicon (c-Si). The lack of long-range order in a-Si implies that there is no well defined E-$k$ relationship. As a result, conservation of crystal momentum is not relevant in a-Si [7]. The amorphous microstructure in a-Si results in lower carrier mobilities and shorter minority carrier lifetimes [85], resulting in poor transport properties compared to c-Si.

a-Si is typically prepared by plasma-enhanced chemical vapor deposition (PECVD) [5], which relies on the decomposition of silane gas ($SiH_4$). This technique proved beneficial in the development of a-Si, since it allowed the incorporation of hydrogen into the thin film. Prior to 1969, a-Si films were primarily deposited using PVD techniques which resulted in films with a defect density $> 10^{19}$ cm$^{-3}$ [79]. In c-Si, each silicon atom is tetrahedrally bonded to four other silicon atoms. Due to the amorphous, random microstructure in a-Si, each silicon atom may not be bonded with four silicon atoms, resulting in the presence of a large density of dangling bonds [5]. Hydrogen present in silane during thin-film fabrication passivates these unterminated silicon bonds and reduces the defect density to $10^{15}$ - $10^{16}$ cm$^{-3}$ [62]. Thus, a-Si thin films used for TFSCs are primarily called hydrogenated

amorphous silicon (a-Si:H). Similar to c-Si, a-Si:H can be doped both *n*- and *p*-type by the addition of phosphorus or boron [86]. An inherent advantage of using PECVD to deposit a-Si:H thin-films is that the constituent dopant can be introduced via the process gas during film deposition [32]. However, incorporation of these dopants into a-Si:H introduces additional mid-gap trap states, further reducing the minority carrier lifetime [79]. As a result, unlike c-Si, the doped layers are not utilized as the active absorber layers. Alloying a-Si:H with Ge or C provides the ability to tune the band gap of a-Si:H. Band gap values as low as 1.3 eV can be obtained for a-Si:Ge:H and 2.0 eV for a-Si:C:H [41], allowing the development of tandem, or multi-junction TFSCs.

The optical absorption characteristics comparing c-Si and a-Si:H is shown in Fig. 2.20. Unlike c-Si which is an indirect band gap semiconductor exhibiting a non-abrupt, sluggish onset of absorption at $E_G = 1.1$ eV, the absorption coefficient for a-Si:H exhibits a steep onset of absorption near the band gap, and exhibits strong absorption across the entire solar spectrum. Hydrogen incorporation in a-Si:H not only serves to passivate unterminated silicon bonds, but also serves to increase the band gap compared to c-Si. Typically 5 - 10% hydrogen is incorporated into the a-Si:H film, increasing the band gap to $E_G \sim 1.7$ eV [41]. The band-gap of an a-Si:H thin-film can be estimated from a Tauc plot [87], which is a plot of $(\alpha \times E)^{1/2}$ versus energy, as shown in Fig. 2.20(b). The x-intercept provides a band-gap for a-Si:H as 1.7 eV.

Besides the absorption coefficient, the amorphous microstructure affects transport properties of a-Si:H. Due to the lack of long-range order, carrier mobilities in a-Si:H are much lower than c-Si, typically on the order of 1 and 0.1 $cm^2\ V^{-1}s^{-1}$ [88], for electrons and

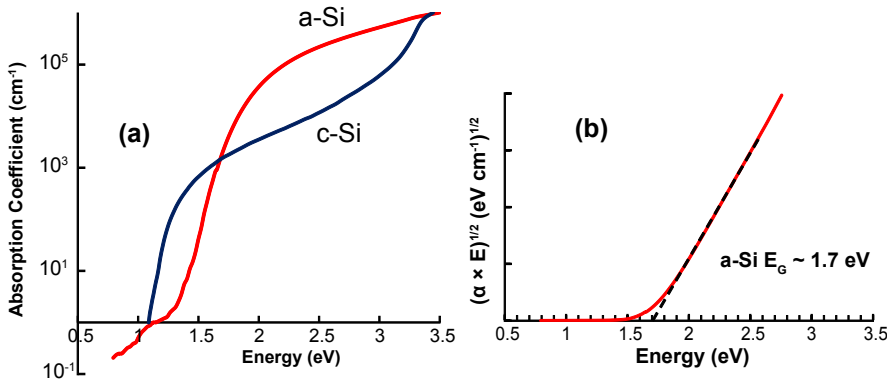


Figure 2.20: (a) Absorption coefficient plot comparing c-Si and a-Si, and (b) band gap estimation for a-Si as $E_G \sim 1.75$ eV.

holes respectively. Undoped a-Si:H typically has a carrier concentration between $10^{14}$ - $10^{15}$ $cm^{-3}$ [79].

Since a-Si:H has poor transport properties compared to c-Si, utilizing a-Si:H in a diffusion-cell configuration would yield a low photo-conversion efficiency. As a result, a-Si:H-based TFSCs are commonly employed in a drift-cell configuration [41] as shown in Fig. 2.21 The inset of Fig. 2.21 shows a superstrate device structure consisting of the following layers: substrate/ n-TCO/ a-Si:H (p)/ a-Si:H (i)/ a-Si:H (n)/ aluminum contact. To reduce light absorption and recombination in the doped layers, their thickness is constrained to 10 - 20 nm [5], while the intrinsic a-Si:H is typically $\sim$ 500 nm thick [89]. The p-i-n (drift-cell) configuration is beneficial for an a-Si:H TFSC, since the doped layers provide a large built-in electric field across the intrinsic absorber layer, effectively sweeping the slow moving photogenerated carriers towards their respective contact. Since the band gap of a-Si:H is higher than the optical range required for solar absorption, a multi-junction TFSC is commonly fabricated using a-Si:Ge:H and/or a-Si:C:H [41] to boost the efficiency.

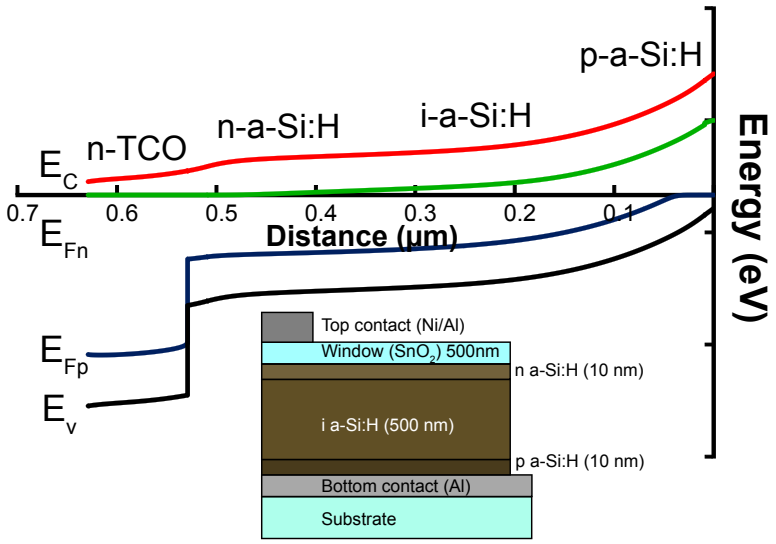


Figure 2.21: Energy band diagram for an a-Si:H TFSC corresponding to a p-i-n (or drift-cell) configuration and, (inset) device configuration.

Currently, a-Si:H-based TFSCs exhibit efficiencies $\sim$ 10% [39]. One reason for the low efficiency is the Stabler-Wronski effect (SWE) [90], or light-induced degradation of a-Si:H. Under illumination, the conductivity of an a-Si:H thin-film degrades and can be reduced by as much as an order of magnitude [79]. While this effect is reversible, via annealing of the thin film at T $\sim$ 150°C [24], it results in up to a 30% reduction of cell efficiency within six months ($\sim$ 1000 hours) [5]. SWE is ascribed to the light-induced creation of additional defects in a-Si:H [32], which serve as recombination centers. To mitigate the SWE, a-Si:H thin films are commonly deposited using a mixture of silane and hydrogen to increase the concentration of hydrogen incorporated into the growing a-Si film [79] which alters a-Si to a nano- or microcrystalline structure [41], which is more stable than a-Si:H. While a-Si:H provides a route for low-temperature deposition along with fabrication over a large area and on a variety of substrates, the inherent instability and lower efficiencies compared to other TFSC technologies can limit the large-scale commercialization of a-Si:H-based TFSCs.

### 2.3.4 Iron Pyrite - $FeS_2$

Iron pyrite, $FeS_2$ has attracted a lot of attention as an Earth-abundant solar absorber material since iron and sulfur are among the most abundant elements in the Earth's crust [91]. Pyrite has an optical energy gap, $E_G$ between 0.85 eV to 0.95 eV depending on the method of preparation. Ennaoui *et al.* measured the absorption properties of $FeS_2$ thin-films fabricated via MOCVD and reported an exceptionally strong absorption coefficient reaching $\alpha = 5 \times 10^5$ cm$^{-1}$ at $E_G$ + 0.6 eV [92], as a result of an abrupt onset of absorption, shown in Fig. 2.22. The VBM in pyrite is composed of sulfur p-orbital and partially-filled iron d-orbital-derived bands, while the CBM is composed of partially-empty iron d-orbital bands [92]. The presence of narrow d-orbital-derived bands at both the VBM and CBM along with allowed p $\rightarrow$ d transitions results in the strong absorption observed in pyrite. This high absorption coefficient is larger than that of current TFSC absorbers and implies that the active thickness required for pyrite to absorb the entire solar spectrum is only 100 nm [93]. The low thickness requirement along with cheap and abundant elements in the $FeS_2$ composition makes pyrite attractive as a solar absorber material.

Pyrite thin-films have been fabricated via numerous techniques including sulfurization of iron films [94], sulfurization of iron oxide films [95], RF magnetron sputtering using an $FeS_2$ sputter target, MOCVD [96], and CVT [97] techniques. Tributsch *et al.* used reactive RF magnetron sputtering of an Fe target using a mixture of Ar/$H_2S$ (20/80) as the process gas with a 200°C substrate temperature [98]. The 200°C substrate temperature was necessary to avoid formation of the marcasite phase, while sulfur-deficient phases began to form at temperatures above 200°C. Marcasite has the same chemical formula as pyrite ($FeS_2$), however it has a band gap of 0.34 eV and a different crystal structure [99]. Compositional analysis of

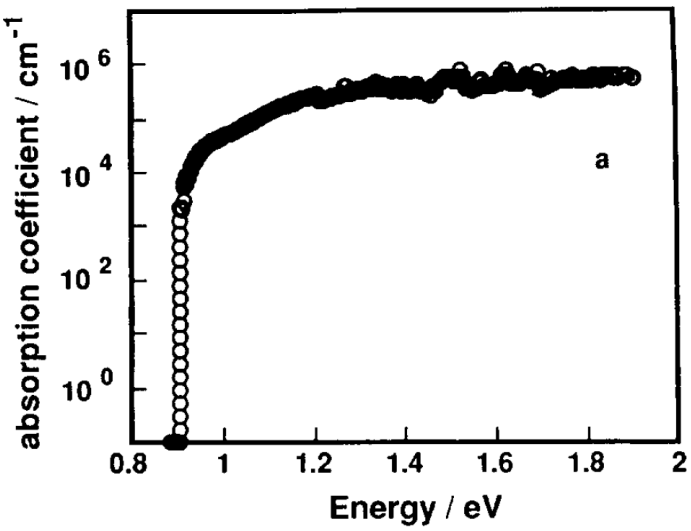


Figure 2.22: Absorption coefficient plot for $FeS_2$ thin-films fabricated via MOCVD [92]. The thin-film has a band gap of 0.95 eV and an absorption coefficient reaching a maximum value of $\alpha = 5 \times 10^5$ cm$^{-1}$

the sputtered thin-film indicated a S: Fe ratio of $\sim$ 1.8, indicating a slightly sulfur-deficient thin-film. $FeS_2$ thin films were p-type based on Hall measurements with a hole mobility of 25 cm$^2$ V$^{-1}$s$^{-1}$, and a carrier concentration between $10^{19}$ - $10^{20}$ cm$^{-3}$, indicating degenerate p-type semiconductor behavior. Willeke *et al.* investigated properties of sputtered pyrite thin films using an $FeS_2$ sputter target [100]. The authors demonstrated that using pure argon as the process gas resulted in films with a significant lack of sulfur. In addition, using other inert gases or inert gas mixtures did not lead to any further improvement, while incorporating a thermally-evaporated sulfur source led to an unstable plasma [100]. Hall measurements indicated p-type thin-films with a hole carrier concentration of $5 \times 10^{18}$ cm$^{-3}$ and a measured mobility value of 5 cm$^2$ V$^{-1}$s$^{-1}$, a value much lower than that reported by Tributsch *et. al.*

Wagner demonstrated a pyrite-based solar cell by evaporating a CdS thin-film onto a polished pyrite single crystal, and measured a maximum photovoltage of 70 mV [93]. Schottky barrier solar cells were explored by depositing thin (5 - 10 nm) metal layers of Pt, Nb or

Au onto chemically-etched n-$FeS_2$ single crystals by Tributsch *et al.* [101]. Electrical characterization indicated poor rectification behavior with virtually no photovoltage. However, photocurrents close to 30 mA $cm^{-2}$ were obtained from an n-pyrite / Pt device [92].

Photoelectrochemical (PEC) measurements have been relatively successful in demonstrating the photovoltaic potential of pyrite. A PEC cell based on an n-type $FeS_2$ crystal using an iodide/tri-iodide electrolyte solution was fabricated as early as 1986 [102]. Under illumination, a $J_{SC}$ of 40 mA $cm^{-2}$ was measured with a $V_{OC}$ of 200 mV. Pre-treating the single crystals to passivate the surface resulted in an increased $J_{SC}$. However the $V_{OC}$ was limited to 200 mV regardless of optimization. This value for $V_{OC}$ is less than the ideal maximum for $FeS_2$ ($\sim$ 500 mV) and has been commonly interpreted to be due to sulfur vacancies [92]. These sulfur vacancies can induce charged defect states within the band gap, pinning the Fermi level [103] at a fixed energy level, screening any additional applied voltage.

Recently, sulfurization of a 400 nm iron oxide thin film deposited by successive ionic layer adsorption and reaction (SILAR) was explored as a non-vacuum and low-cost deposition route towards pyrite thin-films [104]. The authors measured an indirect band gap of 0.75 eV, which is lower than values obtained via physical vapor deposition techniques. Hall measurements indicated a hole carrier concentration of $2.5 \times 10^{18}$ $cm^{-3}$ and a carrier mobility of 12 $cm^2\ V^{-1}\,s^{-1}$. PEC measurements indicated the presence of a small photocurrent, but no $V_{OC}$ values were reported. Thus, despite early identification of pyrite as a promising absorber material, extensive development is still required to realize a pyrite-based TFSC.

## 2.4 Summary

In this section, the interaction between light and a semiconductor material is described to understand the necessary parameters required to maximize light absorption in a material. A brief solar cell device physics primer is presented, following which efficiency limits for a single-junction solar cell are discussed. Finally, current solar cell absorber materials are outlined.

# 3. EXPERIMENTAL TECHNIQUES

This chapter describes the fabrication and characterization techniques utilized in this study. Two physical vapor deposition techniques utilized to deposit the absorber materials, RF magnetron sputtering and electron beam evaporation, are discussed initially. To adjust the composition, the as-deposited films are subjected to an anneal step described next. Structural, optical, and electronic characterization of the absorber layer follows. Lastly, device performance of the absorber layer is explored by utilizing a thin-film solar cell simulation software - SCAPS, Solar Cell Capacitance Simulator, developed by the University of Gent.

## 3.1 Thin Film Fabrication

RF magnetron sputtering and electron beam evaporation used to deposit thin films of the absorber materials are discussed in this section. All films used in this research are deposited using the Chalcogenide Deposition System (CDS) designed and developed at Oregon State University by Chris Tasker. The CDS is equipped with two rf magnetron sputter guns, an electron beam evaporator, and a thermal evaporator. In addition, the system has the ability to provide substrate heat and rotation to maintain uniformity.

### 3.1.1 RF Magnetron Sputtering

In a sputter process, a target of the intended material is bombarded by energetic ions, causing ejection of atoms from the surface of the target. The most common sputter technique is DC sputtering which is composed of two parallel plate electrodes. One electrode is connected to the target and is referred to as the cathode, since it is negatively biased. The other electrode is referred to as the anode and is attached to the substrate.

To begin the sputter process, the deposition system, which is initially evacuated to a low base pressure ($10^{-7}$ - $10^{-8}$ Torr) is filled with the sputter gas (or process gas), typically argon which increases the pressure in the chamber to $20 - 40$ mTorr . A stray electron knocks into an argon atom with sufficient energy to ionize it and eject an additional electron. This results in a cascade reaction giving rise to a large number of ionized $Ar^+$ ions and electrons. When a DC bias is applied across the electrodes, the $Ar^+$ ions are attracted towards the cathode and bombard the surface of the target. This results in the ejection of atoms from the target surface which diffuse towards the substrate resulting in film growth. Most of the voltage drop occurs across a sheath next to the cathode, a region known as the *cathode sheath* [105]. This results in bombardment by high energy ions causing sputtering of the target. This voltage drop also sustains the plasma by accelerating secondary electrons from the target towards the plasma causing further ionization. The collective mixture of $Ar^+$ ions, target atoms and electrons is referred to as a glow discharge plasma. The plasma has a characteristic color associated with the sputter gas. This is due to recombination of the ionized ions and free electrons, emitting a photon as the ionized ion relaxes back to ground state.

DC sputtering is efficient only for metallic targets (or conducting materials). When a surface is inserted into the plasma, it becomes negatively charged. For an insulating material, the impinging ions neutralize the surface and charged ions are no longer attracted to the surface ejecting target atoms. By applying an AC potential instead of a DC bias on the target, the oscillating nature of the potential ensures that the plasma can be sustained. A frequency of 13.56 MHz is chosen as the oscillation frequency, since at such high frequencies ions are too large to respond to the frequency change. However, the electrons respond faster and result in a net negative self bias on the target. The frequency value of 13.56 MHz is chosen

intentionally since it lies in the industrial, scientific and medical (ISM) radio bands allotted internationally for applications besides communication [106]. The basic configuration for an RF sputter system is shown in Fig. 3.1.

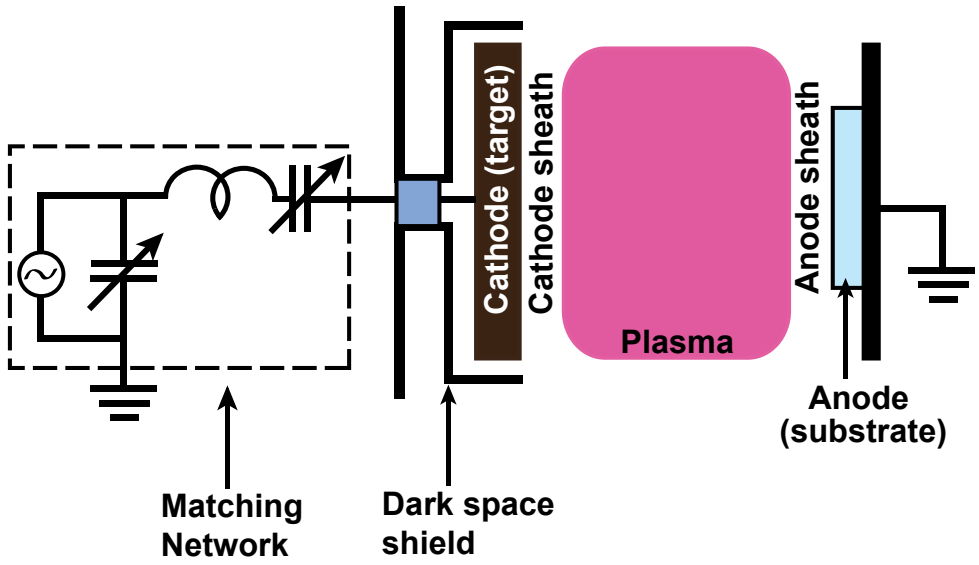


Figure 3.1: Schematic representation of the basic components in an RF sputter system.

Following secondary electrons ejected from the target in Fig. 3.1, they first cross the cathode dark space, or *cathode sheath*. This region is named so since the cathode is negatively biased attracting ions and repelling electrons. As a result, there is little recombination between the two species in this region to cause the emission of photons. They then pass through the *plasma* region, where they ionize gas molecules and recombine with ionized atoms. Close to the anode is another dark space called the *anode sheath*, since the positive bias repels ionized gas molecules resulting in low recombination. The substrate is placed next to the anode sheath since here the ionized atoms do not have sufficient energy to cause re-

sputtering of the growing film. Near the cathode is a *dark space shield*. This shield shrouds the target and limits the location of the plasma thereby preventing the sputtering of regions behind the target such as the cooling water lines and insulation between the cathode and the chamber.

The AC bias is usually maintained by an RF matching network as shown in Fig. 3.1. The function of the matching network is to transform the complex impedance characteristics of the plasma to 50 Ω which is the industry standard for AC function generators. Replacing the DC bias with an AC potential is an added advantage since the oscillatory nature of the potential increases the probability of collisions between the secondary electrons and the process gas [105]. This results in a higher plasma density and reduces the operating pressures to lower values. To improve the efficiency of the sputter yield, magnets are employed to control the behavior of electrons close to the surface of the target. The effect of the magnetron configuration is shown in Fig. 3.2. Electrons in a magnetic field are subject to a Lorentz force which causes them to spiral along magnetic field lines in a helical path [107]. This increases the effective path length of the electrons and increases the probability of ionizing the process gas. In addition, the electrons are strongly constrained near the target surface increasing the ion bombardment of the target, and thus, the sputter yield.

The CDS is equipped with two RF magnetron sputter guns from AJA Inc., incorporating 2" sputter targets and has a vacuum range of $10^{-8}$ torr to $10^{-2}$ torr. A mixture of Argon/Helium (60/40) is used as the process gas and is maintained at 20 standard cubic centimeters per minute (sccm) via an MKS mass flow controller. Commercial sputter target vendors provide targets for common materials; however, new chalcogenide materials investigated in this work were developed by the chemistry department at Oregon State University.

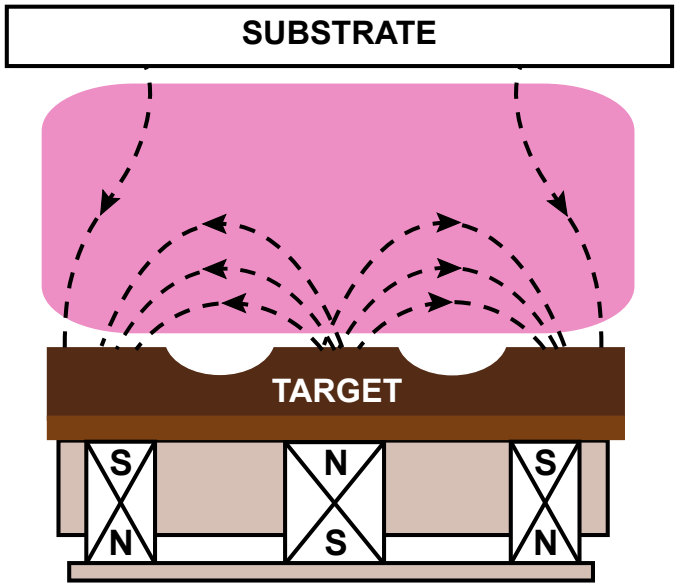


Figure 3.2: Planar magnetron configuration underneath a sputter target The magnetic field around which electrons are confined is indicated. This confinement results in preferential sputtering in certain regions of the target causing the formation of a *racetrack* on the surface.

When utilizing targets developed in house, it is important to ensure their high density. Sputtering from a low density target can release trapped gases (air pockets) causing a sudden spike in pressure, which can turn off the plasma. In addition, a low density target can cause the sputtering of large atomic species which can give rise to non-stoichiometric films and bouldering of the growing film. Typically, sputter targets with density $> 90\%$ are required for films with optimal properties. To mitigate development of sputter targets, electron beam evaporation is also explored as a viable PVD technique to grow thin films.

### 3.1.2 Electron Beam Evaporation

Electron beam (e-beam) evaporation is another PVD technique; however, the operating mechanism is different from that of sputtering. While sputtering relies on ion bombardment of a target to facilitate film growth, e-beam evaporation relies on thermal evaporation of a

source material to generate a flux of evaporant species. E-beam evaporation utilizes high energy electrons accelerated through a magnetic field causing localized heating of the source material resulting in evaporation or sublimation [106]. Thermal evaporation on the other hand relies on the passage of current across a boat containing the source material resulting in evaporation due to resistive heating. While thermal evaporation is sufficient for materials with low melting temperatures such as aluminum ($T_m$ = 660°C) or tin ($T_m$ = 232°C) [69], very large currents are required to evaporate materials with high melting temperatures such as molybdenum ($T_m$ = 2623°C) or tantalum ($T_m$ = 3017°C) [69]. To circumvent this, high energy electrons can be used to facilitate evaporation of the source material. Since the energy of the electrons can be controlled, e-beam evaporation can ideally be used to evaporate any material; metallic, or insulating.

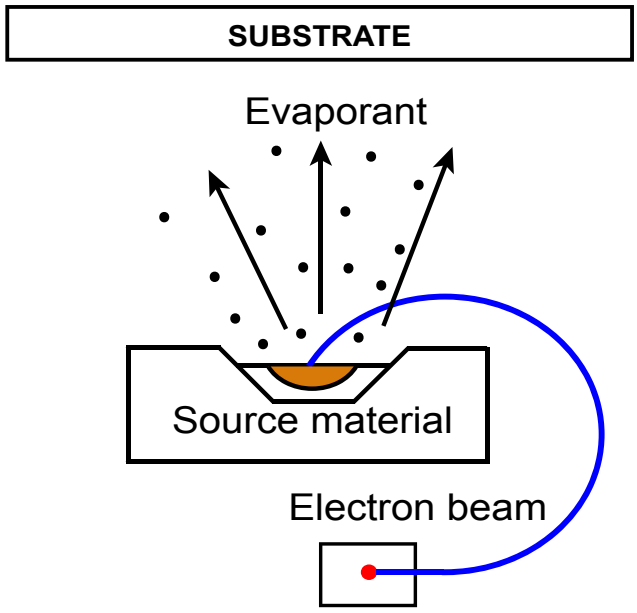


Figure 3.3: Schematic representation of an elecron beam evaporator.

The basic mechanism for e-beam evaporation is shown in Fig. 3.3. A tungsten filament is heated to sufficiently high temperatures causing thermionic emission of electrons. These electrons, guided into a beam, are deflected and accelerated towards the source material which is placed in a graphite crucible. The source material is maintained at a large positive bias to accelerate and attract the electron beam [106]. The deflection of electrons is achieved using a permanent magnet (commonly referred to as the *deflection magnet*) which causes a 270° rotation of the e-beam [107]. When the high energy electrons strike the surface of the source material, the kinetic energy of the electrons is translated into thermal energy which causes localized heating and subsequently evaporation or sublimation. The heating of the source material causes a vapor flux which arrives on the substrate forming a thin film. To understand the power delivered by the e-beam, we can make a simple calculation. For a system designed for 1 A of emission current accelerated through a potential of 10 kV, the power delivered to the source material is 10 kW. Due to the large amount of heat generated by the e-beam, the crucible is water cooled. Another reason for the deflection magnet is to protect the filament from contamination by the source evaporant [106]. As a result, the filament is not located in the line of sight of the evaporant as shown in Fig. 3.3. Typically, the potential is kept constant while the emission current is varied as a percentage of the full scale to cause evaporation.

To improve deposition uniformity, the e-beam can be rastered across the source surface. This is accomplished by a second electromagnet called a *steering magnet*. Controlling the amplitude (raster magnitude) and frequency (raster speed) of the steering magnetic field prevents formation of pits or craters in the source material. In addition, rastering the e-beam improves source material utilization reducing the need to refill the source often. An advantage

of this technique is that high evaporation rates can be achieved reducing the incorporation of background gases into the growing film.

Although e-beam evaporation is a thermal evaporation process, the evaporant atoms leave the surface with low energy ($\sim$ 0.2 eV) [105]. However, the e-beam is sufficiently energetic to cause generation of x-rays when it strikes the source surface. The generated x-rays are not energetic enough to penetrate the vacuum chamber walls but can result in detrimental effects to the substrate [106]. For example, dielectric materials for electronic applications can develop unwanted charge trapping defects and damage due to x-ray impingement.

The thickness of the growing film is monitored using a vibrating quartz crystal mass-deposition monitor, or quartz crystal microbalance (QCM). Quartz, a piezoelectric material generates an oscillating voltage when vibrating at its resonant frequency (typically 5 MHz) [106]. This effect is exploited to monitor the vapor flux using a QCM which consists of a thin quartz plate sandwiched between two gold electrodes. One electrode is exposed to the vapor flux and proceeds to accumulate a mass of deposited material. This increased mass reduces the resonant frequency of the crystal and by comparing this frequency value with the reference quartz frequency, the amount of mass deposited can be calculated [107]. The change in resonant frequency of different materials is incorporated using two parameters - *density* and *acoustic impedance* of the evaporant. In addition, since the QCM may not be placed adjacent to the substrates, another parameter known as *tooling factor* accounts for the geometric difference. For common metals and compounds, values of the density and acoustic impedance are tabulated as shown in [108]. The tooling factor however, needs to be empirically determined by depositing a set thickness (100 - 200 nm) and comparing the measured thickness with that of the QCM reading. For new materials the density can be

measured, however the acoustic impedance has to be empirically determined. It was observed during the course of this study, that the variation of acoustic impedance is not as important as that of the tooling factor. Thus, it is recommended that for new materials, a value of acoustic impedance of a known material be used, while simultaneously accounting for any variation in the acoustic impedance by correctly adjusting the tooling factor.

The CDS is equipped with a 6-pocket Temescal 2CK SuperSource E-gun which provides a maximum power rating of 10 kW. This is delivered by a Temescal CV8 electron beam power supply. A Maxtek TM-350 thickness monitor is used as the QCM along with 5 MHz quartz crystals purchased from Inficon.

### 3.1.3 Post-Deposition Anneal

The vapor flux caused during evaporating or sputtering from a compound target generally does not have the same composition as the source material. This is due to the relative difference in vapor pressures of the constituent atoms. High vapor pressure elements exit the target or source material quicker, resulting in a source material with a variable composition with continuous deposition. This result also occurs on the growing film on the substrate. A post-deposition anneal step is almost always required when working with chalcogenide materials, since the resulting films are generally sulfur deficient.

The post-deposition anneal process not only provides sufficient thermal energy for atoms in the film to rearrange or diffuse to the most energetically favorable positions, chemical reactions intended to fix or alter the stoichiometry of the film can also be facilitated in this step. In addition, annealing enhances grain growth. The post-deposition anneal process is performed by Robert Kokenyesi and Jaeseok Heo in the Chemistry Department at Oregon

State University. Two different methodologies are utilized - a sealed tube anneal or a flowing gas anneal.

- Sealed Tube Anneal: The as-deposited thin film is placed in an evacuated sealed tube ($\sim$ 10 mT) along with the source chalcogenide material. The source material typically has a high vapor pressure and reacts with the film during the anneal. A film is annealed for 1 - 5 hrs at temperatures between 400 - 700 °C.

- Flowing Gas Anneal: In a typical flowing gas anneal, a thin film is placed in a quartz or alumina tube and purged for 5 - 10 mins using an inert gas, typically argon. Following the purge step, the film is subjected to a heating, anneal and cooling cycle in the presence of a chalcogenide-containing gas such as $CS_2$ or $H_2S$. The film is typically maintained at the anneal temperature for 10 - 60 mins. In this technique, the gas reacts with the film, eliminating the need for extra source material.

## 3.2 Material Characterization

In this section, experimental techniques used to characterize the absorber layer thin films are described. Variable-angle spectroscopic ellipsometry and optical spectroscopy are utilized to characterize optical properties such as index of refraction, dielectric constant, band gap, and absorption coefficient. Electrically, films are characterized using Seebeck and Hall measurement systems. A Seebeck measurement provides an estimation of the carrier type and concentration, while a Hall measurement allows for estimation of resistivity and mobility of the majority carriers. Measured parameters for each absorber material, specifically - optical band gap, absorption coefficient, dielectric constant, mobility, and carrier concentration are

used as inputs into SCAPS - a thin-film solar cell simulation software package in order to simulate expected device behavior and to optimize the TFSC for maximum efficiency.

### 3.2.1 Spectroscopic Ellipsometry

Spectroscopic ellipsometry (SE) is a commonly used characterization technique to measure optical properties of thin-films. SE can be used to determine optical constants such as index of refraction, dielectric constant, optical band gap, and absorption coefficient in addition to film thickness and surface roughness. Film properties such as density, porosity and uniformity can also be determined and correlated with process conditions.

Light propagation through a material is typically described by the *complex index of refraction* using the following set of equations

$$\widetilde{N} = n - ik, \tag{3.1a}$$

$$k = \frac{\alpha\lambda}{4\pi}, \tag{3.1b}$$

and

$$I = I_0\, exp(-\alpha\, d). \tag{3.1c}$$

where $\widetilde{N}$ is the complex refractive index [unitless], $n$ is the real portion of the refractive index [unitless] and $k$ is the extinction coefficient [unitless], $\alpha$ is the absorption coefficient [$cm^{-1}$] and $\lambda$ refers to the wavelength of light [nm] in Eqn. 3.1a and Eqn. 3.1b. Equation. 3.1c is referred to as Beer's law [109] which describes the exponential decay of light intensity as it propagates through an absorbing material. Here $I_0$ is the incident light intensity and $I$ is the light intensity transmitted through films of thickness $d$.

When light, an electromagnetic wave, is incident on a material, the oscillating field perturbs positive and negative charges within the material. Under the classical model, this

perturbation of negatively charged electrons bound to the positive nuclear charge is modeled as a spring-like restoring force. Specifically, when an external oscillating electromagnetic field perturbs the solid, electrons oscillate back and forth based on a spring constant and restoring force, an effect known as *electronic polarization* [9]. The magnitude of the polarization generated in a material determines the *dielectric constant* ($\varepsilon$) and can be related to the index of refraction as,

$$\widetilde{\varepsilon} = \widetilde{N}^2 = \varepsilon_1 + i\varepsilon_2 \tag{3.2}$$

where $\widetilde{\varepsilon}$ is the complex dielectric constant with $\varepsilon_1$ and $\varepsilon_2$ representing the real (spring constant) and imaginary (restoring force) components of the dielectric constant. From Eqn. 3.1a, it follows that

$$\varepsilon_1 = n^2 - k^2, \tag{3.3a}$$

and

$$\varepsilon_2 = 2nk. \tag{3.3b}$$

For a material with no absorption, $k = 0$ and Eqn. 3.3a simplifies to

$$\varepsilon_1 = n^2. \tag{3.4}$$

When linearly polarized light is reflected from a sample surface, the reflected light becomes elliptically polarized due to interaction with the sample [110]. In Fig. 3.4, linearly polarized light is incident on the sample surface and can be resolved into two components, parallel ($p$) and perpendicular ($s$) to the plane of incidence. For a material that is transparent to incident light, only the amplitude of the reflected wave is affected without any change in polarization [28]. However, for an absorbing material, the reflected light experiences an amplitude and phase change, resulting in the introduction of an additional component to the phase change.

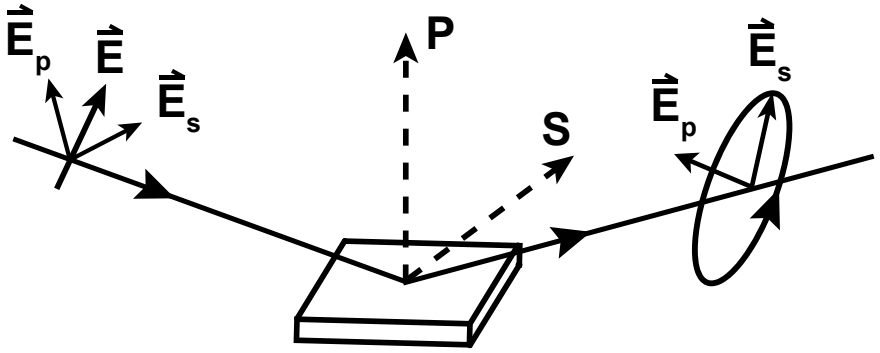


Figure 3.4: Plane of ellipsometery measurements. Linearly polarized light (left) is converted to elliptical polarization (left) after reflection from the sample surface.

Reflection of linearly polarized light from a surface can be expressed using Fresnel's equations [109] as

$$r_p = \frac{E_p^{ref}}{E_p^{inc}} = \frac{n_t\, cos\theta_i - n_i\, cos\theta_t}{n_t\, cos\theta_i + n_i\, cos\theta_t} \tag{3.5a}$$

$$r_s = \frac{E_s^{ref}}{E_s^{inc}} = \frac{n_i\, cos\theta_i - n_t\, cos\theta_t}{n_i\, cos\theta_i + n_t\, cos\theta_t} \tag{3.5b}$$

where $r$ is the reflection coefficient, $E^{inc}$ and $E^{refl}$ are the incident and reflected electric fields, $n_i$ and $n_t$ refer to the index of refraction of the incident and transmitted medium, $\theta_i$ and $\theta_t$ refer to the angle of incident and reflected light. The subscripts $s$ and $p$ refer to $s$- and $p$-polarized light, respectively. Since SE analyzes elliptically-polarized light, the reflection coefficients have to be expressed in polar coordinates [110] as

$$r_p = |r_p|\, e^{i\delta_p}, \tag{3.6a}$$

and

$$r_s = |r_s|\, e^{i\delta_s}. \tag{3.6b}$$

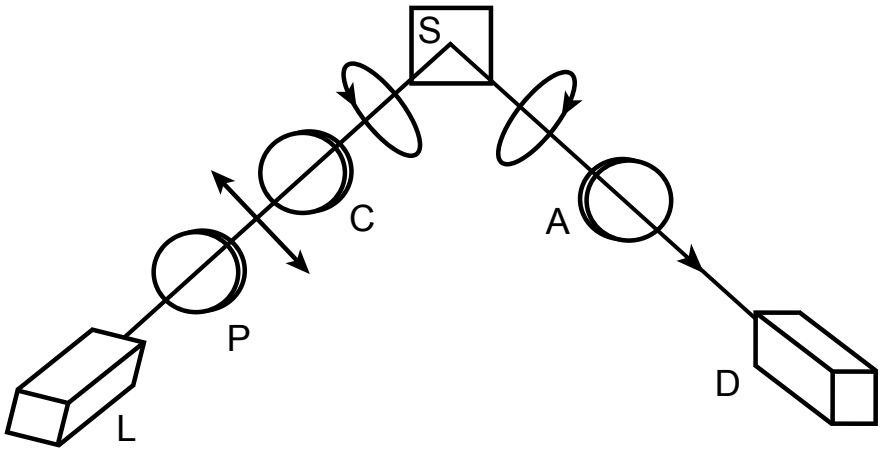


Figure 3.5: Components of an ellipsometer, including a lamp source (L), linear polarizer (P), compensator (C), sample (S), analyzer (A), and detector (D).

The reflection coefficients expressed in Eqns. 3.6a and 3.6b have the advantage of interpreting reflection in terms of amplitude and phase variations. Ellipsometry parameters, $\Delta$ and $\Psi$ can now be defined [111] as

$$\rho = tan\Psi\, e^{i\Delta} = \frac{r_p}{r_s} = \frac{|r_p|\ e^{i\delta_p}}{|r_s|\ e^{i\delta_p}}, \tag{3.7a}$$

$$\Rightarrow tan\Psi\, e^{i\Delta} = \frac{|r_p|}{|r_s|}\, e^{i(\delta_p - \delta_s)}. \tag{3.7b}$$

From Eqn. 3.7b it can be seen that $\Psi$ accounts for the change in amplitude between the reflection coefficients while $\Delta$ represents the phase change upon reflection. Thus, by measuring the variation in amplitude and phase of reflected light, material properties can be extracted.

A typical ellipsometer configuration consisting of the six most common parts is depicted in Fig. 3.5. A *light source* (L), generally a xenon-halogen lamp, emits unpolarized light which can be passed through a monochromator for spectroscopic measurements to scan across a wavelength range. A *linear polarizer* (P) converts the unpolarized light into linearly-polarized light. Calcite ($CaCO_3$) and $MgF_2$ are two commonly used linear polarizers [111] .

A *compensator* (C) converts linearly-polarized light into circularly-polarized light. This generates a phase difference between the two components of the electric field, typically achieved using a quartz quarter-wave plate [112]. This circularly-polarized light is incident on the *sample* surface (S) and upon reflection, passes through the *analyzer* (A). This component is similar to the *polarizer*. However the role of the *analyzer* is to determine the difference in polarization and intensity of the reflected light. Finally, light passes into the *detector* (D) which measures the light intensity. Common detectors are silicon photodetectors in the visible regime (450 - 1000 nm) and a cooled InGaAs for the near infra-red (1000 - 2500 nm) [113].

Since ellipsometry measures changes in the state of polarization, it is a high-precision technique which can be used to measure film thicknesses on the order of 1 Å [113]. However, an inherent drawback of ellipsometry is the indirect nature of the characterization. The measured parameters, $\Delta$ and $\Psi$, do not provide a direct evaluation of the optical constants. Instead one has to first develop a model defined by an initial 'guess' of the optical parameters including film thickness and compare generated $\Delta$ and $\Psi$ results along with experimentally measured values. A low mean-square-error (MSE) indicates convergence between modeled and experimental parameters and optical constants can be extracted with reasonable accuracy.

The choice of models can be guided by the band gap of the measured material. Typically, metals, or degenerately-doped semiconductors are modeled using a *Drude*, free electron model [111]. The Drude model can be expressed in terms of the optical conductivity and the mean scattering time between collisions. It has been shown during the course of this research that amorphous mixed-metal thin films (AMMFs) can be modeled using the Drude model and extracted values of the optical conductivity match quite closely to the experimen-

tally measured values. Semiconductors with an optical band gap in the range of 0.8 - 4 eV are typically described by the *Lorentz* model, or *Tauc-Lorentz* [111] for amorphous oxide semiconductors. These models incorporate interband transitions and are typically used to describe optical properties of semiconductors. For wide band gap insulating materials with optical band gaps greater than 4 eV, the material is transparent to the incident light and a simple *Cauchy* [111] model can be used. The Cauchy model is a mathematical fit describing the dispersion relation using experimentally determined constant rather than the physics-based approach which describes Drude and Lorentz models.

The system used in this study is a variable angle spectroscopic ellipsometer (VASE) from J.A. Woollam Inc. VASE incorporates a 75 W xenon lamp equipped with a monochromator as the light source. The wavelength range provided by the lamp extends from 260 nm to 2500 nm providing a measurement range from deep UV to near IR. To measure this wide spectrum, VASE is equipped with two detectors - a silicon CCD photodetector from 260 nm - 1100 nm, and an InGaAs photodetector for 1100 nm - 2500 nm.

### 3.2.2 Optical Spectroscopy

While SE provides an indirect assessment of the optical properties, optical spectroscopy using transmission and reflectance measurements provides rapid assessment of the absorption properties of a material. The incident light intensity on a material has to equal the sum total of the reflected and transmitted intensities along with the amount absorbed. Thus by measuring the intensities of the incident, transmitted and reflected light on a medium, the absorption coefficient ($\alpha$) can be extracted. This analysis is derived from Beer's law (Eqn. 3.1c) which states that light intensity in a material decays exponentially based on the absorption coefficient and thickness. Since optical spectroscopy is an intensity-dependent measurement,

it is important to ensure no stray light alters the intensity level during the measurement. Very rough samples can also scatter the reflected light such that the detector does not measure the true reflectance leading to spurious results.

Recasting Eqn. 3.1c with the transmitted and reflected intensities, the absorption coefficient can be written as follows,

$$\alpha = -\frac{1}{t} ln \frac{T}{(1-R)}, \tag{3.8}$$

where $t$ is the film thickness, $T$ is the transmission spectrum and $R$ is the reflection spectrum measured as a function of wavelength. Plotting the absorption coefficient as a function of energy provides the absorption spectrum of a material. Since the absorption coefficient is inversely proportional to the thickness, it is necessary to have an accurate thickness estimation to avoid misrepresentation of the absorption properties. In addition, the onset of absorption occurs at the optical band gap ($E_G$) which can be extracted from the absorption profile. Since the position of the onset on absorption can be subjected to debate, all absorption coefficient plots in this study are plotted on a semi-log scale. Using this approach, the onset can be determined with higher accuracy. To resolve the low energy portion (close to the band gap) with higher accuracy, thick ($>$ 500 nm) films are required, while resolution of the high energy portion (plateau in the absorption coefficient) can be achieved using thin ($\sim$ 100 - 200 nm) films.

The system used in this study is a custom-built, fiber-optics-based Ocean Optics spectrometer. It is equipped with a halogen lamp as the light source and uses optical fibers to guide the reflection and transmission signals towards the detector. As a result, measurements over the entire spectral range is performed simultaneously, eliminating the need for

a monochromator at the source. Similar to the ellipsometer, this system uses both Si and InGaAs detectors allowing for a spectral measurement range from 250 - 2060 nm.

### 3.2.3 Hall Effect Measurements

Resistivity is a fundamental electrical property of a material since it is related to carrier concentration and mobility. For a p-type material, the resistivity can be expressed as,

$$\rho = \frac{1}{q\mu_p p}, \tag{3.9}$$

where $\rho$ is the resistivity [Ω-cm], $\mu_p$ is the hole mobility [cm$^2$ V$^{-1}$s$^{-1}$] and $p$ is the carrier concentration [cm$^{-3}$]. Hall measurements provide a route to assess the carrier concentration and the mobility simultaneously.

In a Hall effect measurement, a magnetic field applied perpendicular to the direction of current flow produces an electric field perpendicular to the magnetic field and current [28]. The generated electric field is a consequence of the Lorentz force which deflects carriers towards one side of the material relative to the other, resulting in a Hall voltage given as [28],

$$V_H = \frac{BI}{qpt}, \tag{3.10}$$

where $B$ is the applied magnetic field [kG], $I$ is the current density [mA cm$^{-2}$], $q$ is charge [$C$], $p$ is the hole carrier concentration [cm$^{-3}$] and $t$ is the thickness of the sample. The Hall coefficient ($R_H$) for a p-type material is given as,

$$R_H = \frac{r}{qp}, \tag{3.11}$$

where $r$ is the scattering factor, and can be assumed as 1 [28]. Equation 3.11 shows that $R_H$ is inversely proportional to the carrier concentration and the sign of of $R_H$ indicates the type

of majority carriers (positive for holes). The Hall mobility ($\mu_H$) is then given as,

$$\mu_H = \frac{|R_H|}{\rho}. \tag{3.12}$$

The resistivity ($\rho$) of a material can be measured without complete knowledge of sample geometry using the *van der Pauw* method . For a homogeneous sample, resistivity can be determined using four symmetric contacts having negligible thickness compared to the spacing between contacts and placed at the edge of the sample. For such a configuration, the resistivity is given as [28],

$$\rho = \frac{\pi t}{ln(2)} \frac{V_{43}}{I_{12}} \frac{V_{14}}{I_{23}} \tag{3.13}$$

where $t$ is the thickness of the material, $V_{43}$ and $V_{14}$ refer to the measured voltage (V) across contacts 4-3 and 1-4 by applying a dc current ($I_{12}$ and $I_{23}$) (A) along contacts 1-2 and 2-3.

A Lakeshore 7504 Hall system is used to measure electrical properties of the absorber thin films. Ohmic contacts are made by attaching Pt wires to the sample using In solder. Typically, a DC magnetic field of 5-20 kG is used. However at these fields, accurate estimation of mobility and carrier concentration is possible only if $\mu_p \geq 1\ cm^2/Vs$ and $p > 10^{15}$ $cm^{-3}$ [114], which may not be the case in new materials development without optimization. To circumvent this, an AC field can be used to measure low mobility, insulating materials in the Hall setup. Alternatively, Seebeck measurements can be used to measure the carrier concentration and together with the measured resistivity, mobility can be estimated.

### 3.2.4 Seebeck Measurements

The Seebeck measurement is a thermoelectric characterization technique, in which application of temperature gradient ($\Delta T$) results in an induced electrical potential ($\Delta V$). The magnitude of generated potential in a material, or the thermopower, is described by the *See-*

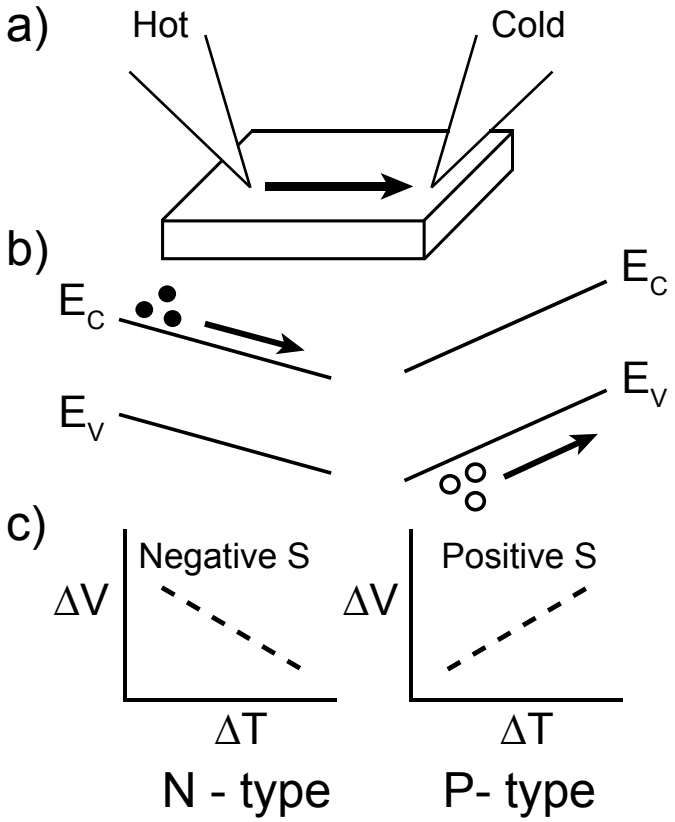


Figure 3.6: (a) Basic components of a Seebeck measurement. (b) Energy band diagrams for n- and p-type materials showing majority carriers diffusing under the influence of a thermal gradient. (c) Plots of ΔV versus ΔT. Direction of the slope indicates carrier type and the magnitude is related to the carrier concentration.

*beck coefficient*,

$$S = -\frac{\Delta V}{\Delta T}. \tag{3.14}$$

In a typical Seebeck measurement as shown in Fig. 3.6, a temperature gradient of 3-4 K is applied across a material, metallic or semiconducting. This temperature gradient results in a built-in electric field (refer to Fig. 3.6) across the material, inducing majority carriers to diffuse away from the hot side. A potential difference is thus generated across the hot and cold side as a consequence of carrier diffusion. The sign of the Seebeck coefficient

| Seebeck coefficient [$\mu$V/K] | Carrier concentration [cm$^{-3}$] |
|---|---|
| 0.5 - 100 | $< 10^{21}$ |
| 120 - 150 | $< 10^{19}$ |
| 500 and above | $< 10^{17}$ |

Table 3.1: Seebeck coefficients and corresponding approximate carrier concentrations.

is indicative of the majority carrier type in the material. As shown in Fig. 3.6, $S$ has a negative value for an n-type material and conversely, a positive value for a p-type material. The magnitude of the coefficient is related to the majority carrier concentration for a p-type material as follows [46],

$$S = \frac{k_B}{q}\left[A + ln\frac{2\left(2\pi m^* k_B T\right)^{3/2}}{h^3 p}\right], \tag{3.15}$$

where $h$ is Planck's constant and $A$ is a scattering factor [46]. It can be seen from Eqn. 3.15 that a Seebeck measurement does not provide direct assessment of carrier concentration. The Seebeck coefficient has a non-linear dependence on the carrier concentration and approximate Seebeck values with corresponding carrier concentrations are listed in Table 3.1. In this study, Seebeck measurements are used to provide a rapid assessment of the carrier concentration.

## 3.3 Device Simulations

Solar cell capacitance simulator (SCAPS) is a one dimentional thin-film solar cell device simulator software program developed by the University of Gent. It provides numerical solutions to the basic equations governing behavior of carriers in semiconductors - Poissons's

equation, continuity equations for electrons and holes and the Boltzman transport equation - subject to initial conditions and appropriate boundary conditions. Recombination types such as radiative and SRH are taken into account while defects in the bulk and interface can also be included in the model. In developing new materials for thin-film solar cells, device simulations provide an assessment of the expected behavior of an absorber in a device, without having to fabricate and optimize a full solar cell structure, providing a rapid method to identify best of class materials. In addition, device simulations can be used to provide an optimal set of target properties for high-efficiency thin-film solar cells.

The *Poisson equation* is derived from Gauss' law and can be written for a one-dimentional semiconductor as [12],

$$\frac{d^2\psi_i}{dx^2} = -\frac{d\xi}{dx} = -\frac{\rho}{\varepsilon_s} = \frac{q(n-p+N_A-N_D)}{\varepsilon_s} \tag{3.16}$$

where $\psi_i$ is the potential [V] , $\xi$ is the electric field [V cm$^{-1}$], $\varepsilon_s$ is the dielectric constant [F cm$^{-1}$] of the semiconductor and $\rho$ is the space charge [C cm$^{-3}$] in the semiconductor which equals the total concentration of electrons ($n$) and holes ($p$) as well as the acceptor ($N_A$) and donor ($N_D$) concentrations in the depletion region.

Charge transport in a semiconductor material is typically modeled by the inclusion of a drift term due to an electric field as well as a diffusion term associated with a gradient in the carrier concentration [12] and is expressed as,

$$J_n = q\mu_n n\xi + qD_n\nabla n, \tag{3.17a}$$

$$J_p = q\mu_p p\xi + qD_p\nabla p, \tag{3.17b}$$

and

$$J_{tot} = J_n + J_p, \tag{3.17c}$$

where $J_n$ and $J_p$ are the current densities of electrons and holes [mA cm$^{-2}$], $\mu_n$ and $\mu_p$ are the mobilities of electrons and holes [cm$^2$ V$^{-1}$s$^{-1}$], $D_n$ and $D_p$ refer to the diffusivities of electrons and holes [cm$^2$ s$^{-1}$], while $J_{tot}$ is a sum of the electron and hole current densities [mA cm$^{-2}$]. For a one-dimentional case, Eqns. 3.17a and 3.17b simplify to,

$$J_n = q\mu_n n\xi + qD_n\frac{dn}{dx} = q\mu_n\left(n\xi + \frac{k_BT}{q}\frac{dn}{dx}\right) = \mu_n n\frac{dE_{Fn}}{dx}, \tag{3.18a}$$

and

$$J_p = q\mu_p p\xi + qD_p\frac{dp}{dx} = q\mu_p\left(p\xi + \frac{k_BT}{q}\frac{dp}{dx}\right) = \mu_p p\frac{dE_{Fp}}{dx}, \tag{3.18b}$$

where $E_{Fn}$ and $E_{Fp}$ are quasi-Fermi levels for electrons and holes.

The *continuity equations* are conservation of species equations for electrons and holes. For an infinitesimal charge control volume in a semiconductor, the time rate of change in the carrier concentration is the difference between the net flux in and out of the control volume and the net generation rate (generation minus recombination). The continuity equations for electrons and holes are given by

$$\frac{\partial n}{\partial t} = G_n - R_n + \frac{1}{q}\nabla J_n, \tag{3.19a}$$

and

$$\frac{\partial p}{\partial t} = G_p - R_p + \frac{1}{q}\nabla J_p, \tag{3.19b}$$

where $G_n$, $G_p$ and $R_n$, $R_p$ are the generation (cm$^{-3}$s$^{-1}$) and recombination rates (cm$^{-3}$s$^{-1}$) for electrons and holes, respectively.

SCAPS uses the above family of equations along with the appropriate boundary conditions at the interfaces and contacts to solve for the current-voltage characteristics. To do

so, SCAPS discretizes the device configuration by creating a mesh and solves the above one-dimensional semiconductor equations numerically using a Newton-Gummel iterative scheme [115]. Since optical properties such as band gap and absorption coefficient are used as inputs to the model, SCAPS also computes the quantum efficiency of the device. As a starting point for a device simulation, model parameters obtained from reference [31] are used, thereby setting up a baseline for CdTe based thin-film solar cells. Examples of results obtained from the baseline simulation is shown in Fig. 3.7.

Table 3.2 along with Fig. 3.7a are used as typical model parameters and device configuration inputs to SCAPS. Figure 3.7b shows the energy band of the cell configuration under short-circuit conditions and illumination. Resulting J-V and QE plots are shown in Figs. 3.7c and 3.7d. It can be seen that for this device configuration, $V_{oc}$ = 0.87 V while $J_{sc}$ = 24.1 mA/cm$^2$ with an efficiency of 16%, while the QE shows a strong onset at the band edge (855 nm) and reaches a maximum value of 90%.

## 3.4 Conclusions

An understanding of the fabrication and characterization techniques employed in support of the research described in this dissertation provides a technical foundation that is used in the presentation of results in later chapters. Techniques utilized to fabricate chalcogenide thin-films for solar absorbers such as RF magnetron sputtering and electron-beam evaporation are described. Materials characterization techniques including optical and electrical methods are reviewed next. TFSC device simulations using SCAPS to explore variations of absorber layer properties are outlined.

| General Device Properties | | | |
|---|---|---|---|
| Parameter | Front Contact | Back Contact | |
| $\phi_b$ [eV] | $\phi_{bn} = 0.1$ | $\phi_{bp} = 0.3$ | |
| WF [eV] | 4.1 | 5.1 | |
| $S_n$ [cm/s] | $10^7$ | $10^7$ | |
| $S_p$ [cm/s] | $10^7$ | $10^7$ | |
| Reflectivity | 0.1 | 0.8 | |
| **Layer Properties** | | | |
| Parameter | $SnO_2$ | CdS | CdTe |
| W [nm] | 500 | 25 | 4000 |
| $\varepsilon/\varepsilon_0$ | 9 | 10 | 9.4 |
| $\mu_n$ [$cm^2$/s] | 100 | 100 | 320 |
| $\mu_p$ [$cm^2$/s] | 25 | 25 | 40 |
| n(or p) [$cm^{-3}$] | n: $10^{17}$ | n: $10^{17}$ | p: $10^{14}$ |
| $E_G$ [eV] | 3.6 | 2.4 | 1.45 |
| $N_C$ [$cm^{-3}$] | $2.2\times10^{18}$ | $2.2\times10^{18}$ | $8\times10^{17}$ |
| $N_V$ [$cm^{-3}$] | $1.8\times10^{19}$ | $1.8\times10^{19}$ | $1.8\times10^{19}$ |
| **Midgap Defect States** | | | |
| Parameter | $SnO_2$ | CdS | CdTe |
| $N_D$,$N_A$ [$cm^{-3}$] | A: $10^{15}$ | A: $10^{18}$ | D: $10^{14}$ |
| $\sigma_n$ [$cm^2$] | $10^{-12}$ | $10^{-15}$ | $10^{-12}$ |
| $\sigma_p$ [$cm^2$] | $10^{-15}$ | $10^{-12}$ | $10^{-15}$ |

Table 3.2: Table 1. List of parameters for a CdTe thin-film solar cell used for a baseline simulation.

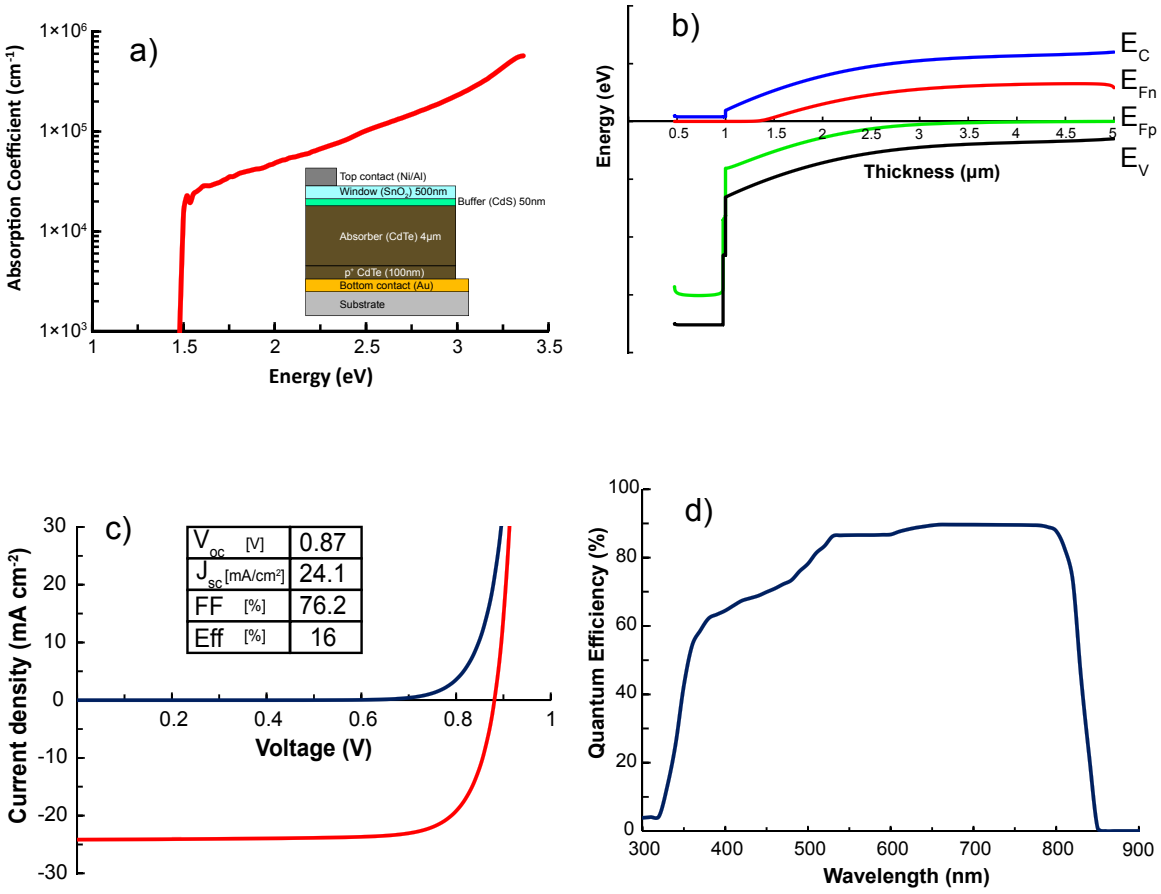


Figure 3.7: (a) Absorption coefficient plot of CdTe and thin-film solar cell configuration (inset). (b) Energy band diagram of a CdTe solar cell. (c) Output current-voltage curves, and (d) quantum efficiency plot for a CdTe thin-film solar cell.

# 4. TFSC DEVICE SIMULATION OF HIGH ABSORPTION MATERIALS

This chapter presents simulations of an idealized absorber material in a TFSC in order to establish the necessary absorber layer properties required for high photoconversion efficiency. Parameters such as absorption coefficient, carrier concentration, minority carrier lifetime, carrier mobility, and absorber layer thickness are varied in order to determine the necessary requirements for a TFSC to achieve an efficiency $>20\%$.

## 4.1 Primary questions addressed by device simulations

The goal of this effort is to develop ultra-high absorbers capable of achieving a TFSC with an efficiency $\eta > 20\%$. To achieve this objective, two questions are posed.

1. What is the relationship between the absorption strength (absorption coefficient) and material properties - carrier concentration ($N_A$), minority carrier lifetime ($\tau$), carrier mobilities ($\mu_n$, $\mu_p$), and thickness ($t$) of the absorber?

2. What advantages (if any) does a drift-based TFSC offer compared to a diffusion-based TFSC?

In an attempt to answer these questions and establish the necessary material properties for a high-performance solar absorber material, a hypothetical TFSC with an idealized absorber layer is simulated using SCAPS, a TFSC simulation software tool, developed by the University of Gent [53]. While other TFSC simulation software tools are available, including AMPS, PC1D, AFORS-HET, and SILVACO to name a few [24], SCAPS is chosen in this study because of its intuitive LabView interface, along with the ease of adding a new material not already in the SCAPS database.

Two different device operation modes based on the mechanism of carrier transport are pursued here, drift- and diffusion-based TFSC. In a drift cell (e.g., an amorphous silicon or CdTe-based TFSC), carrier transport is aided by an internal electric field across the entire absorber layer. In a diffusion cell (e.g., a CIGS or CZTS-based TFSC), photogenerated minority carriers diffuse to the edge of the space-charge region, where the electric field in the depletion region sweeps these carriers towards their contact. Two aspects of photovoltaic operation are investigated via simulation. First, by varying the absorption coefficient, the propensity of a material to generate a large number of photocarriers is explored. Second, the ability of a TFSC to extract photogenerated carriers (transport properties) is assessed by varying the carrier concentration, minority carrier lifetime, carrier mobilities, and thickness. The objective here is to establish the necessary properties for a TFSC to operate at an efficiency $\geq 20\%$.

## 4.2 The Absorber

A hypothetical p-type absorber is modeled with properties similar to that of CdTe, i.e., a direct band gap semiconductor with a band gap $E_G$ = 1.45 eV. The band gap of the absorber layer affects both the photocurrent ($J_{ph}$) and the open-circuit voltage (refer Ch. 2) as,

$$J_{ph} = q \int_{E_G}^{\infty} (1-R)\, \Phi_b\, exp(-\alpha x_a) dE, \tag{4.1a}$$

and

$$qV_{oc} = nk_BT \left( \frac{J_{ph}}{J_{00}} \right) + E_G. \tag{4.1b}$$

A smaller band gap absorber ($E_G$ <1.0 eV) absorbs a larger portion of the solar spectrum, resulting in an increased $J_{ph}$ (refer to Fig. 2.13a), and a reduced $V_{OC}$ (refer to

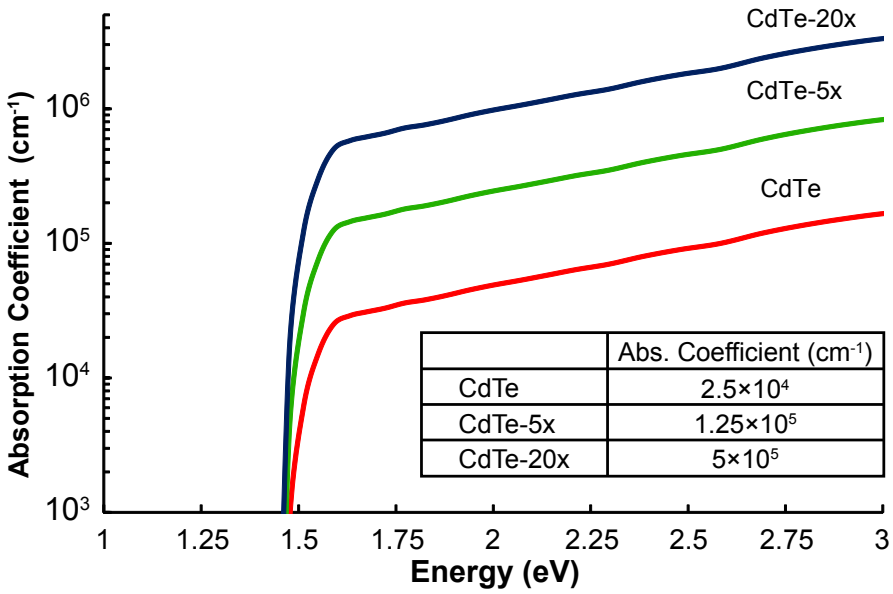


Figure 4.1: Idealized absorption coefficients used in the simulation plotted as a function of photon energy. The absorption coefficients reach a maximum value of $\alpha = 2.5 \times 10^4$ cm$^{-1}$ (CdTe), $1.25 \times 10^5$ cm$^{-1}$ (CdTe-5x), and $5 \times 10^5$ cm$^{-1}$ (CdTe-20x), respectively near the band gap.

Fig. 2.13b). Conversely, a larger band gap absorber leads to a smaller $J_{ph}$ but a larger $V_{OC}$. The Shockley-Queisser efficiency limit indicates that 1.1 - 1.5 eV is an ideal band gap range for a solar absorber [44].

The absorption properties of the hypothetical absorber are modeled after CdTe and three absorption coefficients are simulated: CdTe, CdTe-5x (the absorption coefficient for CdTe multiplied by a factor of 5), and CdTe-20x (the CdTe absorption coefficient is multiplied by a factor of 20). The three absorption coefficients are plotted as a function of photon energy in Fig. 4.1. The absorption values are scaled such that the absorption coefficients reach a maximum value of $\alpha = 2.5 \times 10^4$ cm$^{-1}$ (CdTe), $1.25 \times 10^5$ cm$^{-1}$ (CdTe-5x), and $5 \times 10^5$ cm$^{-1}$ (CdTe-20x), respectively, near the band gap.

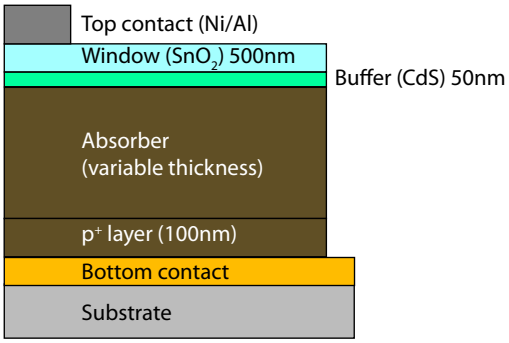


Figure 4.2: The TFSC device configuration utilized for simulation. The simulated TFSC contains the following layers: front contact / n-$SnO_2$/ n-CdS/ p-absorber/ $p^+$-absorber/ back-contact.

## 4.3 TFSC Device Configuration

The TFSC device configuration utilized in this simulation study is a n-p-$p^+$ heterojunction TFSC [54], where the absorber layer is the intermediate p-type layer with a band gap of 1.45 eV, and absorption properties shown in Fig. 4.1. The cell configuration is comprised of the following layers: front contact/ n-$SnO_2$/ n-CdS/ p-absorber/ $p^+$-absorber/ back-contact, shown in Fig. 4.2. A complete list of material parameters used in the simulation is listed in Table 4.1.

To mitigate the effect of back surface recombination, a $p^+$ layer ($N_A = 2\times10^{18}$ $cm^{-3}$) with the same properties as the absorber layer is included between the absorber and the back contact. This $p^+$ layer results in a conduction band offset, providing a barrier ($\sim$ 0.2 eV) for electrons, preventing them from recombining with holes at the back (hole transport) contact. This barrier serves to reflect any stray electrons, driving them towards the n-type contact. The $p^+$ layer, defined here as a separate layer, is commonly present in a solar cell, irrespective of the absorber type or device configuration. For example, in a CdTe-based TFSC, a Te-rich layer is typically formed between the CdTe absorber layer and the back contact [56] during

| General Device Properties | | | | |
|---|---|---|---|---|
| Parameter | Front Contact | | Back Contact | |
| $\phi_b$ [eV] | $\phi_{bn} = 0.1$ | | $\phi_{bp} = 0.3$ | |
| WF [eV] | 4.1 | | 5.1 | |
| $S_n$ [cm-s$^{-1}$] | $10^7$ | | $10^7$ | |
| $S_p$ [cm-s$^{-1}$] | $10^7$ | | $10^7$ | |
| Reflectivity | 0.1 | | 0.8 | |
| **Layer Properties** | | | | |
| Parameter | $SnO_2$ | CdS | p-absorber | $p^+$-absorber |
| W [nm] | 500 | 25 | variable | 100 |
| $\varepsilon/\varepsilon_0$ | 9 | 10 | 9.4 | 9.4 |
| $\mu_n$ [cm$^2$V$^{-1}$s$^{-1}$] | 100 | 100 | 320 | 320 |
| $\mu_p$ [cm$^2$V$^{-1}$s$^{-1}$] | 25 | 25 | 40 | 40 |
| n (or p) [cm$^{-3}$] | n: $10^{17}$ | n: $10^{17}$ | p: $10^{16}$ | $p^+$: $10^{18}$ |
| $E_G$ [eV] | 3.6 | 2.4 | 1.45 | 1.45 |
| $N_C$ [cm$^{-3}$] | $2.2\times10^{18}$ | $2.2\times10^{18}$ | $8\times10^{17}$ | $8\times10^{17}$ |
| $N_V$ [cm$^{-3}$] | $1.8\times10^{19}$ | $1.8\times10^{19}$ | $1.8\times10^{19}$ | $1.8\times10^{19}$ |
| **Mid-gap Trap State Properties** | | | | |
| Parameter | $SnO_2$ | CdS | p-absorber | $p^+$-absorber |
| $N_D$, $N_A$ [cm$^{-3}$] | A: $10^{15}$ | A: $10^{18}$ | D: variable | D: $10^{14}$ |
| $\sigma_n$ [cm$^2$] | $10^{-12}$ | $10^{-15}$ | $10^{-12}$ | $10^{-12}$ |
| $\sigma_p$ [cm$^2$] | $10^{-15}$ | $10^{-12}$ | $10^{-15}$ | $10^{-15}$ |

Table 4.1: Material parameters used for idealized TFSC simulations.

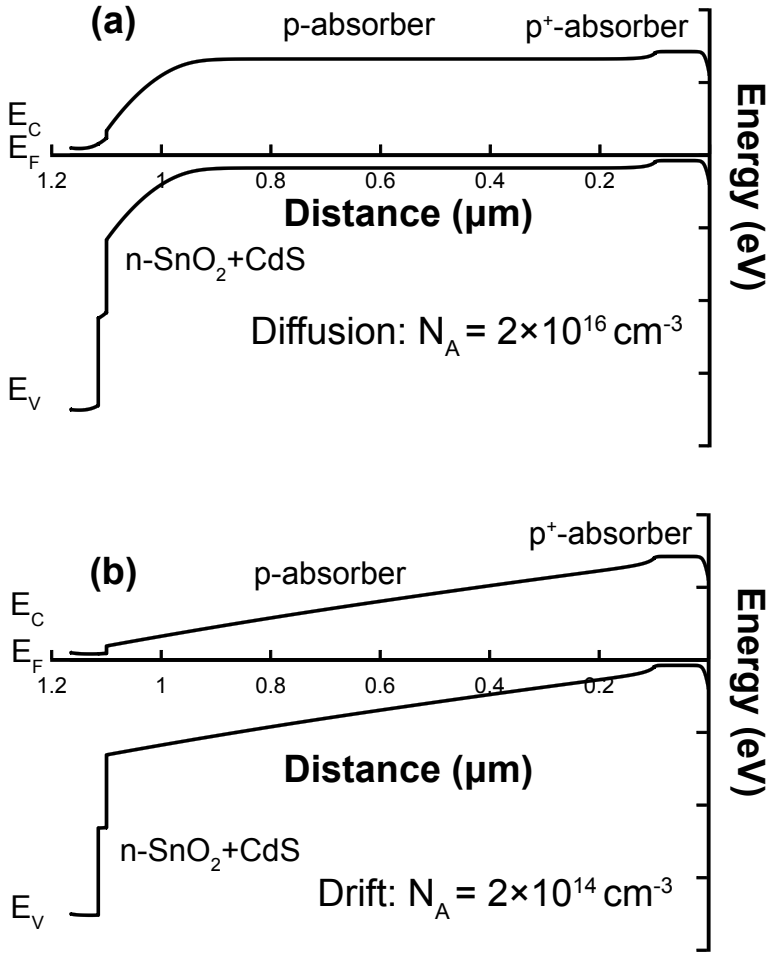


Figure 4.3: Simulated energy band diagrams for an idealized TFSC in (a) diffusion-cell configuration, and (b) drift-cell configuration. The two configurations are used for subsequent device simulations.

device fabrication which provides a highly-doped $p^+$ back surface. In a CIGS-based TFSC, the presence of $MoSe_2$ at the back surface facilitates the formation of a $p^+$-layer [80] with the p-type CIGS absorber. This $p^+$ layer is also present in crystalline silicon solar cells, where the p-type absorber is commonly alloyed with Al, increasing the carrier concentration towards the back surface to $\sim 10^{19}$ cm$^{-3}$ [116] resulting in a back surface field [117].

## 4.4 Carrier concentration variation

By varying the carrier concentration of the absorber layer, two different device operation modes based on the mechanism of charge transport can be recognized, as shown in Fig. 4.3. With $N_A = 2 \times 10^{16}$ cm$^{-3}$, a diffusion cell is realized (Fig. 4.3a), in which band bending is restricted to the depletion region at the interface between the p-type absorber and the n-type buffer layer. In such a configuration, (photogenerated) minority carriers have to diffuse to the edge of the depletion region before they are swept to their contact. If $N_A$ is reduced to $2 \times 10^{14}$ cm$^{-3}$, a drift cell is realized (Fig. 4.3b) where the electric field drops across the entire (lower doped) absorber. In such a configuration, minority carriers experience a built-in electric field, which sweeps them towards their contact. Since the electric field drives carriers towards their contacts, it minimizes stray electrons (or holes) from recombining at the opposite contact. Comparing the energy band diagram for a diffusion cell to that of a drift cell (shown in Fig. 4.3) indicates that if the absorber layer thickness in a diffusion-based TFSC is reduced to $<$300 nm, the depletion region can cover the entire absorber layer thickness. This indicates that drift/diffusion operation modes depends on both the carrier concentration as well as the absorber thickness.

To understand the critical thickness differentiating a drift- and a diffusion-based TFSC, the depletion width is calculated as a function of the absorber layer thickness for different carrier concentrations. In a typical TFSC, the n-type buffer layer has a higher carrier concentration ($\sim 10^{17}$ - $10^{18}$ cm$^{-3}$) than the p-type absorber layer ($\sim 10^{14}$ - $10^{16}$ cm$^{-3}$). As a result, the depletion width for a one-sided, abrupt p-n junction is defined mathematically as [12],

$$W_d = \sqrt{\frac{2\varepsilon}{q \times N_A} \times V_{bi}}, \tag{4.2}$$

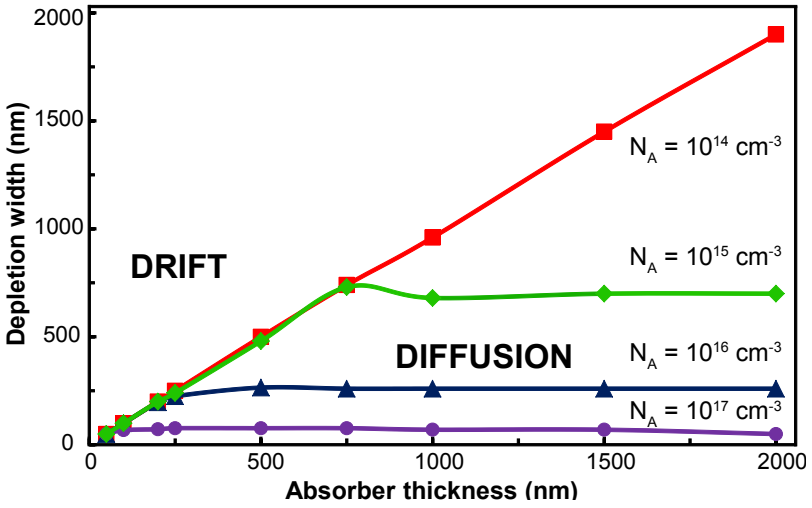


Figure 4.4: Variation of depletion width as a function of the absorber layer thickness, for different carrier concentration values. It can be seen that a drift-cell configuration has a linear increase in depletion width with increasing absorber layer thickness values. The depletion layer width for a diffusion-cell configuration does not increase linearly, instead, saturates beyond a critical thickness.

where $W_d$ is the width of the depletion region [nm], $\varepsilon$ is the dielectric constant of the absorber layer [unitless], and $V_{bi}$ is the built-in potential [V], approximated as $E_G/q$ ($E_G$ = 1.45 eV). Figure 4.4 is a plot of the depletion width as a function of absorber layer thickness for different carrier concentrations using Eqn. 4.2. For $N_A = 10^{14}$ cm$^{-3}$, the depletion width increases linearly with increasing absorber layer thickness since the internal electric field drops across the entire absorber. For $N_A = 10^{15}$ cm$^{-3}$, the depletion width increases linearly with the absorber thickness until 750 nm, beyond which the depletion width does not increase and is constant. This suggests that if the absorber layer thickness is greater than 750 nm, carriers have to diffuse to the edge of the depletion width, indicating that a high carrier mobility may be required to avoid recombination. For $N_A = 10^{16}$ cm$^{-3}$, the depletion width increases linearly up to 250 nm, beyond which the depletion width is constant. Thus, a *drift*-based TFSC can be defined when the depletion width is equal to the thickness of the absorber layer,

while a *diffusion*-based TFSC is one where the depletion width is restricted to a portion of the absorber layer thickness. In this chapter, a drift-based TFSC is simulated with $N_A = 2 \times 10^{14}$ cm$^{-3}$, while a diffusion-based TFSC is assumed to have $N_A = 2 \times 10^{16}$ cm$^{-3}$.

## 4.5 Absorber layer thickness variation

The thickness of a solar absorber is related to its absorption length ($1/\alpha$). A material with a low absorption coefficient requires a thick layer to absorb the solar spectrum. Increasing the absorption coefficient allows a thin absorber to effectively absorb the incident solar spectrum. In addition, if the absorber is thicker than the absorption length, photogenerated minority carriers can recombine prior to extraction, reducing the phototocurrent and efficiency. In this section, variation of the TFSC efficiency with increasing absorption strength and the subsequent effect on the absorber layer thickness is explored. Two device operation modes based on the mechanism of carrier transport, drift and diffusion (see Fig. 4.4), are simulated. In addition, two carrier mobilities are simulated for the device operation modes. The high mobility case is defined as $\mu_n, \mu_p$ = 320, 40 cm$^2$V$^{-1}$s$^{-1}$, while the low mobility case is defined as $\mu_n, \mu_p$ = 10, 1 cm$^2$V$^{-1}$s$^{-1}$. In this section, the minority carrier lifetime is assumed to be 10 ns.

### 4.5.1 Drift-based TFSCs

The *drift* length, $L^{drift}$, for minority carrier electrons in a p-type semiconductor is given as [12],

$$L^{drift} = \mu_n \tau_n \times \xi = \mu_n \tau_n \times \frac{E_G}{q\, L^A}, \tag{4.3}$$

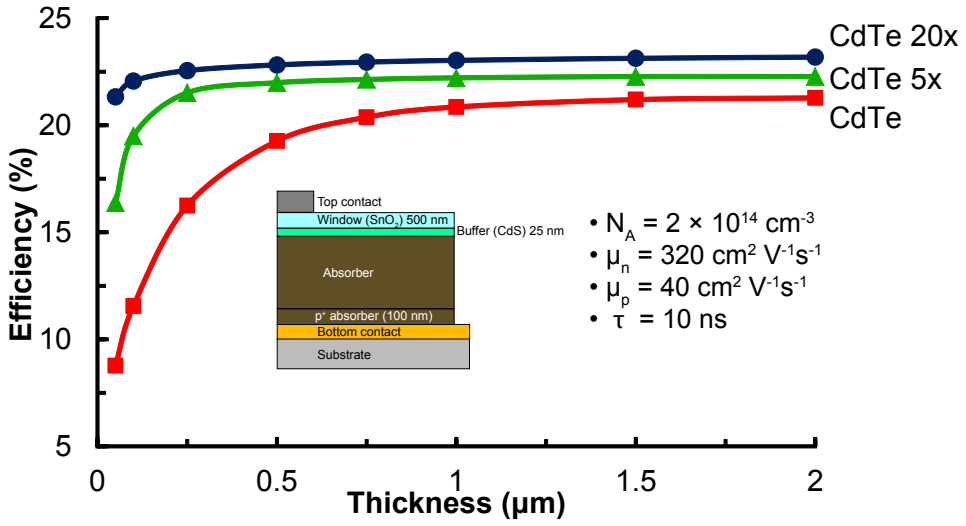


Figure 4.5: Simulated device efficiency as a function of the absorber thickness for a high carrier mobility, drift-based TFSC. The three curves correspond to the three absorption coefficients - CdTe, CdTe-5x, and CdTe-10x.

while the diffusion length ($L^{diff}$) is given as [12],

$$L^{diff} = \sqrt{D_n \tau_n} = \sqrt{\mu_n \tau_n \times \frac{k_B T}{q}}. \tag{4.4}$$

Taking the ratio between Eqn. 4.3 and Eqn. 4.4 yields,

$$\frac{L^{drift}}{L^{diff}} = \kappa = \mu_n \tau_n \times \frac{E_G}{q\,L^A} \times \sqrt{\frac{q}{\mu_n \tau_n k_B T}}, \tag{4.5a}$$

$$= \sqrt{\frac{\mu_n \tau_n}{q \times k_B T}} \times \frac{E_G}{L^A}. \tag{4.5b}$$

If Eqn. 4.5b is evaluated using $\mu_n$ = 320 $cm^2V^{-1}s^{-1}$, $\tau$ = 10 ns and $E_G$ = 1.4 eV, $\kappa$ = 156 for $L^A$ = 1 $\mu$m, while $\kappa$ = 623 for $L^A$ = 250 nm, indicating that $L^{drift} \gg L^{diff}$.

The variation in device efficiency for a high mobility ($\mu_n, \mu_p$ = 320, 40 $cm^2V^{-1}s^{-1}$) drift-based TFSC as a function of the absorber layer thickness is shown in Fig. 4.5 for the three absorption strengths. For the CdTe absorption, the efficiency increases dramatically as the absorber layer thickness increases. The efficiency is small for CdTe when the absorber

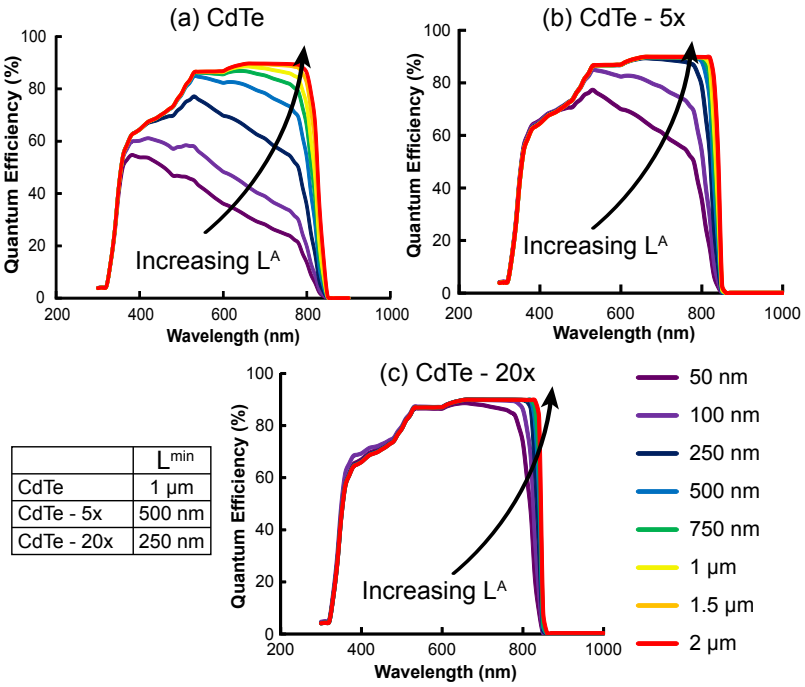


Figure 4.6: Simulated quantum efficiency for a high mobility drift-based TFSC for the three absorption coefficients a) CdTe, b) CdTe-5x, and c) CdTe-20x.

is thin since it does not effectively absorb the solar spectrum. Increasing the absorber thickness increases the photocurrent, leading to an improvement in efficiency. However, beyond a critical thickness ($\sim$ 1 $\mu$m), the efficiency essentially saturates since the absorber is now sufficiently thick to absorb the entire spectrum. The critical thickness is defined as the thickness beyond which the efficiency saturates. Increasing the absorption strength beyond that of CdTe not only improves the efficiency at reduced thicknesses, but it also increases the overall efficiency and decreases the critical thickness due to increased carrier photogeneration. For example, at an absorber layer thickness of 250 nm, CdTe absorption provides an efficiency of 16%, while CdTe-5x absorption gives rise to a 21.5% efficient TFSC, and CdTe-20x absorption yields an efficiency of 22.6%. At 1 $\mu$m, CdTe is 20.9% efficient, while the CdTe-5x and CdTe-20x absorption cases provide a simulated efficiency of 22.2% and 23%, respectively.

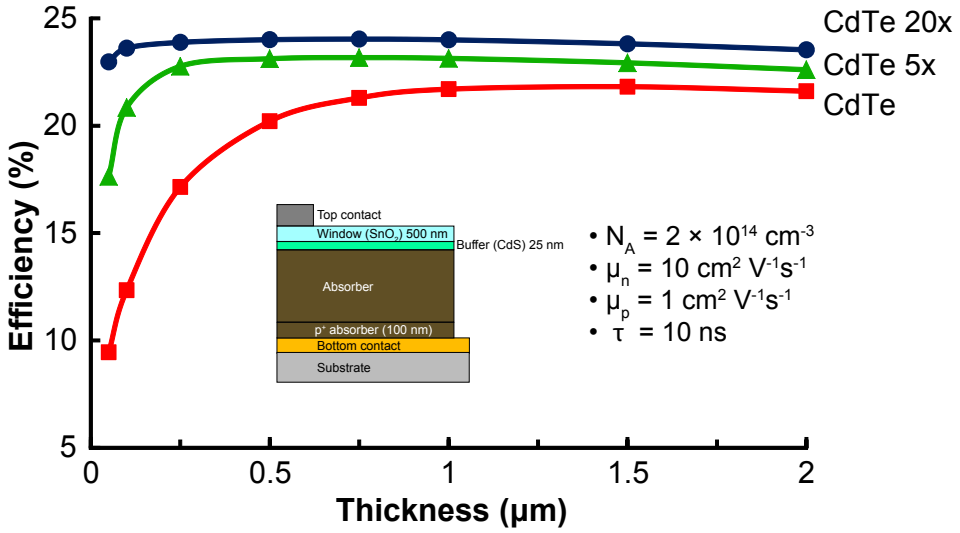


Figure 4.7: Simulated device efficiency as a function of the absorber thickness for a low carrier mobility, drift-based TFSC. The three curves correspond to the three absorption coefficients - CdTe, CdTe-5x, and CdTe-20x.

The critical thickness required to fully absorb the solar spectrum can be identified using quantum efficiency simulations. Figure 4.6 shows the quantum efficiency for the three absorption strength cases as a function of increasing absorber layer thickness. For CdTe, a minimum of 1 $\mu$m is required for effective absorption of the entire solar spectrum, while for CdTe-5x absorption, the minimum thickness needed is 500 nm, and for the CdTe-20x absorption case the thickness requirement reduces to 250 nm. This confirms that improving the absorption strength beyond that of CdTe reduces the thickness required for full absorption of the solar spectrum.

The ratio $\kappa$ can be recalculated for the low mobility case ($\mu_n, \mu_p$ = 10, 1 cm$^2$V$^{-1}$s$^{-1}$) using Eqn. 4.5b and identical absorber material properties. For $L^{abs}$ = 1 $\mu$m, $\kappa$ = 27.5, and for $L^A$ = 250 nm, $\kappa$ = 110. While $\kappa$ is not as large as that of the high mobility case, $L^{drift}$ is still greater than $L^{diff}$, especially for a thin absorber. The variation in device efficiency as a

function of absorber layer thickness is shown in Fig. 4.7 for the three absorption strengths. Similar to Fig. 4.5, the efficiency increases with increasing absorber layer thickness before saturating at a critical thickness. For CdTe, the efficiency reaches a maximum of 21.7% at 1 $\mu$m. For CdTe-5x absorption, the efficiency reaches a maximum of 23% at 500 nm, beyond which the efficiency reduces slightly to 22.6% at 2 $\mu$m. This trend is also observed for the CdTe-20x absorption curve, where the efficiency maximizes at 24% for $L^A$ = 250 nm, and reduces to 23.5% at $L^A$ = 2 $\mu$m. The efficiency reduces for a thick absorber since the electric field which drives minority carrier extraction is now reduced. This reduced driving field, along with low carrier mobilities can increase recombination, reducing the photocurrent and the overall efficiency.

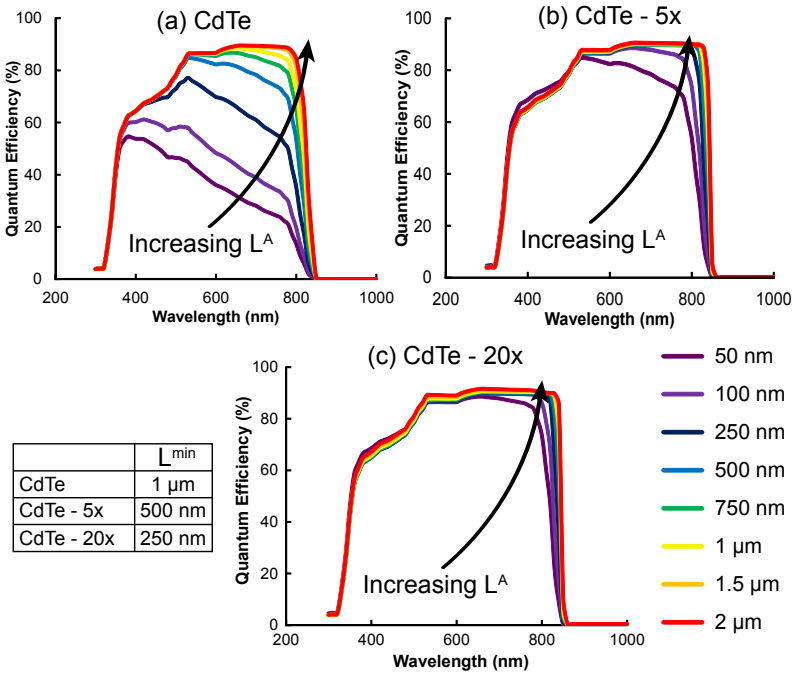


Figure 4.8: Simulated quantum efficiency for a low mobility drift-based TFSC for the three absorption coefficients a) CdTe-base, b) CdTe-5x, and c) CdTe-20x.

| Absorption Strength | Low mobility case | | High mobility case | |
|---|---|---|---|---|
| | $L^A$ [nm] | $\eta$ [%] | $L^A$ [nm] | $\eta$ [%] |
| CdTe | 1000 | 21.7 | 1000 | 20.9 |
| CdTe-5x | 500 | 23.1 | 500 | 22 |
| CdTe-20x | 250 | 23.8 | 250 | 22.6 |

Table 4.2: Efficiency at the critical thickness for an absorber in a drift-based TFSC for three absorption strengths. Both low and high mobility cases are tabulated.

The quantum efficiencies of the *low* mobility drift-based TFSC for the three absorption strengths are shown in Fig. 4.8 and are similar to Fig. 4.6. The minimum thicknesses for complete absorption of the solar spectrum are similar to those of the high mobility case, i.e., for CdTe, $L^A$ = 1 $\mu$m, while for CdTe-5x, $L^A$ = 500 nm, and for CdTe-20x, $L^A$ = 250 nm,. This suggests that a drift-based solar cell incorporating a thin absorber layer ($L^A$ <1 $\mu$m), is relatively insensitive to a reduction in carrier mobility. Table 4.2 summarizes the critical absorber thicknesses and corresponding efficiencies for both the low- and high-mobility cases.

### 4.5.2 Diffusion-based TFSCs

The diffusion length, $L^{diff}$, for the idealized solar absorber can be calculated using Eqn. 4.4. For a band gap of $E_G$ = 1.4 eV, a minority carrier mobility of $\mu_n$ = 320 $cm^2V^{-1}s^{-1}$, and a minority carrier lifetime of $\tau$ = 10 ns, $L^{diff}$ = 2.8 $\mu$m. Since $L^{diff}$ >$L^A$ for a 1 $\mu$m thick absorber, all minority carriers can be assumed to reach the depletion region. The variation in device efficiency as a function of absorber layer thickness is shown in Fig. 4.9 for the

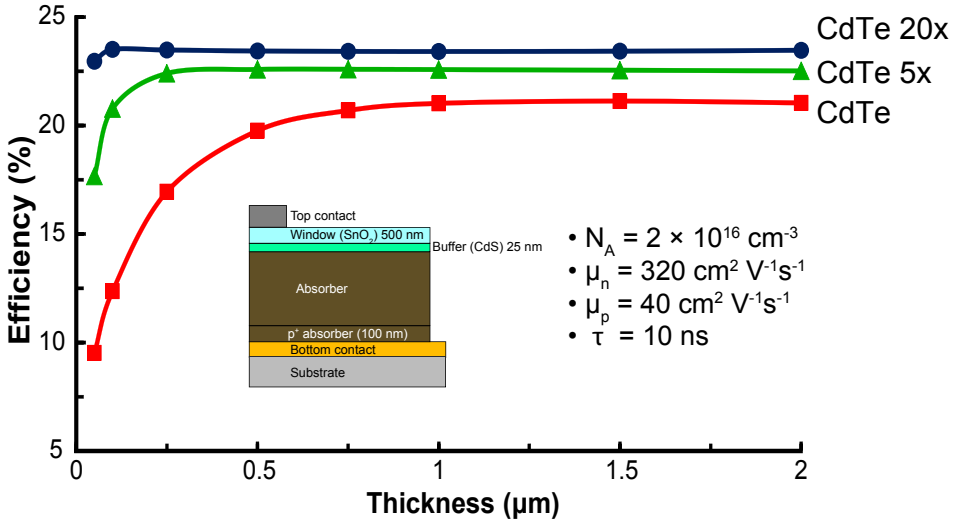


Figure 4.9: Simulated device efficiency as a function of the absorber thickness for a high carrier mobility, diffusion-based TFSC. The three curves correspond to the three absorption coefficients - CdTe, CdTe-5x, and CdTe-20x.

three absorption strengths. The efficiency for CdTe absorption increases significantly with an increase in absorber thickness until $L^A$ = 1 $\mu$m, at which a simulated efficiency of 21.6% is obtained. Beyond 1 $\mu$m, the efficiency saturates with increasing absorber layer thickness. Similar to Fig. 4.5, increasing the absorption strength to CdTe-5x and CdTe-20x improves the overall efficiency, reaching a maximum of 22.6% at 500 nm for the CdTe-5x absorption, and 23.5% at 250 nm for the CdTe-20x absorption. Compared to the high mobility drift-based TFSC (Fig. 4.5), the high mobility diffusion-based TFSC has an efficiency improvement of 1 - 2%.

The critical thickness required to fully absorb the solar spectrum is again identified using quantum efficiency simulations. Figure 4.10 shows the quantum efficiency for the three absorption strength cases with increasing absorber layer thicknesses. For CdTe, a minimum of 1 $\mu$m is required for effective absorption over the entire solar spectrum, while for CdTe-

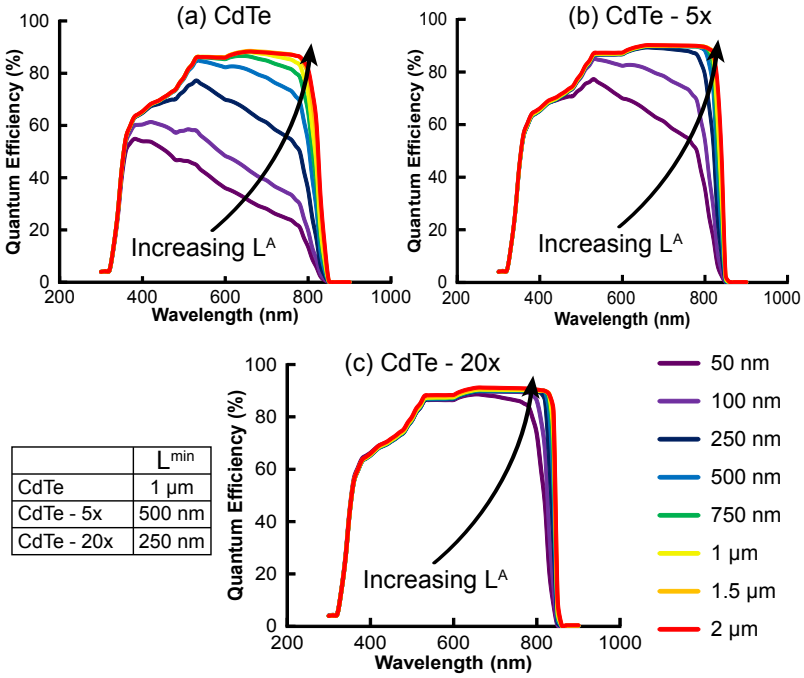


| | $L^{min}$ |
|---|---|
| CdTe | 1 µm |
| CdTe - 5x | 500 nm |
| CdTe - 20x | 250 nm |

Figure 4.10: Simulated quantum efficiency for a high mobility, diffusion-based TFSC for the three absorption coefficients a) CdTe, b) CdTe-5x, and c) CdTe-20x.

5x the minimum thickness is 500 nm, and for the CdTe-20x case the thickness requirement reduces to 250 nm.

When the minority carrier mobility is reduced to 10 $cm^2V^{-1}s^{-1}$, the diffusion length $L^{diff}$ decreases to 0.5 $\mu$m, or 500 nm, significantly lower than $L^{diff}$ (2.8 $\mu$m) for the high mobility diffusion-based TFSC. The variation in device efficiency as a function of absorber layer thickness is shown in Fig. 4.11 for the three absorption strengths. Compared to the high mobility diffusion-based TFSC (Fig. 4.9) the CdTe absorption in Fig. 4.11, shows a reduced efficiency, reaching a maximum of 18.3% at 500 nm, before reducing to 17.4% at 2 $\mu$m. Since $L^{diff}$ is 500 nm, a maximum efficiency is reached at this thickness, beyond which the efficiency decreases due to increased recombination. For the CdTe-5x and CdTe-20x absorption cases, while the overall efficiency increases compared to that of CdTe, the

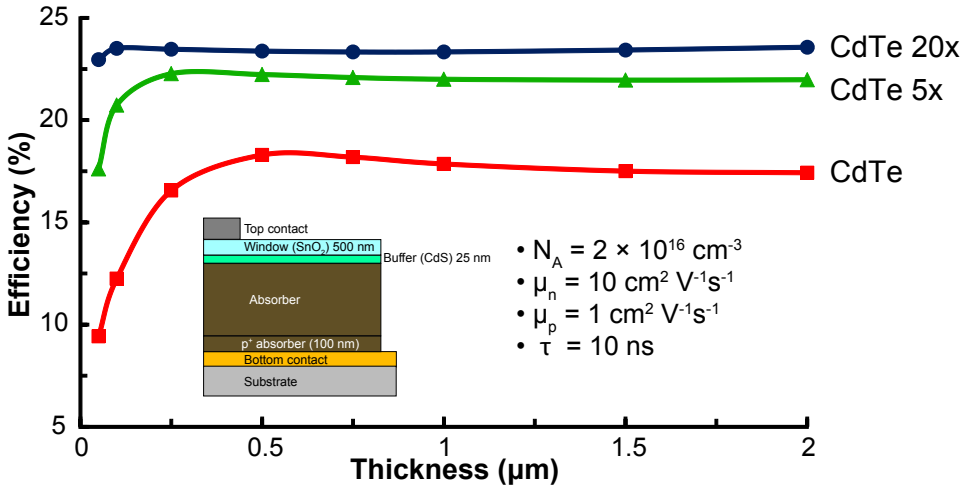


Figure 4.11: Simulated device efficiency as a function of the absorber thickness for a low mobility diffusion-based TFSC

efficiency reaches a maximum of 22.3% at 250 nm for the CdTe-5x absorption, and 23.5% at 100 nm for the CdTe-20x absorption. The efficiencies of the low mobility diffusion-based TFSC for absorption coefficients beyond CdTe are comparable to the high mobility diffusion-based TFSC. However, it should be noted that at these thicknesses, 250 nm (for CdTe-5x) and 100 nm (for CdTe-20x), the TFSC is actually a drift cell. This is evident from Fig. 4.4 which indicates that for a carrier concentration $N_A = 2 \times 10^{16}$ cm$^{-3}$, the depletion width is $\sim$ 250 nm. Since the absorber thickness is equivalent to the depletion width, the transport mechanism here is closer to drift than diffusion.

The reduction in critical thickness for the low mobility diffusion-based TFSC is confirmed from quantum efficiency simulations in Fig. 4.12. CdTe absorption shows a maximum QE for $L^A = 500$ nm, while the maximum QE for CdTe-5x occurs at $L^A = 250$ nm, and CdTe-20x has a maximum QE at $L^A = 100$ nm. This indicates that an improvement in the absorption coefficient compared to CdTe can provide a 20% efficient TFSC operating in a drift mode even with a carrier concentration of $10^{16}$ cm$^{-3}$ and low carrier mobilities.

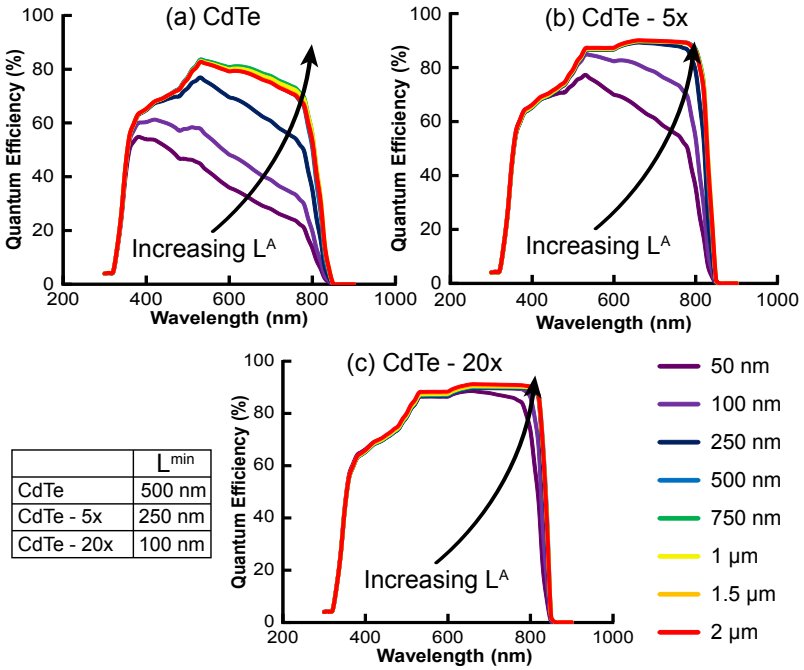


| | $L^{min}$ |
|---|---|
| CdTe | 500 nm |
| CdTe - 5x | 250 nm |
| CdTe - 20x | 100 nm |

Figure 4.12: Simulated quantum efficiency for a low mobility diffusion-based TFSC for the three absorption coefficients a) CdTe, b) CdTe-5x, and c) CdTe-20x.

Table 4.3 summarizes the critical absorber thickness and the corresponding efficiency for the diffusion-based TFSC in both the low and high-mobility cases.

Thus, improving the absorption coefficient compared to CdTe-base has a significant effect on the absorber layer thickness. First, the increased absorption strength improves the overall TFSC efficiency due to more effective photogeneration, leading to an increased photocurrent. Second, increased absorption implies that a thinner absorber can effectively absorb the solar spectrum. Third, the device operation mode can be drift-based with a thin absorber, even with a wide range of carrier concentrations ($10^{14}$ - $10^{16}$ $cm^{-3}$), and carrier mobility need not be very large to provide an efficient TFSC.

| Absorption Strength | Low mobility case | | High mobility case | |
|---|---|---|---|---|
| | $L^{abs}$ [nm] | $\eta$ [%] | $L^{abs}$ [nm] | $\eta$ [%] |
| CdTe-base | 500 | 18.3 | 1000 | 21 |
| CdTe-5x | 250 | 22.3 | 500 | 22.6 |
| CdTe-20x | 100 | 23.5 | 250 | 23.5 |

Table 4.3: Efficiency at the critical thickness for an absorber in a diffusion-based TFSC for the three absorption strengths. Both low and high mobility cases are tabulated.

## 4.6 Minority carrier lifetime

Ultra-thin absorber layers in a TFSC are an attractive option since photogenerated carriers travel a shorter distance prior to being collected. To minimize recombination, the lifetime of a photogenerated carrier has to be longer than the time required to travel across the absorber layer, i.e., the transit time. An approach described by Sze and Ng [12] can be used to estimate the approximate defect density tolerable in an absorber. In the absence of charged traps, the electric field ($\xi$) within the absorber can be assumed to be uniform and is given as,

$$\xi = \frac{E_G}{q \times L^A}, \tag{4.6}$$

where $L^A$ is the thickness of the absorber. The presence of charged defect states alters the electric field by [12],

$$\Delta\xi = \frac{qN_T L^A}{\varepsilon_s}, \tag{4.7}$$

where $N_T$ is the concentration of charged defects [$cm^{-3}$] and $\varepsilon_s$ is the absorber low frequency dielectric constant. For an absorber with a band gap of 1.4 eV and a dielectric constant of

| Absorber Thickness [nm] | Electric Field [V $cm^{-1}$] | Defect Concentration [$cm^{-3}$] |
|---|---|---|
| 1000 | $1.4 \times 10^4$ | $7.8 \times 10^{14}$ |
| 500 | $2.8 \times 10^4$ | $2.9 \times 10^{15}$ |
| 250 | $5.6 \times 10^4$ | $1.6 \times 10^{16}$ |
| 100 | $1.5 \times 10^5$ | $7.3 \times 10^{16}$ |

Table 4.4: Assessment of tolerable defect concentrations for different absorber layer thicknesses along with the corresponding electric field across the absorber.

CdTe ($\varepsilon_s = 9.4$) [46], Eqns. 4.6 and 4.7 can be equated to estimate the maximum concentration of tolerable defects for different absorber layer thicknesses tabulated in Table 4.4.

Table 4.4 indicates that an increase in the electric field across a thin absorber increases the concentration of defects that can be tolerated without affecting carrier collection. Also, defect densities as high as $10^{14}$ $cm^{-3}$ (or $\tau$ = 1 ns) can be tolerated in a TFSC with an 1 $\mu$m thick absorber, while defect densities $10^{16}$ $cm^{-3}$ ($\tau$ = 0.01 ns) can be tolerated in a TFSC with an 100 nm thick absorber. Since a minimum thickness was identified for each absorption strength in the previous section (Tables 4.2 and 4.3), the minority carrier lifetime is simulated for the three absorption strengths to confirm whether ultra-thin absorbers in a TFSC can indeed tolerate such high defect concentrations. The variation in minority carrier lifetime is simulated by changing the concentration of defects using Table 2.1 to cover the range from disordered amorphous materials ($\tau$ = 0.1 ns), to polycrystalline thin-films with a low density of defects ($\tau$ = 100 ns).

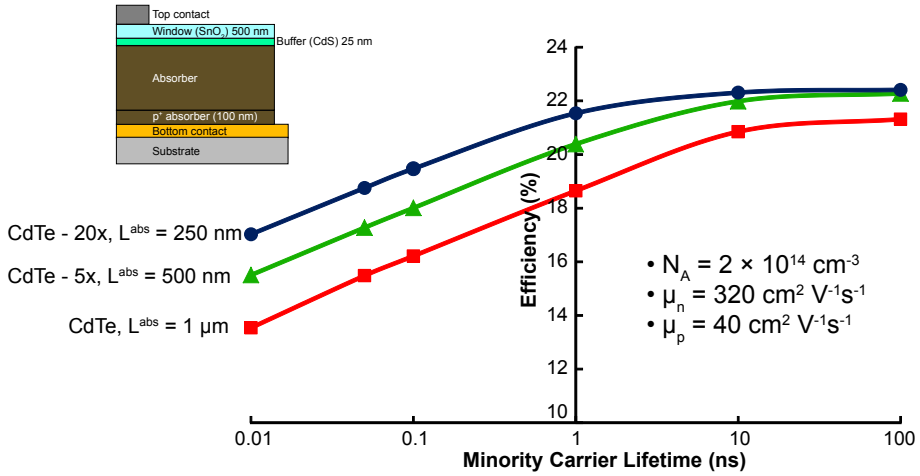


Figure 4.13: Variation in efficiency for a *high*-mobility drift-based TFSC as a function of minority carrier lifetime for three absorption strengths.

### 4.6.1 Drift-based TFSCs

The efficiency of a *high*-mobility drift-based TFSC as a function of minority carrier lifetime for three absorption strengths is shown in Fig. 4.13. The efficiency increases with increasing minority carrier lifetime (or decreasing concentration of mid-gap defects) for all absorption strengths. However, beyond a minority carrier lifetime of 100 ns, there is no appreciable increase in efficiency. For the CdTe absorption case, increasing the lifetime from 1 ns to 10 ns increases the efficiency from 18.6% to 20.9%, suggesting that improving the minority carrier lifetime is one route for a CdTe-based TFSC to have a comparable efficiency to that of c-Si. Increasing the absorption strength beyond CdTe increases the overall efficiency for all minority carrier lifetimes. For example, the CdTe-5x has a simulated efficiency of 20.4% at $\tau = 1$ ns, while the CdTe-20x absorption case provides an efficiency of 21.5% at $\tau = 1$ ns. In addition, increasing the minority carrier lifetime beyond 10 ns for the CdTe-5x and CdTe-20x absorption cases has a small (0.1 - 0.4%) improvement in efficiency. At lifetimes

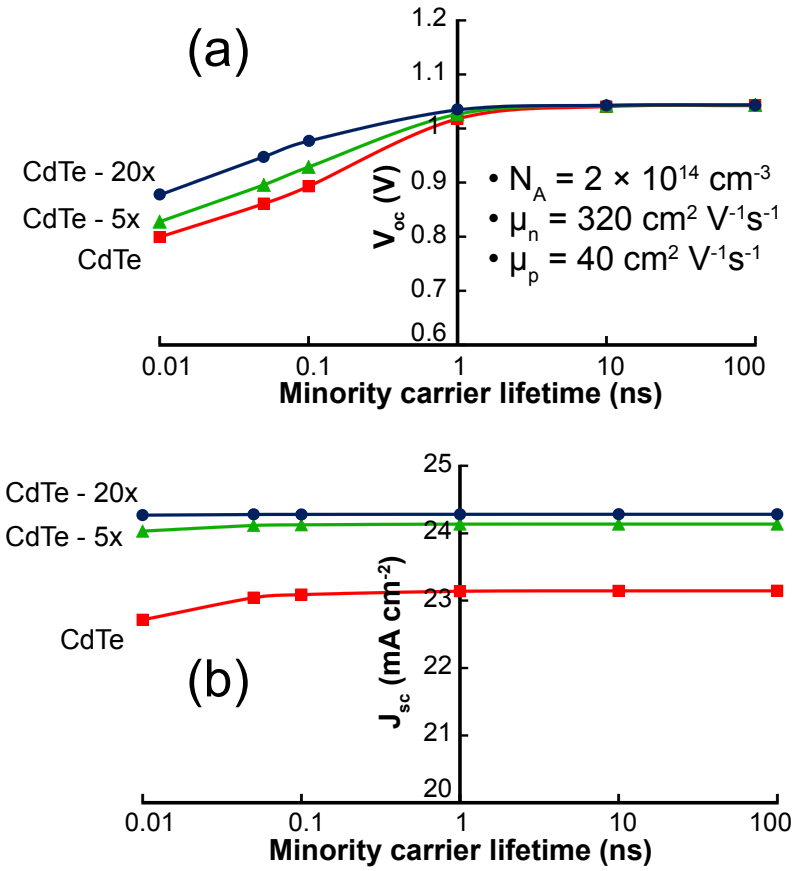


Figure 4.14: Variation in (a) $V_{OC}$ and (b) $J_{SC}$ of a *high*-mobility drift-based TFSC as a function of minority carrier lifetime for three absorption strengths.

below 1 ns, the *high*-mobility drift-based TFSC shows efficiencies above 12% for $\tau = 0.01$ ns (or $N_T = 10^{16}$ $cm^{-3}$) irrespective of the absorption strength. The efficiency for the CdTe-5x absorption at $\tau = 0.01$ ns is 15.5%, while for the CdTe-20x absorption case, the efficiency is 17% for the same carrier lifetime.

The mechanism for the efficiency trends can be understood by plotting the open-circuit voltage ($V_{OC}$) and short-circuit current density ($J_{SC}$) as a function of the minority carrier lifetime for the three absorption strengths shown in Fig. 4.14. The variation of $V_{OC}$ as a function of the minority carrier lifetime is shown in Fig. 4.14 (a) and indicates that $V_{OC}$

converges at $\sim$ 1 V for $\tau$ = 1 ns irrespective of the absorption strength. For a low minority carrier lifetime of $\tau$ = 0.01 ns, the $V_{OC}$ for CdTe reduces to 0.8 V. Increasing the absorption strength for low minority carrier lifetimes still shows a reduced $V_{OC}$ compared to $\tau$ = 1 ns, and the $V_{OC}$ for CdTe-5x reduces to 0.83 V, while $V_{OC}$ for CdTe-20x reduces to 0.88 V. The simulated $V_{OC}$ is consistent with the rule of thumb that $V_{OC} \sim E_G/q$ - 0.4 V. In this simulation study, $E_G$ = 1.4 eV, giving rise to $V_{OC}$ of $\sim$ 1 V. Figure. 4.14 (b) plots $J_{SC}$ as a function of the minority carrier lifetime and indicates that $J_{SC}$ increases with increasing absorption strength. Also, $J_{SC}$ is relatively constant irrespective of the minority carrier lifetime, while the CdTe absorption case has a slight decrease at $\tau$ = 0.01 ns.

The trends in Fig. 4.14 can be understood as follows. The maximum $V_{OC}$ generated in the absorber layer due to illumination is related to the quasi-Fermi level (QFL) splitting. Mid-gap defects act as recombination centers capturing photogenerated minority carriers, reducing the overall QFL splitting and lowering $V_{OC}$. $J_{SC}$ remains unaffected since the drift field circumvents recombination by sweeping carriers towards their respective contacts.

The variation in efficiency as a function of the minority carrier lifetime for three absorption strengths in a *low*-mobility drift-based TFSC is shown in Fig. 4.15. Values of the absorber layer thickness from Table 4.2 are used in this simulation. Similar to the *high*-mobility drift-based TFSC (Fig. 4.13), increasing the absorption strength compared to CdTe increases the overall efficiency. For the CdTe absorption case, the efficiency is 18.1% at $\tau$ = 1 ns and increases to 23.1% at $\tau$ = 100 ns. The CdTe-20x absorption on the other hand, has a simulated efficiency of 21.8% at $\tau$ = 1 ns, while a minority carrier lifetime of $\tau$ = 100 ns provides an efficiency of 24.3%. Decreasing the minority carrier lifetime below 1 ns results in a significant decrease in the efficiency for CdTe. In fact, SCAPS was unable to simulate

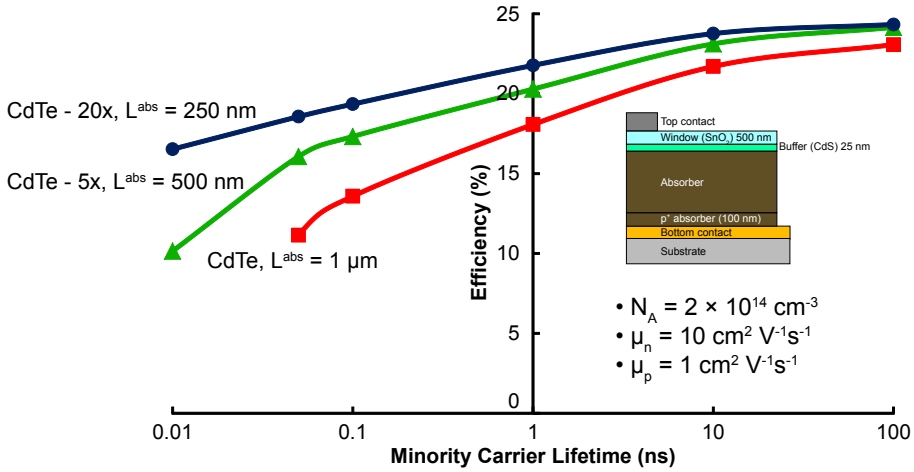


Figure 4.15: Variation of a *low*-mobility drift-based TFSC device efficiency as a function of minority carrier lifetime for the three absorption strengths.

the $\tau = 0.01$ ns condition, indicating a dramatic decrease in the efficiency of a thick ($L^A = 1$ $\mu$m) absorber in the presence of a large concentration of defects ($N_T > 10^{15}$ cm$^{-3}$). Increasing the absorption strength to CdTe-5x results in an efficiency of 10.1% at $\tau = 0.01$ ns, while the CdTe-20x absorption provides a simulated efficiency of 16.5% at $\tau = 0.01$ ns.

Similar to Fig. 4.14, $V_{OC}$ and $J_{SC}$ of the *low*-mobility drift-based TFSC can be plotted as a function of the minority carrier lifetime for the three absorption strengths shown in Fig. 4.16. While $V_{OC}$ in Fig. 4.14 essentially saturated at $\sim 1$ V for a minority carrier lifetime of 1 ns, Fig. 4.16 indicates that $V_{OC}$ increases slightly from 1.04 V to 1.09 V as the absorption strength is increased from CdTe to CdTe-20x. Increasing the minority carrier lifetime beyond 10 ns results in $V_{OC}$ saturating at 1.12 V for all three absorption strengths. Decreasing the minority carrier lifetime below 1 ns decreases $V_{OC}$ for all three absorption strengths. At $\tau =$ 0.01 ns, $V_{OC}$ for the CdTe-5x absorption is 0.85 V, while $V_{OC}$ for the CdTe-20x absorption

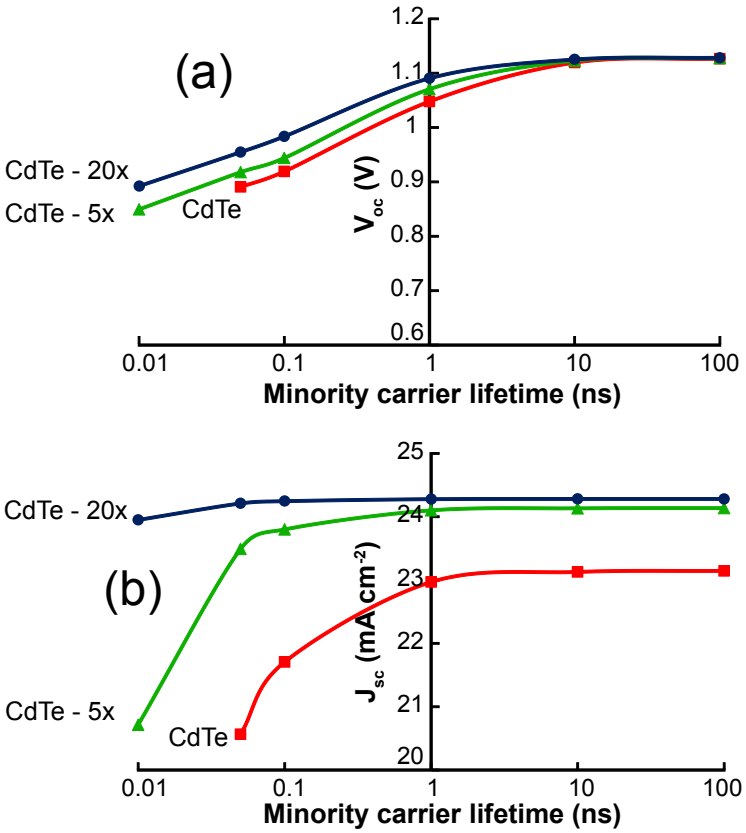


Figure 4.16: Variation in (a) $V_{OC}$ and (b) $J_{SC}$ of a *low*-mobility drift-based TFSC as a function of minority carrier lifetime for three absorption strengths.

is 0.9 V, and these $V_{OC}$ values are similar to the *high*-mobility drift-based TFSC simulations in Fig. 4.14 (a).

Figure 4.16 (b) plots $J_{SC}$ as a function of minority carrier lifetime for the *low*-mobility drift-based TFSC. Unlike Fig. 4.14 (b), $J_{SC}$ is not constant as a function of decreasing minority carrier lifetimes. $J_{SC}$ for CdTe reduces from 23 mA cm$^{-2}$ at $\tau$ = 1 ns to 20.5 mA cm$^{-2}$ at $\tau$ = 0.1 ns. $J_{SC}$ decreases significantly from 24.1 mA cm$^{-2}$ at $\tau$ = 1 ns to 20.7 mA cm$^{-2}$ at $\tau$ = 0.01 ns for the CdTe-5x absorption case. $J_{SC}$ for the CdTe-20x absorption, on the other hand, does not show a significant decrease for low minority carrier lifetimes and drops by 0.4 mA cm$^{-2}$ in going from $\tau$ = 1 ns to 0.01 ns. This suggests that improving the absorption coefficient beyond CdTe by at least an order of magnitude allows for an ultra-thin absorber layer ($L^A$ = 100 - 500 nm) in a drift-based operation mode. Additionally, a low mobility material in such a configuration can still provide a high efficiency ($\eta$ >15%) TSFC even with a large density of defects, suggesting that both mobility and minority carrier lifetime constraints may not limit the performance of a TFSC incorporating an ultra-thin high absorption material.

### 4.6.2 Diffusion-based TFSCs

The efficiency for a *high*-mobility diffusion-based TFSC as a function of minority carrier lifetime for three absorption strengths is shown in Fig. 4.17. As expected, efficiency increases with increasing minority carrier lifetime for all absorption strengths. The efficiency for CdTe absorption increases from 18.3% at $\tau$ = 1 ns to 22.5% at $\tau$ = 100 ns. Increasing the absorption strength to CdTe-5x increases the efficiency at 1 ns to 20.9% and to 23.8% at $\tau$ = 100 ns. Unlike the high-mobility *drift*-based TFSC (Fig. 4.13) where efficiency saturated at 22.3% beyond $\tau$ = 10 ns, the efficiency for a high-mobility *diffusion*-based TFSC with CdTe-20x absorption increases from 21.7% at $\tau$ = 1 ns to 23.8% $\tau$ = 100 ns. The efficiency

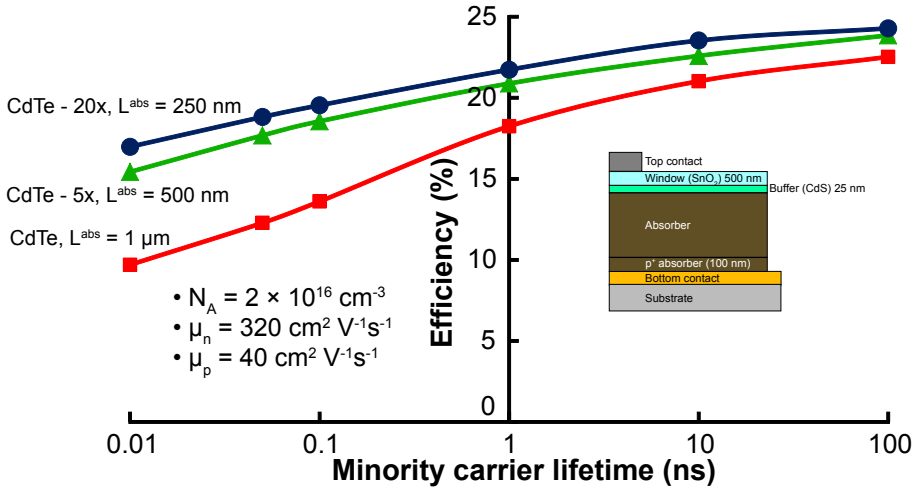


Figure 4.17: Variation of a *high*-mobility diffusion-based TFSC device efficiency as a function of minority carrier lifetime for three absorption strengths.

increases with increasing minority carrier lifetime since minority carriers can be more effectively extracted after they diffuse to the edge of the space charge region (SCR).

The CdTe absorption case has significant loss in efficiency for a lifetime below 1 ns. The efficiency at $\tau = 0.1$ ns is 13.6% and reduces to 9.7% for $\tau = 0.01$ ns. The high-mobility *drift*-based TFSC (Fig. 4.13) indicated that a 1 $\mu$m thick CdTe absorber could provide an efficiency of 13.5% at $\tau = 0.1$ ns. Fig. 4.17 implies that a *diffusion*-based TFSC incorporating an absorber with an absorption coefficient similar to that of CdTe requires a minority carrier lifetime $\tau > 0.1$ ns for an efficiency greater than 10%. Increasing the absorption strength beyond that of CdTe significantly improves the efficiency at a low carrier lifetime. For CdTe-5x absorption, the efficiency at $\tau = 0.01$ ns is 15.4%, while for the CdTe-20x absorption case, the efficiency is 17% at the same lifetime.

The variation in $V_{OC}$ and $J_{SC}$ for a high-mobility diffusion-based TFSC as a function of the minority carrier lifetime in Fig. 4.18 differs from that of the high-mobility drift-based

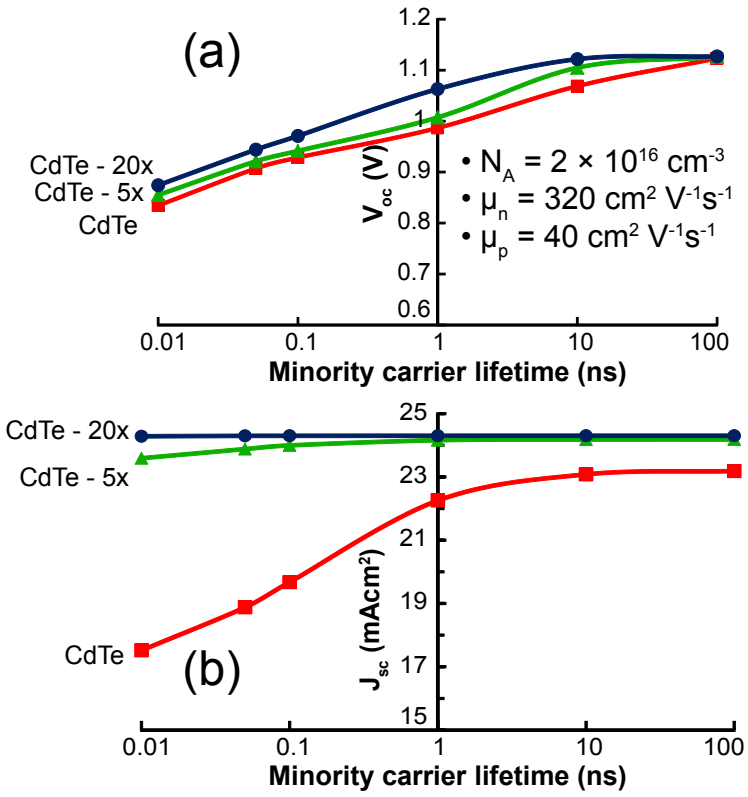


Figure 4.18: Variation in (a) $V_{OC}$ and (b) $J_{SC}$ of a *high*-mobility diffusion-based TFSC as a function of minority carrier lifetime for three absorption strengths.

TFSC (Fig. 4.14). Figure. 4.18 (a) displays $V_{OC}$ as a function of the minority carrier lifetime for the high-mobility diffusion-based TFSC. It indicates that $V_{OC}$ for CdTe and CdTe-5x absorption cases is $\sim$ 1 V, while $V_{OC}$ for CdTe-20x increases slightly to 1.05 V. At $\tau$ = 100 ns, $V_{OC}$ for all three absorption strengths converge at 1.13 V. For a low minority carrier lifetime of $\tau$ = 0.01 ns, $V_{OC}$ for CdTe is 0.83 V, while CdTe-5x absorption has a simulated $V_{OC}$ of 0.85 V and the CdTe-20x absorption is 0.87 V, indicating that $V_{OC}$ does not change appreciably. Fig. 4.18 (b) plots $J_{SC}$ as a function of minority carrier lifetime. $J_{SC}$ of the higher absorption cases compared to CdTe show a higher value. However, $J_{SC}$ does not change appreciably going from CdTe-5x to the CdTe-20x absorption case. For low minority carrier lifetimes, $J_{SC}$ for CdTe decreases significantly from 22 mA cm$^{-2}$ at $\tau$ = 1 ns to 17 mA cm$^{-2}$ at $\tau$ = 0.01 ns. The decrease in $J_{SC}$ is not as significant for the CdTe-5x absorption case where $J_{SC}$ decreases by 0.4 mA cm$^{-2}$, while $J_{SC}$ is constant at 24 mA cm$^{-2}$ for the CdTe-20x absorption case.

The $V_{OC}$ in a diffusion-based TFSC is a consequence of QFL splitting only in the SCR. $V_{OC}$ increases with increasing minority carrier lifetime since fewer recombination centers in the SCR can capture photogenerated minority carriers during transport across the depletion region. However, $J_{SC}$ decreases significantly for the CdTe absorption case since minority carriers generated in the 'bulk' of the absorber have to diffuse to the edge of the SCR. Increased recombination in the 'bulk' of the absorber reduces $J_{SC}$. Increasing the absorption strength to CdTe-20x significantly increases the rate of carrier generation such that the photocarriers lost to recombination constitute a small fraction of the total number carriers extracted.

The variation in efficiency for a *low*-mobility diffusion-based TFSC as a function of the minority carrier lifetime for three absorption strengths is shown in Fig. 4.19. For the CdTe absorption case, the efficiency is 12.7% at $\tau$ = 1 ns and increases to 21.8% at $\tau$ = 100

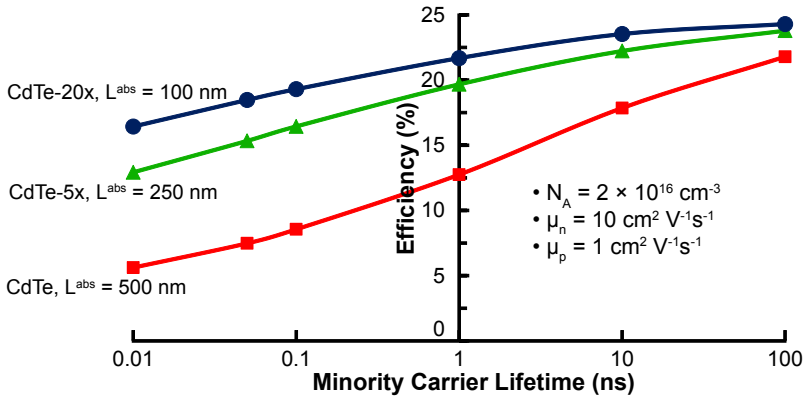


Figure 4.19: Variation of a *low*-mobility diffusion-based TFSC device efficiency as a function of minority carrier lifetime.

ns. The efficiency at $\tau$ = 1 ns for CdTe-5x is 19.7% and increases to 24.3% at $\tau$ = 100 ns. CdTe-20x, on the other hand, has an efficency of 21.7% at $\tau$ = 1 ns and increases to 24.3% at $\tau$ = 100 ns. For a minority carrier lifetime less than 1 ns, the efficiency for CdTe decreases to 5.6% at $\tau$ = 0.01 ns, while the efficency for CdTe-20x is 16.4% at the same minority carrier lifetime. The efficiency of the CdTe-20x absorption case in a low-mobility *diffusion*-based TFSC is similar to that of the low-mobility *drift*-based TFSC. This is expected since $L^{abs}$ for CdTe-20x is 100 nm, so that the TFSC is essentially a drift cell.

Figure 4.20 (a) plots $V_{OC}$ for a *low*-mobility diffusion-based TFSC as a function of minority carrier lifetime for three absorption strengths. $V_{OC}$ for all three absorbers converge at 1.13 V at $\tau$ = 100 ns. $V_{OC}$ for the low-mobility *drift*-based TFSC plotted in Fig. 4.16 (a) converges to 1.12 V at $\tau$ = 10 ns, suggesting that the same value can be obtained with a lower carrier lifetime in a drift-based TFSC. Increasing the absorption strength to CdTe-20x has a small increase (0.06 V) in $V_{OC}$. Decreasing the minority carrier lifetime below 1 ns decreases $V_{OC}$ for all three absorption strengths. For CdTe, $V_{OC}$ at $\tau$ = 0.01 ns is 0.84 V and increases

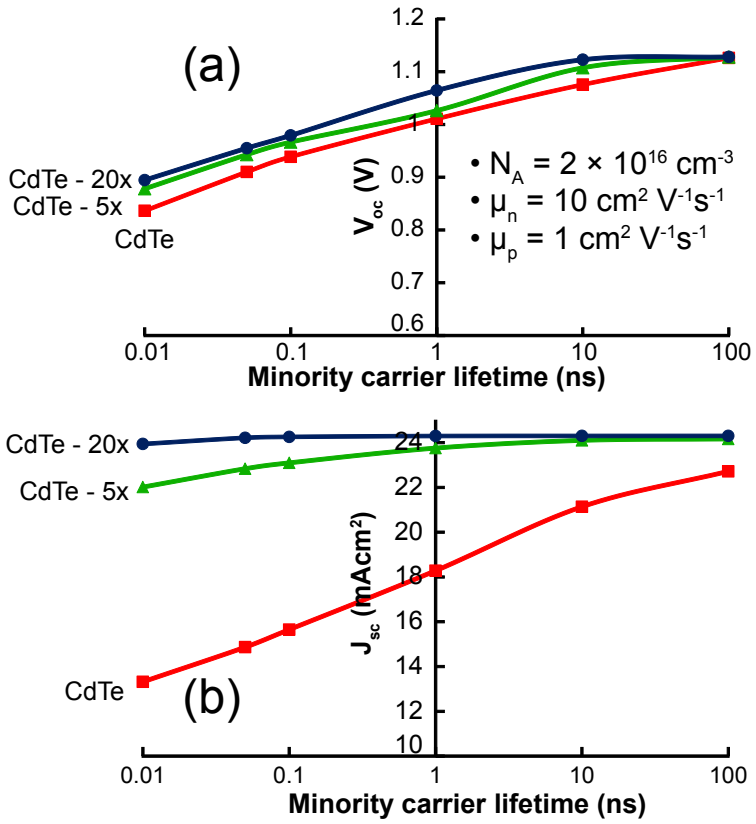


Figure 4.20: Variation in (a) $V_{OC}$ and (b) $J_{SC}$ of a *low*-mobility diffusion-based TFSC as a function of minority carrier lifetime for three absorption strengths.

to 0.88 V for CdTe-5x and 0.89 V for CdTe-20x. Figure 4.20 (b) plots $J_{SC}$ as a function of minority carrier lifetime for three absorption strengths. $J_{SC}$ for CdTe reduces from 22.7 mA $cm^{-2}$ at $\tau$ = 100 ns to 18.3 mA $cm^{-2}$ at 1 ns and continues to decrease to 13 mA $cm^{-2}$ for $\tau$ = 0.01 ns. When the absorption strength is increased to CdTe-5x, $J_{SC}$ has a maximum of 24.3 mA $cm^{-2}$ at $\tau$ = 100 ns and decreases by 2 mA $cm^{-2}$ to 22 mA $cm^{-2}$ at $\tau$ = 0.01 ns. $J_{SC}$ for CdTe-20x is essentially constant at 24.3 mA $cm^{-2}$ and reduces by 0.04 mA $cm^{-2}$ to 23.9 mA $cm^{-2}$ at $\tau$ = 0.01 ns.

## 4.7 Conclusions

This chapter presents a simulation study focusing exclusively on properties of the absorber layer. The absorption coefficient of CdTe was scaled (5x and 20x) and photovoltaic properties of a drift- and a diffusion-based TFSC were compared. In addition, carrier mobilities of CdTe were used (high mobility case) along with reduced values of $\mu_n$,$\mu_p$ = 10, 1 $cm^2V^{-1}s^{-1}$ (low mobility case) and TFSC properties were compared. Increasing the absorption coefficient beyond that of CdTe has a significant impact on the design of a TFSC. An increased absorption coefficient (CdTe-5x or CdTe-20x) results in increased concentration of photogenerated carriers and implies that light from the solar spectrum is absorbed using a thinner absorber. The thicknesses shown in this chapter (100 - 500 nm) are significantly lower than those required for a TFSC utilizing CIGS (1 - 2 $\mu$m) or CdTe (2 - 4 $\mu$m). Such a thin absorber can be integrated into a drift-based TFSC, where transport of photogenerated carriers is governed by a built-in drift field which aids carrier separation and collection.

A drift-based TFSC incorporating an ultra-thin absorber with a strong absorption coefficient has several advantages. First, the increased absorption strength improves the overall

TFSC efficiency due to more effective photogeneration, leading to an increased photocurrent. Second, the device operation mode can be drift-based with a thin absorber, even with a wide range of carrier concentrations ($10^{14}$ - $10^{16}$ $cm^{-3}$). Third, transport properties such as carrier mobility and minority carrier lifetime, which have historically required large values for an efficient TFSC can be significantly relaxed. It is important to note that a *low*-mobility drift-based TFSC has a comparable efficiency to that of a *high*-mobility diffusion-based TFSC for a thin absorber ($L^A$ <750 nm). This is significant since improving the absorption coefficient beyond CdTe can be expected to lower the requisite mobility of a photogenerated carrier (refer to Ch. 2). Thus, while the CdTe-20x absorption case is simulated with a high carrier mobility, the high mobilities ($\mu_n$,$\mu_p$ = 320, 40 $cm^2V^{-1}s^{-1}$) used in this study might be unrealistic to achieve.

This chapter also indicates that a material with an improved absorption coefficient (compared to CdTe) integrated into a drift-based TFSC is tolerant towards the presence of a large defect density in the absorber layer. This is important from a manufacturing perspective. A TFSC with a higher defect tolerance would imply that intensive processing to develop a defect-free material would not be required, leading to a more cost effective manufacturing process. Thus, the questions posed at the beginning of this chapter can now be answered. Improving the absorption coefficient beyond CdTe (by an order of magnitude) allows for the possibility of using an ultra-thin absorber layer ($L^A$ = 100 - 500 nm) in a drift-based operation mode. In such a configuration, absorber layer material properties such as carrier concentration, carrier mobility, and minority carrier lifetime do not play a critical role in determining the efficiency of the TFSC. The remainder of this thesis focuses on the development of new materials that can have absorption coefficients significantly higher than that of CdTe.

# 5. IRON BASED SOLAR ABSORBERS

This chapter presents thin-film fabrication, characterization, and TFSC device simulations of two iron- (Fe) sulfide based solar absorbers. The study of high absorption materials begins with an investigation of $FeS_2$ thin-films fabricated via RF-magnetron sputtering. The performance limitations of $FeS_2$, as described in Ch. 2, are addressed using a combined experimental and theoretical approach. Thin films of a new inorganic solar absorber material, $Fe_2GeS_4$ are fabricated using RF-magnetron sputtering using design paradigms identified from the limitations of $FeS_2$. Finally, measured opto-electronic properties are input into SCAPS and the photovoltaic performance of $Fe_2GeS_4$ is predicted using device simulations.

## 5.1 $FeS_2$ - Pyrite

Fe-based solar absorbers such as iron pyrite ($FeS_2$) were identified early on as a viable Earth-abundant solar absorber [92]. As described in Ch. 2, pyrite exhibits a suitable band gap of $E_G \sim 0.9$ eV and a remarkably abrupt onset of absorption with an absorption coefficient reaching $1 \times 10^5$ cm$^{-1}$ at $E_G + 0.6$ eV, shown in Fig. 2.22. This strong absorption implies that the pyrite absorber layer thickness can be reduced to less than 1 $\mu$m without significant decrease in device performance [93]. Not only is this thickness requirement reduced from current TFSC absorber materials (CIGS = 1.5 - 2 $\mu$m [5]; CdTe = 2 - 4 $\mu$m [24]), it also enables the development of ultra-thin, drift-based TFSCs, as described in the previous chapter. A photoelectrochemical (PEC) cell using an n-$FeS_2$ single crystal in contact with an iodide/tri-iodide redox electrolyte exhibited a solar conversion efficiency of 2.8%, with a $V_{OC}$ of only 0.2 V [101]. This value is considerably lower than the theoretical maximum of $\sim 0.5$ V and

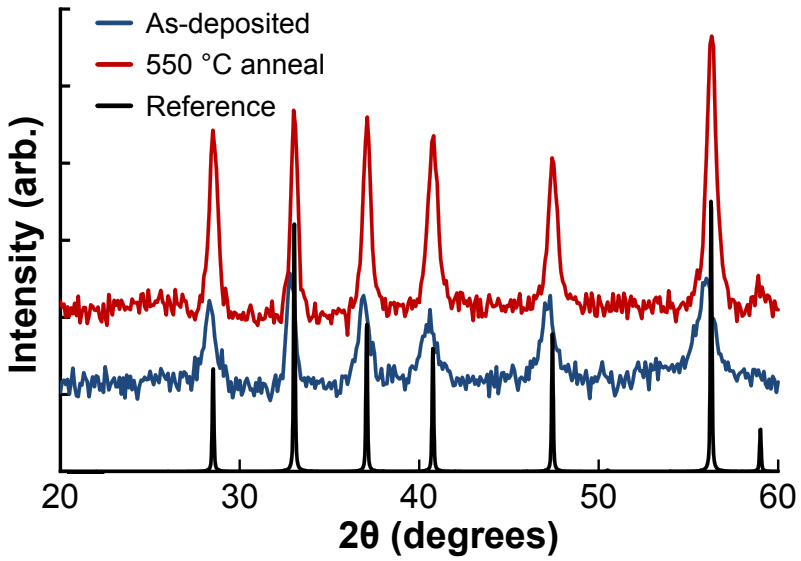


Figure 5.1: XRD plot of as-deposited $FeS_2$ thin-films and the same film annealed at 550 °C in a sulfur environment. An increase in crystallinity is observed post anneal.

has been historically attributed to Fermi level pinning due to sulphur vacancies [103]. In spite of extensive development spanning more than a decade, a pyrite-based TFSC has not yet been realized. To understand the cause for the $V_{OC}$ limitation, opto-electronic properties of pyrite thin films are studied and compared with theoretical calculations carried out by collaborators at NREL [118].

$FeS_2$ thin films were fabricated using RF magnetron sputtering of an FeS target purchased from AJA Incorporated. Sputter deposition parameters such as pressure, power, and gas flow were varied initially to optimize process parameters. Deposition rates of $\sim$ 8 nm/min were achieved using an RF power of 85 W with 5 mTorr of Ar/He (60/40) as the process gas, flowing at 20 sccms. No additional sulfur source was added during the deposition. The as-deposited films exhibited slight crystallinity which was improved with a 550°C post-deposition anneal, as shown in Fig. 5.1.

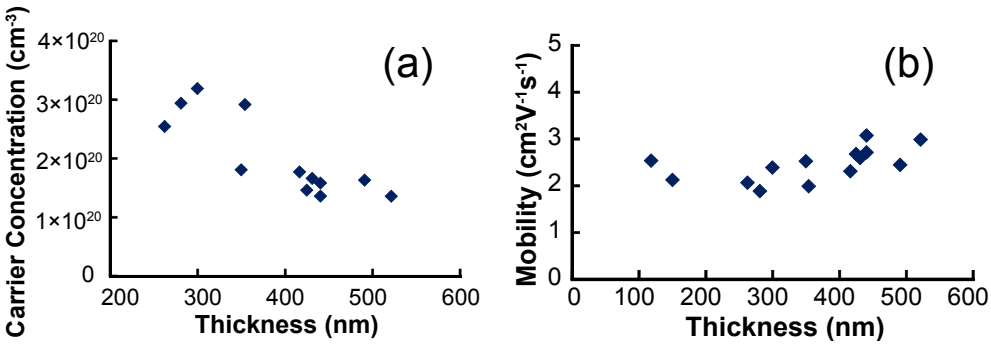


Figure 5.2: Hall measurement results from annealed $FeS_2$ thin films. The films exhibit (a) carrier concentrations greater than $10^{20}$ cm$^{-3}$, and (b) average hole mobilities of 2 - 3 cm$^2$ V$^{-1}$s$^{-1}$

Energy dispersive x-ray spectroscopy (EDS) measurements indicated that the annealed films have a S/Fe ratio of $\sim$ 1.7. To improve the stoichiometry of the films, optimized annealing conditions were explored in the Oregon State University Chemistry Department. As-deposited thin films were annealed in a sealed tube containing excess sulfur powder for one hour between 400 - 600 °C to yield single-phase pyrite thin films. During the anneal, excess sulfur powder vaporizes at the annealing temperature to react with the $FeS_2$ thin film improving the stoichiometry and crystallinity. An annealing temperature of 550 °C was found to be the optimal anneal temperature and the xray diffractograph is shown in Fig. 5.1.

Electrical characterization indicated that the annealed pyrite thin-films are p-type based on the sign of the Seebeck coefficient (S $\sim$ + 65 $\mu$V K$^{-1}$), and the high Seebeck coefficient indicates carrier concentration greater than $10^{20}$ cm$^{-1}$ (refer to Table. 3.1). In addition, results from Hall measurements are shown in Fig. 5.2. Figure 5.2a is a plot of the hole carrier concentration for $FeS_2$ thin films as a function of film thickness, and indicates that the films have an average value of $N_A \sim 3 \times 10^{20}$ cm$^{-3}$, a large carrier concentration value in accordance with the low observed Seebeck coefficient. This large carrier concentration value was

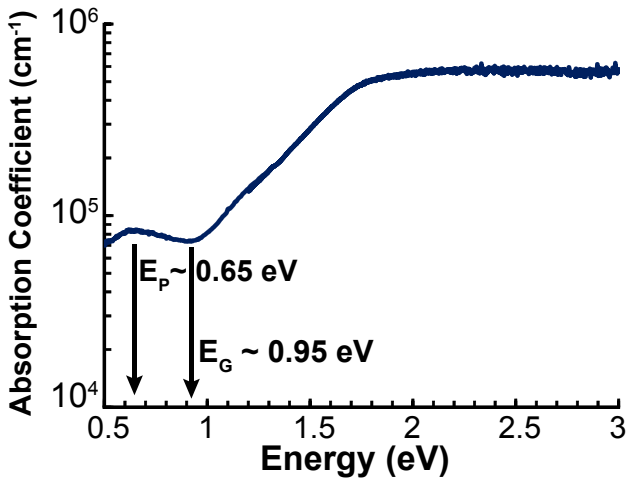


Figure 5.3: Absorption coefficient plot for a 120 nm $FeS_2$ thin film. The optical band gap value is indicated as 0.95 eV. In addition, the presence of a plasma energy can be seen at 0.65 eV.

independent of film thickness, process parameters variations for thin-film deposition or post-deposition anneal conditions. In addition, the films have an average hole mobility value of 2 - 3 $cm^2\ V^{-1}s^{-1}$, as shown in Fig. 5.2b. These measured electrical properties (i.e., p-type films with a high carrier concentration value) are similar to previously reported values on RF sputtered $FeS_2$ films [98] [100].

A plot of the measured absorption coefficient for a 120 nm $FeS_2$ thin-film is shown in Fig. 5.3 and indicates that $FeS_2$ is indeed a strong optical absorber, reaching a maximum value of $\alpha = 5\times\ 10^5\ cm^{-1}$ at $E_G$ + 1.8 eV. The slow onset of absorption indicates that $FeS_2$ has an indirect band gap value of $\sim$ 0.95 eV, as shown in Fig. 5.4a. However, a direct band gap is positioned at 1.1 eV (refer Fig. 5.4b, or 0.15 eV from the indirect band gap at the VBM. As a result, in spite of an indirect fundamental optical band gap, the direct band gap positioned 0.15 eV away from the VBM provides a strong absorption coefficient. However, the films exhibit a large sub-band gap absorption of $\alpha \sim 7\ \times\ 10^4\ cm^{-1}$, in spite of variations

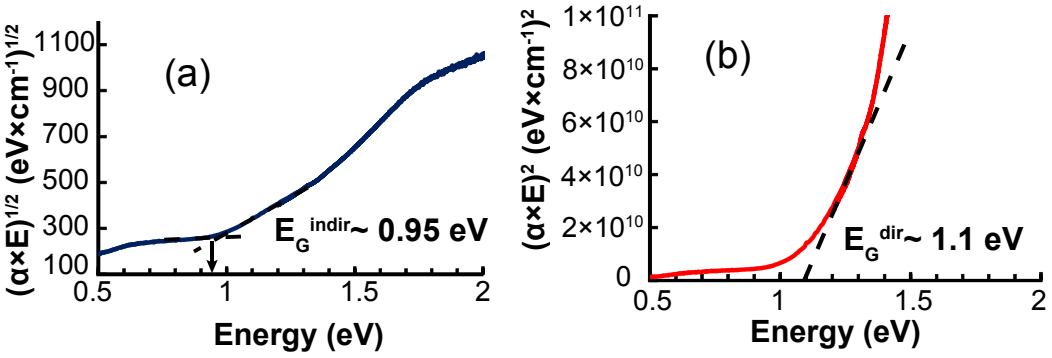


Figure 5.4: $FeS_2$ thin-films have (a) an indirect band gap value of $\sim$ 0.95 eV, and (b) a direct band gap of $\sim$ 1.1 eV.

in process conditions. This high sub-band gap absorption can arise due to a high carrier concentration from the presence of additional lower band gap phases.

The sub-band gap characteristics in Fig. 5.3 also indicate the presence of a plasma frequency ($\omega_p$) [Hz] at an energy $E_p \sim 0.65$ eV. The presence of the plasma frequency is evidence of a high carrier concentration value present in the thin film, and this energy value can be used to calculate an approximate carrier concentration ($N$) [cm$^{-3}$] value. Assuming an effective mass ($m^*$) = 1 and a dielectric constant of $\varepsilon_\infty = 26$ [119],

$$\omega_p = \frac{E_p}{h} = \sqrt{\frac{N q^2}{m^* M_e \varepsilon_0 \varepsilon_\infty}}, \tag{5.1a}$$

$$1.57 \times 10^{14}\,\text{Hz} = \sqrt{\frac{N q^2}{M_e \varepsilon_0 \times 26}}, \tag{5.1b}$$

$$\Rightarrow N = 2.01 \times 10^{20}\ [\text{cm}^{-3}]. \tag{5.1c}$$

The carrier concentration value extracted from the absorption coefficient plot provides a close match to that measured using Hall measurement techniques.

Results from transmission electron microscopy (TEM) and high resolution transmission electron microscopy (HRTEM) are shown in Fig. 5.5. Figure 5.5a is a cross-sectional

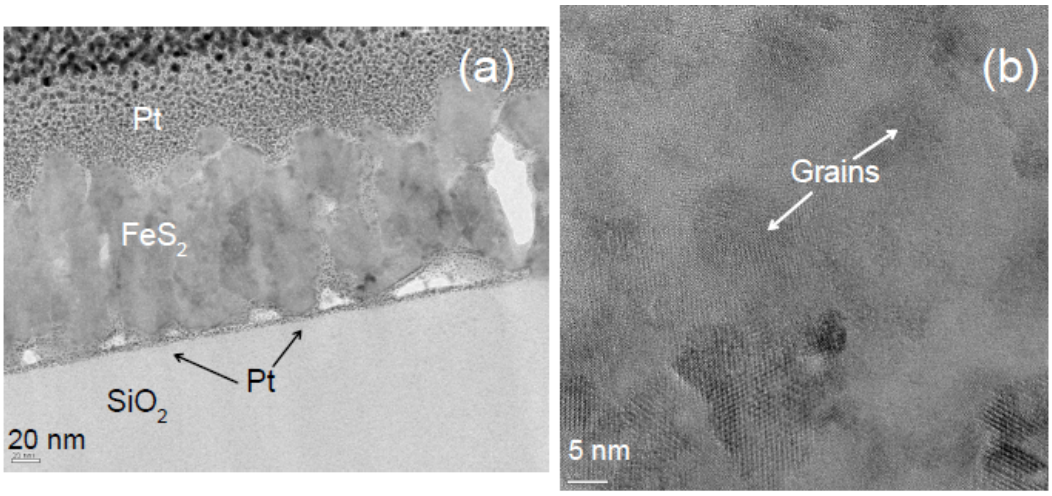


Figure 5.5: (a) Cross-sectional transmission electron micrograph and (b) High resolution transmission electron micrograph of an $FeS_2$ thin film.

view of a 125 nm $FeS_2$ thin film deposited on a fused-silica ($SiO_2$) substrate with platinum as a capping layer. Not only do the films exhibit low density and high porosity, as evidenced by the platinum aggregating at the $FeS_2$ - $SiO_2$ interface, but the films also exhibit small grain sizes (20 - 40 nm) in spite of a post-deposition anneal in excess sulfur at 550 °C. Figure 5.5b is a HRTEM of the same film and confirms the small grain sizes. It also indicates that the $FeS_2$ grains are dispersed in a large amorphous component. Since EDS measured thin films with a sulfur deficiency (S/Fe = 1.7), this suggests that Fe-S phases in addition to stoichiometric $FeS_2$ exist in the thin-film. Marcasite has the same chemical composition as pyrite, but has a different crystal structure and a lower band gap of 0.34 eV [99]. Other phases in the pyrite phase diagram include greigite ($Fe_3S_4$), pyrrhotite ($Fe_7S_8$), mackinawite ($Fe_{1+x}S$) in addition to a metallic troilite (FeS) phase [92].

Theoretical calculations provide insight into the defect formation in $FeS_2$. The formation energy for defects ($\Delta H_D$) as a function of the chemical potential using density functional

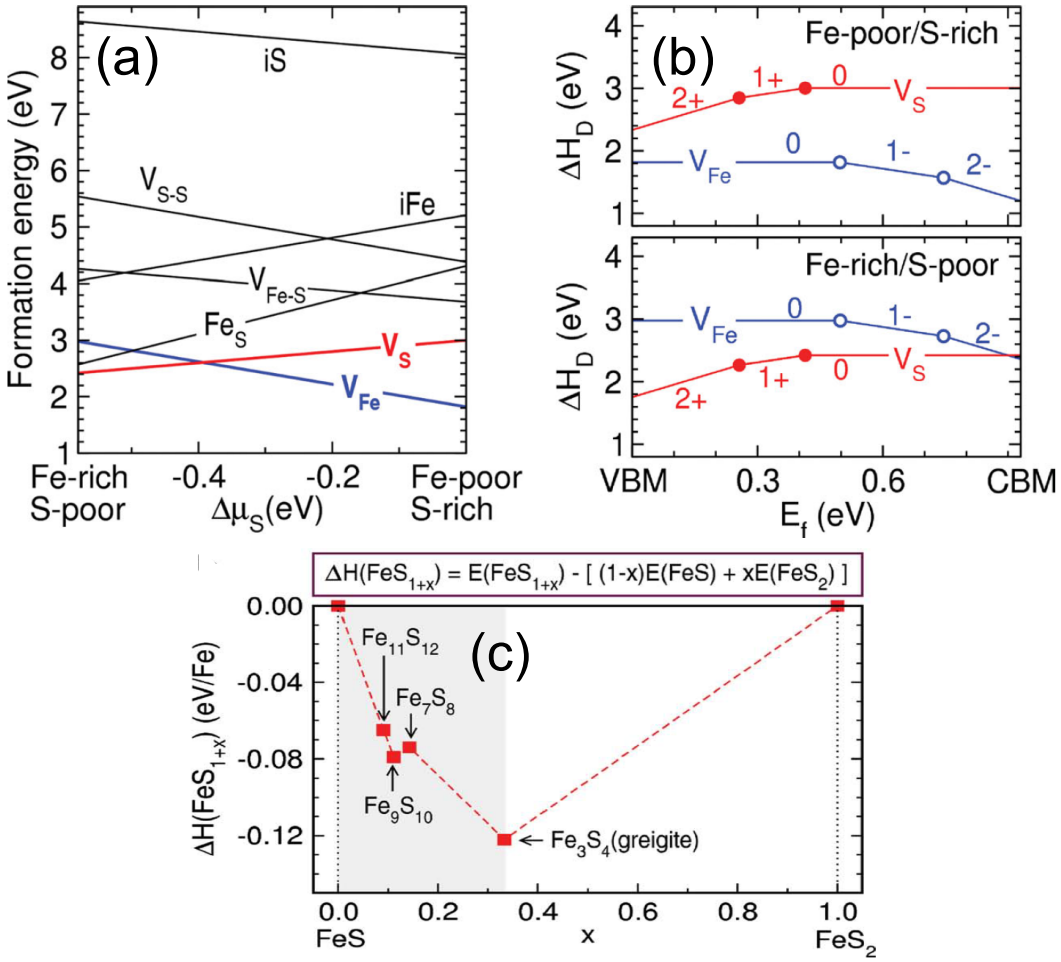


Figure 5.6: Theoretical calculations on $FeS_2$. (a) Enthalpy of formation as a function of chemical potential, showing different experimental growth conditions, and indicates that the formation energy of sulfur vacancies ($V_S$) is very high. (b) Enthalpy of formation as a function of Fermi energy. Since the lines for $V_S$ and $V_{Fe}$ do not intersect, calculations suggest that Fermi level pinning due to sulfur vacancies may not be the cause for the poor performance in $FeS_2$. (c) Enthalpy of formation for sulfur deficient phases. Intermediate sulfur deficient phases have lower formation energies that the end members, indicating that these intermediate phases can form if FeS is formed during film growth.

theory calculations is shown in Fig. 5.6a. The chemical potential is linked to experimental growth conditions ranging from Fe-rich/S-poor to Fe-poor/S-rich [118]. The defects shown include: Fe vacancies ($V_{Fe}$), S vacancies ($V_S$), Fe on S antisite substitution ($Fe_S$), Fe-S vacancy pair ($V_{Fe-S}$), S-S vacancy pair ($V_{S-S}$), interstitial Fe ($Fe_i$) and interstitial S ($S_i$). $FeS_2$ has been traditionally thought to be dominated by sulfur vacancies ($V_S$) [92]. However, in Fig. 5.6a, $V_S$ has a high formation energy of $\Delta H_D \sim 2.42$ eV. This suggests that $V_S$ would occur in low densities and may not be the reason behind the high carrier concentration values observed. Figure. 5.6b indicates that $V_S$ may not cause $E_F$-pinning in bulk $FeS_2$. In defect diagrams, $E_F$ will be pinned at an energy value where defect formation enthalpy lines intersect [32] [120]. In the case of $FeS_2$, Fig. 5.6b indicates that the positively charged donor defect ($V_S$) and the negatively charged acceptor defect ($V_{Fe}$) do not intersect within the band gap between any limiting growth (chemical potential) condition. This suggests that bulk defects are not responsible for $E_F$-pinning [118]. While bulk sulfur vacancies have a high defect formation energy ($\Delta H_D \sim 2.42$ eV) along the 011 plane [118], additional theoretical calculations by Krishnamoorthy *et al.* show that the formation energy for sulfur vacancies at the surface is reduced to $\Delta H_D \sim 0.4$ eV [121], implying that the sulfur vacancies can easily form at the surface compared to the bulk. In addition, Fig. 5.6c is a plot of the enthalpy of formation for sulfur deficient phases with respect to the end points FeS and $FeS_2$. Intermediate sulfur deficient phases such as $Fe_{11}S_{12}$, $Fe_9S_{10}$, $Fe_7S_8$ and $Fe_3S_4$ have lower formation energies than the FeS or $FeS_2$ end points in Fig. 5.6c, indicating that additional sulfur deficient phases can spontaneously form if sufficient sulfur is not provided during film growth. This can lead to an inhomogeneous microstructure with multiple phases observed in the thin film [118].

A combined theoretical and experimental investigation into the properties of $FeS_2$ suggests that while the optical characteristics of $FeS_2$ indicate a promising solar absorber, the spontaneous decomposition into sulfur deficient phases, including a metallic-like FeS phase, results in a thin film with a high carrier concentration and a significant sub-band gap absorption, unsuitable for a solar absorber material. True to its name, pyrite indeed is "Fool's Gold" even as a solar absorber!

## 5.2 $Fe_2GeS_4$-Based Absorbers

In an attempt to explore a viable alternative to $FeS_2$, three design paradigms were identified [118]. A stable iron-sulfide system which does not spontaneously phase-separate into sulfur-deficient, narrow-band gap phases has to be selected first. To have an optical band gap for solar absorption, the $Fe^{2+}$ ion has to be octahedrally coordinated, i.e., an iron atom has to be bonded to six nearest-neighbor sulfur atoms. This results in sufficient crystal-field splitting [18] to provide an adequately large band gap. To ensure that octahedral coordination is obtained, addition of a third element to form a strong covalent bond with sulfur is required [118]. Taking into account these considerations led to the development of $Fe_2GeS_4$ (FGS) and $Fe_2SiS_4$ (FSS) as new inorganic photovoltaic absorber materials. Bulk synthesis of FGS pressed powders and single crystals were undertaken in the Oregon State University Chemistry Department. Both powders and single crystals of FGS exhibited a band gap of 1.56 eV and a Seebeck coefficient of 780 $\mu$V $K^{-1}$ [122] [123]. The large positive Seebeck value corresponds to a p-type material with a carrier concentration $N_A \sim 10^{16}$ $cm^{-3}$, which is attractive for a solar absorber. This section describes the structural, electrical, and op-

tical characterization performed, along with simulated TFSC device performance, with an emphasis on $Fe_2GeS_4$ (FGS) thin films.

### 5.2.1 FGS Thin Film Synthesis and Characterization

Similar to $FeS_2$, FGS thin films were fabricated via RF-magnetron sputtering. $2''$ sputter targets were fabricated by Vorranutch Jieratum from the Oregon State University Chemistry Department by grinding synthesized FGS powder and pressing the powder at 11,000 psi for one hour at room temperature. The resulting target was then sintered at 900°C for 12 hours at 20,000 psi in a hot isostatic press (HIP). This process was repeated until a target density $>$90% was achieved. FGS thin films were fabricated by RF-magnetron sputtering using an Ar/He (60/40) mixture as the process gas, with pressures between 2.5 - 5 mTorr and RF powers between 65 - 95 W. A deposition rate of 9 nm/min was achieved at a pressure of 2.5 mTorr, with a process gas flow rate of 5 sccms at a power of 95 W. These process parameters are used throughout this work, unless mentioned otherwise. As-deposited sputtered films are amorphous as shown in Fig. 5.7. A subsequent anneal in a $GeS_2$ environment between 500 - 600°C promotes crystallization. Figure 5.7 shows that a 500°C anneal in a $GeS_2$ environment results in a crystalline film with the peaks providing a close match to reference peaks.

Attempts to crystallize FGS in-situ during sputter deposition using substrate heating resulted in Ge- and S-deficient amorphous films. A post-deposition anneal was always necessary to adjust the composition and crystallinity. $Fe_2SiS_4$ (FSS) was not explored in detail during this study due to difficulty in preparing a sputter target. Thin films of FSS were fabricated by sputtering FeS onto an etched silicon wafer and annealed at 700°C with sulfur in a sealed tube for 24 hours. XRD analysis of the films indicated a close match to reference peaks and reflectance measurements indicated a band gap of approximately 1.5 eV (results

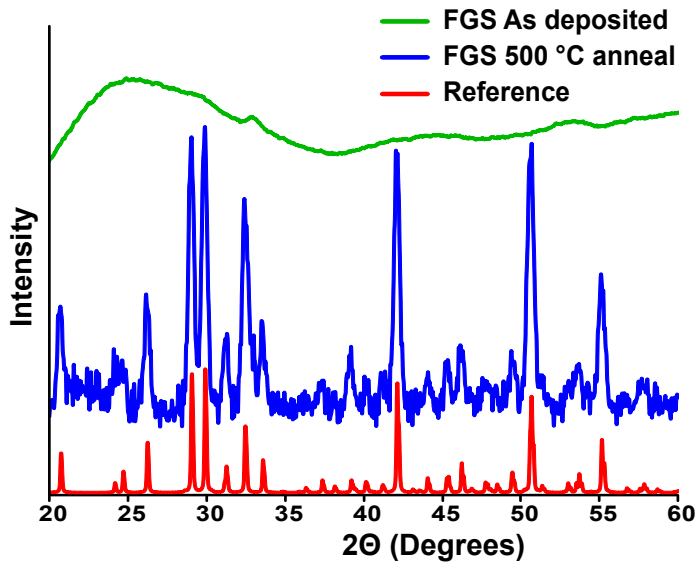


Figure 5.7: X-ray diffractogram of FGS thin films. The as-deposited FGS film is amorphous, while a 500 °C anneal in $GeS_2$ crystallizes the film and provides a close match to reference peaks for FGS.

not shown here). However, the film did not adhere to the silicon substrate and optimization of FSS thin films was not pursued.

A 200 nm FGS thin film was deposited on a $TiN/SiO_2$ substrate and the composition ratio was determined by electron probe micro-analysis (EPMA) to be Fe:Ge = 1.86:1 and Ge:S = 1:3.7, indicating a film with a slight iron and sulfur deficiency. The elemental composition of annealed FGS thin films was investigated using dynamic secondary ion mass spectrometry (SIMS) as shown in Fig. 5.8. The composition ratio from dynamic-SIMS provided a close match to that measured via EMPA. However, the presence of oxygen uniformly distributed throughout the entire thickness of the thin-film was detected. The oxygen concentration present in thin films is similar to that of Ge. Oxygen in the FGS films could be incorporated from the presence of unintentional oxygen in the process gas during thin film deposition, exposure of the as-deposited films to air, or during the annealing step. To reduce

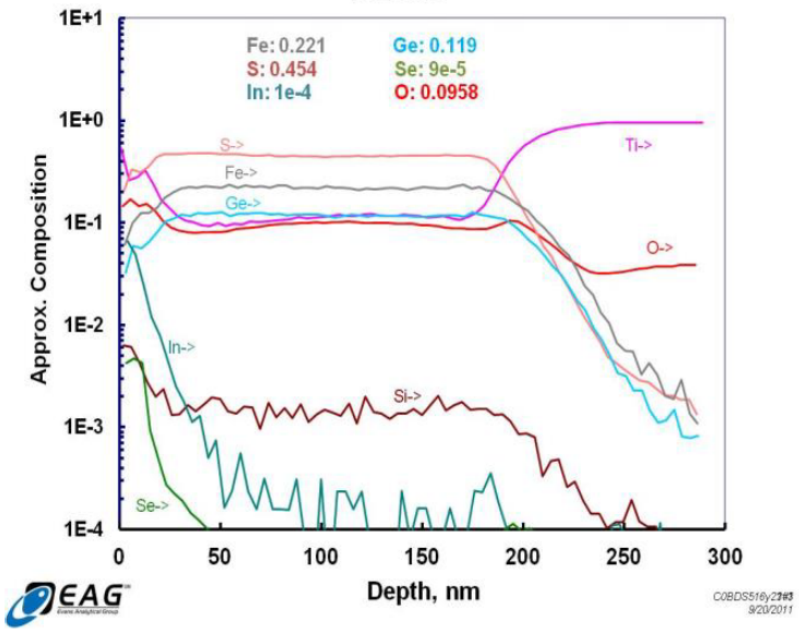


Figure 5.8: Dynamic SIMS for a FGS thin film. A high oxygen concentration is observed throughout the 200 nm thick film.

the concentration of oxygen in the thin films, the as-deposited films were annealed with a small amount of zirconium power in addition to $GeS_2$. Zirconium has a high affinity for oxygen [124] and as a result, getters oxygen to form $ZrO_2$, reducing the amount of oxygen present in the thin films.

Crystalline FGS thin films have a measured resistivity of 15 kΩ-cm. Hall measurements did not yield conclusive results. This typically occurs when low mobility ($\mu < 0.1$ $cm^2V^{-1}s^{-1}$), low carrier concentration ($N_A < 10^{16}$ $cm^{-3}$) materials are measured [114]. Assuming a hole mobility, $\mu_p = 0.1$ $cm^2$ $V^{-1}s^{-1}$ for FGS, the carrier concentration can be estimated from the resistivity as,

$$\rho = \frac{1}{q\mu_p p}, \tag{5.2a}$$

$$15\,k\Omega cm = \frac{1}{q \times 0.1 \times p}, \tag{5.2b}$$

or

$$p \sim 5 \times 10^{15} \text{cm}^{-3}. \tag{5.2c}$$

Thus, FGS thin films have a carrier concentration between $10^{15}$ - $10^{16}$ $\text{cm}^{-3}$, similar to that of bulk FGS as obtained from Seebeck measurements [122]. Further electrical characterization of FGS thin-films was inhibited by the strong tendency of these films to react with a bottom metal contact during the annealing step. Since FGS films were annealed at 500 °C, $GeS_2$ can react with the bottom metal, resulting in the films delaminating from the metal-coated substrate. This delamination was observed irrespective of the metal used. TiN was finally found to be a stable back contact material for FGS.

A photoelectrochemical (PEC) measurement of a FGS thin film prepared on a conductive TiN/$SiO_2$ substrate was measured by the Department of Chemistry at University of Oregon, as shown in Fig. 5.9. PEC results indicate the presence of a photocurrent. However no open-circuit voltage was measured. This could be due to the presence of defects in the thin film limiting $V_{OC}$, or due to a non-optimized PEC setup, including an appropriate choice of electrolyte and an optimized pH for the electrolyte solution.

The absorption coefficient for FGS thin films is compared to the theoretical calculated value, shown in Fig. 5.10. The as-deposited amorphous FGS film does not show a clear onset of absorption at the band-gap. The same FGS film annealed at 500 °C shows a band gap close to 1.5 eV and reaches an absorption coefficient of $\alpha = 1 \times 10^5$ $\text{cm}^{-1}$ at $E_G + 1$ eV. The theoretical absorption coefficient also has a band gap at $E_G = 1.5$ eV at $\alpha = 1$ $\text{cm}^{-1}$. However, the absorption coefficient plot in Fig. 5.10 begins at $\alpha = 1 \times 10^3$ $\text{cm}^{-1}$ to showcase the absorption characteristics of the thin films clearly. Near band gap absorption in FGS arises due to the presence of Fe d-orbital derived bands at both the VBM and CBM, along

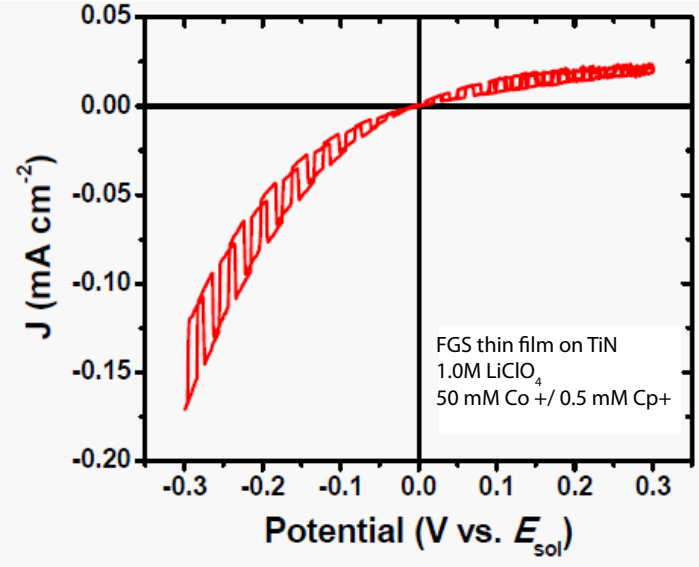


Figure 5.9: Photoelectrochemical measurement result of an FGS thin film on a TiN-coated substrate.

with S p-orbital derived bands at the VBM [118], similar to $FeS_2$. In addition to a large JDOS, allowed transitions between S-3p $\rightarrow$ Fe-3d give rise to the strong absorption strength of FGS. The absorption characteristic is not as strong as $FeS_2$, even though the JDOS and transition matrix are nearly identical, due to the non-uniform coordination environment of Fe in FGS. Unlike $FeS_2$, FGS thin films display a low sub-$E_G$ absorption, and do not indicate the presence of a plasma frequency, suggesting a low carrier concentration, confirmed by electrical measurements. The inset of Fig. 5.10 shows that the fundamental band gap of FGS is indirect ($E_G^{ind} \sim 1.5$ eV), while the direct band gap is positioned at $E_G^{dir} \sim 2.6$ eV.

Annealing FGS thin films in the presence of excess selenium powder allows one to tune the band gap of FGS. The band gap value reduces with increased selenium substitution, shown in Fig. 5.11. While FGS thin films have a band gap of 1.5 eV, $Fe_2GeS_3Se$ has a band gap of 1.2 eV, and $Fe_2GeSSe_3$ has a band gap of 0.8 eV, suggesting that the FGSSe system could be useful in tandem cell applications.

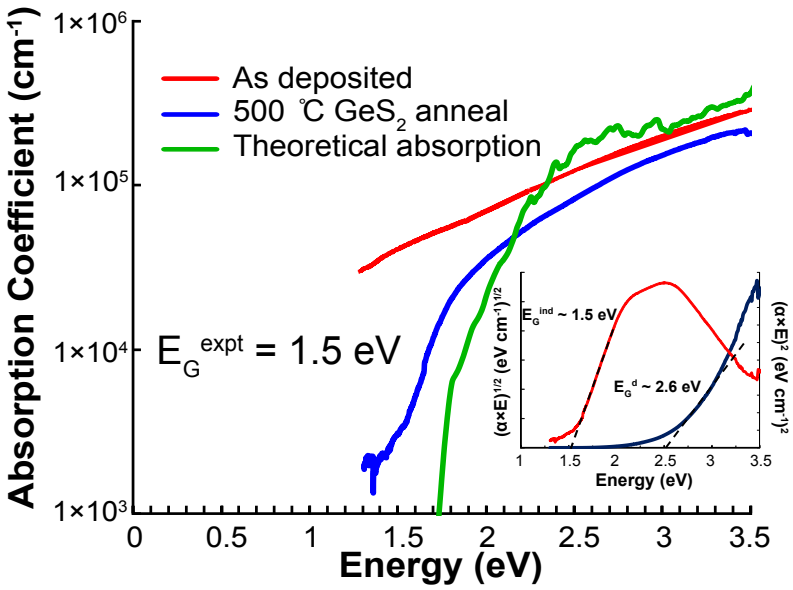


Figure 5.10: Absorption coefficients of FGS. Curves are shown for as-deposited and annealed films and compared to a theoretical curve. (inset) Band gap estimation of FGS. FGS has an indirect band gap of 1.5 eV and a direct band gap of 2.6 eV.

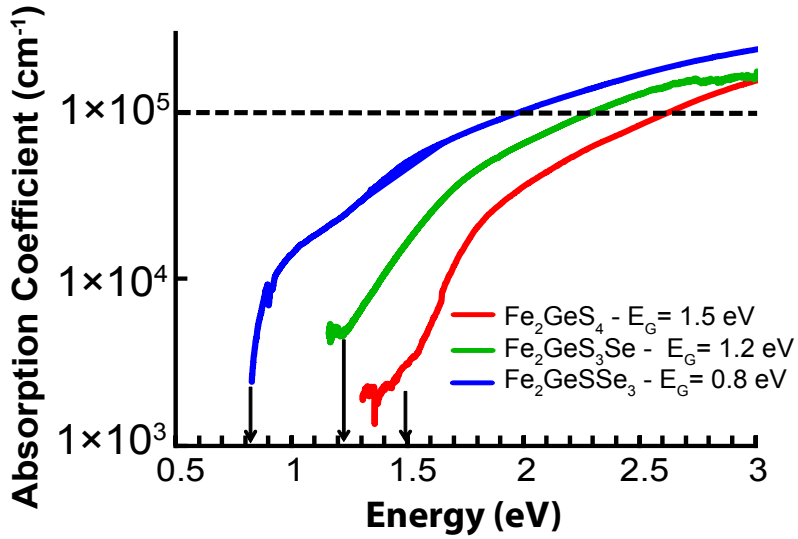


Figure 5.11: Absorption coefficients of FGS thin films with partial selenium substitution. The band gap decreases with increasing selenium substitution.

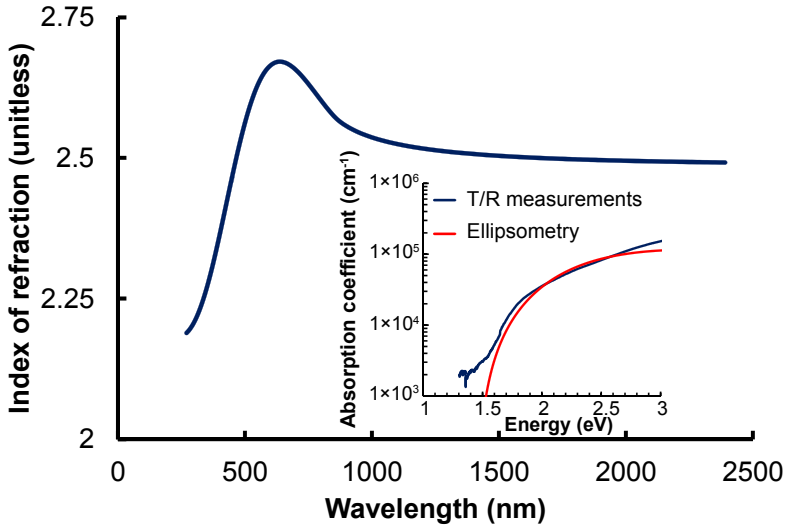


Figure 5.12: Modeled index of refraction from spectroscopic ellipsometry measurements. (inset) Comparison between modeled and measured absorption coefficients.

Spectroscopic ellipsometry results provide additional insight into the optical properties of FGS thin films. 250 nm FGS thin films were measured at wavelengths between 270 - 2400 nm and angles from 55 - 75 °. The modeled dispersion relationship is plotted in Fig. 5.12. The index of refraction has a value of $n = 2.5$ at $\lambda = 1$ $\mu$m, corresponding to a high frequency dielectric constant, $\varepsilon_\infty = 6.34$. The band gap is modeled to be 1.46 eV and the modeled absorption coefficient provides a close match to the experimental absorption coefficient, shown in the inset of Fig. 5.12. A Tauc-Lorentz model provided the best fit for the FGS thin-films. Model parameters are listed in Table. 5.1.

Photoluminescence (PL) is the inverse process of optical absorption and can provide a direct assessment of the absorber layer quality. PL measurements on FGS thin-films shown in Fig. 5.13, were performed at NREL using a HeNe laser ($\lambda = 632$ nm) as the excitation source, operating at an output power of 19 mW. The PL spectrum was collected using a Si CCD detector. Figure. 5.13 shows that PL can be used as a non-destructive process diagnostic

| Parameter | Value |
|---|---|
| Thickness [nm] | $242 \pm 1.18$ |
| E1.Offset | 5.13 |
| A | 26.6 |
| $E_n$ | 2.29 |
| C | 2.45 |
| $E_G$ | 1.46 |
| MSE | 31.6 |

Table 5.1: Tauc-Lorentz parameters used to model the optical properties of FGS thin-films.

technique. FGS thin films annealed in $GeS_2$ alone show a broad PL spectra (FWHM = 0.28 eV) centered around 1.46 eV. The PL spectra for these films are centered around the band gap of FGS. However, the broad, low-intensity spectra suggest low-quality films. The presence of defects can act as recombination centers, trapping photoexcited carriers, giving rise to a low-intensity spectrum. Dynamic-SIMS indicated the uniform presence of oxygen throughout the film, which can potentially act as a recombination site. Low-temperature PL measurements can be used to identify the energetic position of defects [32] and can be used to monitor process improvement. Films annealed with zirconium and $GeS_2$, on the other hand, exhibit a much stronger and narrower (FWHM = 0.11 eV) PL spectrum, as shown in Fig. 5.13, indicating an improvement in film quality.

Unold and Gütay describe a technique [32] to extract the $V_{OC}$ of an absorber layer using PL. In a PL measurement, the equilibrium Fermi level ($E_F$), splits into two quasi-

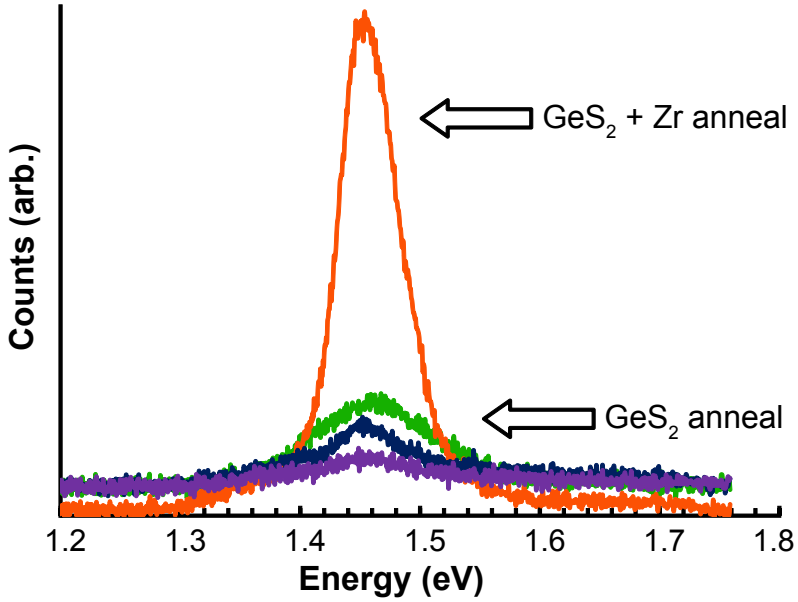


Figure 5.13: Photoluminescence spectra for various FGS thin films. The peak of the spectra corresponds to the band gap of $\sim$ 1.46 eV and films annealed with $GeS_2$ and Zr provide a strong improvement in PL signal.

Fermi levels (QFLs), whose separation from $E_F$ is related to excess carrier generation under illumination. The maximum QFL splitting ($\Delta\mu$ [eV]) is equivalent to the open-circuit voltage ($V_{OC}$) in a TFSC [8]. For a homogeneous material, the photoluminescence yield ($Y_{PL}$) from a sample can be expressed as [32],

$$Y_{PL} = \frac{1}{4\pi\hbar^2c^2}\frac{a(E)E^2}{(E-\Delta\mu)/k_BT)-1}, \tag{5.3a}$$

and

$$a(E) = (1-R_f)\times(1-exp(-\alpha(E)d)). \tag{5.3b}$$

where $a(E)$ is the absorbance [unitless] of the thin-film, $E$ is energy [eV], $\Delta\mu$ is the QFL-splitting [eV], $R_f$ is the reflectivity from the front surface , and $d$ is the film thickness [nm].

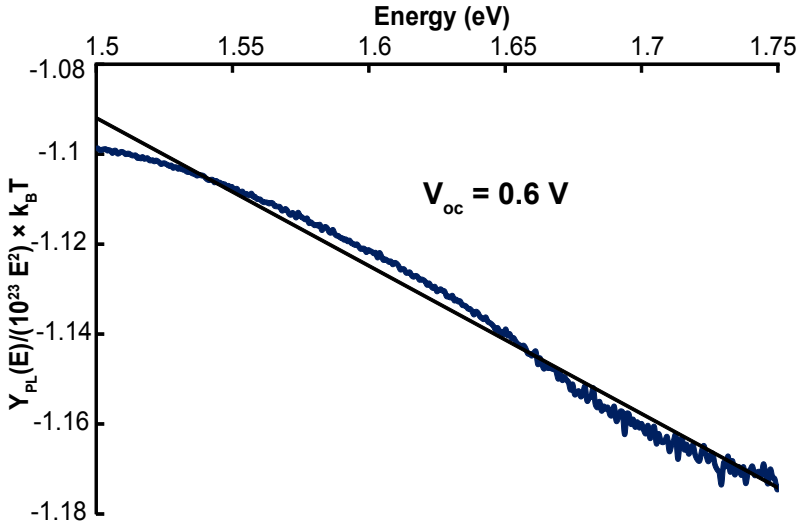


Figure 5.14: $V_{OC}$ extraction from FGS PL spectra.

The prefactor in Eqn. 5.3a can be simplified to,

$$\frac{1}{4\pi\hbar^2c^2} \sim 10^{23}\text{cm}^2\text{eV}-\text{s}. \tag{5.4}$$

Assuming $R_f = 0$ in Eqn. 5.3b, and $a(E) \sim 1$ for $E > E_G$, Eqn. 5.3a can be linearized to give,

$$ln\left(\frac{Y_{PL}(E)}{10^{23}\ E^2}\right) \times k_B T = -(E-\Delta\mu) \tag{5.5}$$

Thus, by plotting Eqn. 5.5 and performing a linear regression fit to the high energy portion of the PL spectrum, the QFL splitting term can be directly assessed. For the PL spectrum of the FGS thin film annealed with Zr, the $V_{OC}$ can be extracted as shown in Fig. 5.14. The extracted $V_{OC}$ value is 0.6 V, which is smaller than the ideal maximum value of $\sim$ 1 V, indicating that the FGS thin films require further optimization. However, the maximum voltage ($V_{OC}$) generated by an absorber material can be directly evaluated using PL as a non-destructive technique, providing a rapid methodology to assess and improve the quality of an absorber layer, without having to fabricate a TFSC stack.

### 5.2.2 Device Simulations of FGS-based TFSCs

The measured opto-electronic properties of FGS are used as inputs into SCAPS to assess TFSC device performance with FGS as an absorber layer. The inset in Fig. 5.16 shows the device configuration used in the simulation, consisting of the following layers: top contact/ n-ZnO/ n-CdS/ p-FGS/ $p^+$-FGS/ bottom contact. A 100 nm $p^+$-FGS layer is included between the absorber and the bottom contact to create a small ($\sim 0.2$ eV) conduction band offset at the p-$p^+$ interface. This conduction band offset provides a barrier, preventing electrons from recombining at the back surface. The properties of $p^+$-FGS are assumed to be identical to the absorber layer, except for an increased carrier concentration of $N_A = 2 \times 10^{18}$ $cm^{-3}$. In addition, SRH recombination via donor-like mid-gap traps is assumed to be the dominant recombination mechanism. A detailed list of parameters used for the simulation is given in Table 5.2.

Using the measured carrier concentration for FGS ($N_A \sim 10^{16}$ $cm^{-3}$), a diffusion-cell configuration is initially explored. The corresponding energy band diagram is shown in Fig. 5.15(a). The variation of device efficiency as a function of FGS absorber layer thickness is shown in Fig. 5.16, and indicates that efficiencies of $\sim 8\%$ can be achieved with a 1$\mu$m FGS absorber layer. The efficiency is low for thicknesses less than 250 nm, above which, the efficiency begins to saturate beyond $\sim 1$ $\mu$m. Low carrier mobility values ($\mu_n, \mu_p$ = 1, 0.1 $cm^2$ $V^{-1}s^{-1}$) along with the non-abrupt onset of absorption in FGS directly translate into the low efficiencies observed in Fig. 5.16. The effect of the non-abrupt onset of absorption is seen in a simulated plot of quantum effiency (QE) as a function of absorber layer thickness, shown in Fig. 5.17. A FGS-based TFSC with an absorber layer thickness less than 250 nm has a quantum efficiency of only 40 - 55% as shown in Fig. 5.17, while for thicknesses greater than

| General Device Properties | | | | |
|---|---|---|---|---|
| Parameter | Front Contact | | Back Contact | |
| $\phi_b$ [eV] | $\phi_{bn} = 0.1$ | | $\phi_{bp} = 0.3$ | |
| WF [eV] | 4.1 | | 5.1 | |
| $S_n$ [cm-s$^{-1}$] | $10^7$ | | $10^7$ | |
| $S_p$ [cm-s$^{-1}$] | $10^7$ | | $10^7$ | |
| Reflectivity | 0.1 | | 0.8 | |
| **Layer Properties** | | | | |
| Parameter | $SnO_2$ | CdS | FGS | $p^+$-FGS |
| W [nm] | 500 | 25 | variable | 100 |
| $\varepsilon/\varepsilon_0$ | 9 | 10 | 6.4 | 6.4 |
| $\mu_n$ [cm$^2$-s$^{-1}$] | 100 | 100 | 1 | 1 |
| $\mu_p$ [cm$^2$-s$^{-1}$] | 25 | 25 | 0.1 | 0.1 |
| n (or p) [cm$^{-3}$] | n: $10^{17}$ | n: $10^{17}$ | p: $10^{16}$ | $p^+$: $10^{18}$ |
| $E_G$ [eV] | 3.6 | 2.4 | 1.46 | 1.46 |
| $N_C$ [cm$^{-3}$] | $2.2\times10^{18}$ | $2.2\times10^{18}$ | $8\times10^{17}$ | $8\times10^{17}$ |
| $N_V$ [cm$^{-3}$] | $1.8\times10^{19}$ | $1.8\times10^{19}$ | $1.8\times10^{19}$ | $1.8\times10^{19}$ |
| **Mid-gap Trap State Properties** | | | | |
| Parameter | $SnO_2$ | CdS | FGS | $p^+$-FGS |
| $N_D$, $N_A$ [cm$^{-3}$] | A: $10^{15}$ | A: $10^{18}$ | D: variable | D: $10^{14}$ |
| $\sigma_n$ [cm$^2$] | $10^{-12}$ | $10^{-15}$ | $10^{-12}$ | $10^{-12}$ |
| $\sigma_p$ [cm$^2$] | $10^{-15}$ | $10^{-12}$ | $10^{-15}$ | $10^{-15}$ |

Table 5.2: Material parameters used for FGS-based TFSC simulations.

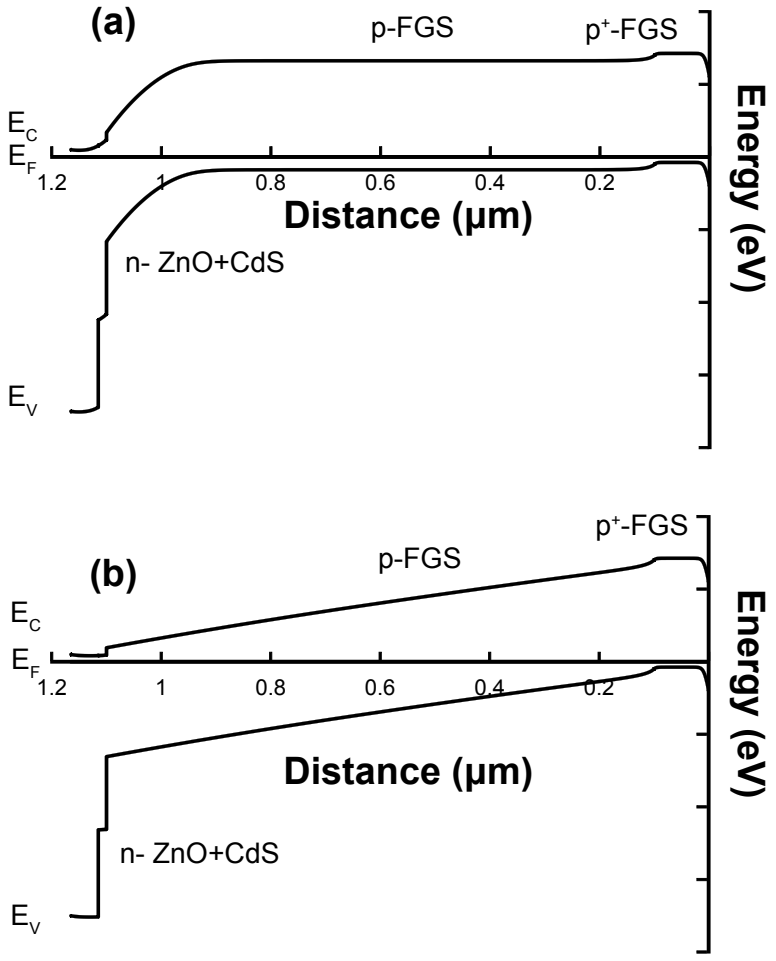


Figure 5.15: Simulated energy band diagrams for a FGS-based TFSC in (a) a diffusion-cell, and (b) a drift-cell configuration. Both configurations have a $p^{+}$-layer beneath the absorber layer to minimize back surface recombination.

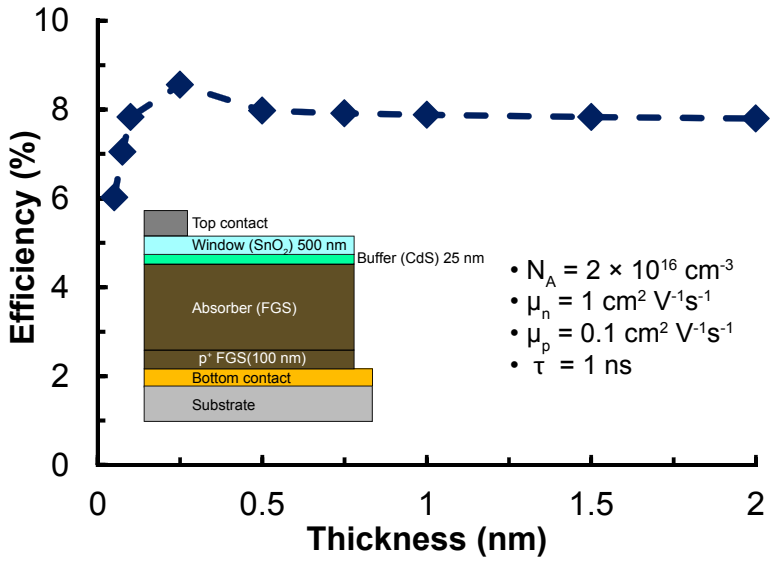


Figure 5.16: Simulated TFSC device efficiency as a function of the FGS absorber thickness in a diffusion-cell configuration. (inset) Device structure used for the simulation. Carrier mobilities ($\mu_n$, $\mu_p$ = 1, 0.1 cm$^2$ V$^{-1}$s$^{-1}$) and the minority carrier lifetime ($\tau$ = 1 ns) are held constant.

250 nm, there is an increase in QE, which converges at a maximum of $\sim$ 65%. The reason for the efficiency saturating beyond 750 nm can be seen in Fig. 5.17. The QE maximizes between 750 nm - 1 $\mu$m, indicating that a thickness greater than 1 $\mu$m of FGS is required to fully absorb the solar spectrum. In addition, the diffusion length of minority carrier electrons in FGS can be calculated by first estimating the diffusivity $D_n$ [cm s$^{-1}$] [12] as,

$$D_n = \mu_n \frac{k_B T}{q} = 1 \text{ cm}^2 \text{ V}^{-1}\text{s}^{-1} \times 0.0259\, V, \tag{5.6a}$$

or

$$D_n = 0.026 \text{ cm}^2 \text{ s}^{-1}. \tag{5.6b}$$

The diffusion length $L_n$ can be calculated using a minority carrier lifetime of $\tau$ = 1 ns [12] as,

$$L_n = \sqrt{D_n \times \tau} = \sqrt{0.026 \text{ cm}^2 \text{ s}^{-1} \times 1\, ns}, \tag{5.7a}$$

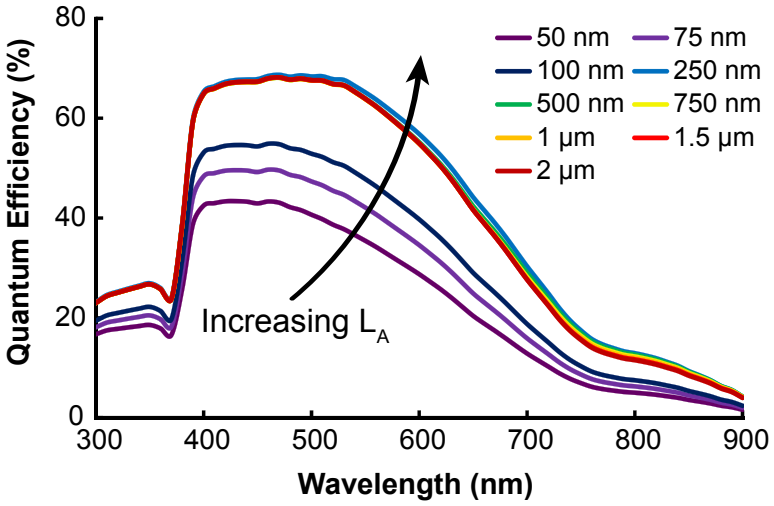


Figure 5.17: Simulated quantum efficiency as a function of FGS absorber thickness for a diffusion-cell configuration. Carrier mobilities ($\mu_n, \mu_p$ = 1, 0.1 cm$^2$ V$^{-1}$s$^{-1}$) and the minority carrier lifetime ($\tau$ = 1 ns) are held constant.

or

$$L_n = 50\,nm. \tag{5.7b}$$

Thus, the low simulated efficiencies are a direct consequence of a very short minority carrier diffusion length ($\sim$ 50 nm) in comparison to the absorber thickness (1 $\mu$m) required to fully absorb the solar spectrum. This implies that a large fraction of photogenerated carriers recombine as they slowly diffuse towards the space-charge region. Since the efficiency saturates beyond $\sim$ 1 $\mu$m in Fig. 5.16, a thickness of 1 $\mu$m is used for subsequent diffusion-cell simulations.

With the thickness constrained to 1 $\mu$m for a FGS-based diffusion cell, the minority carrier lifetime is then varied, shown in Fig. 5.18. While a minority carrier lifetime of 1 ns, corresponding to a mid-gap trap density of 1 $\times$ 10$^{14}$ cm$^{-3}$ (refer to Table. 2.1), provides an efficiency of 8%, higher efficiencies can be obtained with an increasing minority carrier

lifetime (or a decreasing trap density). Efficiencies approaching 15% are simulated assuming a lifetime of 10 ns, while a minority carrier lifetime of 100 ns provides an efficiency of $\sim$ 22%, indicating that high-quality, low trap density FGS thin-films are required for efficient FGS-based TFSCs. For minority carrier lifetimes below 1 ns, FGS-based TFSCs exhibit poor photo-conversion efficiencies of 5% and lower. This drastic drop in efficiency for high trap densities is a consequence of the low carrier mobility of FGS in a diffusion-cell configuration, leading to an increase in recombination and a decrease in $J_{SC}$.

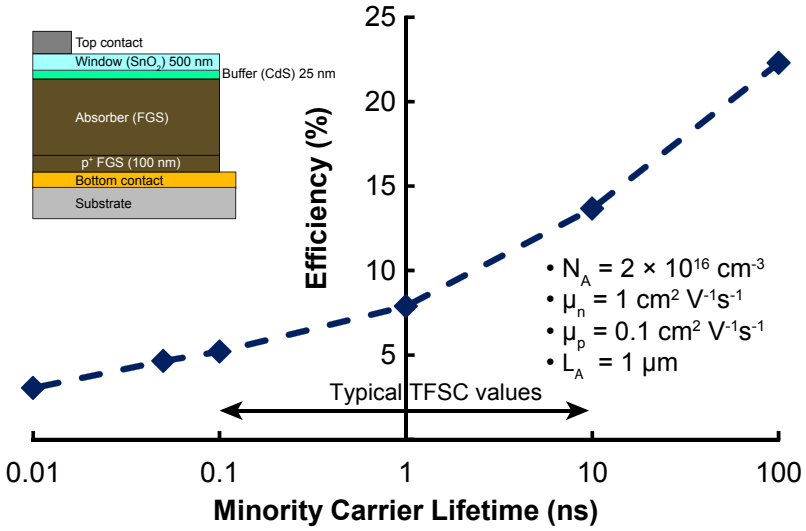


Figure 5.18: Simulated TFSC device efficiency as a function of the minority carrier lifetime for a FGS absorber layer in a diffusion-cell configuration. The FGS absorber layer thickness ($t$ = 1 $\mu$m) and carrier mobilities ($\mu_n$, $\mu_p$ = 1, 0.1 $cm^2$ $V^{-1}s^{-1}$) are kept constant.

Using an absorber thickness of 1 $\mu$m and a minority carrier lifetime of 1 ns, next the carrier mobility in FGS is varied, as shown in Fig. 5.19. Besides using $\mu_n$, $\mu_p$ = 1, 0.1 $cm^2\,V^{-1}s^{-1}$, two other sets of values are simulated: $\mu_n$, $\mu_p$ = 10, 1 and 100, 10 $cm^2\,V^{-1}s^{-1}$,

respectively. Increasing the carrier mobility yields a near-linear increase in efficiency, reaching a value of 15.5% for mobilities of $\mu_n$, $\mu_p$ = 100, 10 $\mathrm{cm^2\,V^{-1}s^{-1}}$.

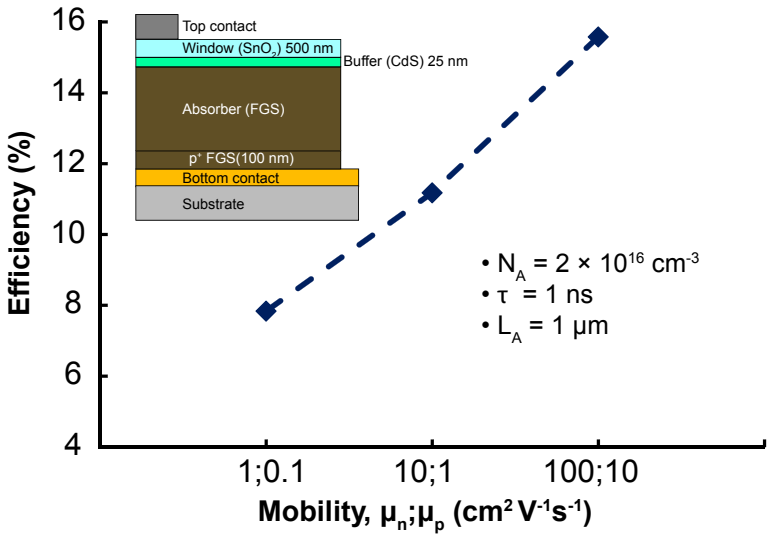


Figure 5.19: Simulated TFSC device efficiency as a function of carrier mobility in an FGS absorber layer in a diffusion-cell configuration. The absorber layer thickness ($L^A$ = 1 $\mu$m) and minority carrier lifetime ($\tau$ = 1 ns) are held constant.

If the carrier concentration in FGS is reduced to $N_A = 10^{14}$ $\mathrm{cm^{-3}}$, a drift-cell configuration can be realized, and the variation in thickness, lifetime, and mobility can be assessed for this configuration. The corresponding energy band diagram is shown in Fig. 5.15(b) and the variation in device efficiency as a function of thickness is shown in Fig. 5.20. Unlike the diffusion cell case (Fig. 5.16), where the efficiency saturates with increasing thicknesses, the efficiency for a drift cell shows a strong decrease with thicknesses beyond 750 nm. The maximum efficiency for the drift-cell configuration at 750 nm is $\sim$ 15%. One reason for the observed decrease in efficiency with increasing thickness is that the electric field across the absorber layer is reduced and is no longer efficient in extracting the slow-moving photogen-

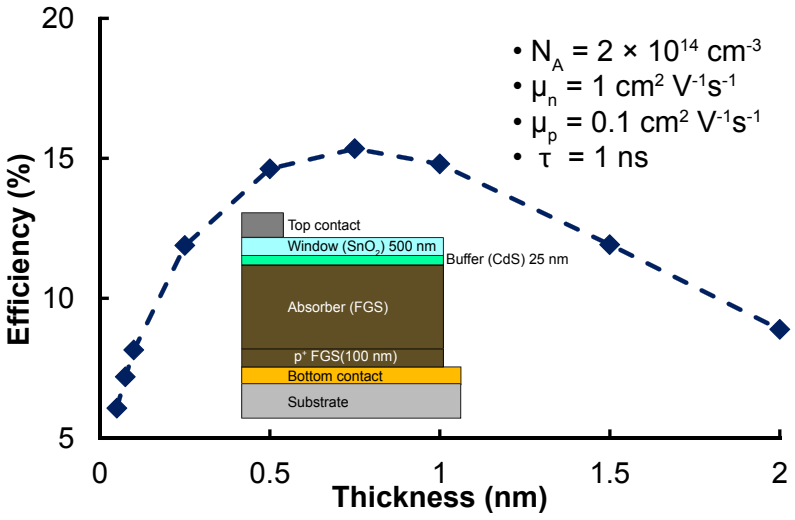


Figure 5.20: Simulated TFSC device efficiency as a function of FGS absorber layer thickness in a drift-cell configuration. Carrier mobilities ($\mu_n$, $\mu_p$ = 1, 0.1 cm$^2$ V$^{-1}$s$^{-1}$) and the minority carrier lifetime ($\tau$ = 1 ns) are held constant.

erated carriers. For thicknesses less than 1 $\mu$m, the advantage of a drift-cell configuration over a diffusion-cell configuration is evident from Fig. 5.20. In a drift cell, a strong built-in field across a thin absorber layer efficiently extracts slow moving photogenerated carriers, thereby providing efficiencies higher than 10% even for a 250 nm thick FGS absorber layer.

Assuming an FGS absorber thickness of 750 nm, the minority carrier lifetime is varied next, shown in Fig. 5.21. As expected, improving the minority carrier lifetime by decreasing the concentration of mid-gap traps provides a strong efficiency increase, nearing 20% with a minority carrier lifetime value of 10 ns (corresponding to a mid-gap trap density of $1\times10^{13}$ cm$^{-3}$). Efficiency decreases considerably with reducing minority carrier lifetimes for both the drift- and diffusion-cell configurations, indicating that pristine, trap-free FGS thin-films are required for efficient TFSC performance.

Increasing the carrier mobility for electrons and holes in an FGS-based drift cell, shown in Fig. 5.22, does not result in a linear increase in efficiency as compared to a dif-

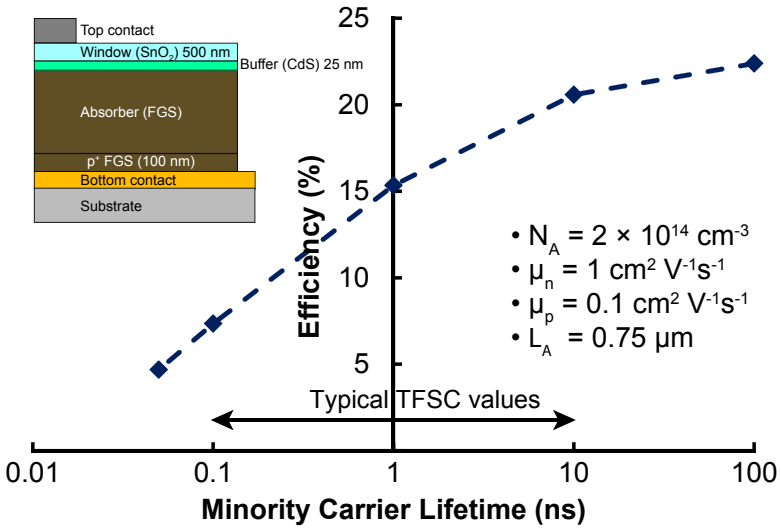


Figure 5.21: Plot of the simulated TFSC device efficiency as a function of FGS absorber layer minority carrier lifetime in a drift-cell configuration. The FGS absorber layer thickness ($t$ = 750 nm) and carrier mobilities ($\mu_n$, $\mu_p$ = 1, 0.1 cm$^2$ V$^{-1}$s$^{-1}$) are kept constant.

fusion cell as shown in Fig. 5.19. Instead, Fig. 5.22 indicates that the efficiency does not vary significantly with increasing carrier mobility in a drift-cell configuration. A factor of 100 increase in carrier mobility yields less than a 4% improvement in efficiency for an FGS-based drift cell, while for a diffusion-based TFSC (Fig. 5.19), this increase in efficiency is close to 8%. This confirms the assertion that a drift-cell configuration best suits a low mobility absorber in a TFSC.

Device simulations for an FGS-based TFSC in a drift configuration indicate that efficiencies approaching 20% can be obtained when the FGS absorber layer has high carrier mobilities, low carrier concentration, and a low density of traps. However, this prediction of device performance must be tempered by what is achievable in the laboratory, or more importantly, in the context of high-volume manufacturing of TFSCs over large areas at low cost. The measured carrier concentration of FGS is $\sim 10^{16}$ cm$^{-3}$. Attempts to reduce the

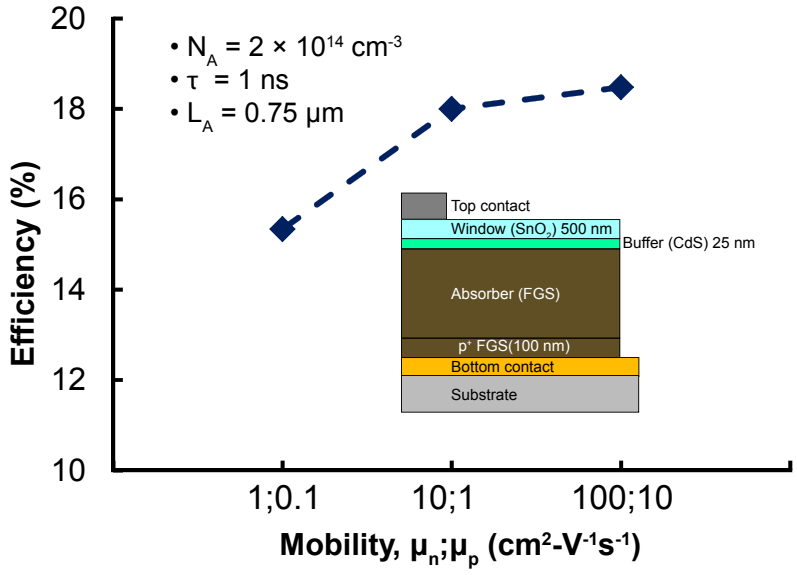


Figure 5.22: Plot of the simulated TFSC device efficiency as a function of carrier mobilities in the FGS absorber layer for a drift-cell configuration. The absorber layer thickness ($t$ = 750 nm) and minority carrier lifetime ($\tau$ = 1 ns) are held constant.

carrier concentration by doping FGS were not successful in this study. Reducing the carrier concentration of FGS to $\sim 10^{14}$ cm$^{-3}$, i.e., that required for the drift-cell configuration simulated to yield an efficiency above 15% appears to be unlikely. Carrier mobility depends on effective mass (an intrinsic property of a material depending on its band structure [12]), and the momentum relaxation time (dependent on intrinsic transport considerations as well as the extrinsic quality of the thin-film such as crystallinity, defect density and impurities [13]) . While high carrier mobilities in FGS can be simulated, increasing the carrier mobility by a factor of 100 to $\mu_n$, $\mu_p$ = 100/10 cm$^2$ V$^{-1}$ s$^{-1}$ is unrealistic. Given these carrier concentration and mobility constraints in FGS, two scenarios can be considered. First, if the carrier concentration can be reduced to $N_A = 10^{14}$ - $10^{15}$ cm$^{-3}$, then with a carrier mobility of $\mu_n$, $\mu_p$ = 1, 0.1 cm$^2$ V$^{-1}$s$^{-1}$ and a lifetime of $\tau = 1$ ns ($N_T = 10^{14}$ cm$^{-3}$), a $\sim$ 15% efficient TFSC is simulated. Second, if $N_A$ cannot be lowered from $10^{16}$ cm$^{-3}$, then with a mobility

| Property | Diffusion | Drift |
|---|---|---|
| Thickness [$\mu$m] | 1 - 1.5 | 0.75 |
| Carrier concentration [$cm^{-3}$] | $1 \times 10^{16}$ $cm^{-3}$ | $1 \times 10^{14}$ $cm^{-3}$ |
| Carrier mobility [$cm^2\,V^{-1}\,s^{-1}$] | $\mu_n$ =1; $\mu_p = 0.1$ | $\mu_n$ =1; $\mu_p = 0.1$ |
| Minority carrier lifetime [ns] | 10 ($N_T = 10^{13}$ $cm^{-3}$) | 1 ($N_T = 10^{14}$ $cm^{-3}$) |
| Efficiency [%] | 13 | 15 |

Table 5.3: Required material parameters for diffusion and drift-cell FGS-based TFSCs simulated to yield efficiencies of 13% and 15%, respectively.

of $\mu_n$, $\mu_p$ = 1, 0.1 $cm^2$ $V^{-1}s^{-1}$ and a lifetime of 10 ns ($N_T = 10^{13}$ $cm^{-3}$), a 13% efficient FGS based TFSC can be simulated. The parameters employed in these two simulations are summarized in Table. 5.3.

## 5.3 Conclusions

In this chapter, $FeS_2$ was explored as a possible high absorption material for TFSCs. It is asserted that the opto-electronic properties of $FeS_2$ thin-films are largely plagued by large carrier concentrations resulting in high sub-band gap absorption. This high carrier concentration ($> 10^{20}$ $cm^{-3}$) arises due to spontaneous decomposition of $FeS_2$ into sulfur-deficient phases, including a metallic FeS phase. In an effort to improve $FeS_2$, a new inorganic absorber material, $Fe_2GeS_4$ (FGS) was identified and thin films were explored in this study. While FGS exhibits a near optimal band gap of $E_G \sim 1.5$ eV, the absorption coefficient plot reaches a maximum of $\alpha = 1 \times 10^5$ $cm^{-1}$ only at $E_G$ + 1 eV, indicating a sluggish, non-abrupt onset of absorption. RF-magnetron sputtering was used to fabricate FGS thin films

in this study and it was determined that a large concentration of oxygen was present in all films investigated, irrespective of how they were processed. While adding Zr powder during the anneal process reduced the oxygen concentration, an improved thin-film processing technique is required to realize high-quality FGS thin films. In addition, FGS films delaminated from a bottom metal contact during the anneal step, inhibiting further electrical characterization. Device simulations predict that the best-case efficiency for a fully optimized FGS-based TFSC is only 13 - 15%. Thus, FGS does not appear to be a suitable absorber for high performance TFSC applications.

# 6. COPPER-BASED SOLAR ABSORBERS

Copper-based materials such as $Cu_2S$ [125] and $CuInSe_2$ [62] were among the earliest thin-film solar absorber materials investigated. $Cu_2S$ is a p-type semiconductor with an indirect band gap of 1.2 eV [46] and was used along with n-CdS to form a p-n heterojunction TFSC exhibiting efficiencies as high as 9% in 1980 [126]. However, $Cu_2S$-based thin-film solar cells did not show promise as a result of Cu diffusion into the CdS layer, which degraded the performance of the TFSC [125]. $CuInSe_2$, described in Ch. 2, currently has the highest reported laboratory efficiency at 20.3% [26]. However, scaling up of the CIGS deposition process in addition to the rising cost of indium can potentially limit large-scale implementation of CIGS-based absorbers [5]. This chapter presents the development of novel copper (Cu) based solar absorbers. Based on a design paradigm for high optical absorption, Cu-based absorbers from the Cu-V-VI family of materials (V = Sb, Bi; VI = S, Se) are initially explored. The tetrahedrite family of materials, $Cu_{10}M_2Sb_4Ch_{13}$ (M = Mn, Cu, Zn, In; Ch = S, Se) is then investigated and demonstrated to be a promising solar absorber material candidate for high-efficiency thin-film solar cells.

## 6.1 Cu-V-VI (V = Sb, Bi; VI = S, Se) family of materials

Members of the Cu-V-VI family of materials, including $CuSbS_2$ [127], $Cu_3SbS_3$ [128], $Cu_3SbSe_4$ [129], $CuBiS_2$ [130], $Cu_3BiS_3$ [131], have been recently investigated for solar absorber [132, 133] and thermoelectric applications [129]. This study focuses on $CuSbS_2$ and $Cu_3SbS_4$ as viable absorber materials.

### 6.1.1 Design paradigms for Cu-V-VI materials

Two design paradigms to achieve high optical absorption were identified by Yu *et. al.* [134]. First, choosing a low valence (group V) element as a cation constituent can give rise to an increased DOS contribution from the group V, filled s-orbital derived bands near the VBM and relatively flat, empty p-orbital derived bands near the CBM. Second, selecting a compound with a Cu/V ratio greater than one can lead to localized group V, s-orbital derived bands near the CBM, enhancing the JDOS [134]. These DOS contributions to the band edges, coupled with Cu d-orbital derived bands near the VBM and dipole-allowed Cu d $\rightarrow$ V p and VI s $\rightarrow$ V p transitions can result in an increased absorption coefficient in a Cu-V-VI material. Group V containing compounds were investigated since they typically adopt two oxidation states, 3+ and 5+, resulting in the choice of $CuSbS_2$ (3+) and $Cu_3SbS_4$ (5+) as candidate materials to test the first design paradigm. In addition, $Cu_3SbS_4$ has a Cu/Sb ratio of 3, which also allows the validation of the second design paradigm within the same material family.

The calculated total DOS and partial DOS using density functional theory calculations for $CuInSe_2$, $CuSbS_2$, and $Cu_3SbS_4$ are shown in Fig. 6.1. In these DOS plots, the Fermi level ($E_F$) is positioned at E = 0 eV, with the valence band corresponding to E $<$0 eV, and the conduction band to E $>$0 eV. The total DOS for $CuSbS_2$, $Cu_3SbS_4$, and $CuInSe_2$ are shown in Fig. 6.1(a) and indicate that the valence band in all three materials is similar, corresponding to Cu d- and S (or Se) p-orbital derived bands. However, the conduction band differs considerably in all three materials with both $CuSbS_2$ and $Cu_3SbS_4$ exhibiting a higher DOS in the conduction band compared to $CuInSe_2$. In addition, the partial DOS highlighting the difference in Sb atom contribution to the bands is shown in Fig. 6.1(b). Sb p-orbital derived

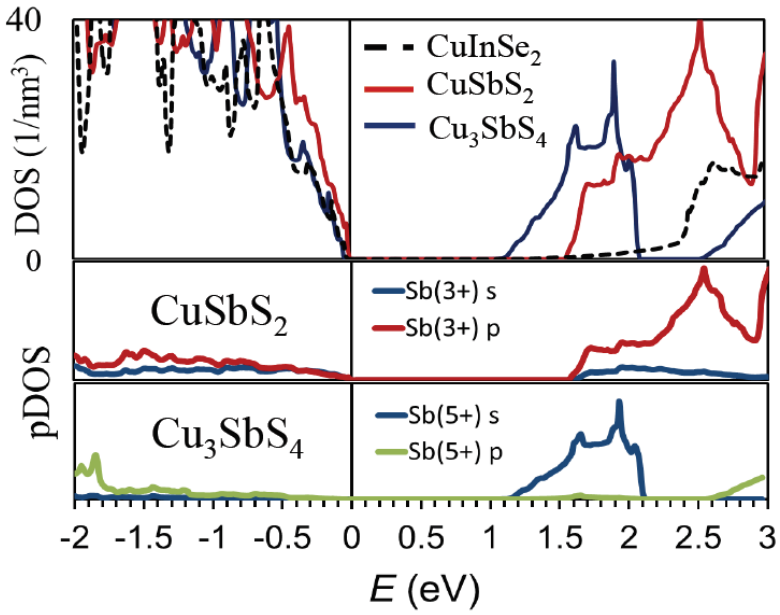


Figure 6.1: (a) Total DOS for $CuInSe_2$, $CuSbS_2$, and $Cu_3SbS_4$. Both $CuSbS_2$ and $Cu_3SbS_4$ exhibit an increased DOS compared to $CuInSe_2$. (b) Partial DOS for $CuSbS_2$ and $Cu_3SbS_4$. $CuSbS_2$ exhibits a contribution from Sb s- and p-orbital derived bands near the VBM and CBM, while $Cu_3SbS_4$ only has a contribution from Sb s-orbital derived bands near the CBM.

bands in $CuSbS_2$ ($Sb^{3+}$) contribute to states near the VBM and CBM, while Sb s-orbital derived bands only have a minor contribution to the VBM and CBM. In contrast, $Cu_3SbS_4$ ($Sb^{5+}$) does not have a significant Sb p-orbital derived band contribution near the VBM or CBM. However, $Cu_3SbS_4$ exhibits an increased Sb s-orbital derived band contribution near the CBM. Sb s-orbital derived bands near the CBM can be attractive for a solar absorber, since s-orbital derived bands can provide for a higher carrier mobility. While the band gap of $CuInSe_2$ is 1.1 eV, there is not a significant increase in DOS until 2.4 eV, or $E_G$ + 1.3 eV (refer to Fig. 6.1(a)). The variation in the electronic structure of $CuSbS_2$ and $Cu_3SbS_4$ is related to the crystal structure adopted by the two compounds, as shown in Fig. 6.2. $CuSbS_2$ adopts a layered structure [131], while $Cu_3SbS_4$ has isolated Sb atoms amidst a Cu-S network. The

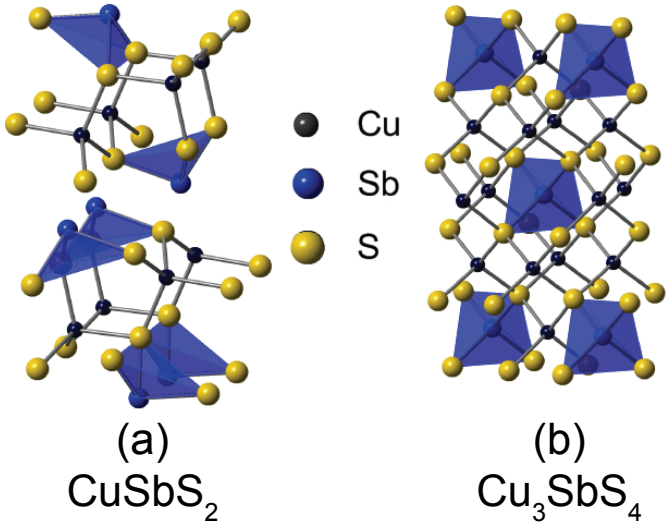


Figure 6.2: Crystal structure for (a) $CuSbS_2$, and (b) $Cu_3SbS_4$. $CuSbS_2$ exhibits a layered crystal structure, while $Cu_3SbS_4$ has an isolated Sb atom surrounded by a Cu-S network.

isolated Sb atom in $Cu_3SbS_4$ is a consequence of the lone pair effect [135] which results in the localized s-orbital derived band near the CBM seen in Fig. 6.1(b).

### 6.1.2 Thin-film deposition and characterization

Thin-films of Cu-V-VI materials were fabricated by sequential deposition of Cu and $Sb_2S_3$ using electron beam (e-beam) evaporation on a fused silica substrate, with source materials purchased from Alfa Aesar. For a $CuSbS_2$ thin-film, $Sb_2S_3$/ Cu/ $Sb_2S_3$ thicknesses of 50/ 18/ 50 nm were used, and repeated for thicker films. For a $Cu_3SbS_4$ thin-film, $Sb_2S_3$/ Cu/ $Sb_2S_3$ = 30/ 20/ 30 nm was used, and repeated for thicker films. As-deposited stacks were annealed in a tube furnace using $CS_2$ gas as the sulfur containing source for 30 mins at 300 °C. Figure 6.3(a) shows the x-ray diffractogram of a $CuSbS_2$ thin film, and indicates a close match when compared with the computed reference pattern. The broad feature between 15 - 25° is due to the amorphous fused-silica substrate. The x-ray diffractogram for a $Cu_3SbS_4$ thin film shown in Fig. 6.3(b) also indicates a close match to the reference peak, with the

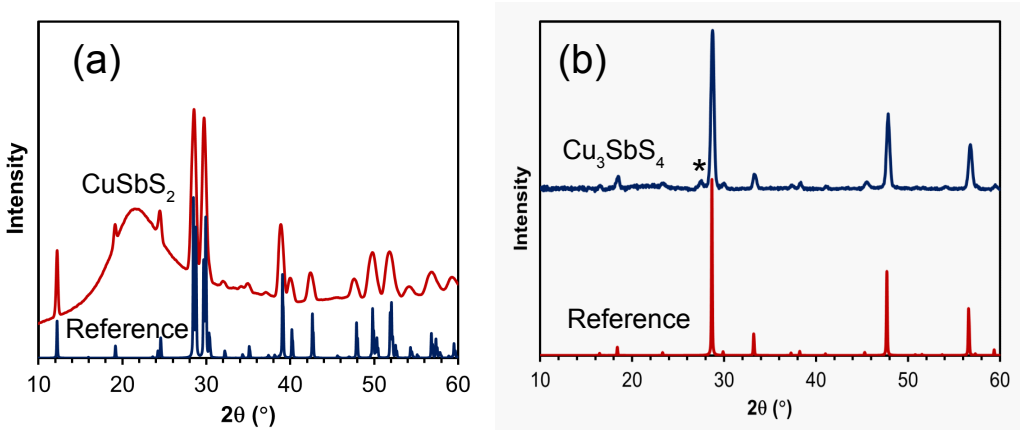


Figure 6.3: X-ray diffractograms for a (a) $CuSbS_2$, and (b) $Cu_3SbS_4$ thin-film. $CuSbS_2$ exhibits a close match with the reference peaks, while $Cu_3SbS_4$ has a $Cu_{1.8}S$ secondary phase.

exception of an additional peak due to $Cu_{1.8}S$ observed at $\sim 29^{\circ}$, indicating the presence of a secondary phase. The amorphous substrate peak is not visible in Fig. 6.3(b) since the signal from the background and substrate has been subtracted to emphasize the properties of $Cu_3SbS_4$. A cross-sectional SEM image of a $\sim$ 350 nm annealed $Cu_3SbS_4$ thin-film is shown in Fig. 6.4. In spite of the use of sequential deposition of pre-cursor layers, the SEM image shows uniform mixing of the layers, with grain sizes $\sim$ 200 nm.

Electrical characterization from Hall measurements indicated that the $CuSbS_2$ thin-film is p-type with a carrier concentration, $N_A \sim 10^{17}$ cm$^{-3}$ and a hole mobility, $\mu_p \sim 0.1$ cm$^2$ V$^{-1}$s$^{-1}$. Tang *et al.* used electrodepostion to fabricate thin films of $CuSbSe_2$ and measured a hole mobility of 1.2 cm$^2$ V$^{-1}$s$^{-1}$ [136]. While these material systems are analogous, a value nearly an order of magnitude higher than e-beam evaporated films can indicate that the mobility value measured for $CuSbS_2$ may be underestimated or be due to a non-optimized process. $Cu_3SbS_4$ thin films were also p-type, exhibiting a carrier concentration $N_A \sim 10^{18}$ cm$^{-3}$ and a hole mobility, $\mu_p \sim 15$ cm$^2$V$^{-1}$s$^{-1}$. While sequential deposition using e-beam

evaporation showed a high $N_A$ value, a 2 inch $Cu_3SbS_4$ sputter target (99.99%) was purchased from Kurt Lesker to investigate an alternative deposition process. Sputtered thin films exhibited a carrier concentration $N_A \sim 10^{17}$ $cm^{-3}$, with a hole mobility, $\mu_p \sim 15$ $cm^2V^{-1}s^{-1}$. Further optimization of the sputter process and reduction of the carrier concentration by doping $Cu_3SbS_4$ with Mn or Zn is suggested for future work.

The optical absorption plots for $CuSbS_2$ and $Cu_3SbS_4$ are shown in Fig. 6.5 and indicate that both materials exhibit high absorption in the visible spectrum. The $CuSbS_2$ thin film (t $\sim$ 130 nm) exhibits a band gap $E_G \sim 1.4$ eV but has significant sub-band gap absorption along with a non-abrupt onset of absorption near the band gap with the absorption coefficient reaching $\alpha = 1 \times 10^5$ $cm^{-1}$ at $E_G$ + 0.9 eV. The absorption plot for a $Cu_3SbS_4$ thin film (t $\sim$ 150 nm), on the other hand, has a band gap $E_G \sim 0.9$ eV and exhibits an abrupt onset of absorption at the band gap, reaching $\alpha = 1 \times 10^5$ $cm^{-1}$ at $E_G$ + 0.6 eV. The abrupt onset of absorption near the band gap along with the ability to reach a maximum of $\alpha \sim 2 \times 10^5$ $cm^{-1}$ at $E_G$ + 1.2 eV indicates that the thickness requirement for a $Cu_3SbS_4$-based TFSC absorber can be less than 1 $\mu$m, thinner than is possible with current solar absorber materials. In addition, theoretical calculations indicated that $Cu_3SbS_4$ is a direct-band gap semiconductor [134], which is confirmed by the abrupt onset of absorption near the band gap. The band gap type for $CuSbS_2$ is shown in Fig. 6.6 and indicates that the fundamental band gap in indirect at $E_G \sim 1.42$ eV. However, a direct band gap is positioned at $E_G \sim 1.58$ eV. This direct gap is responsible for the additional feature seen at $\sim$ 1.6 eV in Fig. 6.5(b).

Figure 6.7 is a plot of the absorption coefficients for $CuSbS_2$, $Cu_3SbS_4$, and $CuInSe_2$ thin-films plotted as a function of E - $E_G$, i.e., the onset of absorption. While both $CuSbS_2$ and $CuInSe_2$ contain low valent elements (Sb 3+ and In 3+), the absorption coefficients ap-

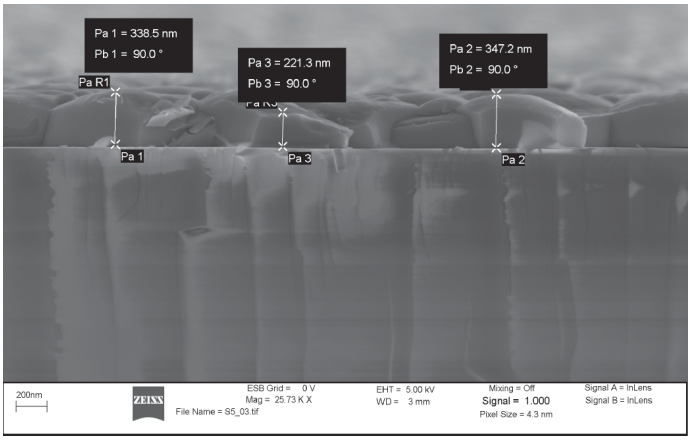


Figure 6.4: Scanning electron micrograph of a $\sim$ 350 nm $Cu_3SbS_4$ thin-film. Large grain sizes ($\sim$ 200 nm) can be observed.

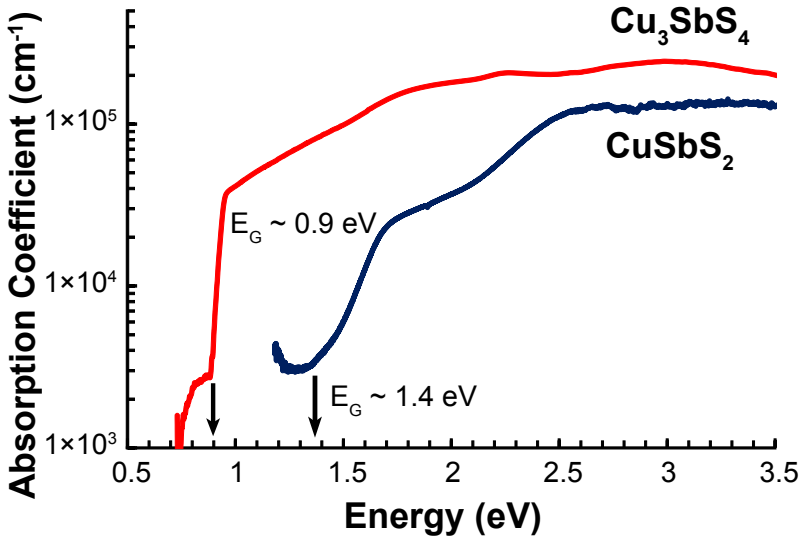


Figure 6.5: Optical absorption plot for a (a) $Cu_3SbS_4$, and (b) $CuSbS_2$ thin film. $Cu_3SbS_4$ exhibits a band gap of $E_G \sim 0.9$ eV, while $CuSbS_2$ has an $E_G \sim 1.4$ eV.

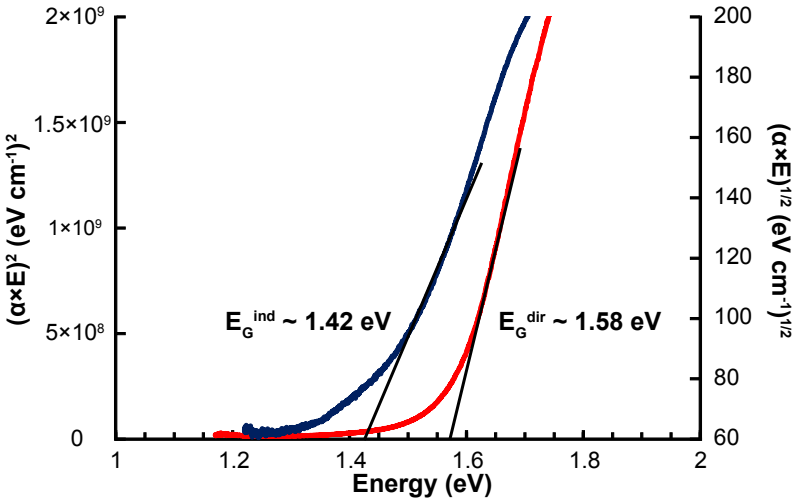


Figure 6.6: Estimation of the band gap type for a $CuSbS_2$ thin film. An indirect band gap is at $E_G \sim 1.42$ eV, while a direct band gap is seen at $E_G \sim 1.58$ eV.

pear similar, until the energy approaches the direct band gap in $CuSbS_2$, where an increase in the absorption coefficient compared to $CuInSe_2$ can be seen. $Cu_3SbS_4$ has a higher valence (Sb 5+) and correspondingly exhibits stronger absorption with a similar abrupt onset of absorption as $CuInSe_2$. Thus, based on design paradigms to provide an increased optical absorption, $Cu_3SbS_4$ was identified as a material with attractive opto-electrical properties for a high efficiency TFSC. In addition, bulk measurements of $Cu_3PS_{4-x}Se_x$ exhibited tunable band gaps between $1.4 \leq E_G \leq 2.4$ eV, with hole mobility values $\sim 10$ cm$^2$ V$^{-1}$s$^{-1}$ [123], indicating that the $Cu_3$-V-$VI_4$ family of materials is potentially useful in single junction and tandem TSFCs.

The dispersion relations for both $CuSbS_2$ and $Cu_3SbS_4$ was obtained using spectroscopic ellipsometry, as shown in Fig. 6.8. The high frequency dielectric constant $\varepsilon_\infty$ at 1000 nm for $CuSbS_2$ is 12.0, while the value for $Cu_3SbS_4$ is 18.5. The extrapolated value for the

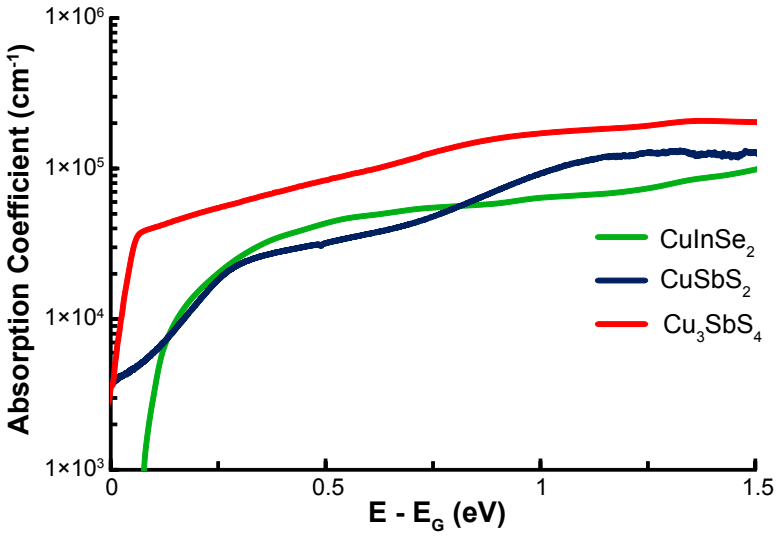


Figure 6.7: Estimation of the band gap type for a $CuSbS_2$ thin film. An indirect band gap is at $E_G \sim 1.42$ eV, while a direct band gap is seen at $E_G \sim 1.58$ eV.

band gap for $CuSbS_2$ was 1.29 eV, while that of $Cu_3SbS_4$ was 0.86 eV. Additional Tauc-Lorentz parameters used for the model are listed in Table 6.1.

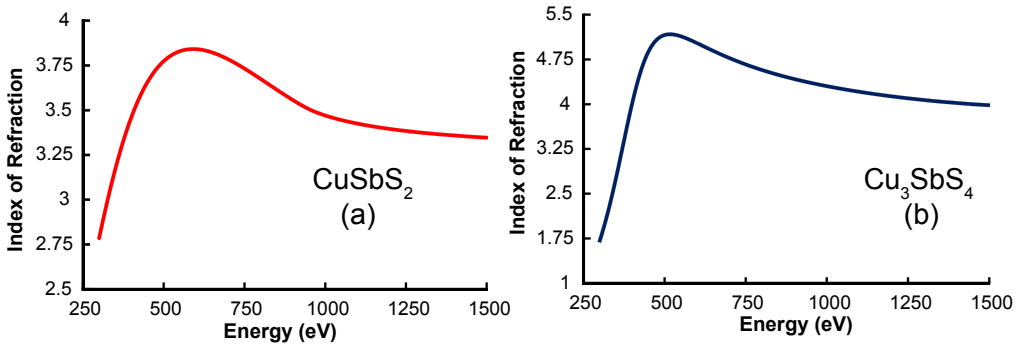


Figure 6.8: Dispersion relationship for (a) $CuSbS_2$, and (b) $Cu_3SbS_4$ measured using spectroscopic ellipsometry.

The modeled dielectric constant for a $CuSbS_2$ and a $Cu_3SbS_4$ thin film can be used to assess electronic properties of the surface using an induced gap states model [12, 137, 138].

| Parameter | $CuSbS_2$ | $Cu_3SbS_4$ |
|---|---|---|
| Thickness [nm] | $117 \pm 0.5$ | $348 \pm 1.1$ |
| E1.Offset | 3.31 | 2.98 |
| A | $125 \pm 17.7$ | $98.9 \pm 10.9$ |
| $E_n$ | 3.3 | 2.98 |
| C | 4.99 | 1.69 |
| $E_G$ | 1.29 | 0.86 |
| $\varepsilon_\infty$ | 12 | 18.5 |
| MSE | 17.3 | 33 |

Table 6.1: Tauc-Lorentz parameters used to model the optical properties of $CuSbS_2$ and $Cu_3SbS_4$ thin films.

The interface parameter ($S$), and the density of surface states ($D_{SS}$) can be estimated as [138],

$$S = \frac{1}{1 + 0.1 \times (\varepsilon_\infty - 1)^2} \tag{6.1a}$$

and

$$D_{SS} = \frac{\varepsilon_0 \varepsilon_\infty}{q \times \delta_i} \left( \frac{1}{S} - 1 \right). \tag{6.1b}$$

where $\varepsilon_\infty$ is the high-frequency relative dielectric constant [unitless] and $\delta_i$ is the interface dipole thickness ($\sim$ 0.4 nm). Calculated values for $S$ and $D_{SS}$ are listed in Table 6.2, and indicate that the interface parameter for both materials is very small. This implies that the Fermi level will be pinned at the charge neutrality level [137], irrespective of the metal work function when forming a metal-semiconductor contact. In addition, the calculated $D_{SS}$ is

| Parameter | $CuSbS_2$ | $Cu_3SbS_4$ |
|---|---|---|
| $E_G$ | 1.4 eV | 0.9 eV |
| $\varepsilon_\infty$ | 12 | 18.5 |
| $S$ | 0.08 | 0.03 |
| $D_{SS} \times 10^{13}$ | 200 | 720 |

Table 6.2: Calculated values for the interface parameter ($S$) and the density of surface states ($D_{SS}$) for a $CuSbS_2$ and a $Cu_3SbS_4$ thin film.

large, on the order of $10^{15}$ $cm^{-3}$. A large concentration of surface states can lead to problems in forming an ohmic contact to $CuSbS_2$ or $Cu_3SbS_4$.

### 6.1.3 TFSC device simulations

The measured material parameters of $CuSbS_2$ and $Cu_3SbS_4$ are used as inputs into SCAPS to assess TFSC device performance for both absorbers. Similar to an FGS-based TFSC, the device configuration used in these simulations consists of the following layers: top contact/ n-ZnO/ n-CdS/ p-absorber/ $p^+$-layer/ bottom contact. A 100 nm $p^+$-layer is included between the absorber and the back contact to provide a $\sim$ 0.2 eV conduction band offset to prevent electrons from recombining at the back surface of the TFSC. SRH recombination via donor-like mid-gap traps is assumed to be the dominant recombination mechanism. A detailed list of parameters used for the simulation is given in Table 6.3. In addition, based on the mechanism of transport, two different device configurations, as shown in Fig. 6.9 are considered. Figure 6.9 (a) shows a simulated energy band diagram for a TFSC utilizing

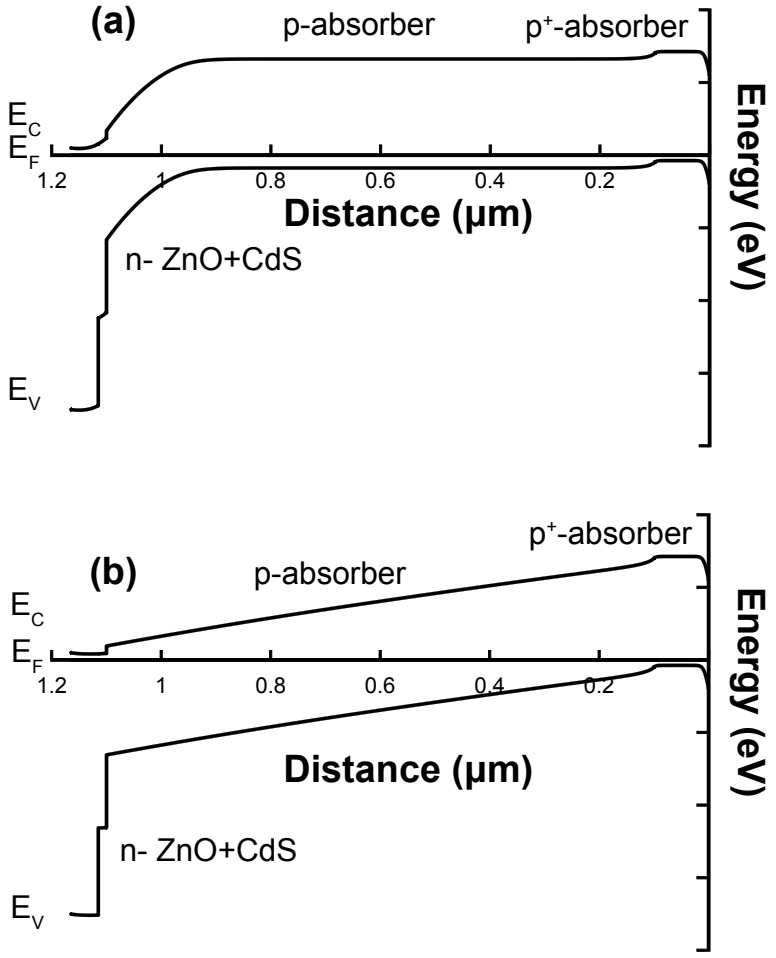


Figure 6.9: Simulated energy band diagrams for a TFSC in (a) a diffusion-cell configuration, and (b) a drift-cell configuration. These two configurations are used for subsequent device simulations.

diffusion as the primary transport mechanism, while Fig. 6.9 (b) is a simulated energy band diagram for a drift-based TSFC.

#### 6.1.3.1 $CuSbS_2$

The measured carrier concentration for a $CuSbS_2$ thin film ($N_A \sim 10^{17}$ cm$^{-3}$) is greater than optimal for a solar absorber. As a result, with the assumption that the carrier concentration can be reduced, two hypothetical carrier concentrations are simulated: $N_A = 2 \times 10^{16}$

| General Device Properties | | | | |
|---|---|---|---|---|
| Parameter | Front Contact | | Back Contact | |
| $\phi_b$ [eV] | $\phi_{bn} = 0.1$ | | $\phi_{bp} = 0.3$ | |
| WF [eV] | 4.1 | | 5.1 | |
| $S_n$ [cm-s$^{-1}$] | $10^7$ | | $10^7$ | |
| $S_p$ [cm-s$^{-1}$] | $10^7$ | | $10^7$ | |
| Reflectivity | 0.1 | | 0.8 | |
| **Layer Properties** | | | | |
| Parameter | $SnO_2$ | CdS | $CuSbS_2$ | $p^+$-$CuSbS_2$ |
| W [nm] | 500 | 25 | variable | 100 |
| $\varepsilon/\varepsilon_0$ | 9 | 10 | 12 | 12 |
| $\mu_n$ [cm$^2$-s$^{-1}$] | 100 | 100 | 1 | 1 |
| $\mu_p$ [cm$^2$-s$^{-1}$] | 25 | 25 | 0.1 | 0.1 |
| n (or p) [cm$^{-3}$] | n: $10^{17}$ | n: $10^{17}$ | p: $2 \times 10^{16}$ | $p^+$: $10^{18}$ |
| $E_G$ [eV] | 3.6 | 2.4 | 1.36 | 1.36 |
| $N_C$ [cm$^{-3}$] | $2.2\times10^{18}$ | $2.2\times10^{18}$ | $8\times10^{17}$ | $8\times10^{17}$ |
| $N_V$ [cm$^{-3}$] | $1.8\times10^{19}$ | $1.8\times10^{19}$ | $1.8\times10^{19}$ | $1.8\times10^{19}$ |
| **Mid-gap Trap Properties** | | | | |
| Parameter | $SnO_2$ | CdS | $CuSbS_2$ | $p^+$-$CuSbS_2$ |
| $N_D$, $N_A$ [cm$^{-3}$] | A: $10^{15}$ | A: $10^{18}$ | D: variable | D: $10^{14}$ |
| $\sigma_n$ [cm$^2$] | $10^{-12}$ | $10^{-15}$ | $10^{-12}$ | $10^{-12}$ |
| $\sigma_p$ [cm$^2$] | $10^{-15}$ | $10^{-12}$ | $10^{-15}$ | $10^{-15}$ |

Table 6.3: Material parameters used for $CuSbS_2$-based TFSC simulations.

$cm^{-3}$ (diffusion cell, shown in Fig. 6.9 (a)), and $N_A = 2 \times 10^{14}$ $cm^{-3}$ (drift cell, shown in Fig. 6.9 (b)). In addition, carrier mobilities of 1 and 0.1 $cm^2$ $V^{-1}$ $s^{-1}$, are used for electrons and holes, respectively. A minority carrier lifetime of $\tau$ = 1 ns (corresponding to $N_T = 10^{14}$ $cm^{-3}$) is used in the simulation, unless otherwise specified.

Device efficiency as a function of the $CuSbS_2$ absorber layer thickness ($L_A$) for a diffusion-cell configuration is shown in Fig. 6.10(a), and indicates that an efficiency of $\sim$ 7.5% can be achieved with a thickness between 750 nm - 1000 nm. Similar to FGS, low carrier mobilities (i.e., $\mu_n = 1$, $\mu_n = 0.1$ $cm^2V^{-1}s^{-1}$) along with a non-abrupt onset of absorption (see Fig. 5.10 for FGS) translate into a low simulated efficiency. The effect of the non-abrupt onset of absorption is revealed in a quantum efficiency (QE) plot as a function of $CuSbS_2$ thickness, as shown in Fig. 6.10(b), which indicates that a maximum QE ($\sim$ 75% at $\lambda$ = 530 nm) is achieved for a thickness greater than 500 nm. For an absorber thickness greater than 750 nm, the QE curves in Fig. 6.10(b) converge and are identical.

Tang *et al.* measured a hole mobility of 1.2 $cm^2$ $V^{-1}$ $s^{-1}$ [136] for a $CuSbSe_2$ thin film. Since $\mu_n$ is typically 5 to 10 $\times$ $\mu_p$ for common TFSC absorber materials [27, 41], an electron mobility of $\mu_n$ = 10 $cm^2$ $V^{-1}$ $s^{-1}$ is assumed, and carrier mobilities of 10 and 1 $cm^2$ $V^{-1}$ $s^{-1}$, for electrons and holes, respectively, are simulated next. Device efficiency as a function of the absorber layer thickness is shown in Fig. 6.11 (a). The increase in carrier mobilities in a diffusion-cell configuration gives rise to an increased diffusion length for photogenerated carriers, and translates directly into a higher photoconversion efficiency. As seen in Fig. 6.11 (a), an increase in carrier mobilities (by an order of magnitude) provides $\sim$ an 11% efficient TFSC with a $CuSbS_2$ absorber layer thickness greater than 750 nm, compared to the $\sim$ 7.5% efficiency given in Fig. 6.10 (a). The increase in mobility on the

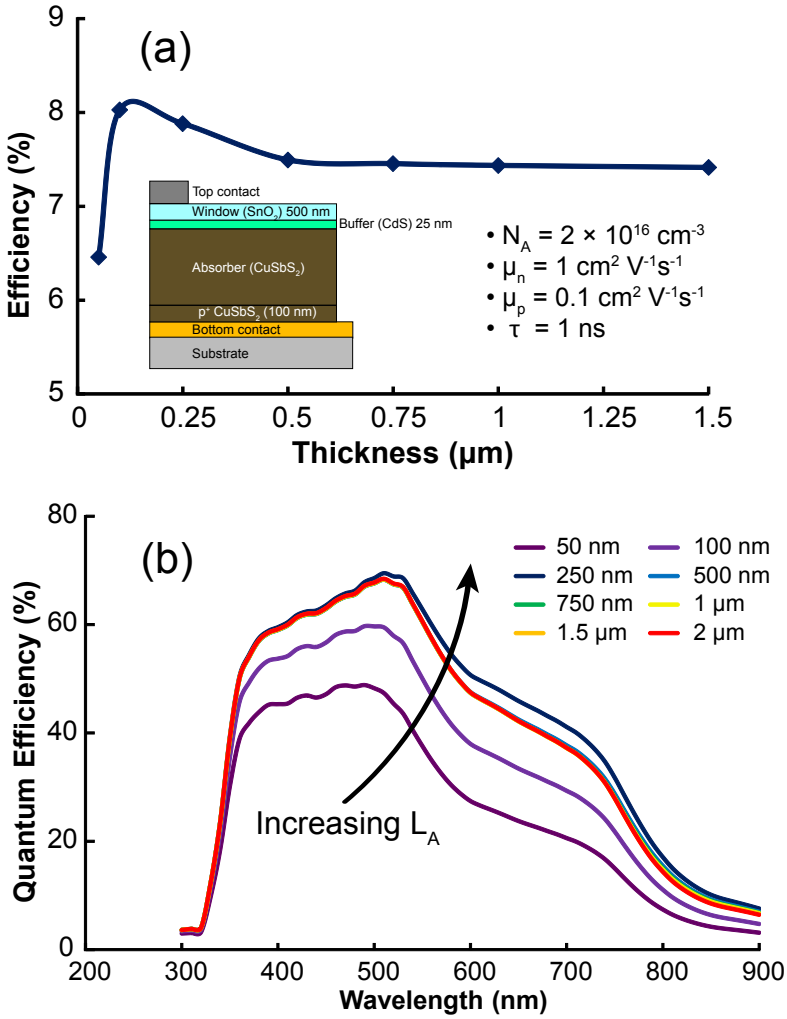


Figure 6.10: (a) Simulated TSFC efficiency as a function of $CuSbS_2$ absorber layer thickness in a diffusion-cell configuration. The efficiency saturates beyond $L_A \sim 750$ nm. (b) Simulated QE as a function of $CuSbS_2$ absorber layer thickness. The QE saturates for thicknesses greater than 750 nm, and curves are identical for $L_A > 750$ nm.

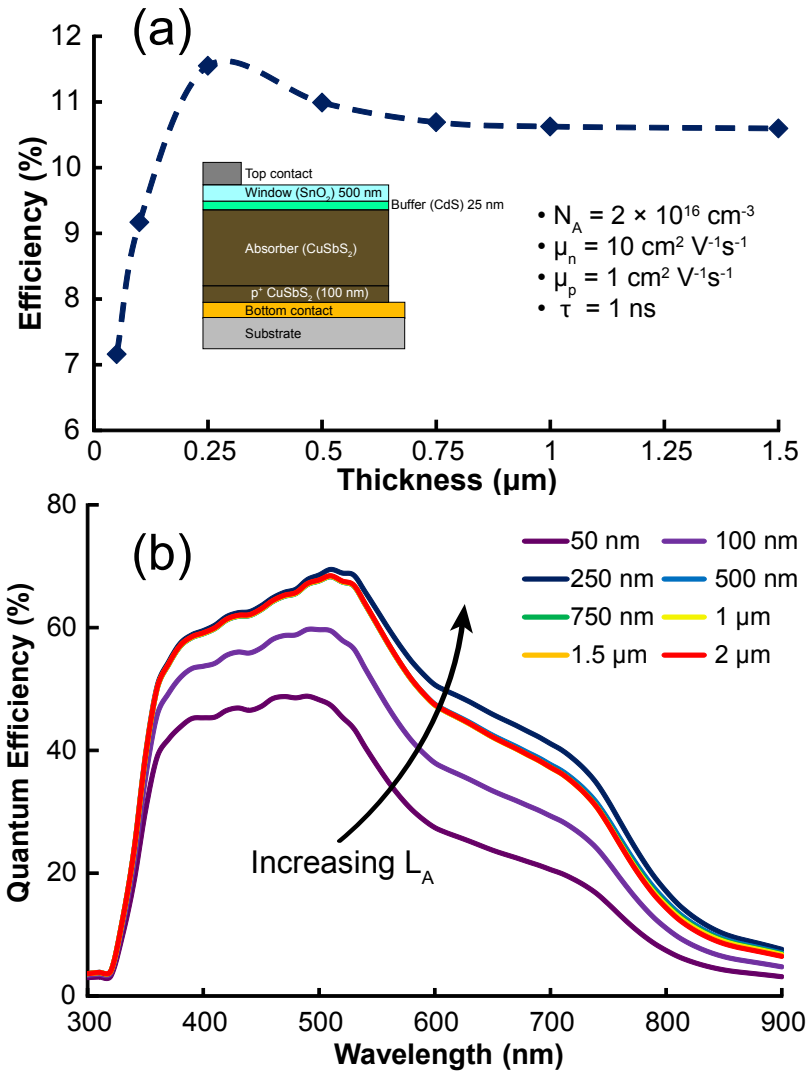


Figure 6.11: (a) Simulated TFSC efficiency as a function of $CuSbS_2$ absorber layer thickness in a diffusion-cell configuration, with the carrier mobilities increased to $\mu_n$, $\mu_p$ = 10, 1 $cm^2$ $V^{-1}$ $s^{-1}$. The efficiency saturates beyond $L_A \sim 750$ nm. (b) Simulated QE as a function of $CuSbS_2$ absorber layer thickness. The QE saturates for thicknesses greater than 750 nm, and curves are identical for $L_A > 750$ nm.

other hand, does not significantly improve the simulated QE (Fig. 6.11 (b)), which maintains the same profile as that of the low mobility case, as shown in Fig. 6.10 (b). The QE curves converge for an absorber thickness greater than 750 nm and are identical in Fig. 6.10 (b).

Since the efficiency begins to saturate beyond 750 nm - 1000 nm in Fig. 6.11, a critical thickness of 1 $\mu$m is identified and is held constant for subsequent simulations in which the minority carrier lifetime ($\tau$) for a $CuSbS_2$ absorber is varied. Carrier mobilities of 10 and 1 $cm^2\ V^{-1}\ s^{-1}$, for electrons and holes, respectively, are used in this simulation. TFSC efficiency as a function of minority carrier lifetime is shown in Fig. 6.12 and indicates that an efficiency of 11% is achieved with a minority carrier lifetime of 1 ns ($N_T = 10^{14}\ cm^{-3}$). Increasing $\tau$ to 10 ns ($N_T = 10^{13}\ cm^{-3}$) increases the efficiency to $\sim$ 16%, while a 100 ns ($N_T = 10^{12}\ cm^{-3}$) lifetime provides for a 20% TFSC. The efficiency is low ($< 5\%$) for minority carrier lifetimes less than 0.1 ns ($N_T = 10^{15}\ cm^{-3}$). While an efficiency of 15% and higher is simulated for a $CuSbS_2$-based diffusion cell with a minority carrier lifetime greater than 10 ns, or $N_T = 10^{13}\ cm^{-3}$, developing a process to manufacture a high-quality defect free material can be time-consuming and expensive. Thus, under achievable laboratory conditions, a $CuSbS_2$-based diffusion ($N_A \sim 10^{16}\ cm^{-3}$) cell, with an absorber layer thickness of 1 $\mu$m and moderate transport properties ($\mu_n$, $\mu_p$ = 10, 1 $cm^2\ V^{-1}\ s^{-1}$ and $\tau$ = 1 ns, or $N_T = 10^{14}\ cm^{-3}$), only an 11% efficient TFSC can be achieved.

Based on the energy band diagram shown in Fig. 6.9, a drift-cell configuration ($N_A \sim 10^{14}\ cm^{-3}$) is pursued next. Device efficiency as a function of the $CuSbS_2$ absorber layer thickness is shown in Fig. 6.13 (a). Carrier mobilities of $\mu_n$, $\mu_p$ = 1, 0.1 $cm^2\ V^{-1}\ s^{-1}$ are used in this simulation. Figure 6.13 confirms the assertion that a drift-cell is the preferred TSFC device configuration for a low mobility absorber. A maximum efficiency of $\sim$ 14% is

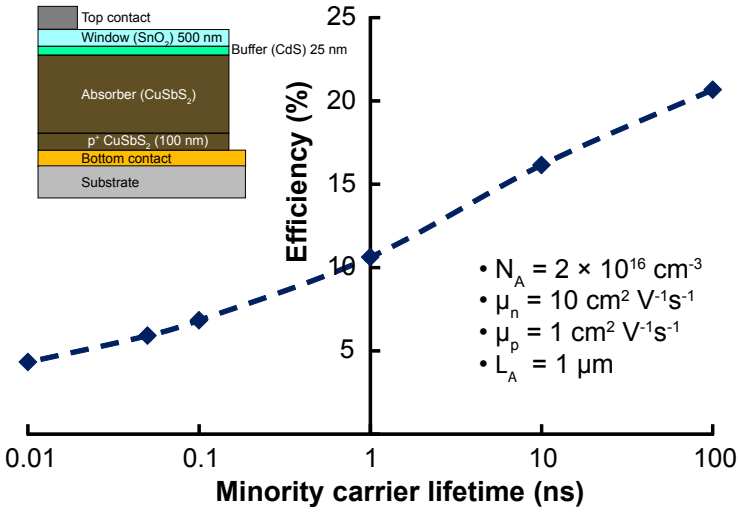


Figure 6.12: Simulated TFSC efficiency as a function of the minority carrier lifetime using a $CuSbS_2$ absorber layer in a diffusion -cell configuration.

obtained for a thickness between 500 - 750 nm in Fig. 6.13 (a). However, for an absorber thickness beyond 750 nm, the efficiency decreases considerably due to an increased recombination of the slow moving carriers. Quantum efficiency (QE) as a function of absorber layer thickness is shown in Fig. 6.13 (b). Unlike the diffusion-cell case (Fig. 6.10 (b)), where the QE curves converge and are identical for an absorber thickness greater than 750 nm, the QE curves for a drift-cell configuration show a systematic increase until $L_A \sim 1$ $\mu$m. While a $CuSbS_2$ diffusion cell displays a maximum quantum efficiency of $\sim 75\%$, the corresponding drift cell exhibits a value of $\sim 80\%$, indicating an improvement in photocollection due to the existence of the built-in field.

Increasing the mobility of the $CuSbS_2$ absorber layer to $\mu_n$, $\mu_p$ = 10, 1 $cm^2$ $V^{-1}$ $s^{-1}$ in a drift-cell configuration has a significant improvement in the photoconversion efficiency, as seen in Fig. 6.14 (a). Efficiencies greater than 16% can be achieved with an absorber layer thickness of 750 nm. While the low mobility $CuSbS_2$ drift cell simulation (Fig. 6.13 (a))

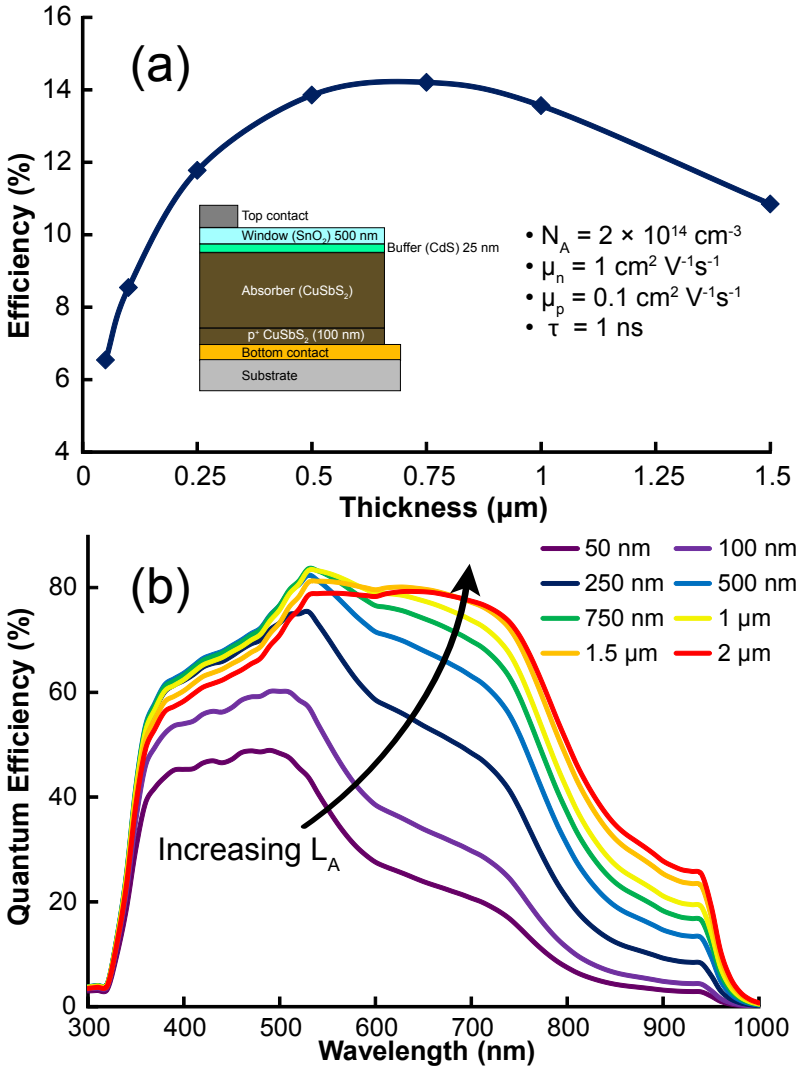


Figure 6.13: (a) Simulated TFSC efficiency as a function of $CuSbS_2$ absorber layer thickness in a drift-cell configuration. The efficiency begins to decrease for a thickness beyond $L_A \sim$ 750 nm. (b) Simulated QE as a function of $CuSbS_2$ absorber layer thickness. A maximum of $\sim$ 80% is obtained for $\lambda \sim$ 530 - 750 nm.

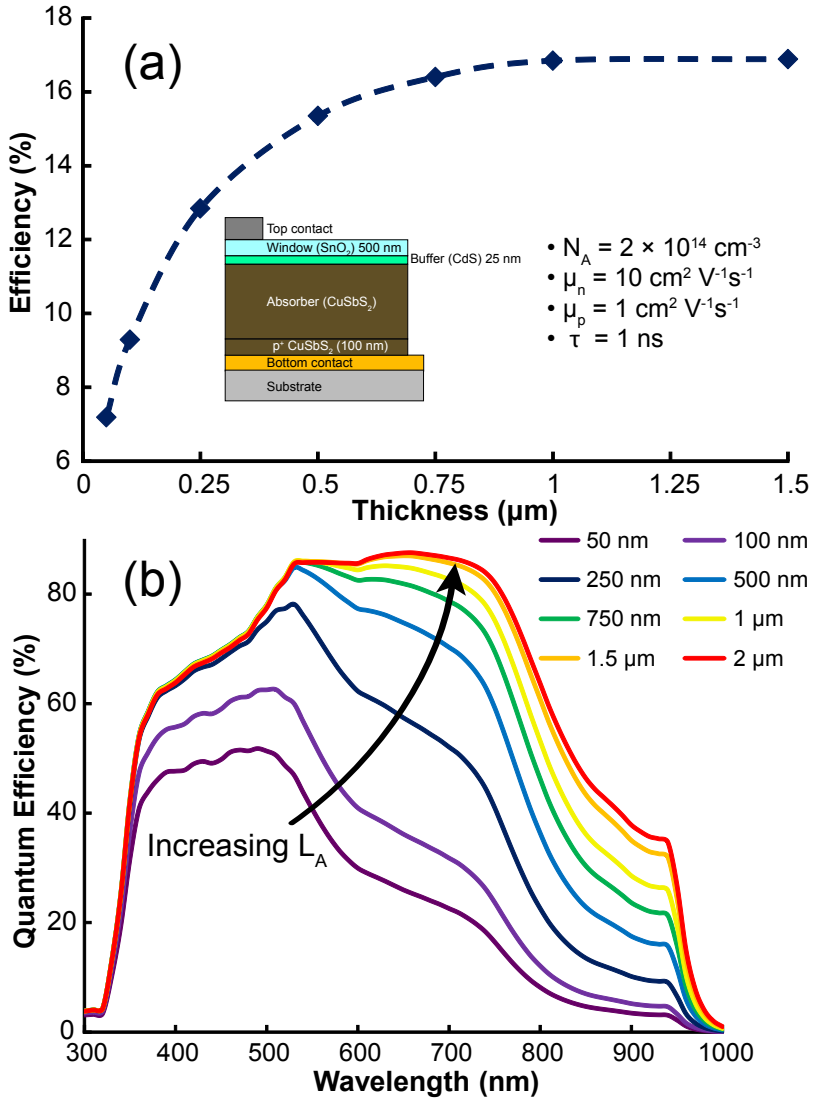


Figure 6.14: (a) Simulated TSC efficiency as a function of $CuSbS_2$ absorber layer thickness in a drift-cell configuration, with the carrier mobilities increased to $\mu_n$, $\mu_p$ = 10, 1 $cm^2V^{-1}s^{-1}$. The efficiency begins to saturate beyond $L_A \sim 750$ nm, and provides for a 16% efficient TFSC. (b) Simulated QE as a function of $CuSbS_2$ absorber layer thickness. A maximum of $\sim 75\%$ is obtained for $\lambda \sim 530$ - 750 nm.

shows a decrease in efficiency beyond $L_A \sim 750$ nm, Fig. 6.14 (a) does not show a decrease in efficiency with increasing thickness. Instead, the efficiency increases until $L_A \sim 750$ nm, beyond which the efficiency does not exhibit an appreciable increase. The QE curves, shown in Fig. 6.14 (b), exhibit a maximum value of 85% for a thickness greater than 750 nm. When comparing QE curves for a $CuSbS_2$ absorber layer with the same carrier mobilities (e.g. $\mu_n$, $\mu_p$ = 1, 0.1 $cm^2V^{-1}s^{-1}$), it is evident that the drift-cell configuration not only provides a higher overall QE value, but also exhibits an increased spectral response for $\lambda > 550$ nm, suggesting improved photocollection compared to the diffusion-cell configuration.

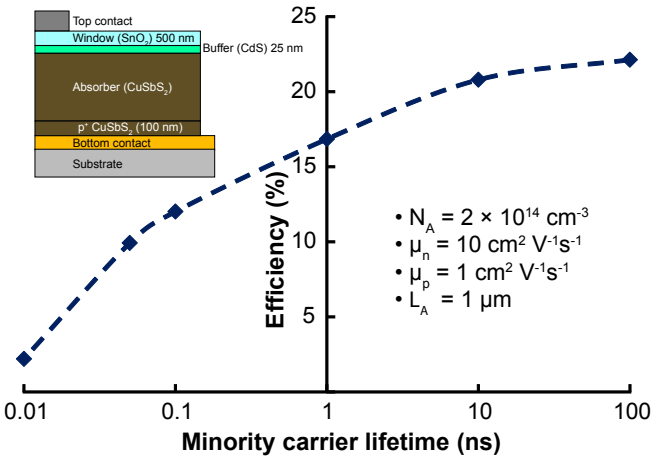


Figure 6.15: Simulated TSFC efficiency as a function of the minority carrier lifetime using a $CuSbS_2$ absorber layer in a drift-cell configuration.

Since the efficiency begins to saturate for an absorber thickness greater than 750 nm in Fig. 6.14 (a), a thickness of 1 $\mu$m is used to simulate the efficiency as a function of minority carrier lifetime. Carrier mobilities of 10, 1 $cm^2$ $V^{-1}$ $s^{-1}$, for electrons and holes, respectively, are used for this simulation. Figure 6.15 indicates that an efficiency of $\sim$ 16% can be

achieved with a 1 ns ($N_T = 10^{14}$ $cm^{-3}$) minority carrier lifetime. Increasing the lifetime of $\tau$ to 10 ns ($N_T = 10^{13}$ $cm^{-3}$), provides for a 20% efficienct TFSC, while a 100 ns ($N_T = 10^{12}$ $cm^{-3}$) lifetime provides an efficiency value of 22%, similar to a diffusion-cell configuration (Fig. 6.11 (a)). For a minority lifetime less than 0.1 ns however, a significant reduction in efficiency to less than 5% is observed. Thus, for a drift-cell configuration utilizing a 1 $\mu$m thick $CuSbS_2$ absorber layer, with moderate transport properties ($\mu_n$, $\mu_p$ = 10, 1 $cm^2V^{-1}s^{-1}$; $\tau$ = 1 ns or $N_T = 10^{14}$ $cm^{-3}$), a 16% efficienct TFSC can be achieved under laboratory conditions.

#### 6.1.3.2 $Cu_3SbS_4$

The photovoltaic capabilities of a $Cu_3SbS_4$-based TFSC is evaluated using properties listed in Table 6.3 and additional material parameters specific to $Cu_3SbS_4$ listed in Table 6.4. The measured hole mobility ($\mu_p$ = 14 $cm^2$ $V^{-1}$ $s^{-1}$) is used in the simulation, while the electron mobility is assumed to be $\mu_n$ = 50 $cm^2$ $V^{-1}$ $s^{-1}$. This assumption for $\mu_n$ is seems viable, since the DOS for $Cu_3SbS_4$ (refer to Fig. 6.1) indicates a significant contribution from Sb s-orbital derived bands near the CBM, which is expected to lead to an increased electron mobility. Since a carrier concentration of $N_A \sim 10^{17}$ $cm^{-3}$ was measured for sputtered $Cu_3SbS_4$ thin films, with the assumption that $N_A$ can be reduced by an order of magnitude, a carrier concentration of $N_A = 2 \times 10^{16}$ $cm^{-3}$ is used in the simulation. The TFSC device configuration is identical to that used for $CuSbS_2$ TFSC simulations and is shown in the inset of Fig. 6.16 (a). TFSC efficiency as a function of $Cu_3SbS_4$ absorber layer thickness ($L_A$) is shown in Fig. 6.16 (a), and indicates an efficiency as high as 19% can be achieved with a $Cu_3SbS_4$ absorber layer thickness between 500 - 750 nm. It must be noted that a minority carrier lifetime of $\tau$ = 1 ns (or $N_T = 10^{14}$ $cm^{-3}$) was used in this simulation, indicating that a relatively high efficiency ($\eta$ >15%) TFSC can be developed using $Cu_3SbS_4$ as an absorber

| Parameter | Value |
|---|---|
| $E_G$ [eV] | 0.89 |
| Dielectric constant [unitless] | 18.5 |
| $\mu_n$ [$cm^2\ V^{-1}\ s^{-1}$] | 50 |
| $\mu_p$ [$cm^2\ V^{-1}\ s^{-1}$] | 14 |

Table 6.4: Additional material parameters used for $Cu_3SbS_4$-based TFSC device simulations.

layer, without having to achieve a highly defect-free material. In addition, this thickness requirement is significantly less than that required for current polycrystalline solar absorbers, i.e., 1 - 2 $\mu$m for CIGS [79] and 2 - 4 $\mu$m for CdTe [24].

Figure 6.16 (b) shows a plot of the simulated quantum efficiency (QE) as a function of $Cu_3SbS_4$ absorber thickness, and emphasizes the importance of an abrupt onset of absorption for a solar absorber since it results in a rapid increase in the QE near the band gap. The abrupt onset of absorption leading to a high absorption coefficient for $Cu_3SbS_4$ indicates that a QE $>$70% can be achieved even with a 500 nm absorber layer. For $L_A$ = 750 nm, the QE is $\sim$ 85% between $\lambda \sim$ 530 - 1350 nm, indicating a very strong spectral response. The QE saturates for $L_A$ $>$750 nm at $\sim$ 85% and the curves are identical for increasing thickness values. An optimum thickess of 750 nm is identified and used for subsequent simulations.

Figure 6.17 is a plot of the photoconversion efficiency as a function of the carrier concentration in the absorber layer and indicates that there is negligible variation in the efficiency between a carrier concentration value of $N_A = 2 \times 10^{14}$ $cm^{-3}$ and $2 \times 10^{16}$ $cm^{-3}$. Unlike the low mobility cases of FGS and $CuSbS_2$, which indicated that a low carrier concentration

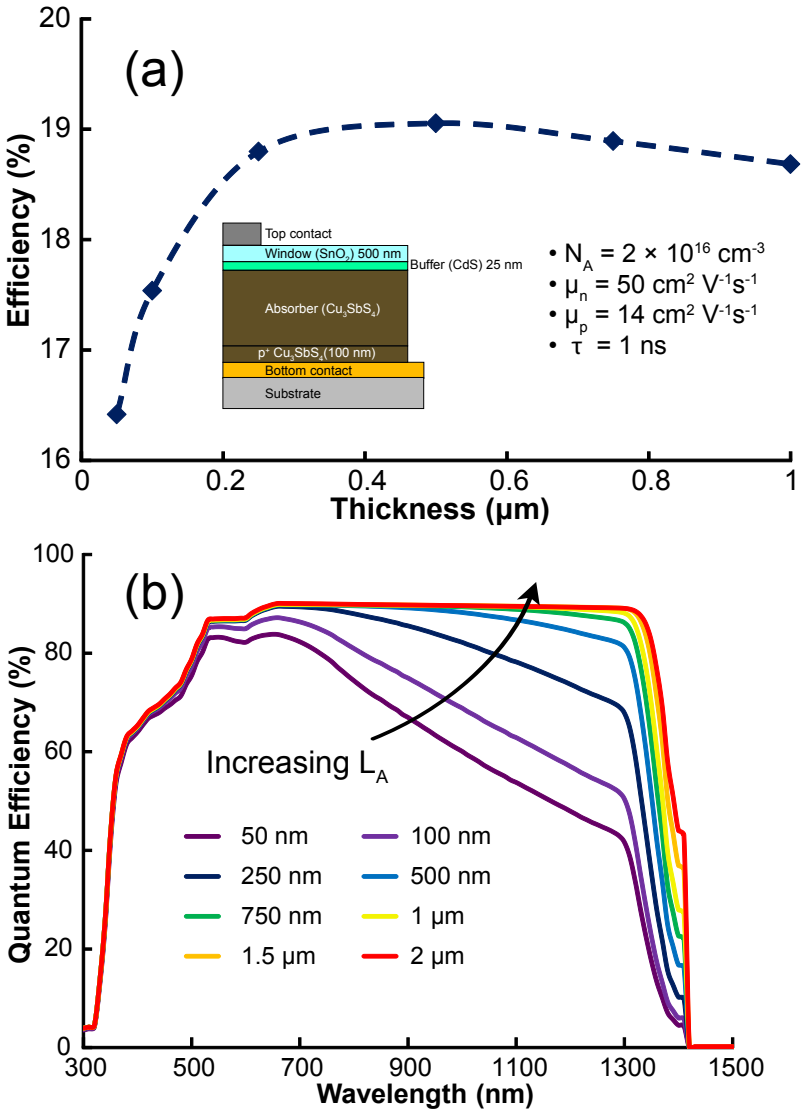


Figure 6.16: (a) Simulated TSFC efficiency as a function of $Cu_3SbS_4$ absorber layer thickness. The efficiency exhibits a maximum value of 19% between 500 - 750 nm. (b) Simulated QE as a function of $Cu_3SbS_4$ absorber layer thickness. A maximum of $\sim$ 85% is obtained for $L_A$ = 750 nm between $\lambda \sim$ 530 - 1350 nm. The QE saturates for $L_A$ greater than 750 nm, and the curves are identical.

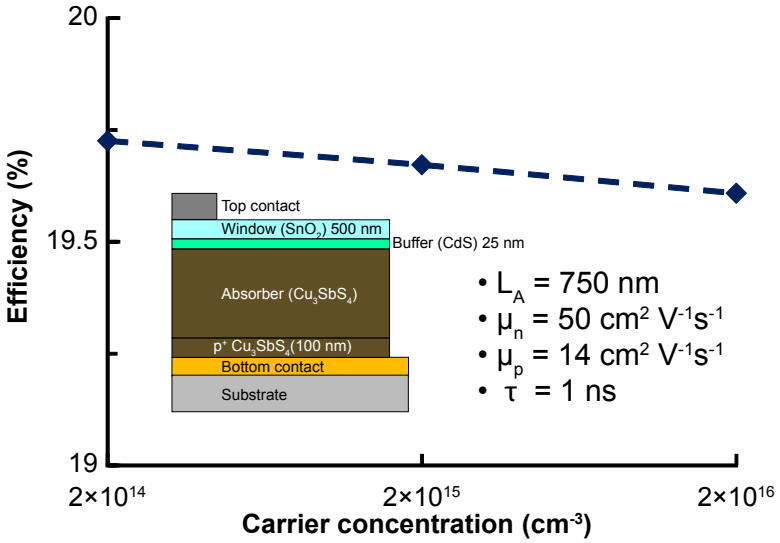


Figure 6.17: Simulated TFSC efficiency as a function of the carrier concentration in a $Cu_3SbS_4$ absorber layer. There is a negligible variation in efficiency with increasing carrier concentration values.

and $L_A \sim 1\ \mu$m is necessary for an efficiency >15%. The moderate carrier mobilities ($\mu_n$, $\mu_p$ = 50 and 14 cm$^2$ V$^{-1}$ s$^{-1}$, respectively), along with an abrupt onset of absorption leading to a strong absorption coefficient and $L_A \sim 750$ nm indicate that the $Cu_3SbS_4$ absorber layer is relatively insensitive to variations in the carrier concentration.

With a critical thickness identified ($L_A$ = 750 nm), a carrier concentration of $N_A = 2 \times 10^{16}$ cm$^{-3}$ is used to simulate the TFSC efficiency as a function of minority carrier lifetime ($\tau$) in the absorber layer, shown in Fig. 6.18. As indicated in Fig. 6.16 (a), a photoconversion efficiency of $\sim$ 19% can be achieved with a minority carrier lifetime of only 1 ns. Increasing the minority carrier lifetime above 1 ns (or $N_T < 10^{14}$ cm$^{-3}$) provides an efficiency increase beyond 20%, indicating that a $Cu_3SbS_4$-based TFSC can exhibit a high photoconversion efficiency with improvement in the absorber layer quality by decreasing the concentration of defects. In addition, for a minority carrier lifetime $\tau$ less than 1 ns (or $N_T > 10^{14}$ cm$^{-3}$), a $Cu_3SbS_4$-based TFSC exhibits efficiencies higher than 10%. In particular, with $\tau$ = 0.01 ns (or

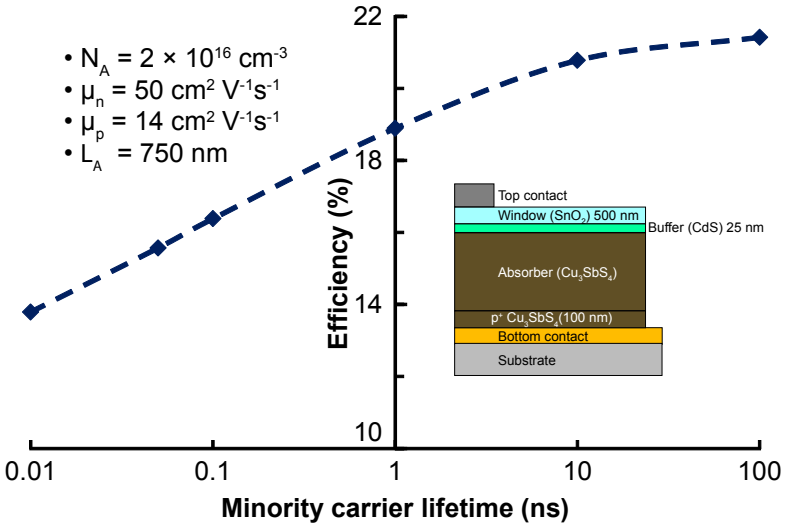


Figure 6.18: Simulated TFSC efficiency as a function of the minority carrier lifetime using a $Cu_3SbS_4$ absorber layer. An efficiency greater than 10% is obtained even with a low minority carrier lifetime , $\tau$ = 0.01 ns (or $N_T \sim 10^{16}$ $cm^{-3}$).

$N_T \sim 10^{16}$ $cm^{-3}$), an efficiency of $\sim$ 14% is simulated. Thus, even in the presence of a high density of traps or defects, a $Cu_3SbS_4$-based TFSC can provide an efficiency value higher than 10%. This indicates that unlike FGS or $CuSbS_2$ which both required a highly defect-free material, the strong absortion with moderate transport properties allows the $Cu_3SbS_4$ absorber to be relatively defect tolerant and still provide a high efficiency.

Thus, device simulations indicate that Cu-V-VI materials can be used in a single-junction TFSC to obtain an efficiency greater than 15%. For $CuSbS_2$, a minimum of 1 $\mu$m thickness is required along with a carrier concentration of 2 $\times$ $10^{14}$ $cm^{-3}$, with a minority carrier lifetime of 1 ns ($N_T$ = $10^{14}$ $cm^{-3}$) and carrier mobilities, $\mu_n$, $\mu_p$ = 10 and 1 $cm^2$ $V^{-1}$ $s^{-1}$ to provide a 16% efficienct TFSC. A $Cu_3SbS_4$-based TFSC, on the other hand, only requires an absorber layer between 500 - 750 nm, a carrier concentration $N_A$ = 2 $\times$ $10^{16}$ $cm^{-3}$, with a minority carrier lifetime of 1 ns ($N_T$ = $10^{14}$ $cm^{-3}$), and carrier mobilities of $\mu_n$, $\mu_p$ =

| Property | $CuSbS_2$ | $Cu_3SbS_4$ |
|---|---|---|
| Thickness [$\mu$m] | 1 - 1.5 | 0.5 - 0.75 |
| Carrier concentration [$cm^{-3}$] | $1 \times 10^{14}$ $cm^{-3}$ | $1 \times 10^{16}$ $cm^{-3}$ |
| Carrier mobility [$cm^2\,V^{-1}\,s^{-1}$] | $\mu_n$ =10; $\mu_p = 1$ | $\mu_n$ =50; $\mu_p = 14$ |
| Minority carrier lifetime [ns] | 1 ($N_T = 10^{14}$ $cm^{-3}$) | 1 ($N_T = 10^{14}$ $cm^{-3}$) |
| Efficiency [%] | 16 | 19 |

Table 6.5: Required material parameters for a $CuSbS_2$- and a $Cu_3SbS_4$-based TFSC simulated to provide an efficiency of 16% and 19%, respectively.

50 and 14 $cm^2$ $V^{-1}$ $s^{-1}$, to provide a 19% efficienct TFSC, suggesting that $Cu_3SbS_4$ can be a competitive solar absorber material in a high efficiency single junction TFSC. In addition, based on the band gap difference between $CuSbS_2$ ($E_G$ = 1.4 eV) and $Cu_3SbS_4$ ($E_G$ = 0.9 eV), the Cu-V-VI system can also be used in a tandem TFSC. The best-case results based on simulations of $CuSbS_2$ and $Cu_3SbS_4$-based TFSCs are summarized in Table 6.5, for a minority carrier lifetime of 1 ns (or $N_T$ = $10^{14}$ $cm^{-3}$).

## 6.2 Tetrahedrites - $Cu_{10}M_2Sb_4Ch_{13}$ (M = Cu, Mn, Zn, Al, In; Ch = S, Se)

An alternative composition not previously explored as a solar absorber is the tetrahedrite family of materials. A naturally-occurring sulfide compound, the basic tetrahedrite mineral can be expressed by the following generalized chemical formula: $A_{10}M_2X_4Ch_{13}$, where A = Cu, Ag; M = Cu, Fe, Zn, Hg, Cd, Pb; X = Sb, As, Bi; and Ch = S, Se [139]. Tetrahedrite compounds have been widely studied by the geology community since they are a common source of Cu and Ag [140, 141], however, they have attracted limited attention in

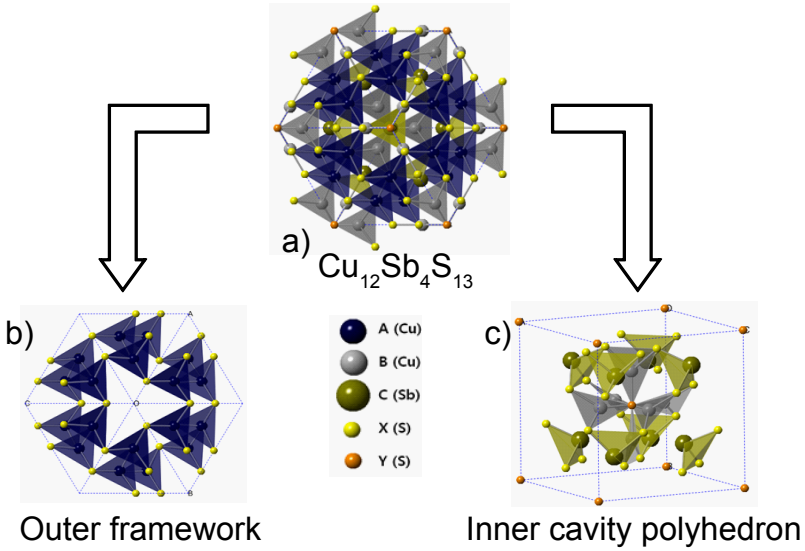


Figure 6.19: Tetrahedrite crystal structure. The structure can be sub-divided into an outer framework formed by Cu-S bonds, within which is a cavity polyhedron formed by Cu-Sb-S atoms.

other fields. Recently tetrahedrites have been identified as a potential p-type thermoelectric material with zT values approaching 1 at T >700 K [142, 143, 144].

The cubic $Cu_{12}Sb_4S_{13}$ crystal structure (Fig. 6.19) is a combination of an outer framework and an inner cavity polyhedron. The outer framework (Fig. 6.19 b) is formed by corner-sharing Cu-S tetrahedrally connected bonds, while the inner cavity polyhedron (Fig. 6.19 c) is formed by Cu, Sb and S. A unique feature of the tetrahedrite crystal structure is that the inner cavity is completely isolated within the outer framework [145], such that the outer framework can facilitate transport of minority carrier electrons, while the inner cavity can provide strong optical absorption. While Fig. 6.19 indicates a complex crystal structure consisting of 58 atoms in a unit cell, the structure itself is cubic. This implies that tetrahedrites have isotropic properties [146], which is beneficial for a solar absorber, and for other opto-electronic applications.

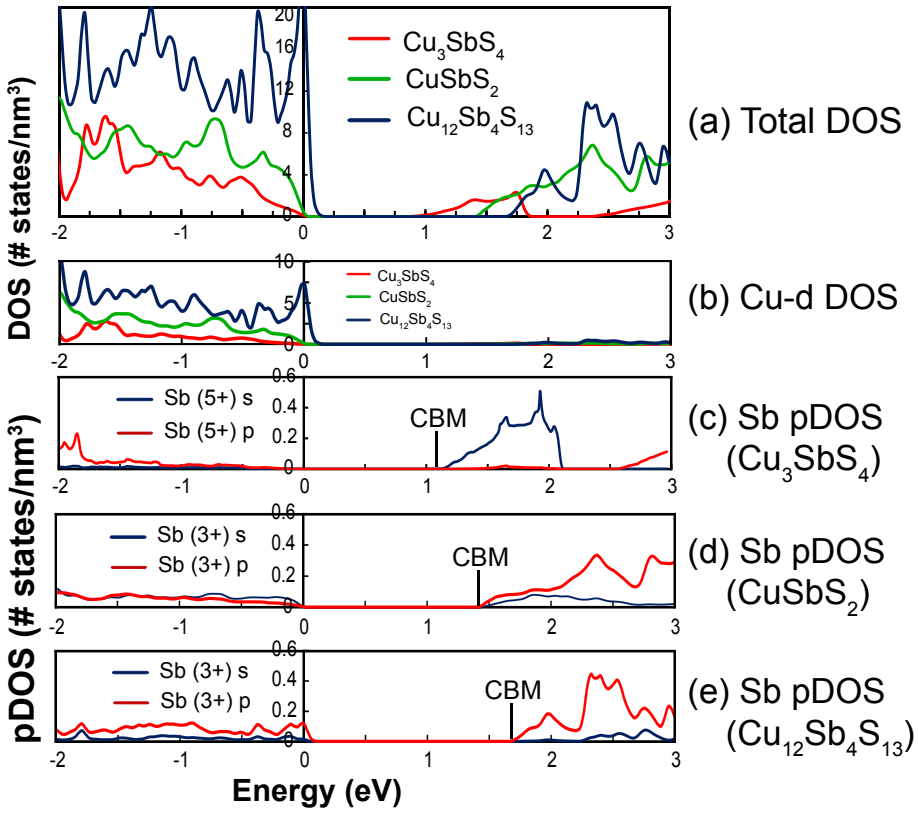


Figure 6.20: (a) Calculated total density of states (DOS) for $Cu_3SbS_4$, $CuSbS_2$, and $Cu_{12}Sb_4S_{13}$.(b) DOS contribution from Cu 3d orbital derived bands for the three compounds. In addition, the partial DOS (pDOS) from Sb 5s and 5p orbital derived bands is shown for (c) $Cu_3SbS_4$, (d) $CuSbS_2$, and (e) $Cu_{12}Sb_4S_{13}$.

The total calculated electronic density of states (DOS) (between -2 eV to 3 eV) comparing $Cu_3SbS_4$, $CuSbS_2$, and $Cu_{12}Sb_4S_{13}$ is shown in Fig. 6.20 (a) to highlight the DOS near the band edges. Figure 6.20 (b) is the DOS contribution from Cu 3d orbital derived bands for the three compounds, and Figs. 6.20 (c-e) show the partial DOS (pDOS) contribution from Sb 5s and 5p orbital derived bands for the three compounds. It should be noted that the full energy range (-10 eV to 10 eV) is not shown in Fig. 6.20 since the DOS near the band edges are more important for an absorber material. In Fig. 6.20, energies E $<$0 eV correspond to the valence band, and the position of the CBM is identified. Figure 6.20 (a) indicates that the

total DOS of $Cu_{12}Sb_4S_{13}$ in the valence band is greater than that of $Cu_3SbS_4$ or $CuSbS_2$. Figure 6.20 (b) plots the DOS contribution of Cu 3d orbital derived bands for $Cu_3SbS_4$, $CuSbS_2$, and $Cu_{12}Sb_4S_{13}$. In all three compounds, Cu 3d orbital derived bands contribute to the valence band. However, the Cu 3d contribution is much larger in $Cu_{12}Sb_4S_{13}$ compared to that of $Cu_3SbS_4$ or $CuSbS_2$.

The pDOS contribution from Sb 5s and 5p orbital derived bands for $Cu_3SbS_4$ is shown in Fig. 6.20 (c). $Cu_3SbS_4$ contains high valence $Sb^{5+}$ ions isolated within the crystal structure (refer to Fig. 6.2) such that the empty $Sb^{5+}$ orbitals (corresponding to an electronic configuration $5s^0$ $5p^0$) are isolated from each other. This causes the $Sb^{5+}$ s-orbital derived conduction band which would normally be broad and dispersed in energy to be quite narrow ($\sim$ 1 eV), as shown in Fig. 6.20 (c). Sb p-orbital derived bands for $Cu_3SbS_4$ (Fig. 6.20 (c)) do not contribute to the CBM. $CuSbS_2$, on the other hand, has low-valence $Sb^{3+}$ ions with a $5s^2 5p^0$ electronic configuration, giving rise to a significant density of empty Sb p-orbital derived conduction bands. Note that these $Sb^{3+}$ p-orbital derived conduction bands for $CuSbS_2$, shown in Fig. 6.20 (d), are much wider and more dispersed in energy i.e., the conduction band width is $>$4 eV (full width not shown in Fig. 6.20 (d)) compared to that found for $Cu_3SbS_4$ $Sb^{5+}$ s-orbital derived conduction bands shown in Fig. 6.20 (c), in which the conduction band width is $\sim$ 1 eV.

$Cu_{12}Sb_4S_{13}$ contains low-valence $Sb^{3+}$ ions sitting inside a cavity polyhedron (formed by Cu-Sb-S atoms) so that they are spatially separated (physically isolated) from the outer framework (formed by Cu-S atoms). The pDOS from $Sb^{3+}$ orbital derived bands for $Cu_{12}Sb_4S_{13}$ is shown in Fig. 6.20 (e). While both $CuSbS_2$ and $Cu_{12}Sb_4S_{13}$ contain low-valence $Sb^{3+}$ ions, the Sb p-orbital derived conduction band for $Cu_{12}Sb_4S_{13}$ in Fig. 6.20 (e) is not as broad and

dispersed in energy as that of $CuSbS_2$ (shown in in Fig. 6.20 (d)). The width of the Sb p-orbital derived conduction band for $Cu_{12}Sb_4S_{13}$ is $\sim 2$ eV (full width is not shown in Fig.6.20 (e)). This suggests that isolated Sb atoms in the $Cu_{12}Sb_4S_{13}$ lattice results in a slightly narrower Sb p-orbital derived band near the CBM compared to that of $CuSbS_2$. The narrower Sb p-orbital derived band near the CBM along with the large contribution from Cu d-orbital derived bands near the VBM increases the total DOS (or JDOS) for $Cu_{12}Sb_4S_{13}$ compared to that of $Cu_3SbS_4$ or $CuSbS_2$. Additionally, allowed electric dipole transitions between Cu 3d (filled) $\rightarrow$ Sb 5p (empty), Cu 3d (filled) $\rightarrow$ S 2p (empty), and Sb 5s (filled) $\rightarrow$ Sb 5p (empty) provide multiple opportunities for a transition from the valence band to the conduction band. Since the absorption coefficient is a combination of the JDOS and the transition matrix element [11], $Cu_{12}Sb_4S_{13}$ is expected to exhibit stronger optical absorption than $Cu_3SbS_4$ or $CuSbS_2$.

Fig. 6.20(a) shows that a portion of the valence band extends into E $>$0 eV, implying that the Fermi level in $Cu_{12}Sb_4S_{13}$ is within the valence band. This indicates that it is a p-type degenerate semiconductor with a hole concentration greater than $10^{18}$ $cm^{-3}$. The $p^+$ nature would make it impossible to employ $Cu_{12}Sb_4S_{13}$ as a TFSC absorber, which typically requires a hole concentration between $10^{14}$ - $10^{17}$ $cm^{-3}$. An alternative application for $Cu_{12}Sb_4S_{13}$ is to use it as a $p^+$ contact in a TFSC, or as a hole injection layer for an OLED, or an organic TFSC. In addition, $Cu_{12}Sb_4S_{13}$ may be useful for facilitating formation of an ohmic contact to other types of p-type semiconductors. While the goal of this study is to develop new solar absorbers for a TFSC, the fabrication and characterization of $Cu_{12}Sb_4S_{13}$ thin films is discussed next in Sec. 6.2.1 to experimentally demonstrate its degenerate semicon-

ductor properties. Then, in Sec. 6.2.2, a strategy for reducing the degeneracy of $Cu_{12}Sb_4S_{13}$ thin films is explored.

### 6.2.1 Fabrication and characterization of $Cu_{12}Sb_4S_{13}$ thin films

Similar to the synthesis of $CuSbS_2$ and $Cu_3SbS_4$, sequential deposition of precursor layers using electron-beam evaporation was used to fabricate $Cu_{12}Sb_4S_{13}$ thin films. Precursor layer thicknesses were chosen to ensure a cation ratio of Cu:Sb = 3:1. A three-layer deposition process was used such that thin-films of $Sb_2S_3$/ Cu/ $Sb_2S_3$ (41 nm/ 48 nm/ 41 nm) were deposited using source materials purchased from Alfa Aesar onto fused silica glass substrates. The constituent stack was annealed in a tube furnace with flowing $CS_2$ gas at 295 °C for 30 min. X-ray diffraction patterns for a $Cu_{12}Sb_4S_{13}$ thin-film and the expected calculated pattern are shown in Fig. 6.21 and indicate a close match to reference peaks. The broad peak between 15 - 25° is due to the amorphous fused silica substrate. EPMA measurements of a $Cu_{12}Sb_4S_{13}$ thin film provided elemental ratios of Cu:Sb = 3.15:1 and S:Sb = 3.25:1, indicating a slightly Cu-rich film.

Absorption coefficient versus photon energy plots for several $Cu_{12}Sb_4S_{13}$ thin films ($\sim$ 200 nm) are shown in Fig. 6.22 All of these films have a band gap $E_G \sim 1.8$ eV, and exhibit strong absorption, consistent with the high calculated DOS for $Cu_{12}Sb_4S_{13}$. Figure 6.22 indicates that a maximum absorption coefficient of $\alpha = 3 \times 10^5$ cm$^{-1}$ is achieved within $E_G$ + 1.0 eV. However, these thin films exhibit significant sub-band gap absorption ($\alpha \sim 3 \times 10^4$ cm$^{-1}$) regardless of how they were processed. The origin of this strong sub-band gap absorption is related to the oxidation state of constituent Cu atoms in $Cu_{12}Sb_4S_{13}$. For charge balance, ten of the twelve Cu atoms in the chemical formula $Cu_{12}Sb_4S_{13}$ are monovalent, while the remaining two Cu atoms are divalent. The two divalent $Cu^{2+}$ atoms in $Cu_{12}Sb_4S_{13}$

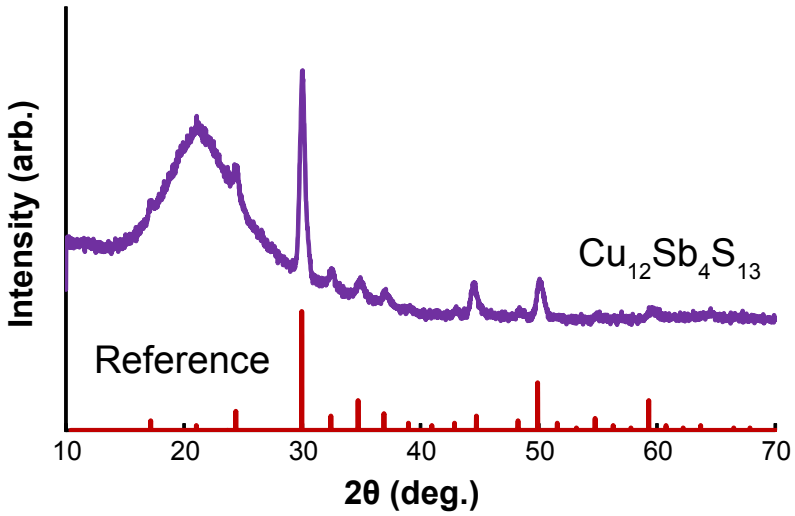


Figure 6.21: X-ray diffractogram for a $Cu_{12}Sb_4S_{13}$ thin-film compared with a simulated x-ray pattern for $Cu_{12}Sb_4S_{13}$, indicating a close match between the two patterns.

give rise to a high density of holes in the valence band, resulting in the p-type degenerate semiconductor behavior observed in the DOS plot (Fig. 6.20a). The p-type degenerate behavior of $Cu_{12}Sb_4S_{13}$ is consistent with the low measured resistivity ($\rho \sim 0.001$ - $0.004\ \Omega$ cm) and the low measured Seebeck coefficient ($S \sim 60\ \mu V\ K^{-1}$, or $N_A \sim 10^{20}\ cm^{-3}$).

As with $FeS_2$ in Chapter 5, optical measurements can be used to extract an estimate of the carrier concentration. A plot of the absorbance (A [unitless]) spectra (A = 1-T-R, where T and R are transmission and reflection spectra, respectively) for a $Cu_{12}Sb_4S_{13}$ thin film as a function of photon energy is shown in Fig. 6.23. The high carrier concentration gives rise to a characteristic peak in the absorbance spectrum seen in Fig. 6.23, indicative of free carrier absorption. The carrier concentration can be estimated from the value of the plasma

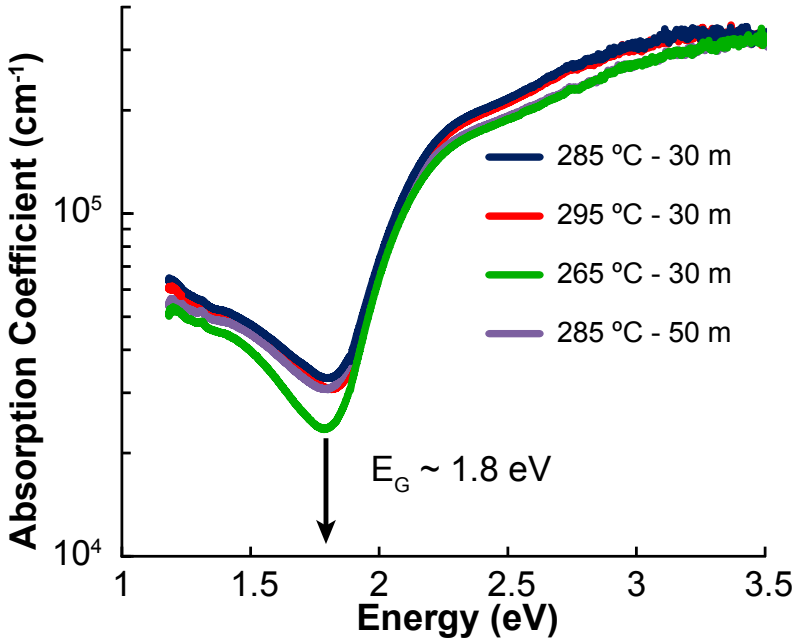


Figure 6.22: Absorption coefficient versus photon energy for several $Cu_{12}Sb_4S_{13}$ thin films. These films exhibit a band gap $E_G$ = 1.8 eV, however also show a significant sub-band gap absorption.

frequency (assuming $m^*$ = 1) as [11],

$$\omega_p = \frac{E_p}{h} = \sqrt{\frac{N q^2}{m^* M_e \varepsilon_0 \varepsilon_\infty}}, \tag{6.2a}$$

$$\varepsilon_\infty = 12.7 \times {E_G}^{-0.74} = 8.1, \tag{6.2b}$$

$$2.1 \times 10^{14}\,\text{Hz} = \sqrt{\frac{N q^2}{M_e \varepsilon_0 \times 8.1}}, \tag{6.2c}$$

$$\Rightarrow N = 1.2 \times 10^{20}\ [\text{cm}^{-3}]. \tag{6.2d}$$

$Cu_{12}Sb_4S_{13}$ thin-films thus exhibit a carrier concentration, $N_A > 10^{20}$ $cm^{-3}$, characteristic of an intrinsic degenerate semiconductor (no extrinsic doping), with thin films exhibiting high sub-band gap absorption and low resistivity. As mentioned earlier, the high carrier concentration makes $Cu_{12}Sb_4S_{13}$ unattractive for TFSC absorber applications. However, alternative applications such as a p-type contact layer are possible.

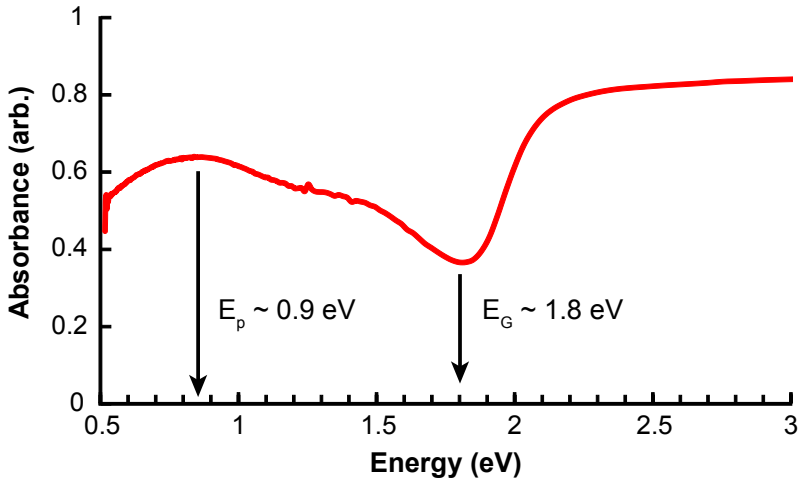


Figure 6.23: Absorbance spectra for a $Cu_{12}Sb_4S_{13}$ thin film. Two prominent features are evident, corresponding to the band gap at $E_G \sim 1.8$ eV and a characteristic peak indicative of free carrier absorption centered at the plasma frequency, $E_p \sim 0.9$ eV.

### 6.2.2 Reducing the carrier concentration in $Cu_{12}Sb_4S_{13}$

A strategy to engineer $Cu_{12}Sb_4S_{13}$ into a suitable TFSC absorber by reducing the carrier concentration is explored. Two of the twelve copper atoms in $Cu_{12}Sb_4S_{13}$ are $Cu^{2+}$ ions with a $3d^9$ electronic configuration. These $Cu^{2+}$ ions function as acceptors in $Cu_{12}Sb_4S_{13}$, providing a hole concentration $N_A \sim 10^{20}$ cm$^{-3}$. Replacing $Cu^{2+}$ with a transition metal having a 2+ oxidation state such as Mn or Zn would decrease the hole concentration, since $Mn^{2+}$ and $Zn^{2+}$ have $3d^5$ and $3d^{10}$ filled shell configurations, respectively. This reduction in the hole concentration moves the Fermi level from its degenerate position within the valence band upward in energy, to within the band gap. The chemical formula of a tetrahedrite substituted with a transition metal having a 2+ oxidation state is $Cu_{10}M_2Sb_4S_{13}$, with M = Mn, or Zn, and have a cation ratio (Cu:M:Sb) of 5:1:2. A similar reduction in hole concentration can be expected with In substitution, since $In^{3+}$ has a $4d^{10}$ filled shell configuration. The chemical formula for a tetrahedrite substituted with a Group III element is $Cu_{11}MSb_4S_{13}$ with a

cation ratio (Cu:M:Sb) of 11:1:4, with M = In. Electron-beam evaporation is used to deposit precursor layers of transition metal sulfide (or metal)/ Cu/ $Sb_2S_3$ thin films onto a fused silica substrate. The cation ratios along with the measured lattice parameters of the precursor layers were used to determine the layer thickness required to fabricate the tetrahedrite compounds. The following thicknesses were used:

- $Cu_{10}Mn_2Sb_4S_{13}$: MnS/ Cu/ $Sb_2S_3$ = 30/ 40/ 80 nm,
- $Cu_{10}Zn_2Sb_4S_{13}$: ZnS/ Cu/ $Sb_2S_3$ = 25/ 37/ 75 nm, and
- $Cu_{11}InSb_4S_{13}$: $In_2S_3$/ Cu/ $Sb_2S_3$ = 20/ 38/ 72 nm.

The as-deposited films were annealed in a tube furnace at 295 °C for 30 min with flowing $CS_2$ gas. Figure 6.24 compares the XRD patterns of the substituted tetrahedrites to $Cu_{12}Sb_4S_{13}$ and its reference pattern, indicating a close match. This demonstrates that tetrahedrite thin films can be fabricated by simply depositing precursor layers of the constituent elements followed by a post-deposition anneal. It is expected that the high diffusivity of copper facilitates layer intermixing, resulting in a thin film with a uniform composition. A cross-section of a $Cu_{10}Mn_2Sb_4S_{13}$ thin film ($\sim$ 200 nm) using scanning electron microscopy is shown in Fig. 6.25 and confirms that inter-mixing occurs as evident from the presence of large columnar grains extending through the thickness of the film. EPMA measurements of a $Cu_{10}Mn_2Sb_4S_{13}$ thin film yield relative composition ratio estimates of Cu:Mn = 5.13, Sb:Mn = 2.32, and S:Mn = 6.2, indicating an elemental composition slightly rich in Cu and Sb.

The variation in the Seebeck coefficient as a function of manganese content (x) in $Cu_{12-x}Mn_xSb_4S_{13}$ thin-films is shown in Fig. 6.26. The Seebeck coefficient increases from 60 $\mu$V/K for $Cu_{12}Sb_4S_{13}$ to 180 $\mu$V/K for $Cu_{10}Mn_2Sb_4S_{13}$, indicating a decrease in the hole

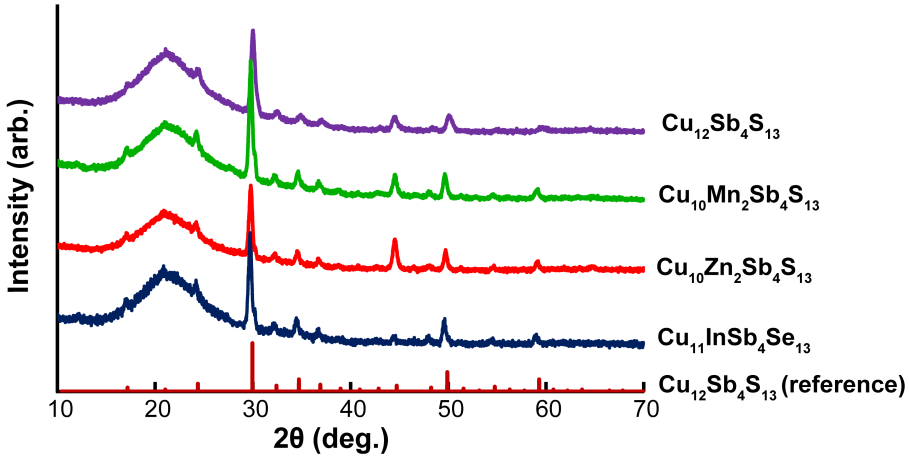


Figure 6.24: X-ray diffraction patterns for a $Cu_{12}Sb_4S_{13}$, $Cu_{10}Mn_2Sb_4S_{13}$, $Cu_{10}Zn_2Sb_4S_{13}$, $Cu_{11}InSb_4S_{13}$ thin-film. The observed x-ray spectrum is a close match to the reference $Cu_{12}Sb_4S_{13}$ spectra. The broad peak between 15 - 25 ° is due to the amorphous fused silica substrate.

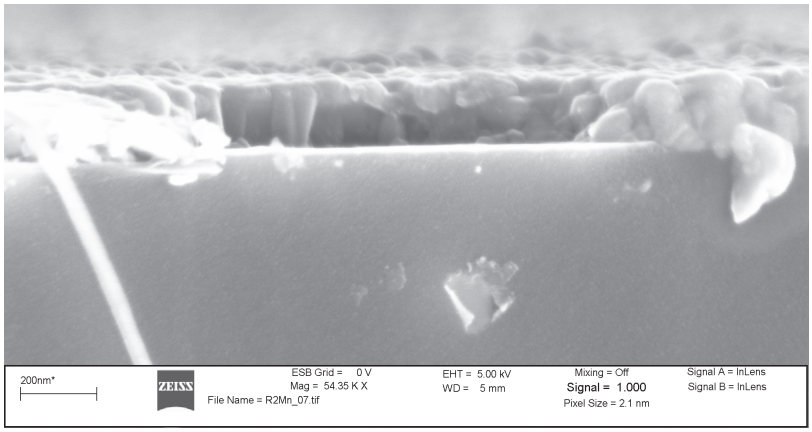


Figure 6.25: SEM cross-section of a $\sim$ 200 nm $Cu_{10}Zn_2Sb_4S_{13}$ thin film, showing large columnar grains.

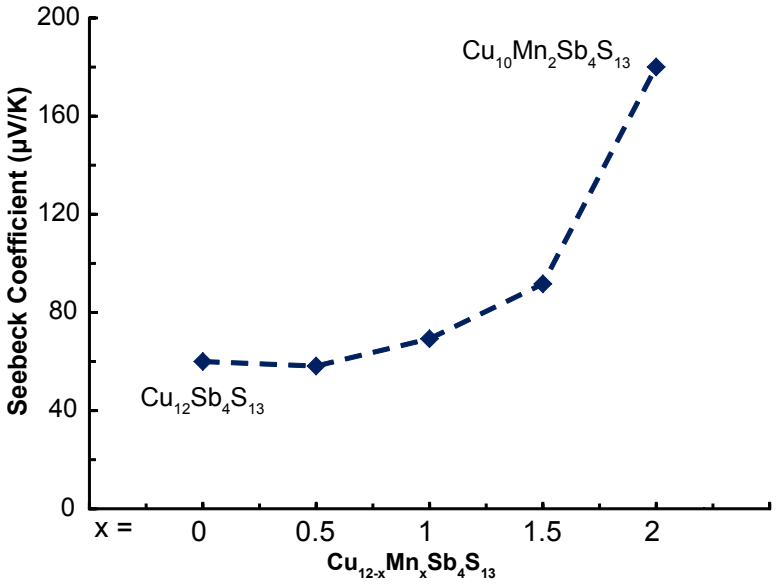


Figure 6.26: Seebeck coefficient as a function of Mn content (x) in $Cu_{12-x}Mn_xSb_4S_{13}$. $Cu_{12}Sb_4S_{13}$ has a low Seebeck coefficient, and correspondingly, a high hole concentration ($\sim 10^{20}$ cm$^{-3}$), while $Cu_{10}Mn_2Sb_4S_{13}$ exhibits a high Seebeck coefficient indicating a lower hole concentration ($\sim 10^{16}$ cm$^{-3}$).

concentration. Seebeck and resistivity measurements of a $Cu_{10}Zn_2Sb_4S_{13}$ thin film provided a Seebeck coefficient S $\sim$ 180 $\mu$V/K and resistivity of $\sim$ 10 $\Omega$ cm, similar to that of $Cu_{10}Mn_2Sb_4S_{13}$, indicating that Mn and Zn substitution lead to thin films with similar electrical properties. The resistivity of the Mn- and Zn-substituted tetrahedrites demonstrate an increase by four orders of magnitude compared to that of a $Cu_{12}Sb_4S_{13}$ thin film. This implies that the hole concentration of a $Cu_{10}Zn_2Sb_4S_{13}$ thin film is $N_A \sim 10^{16}$ cm$^{-3}$. Hall measurements did not provide conclusive results due to the high resistivity of the films, indicating a low hole concentration.

Absorption coefficient versus photon energy plots for Mn, Zn, and In-substituted tetrahedrite thin films are shown in Fig. 6.27 and are compared to $Cu_{12}Sb_4S_{13}$. The absorption coefficients of the substituted tetrahedrite thin films have a lower sub-band gap absorp-

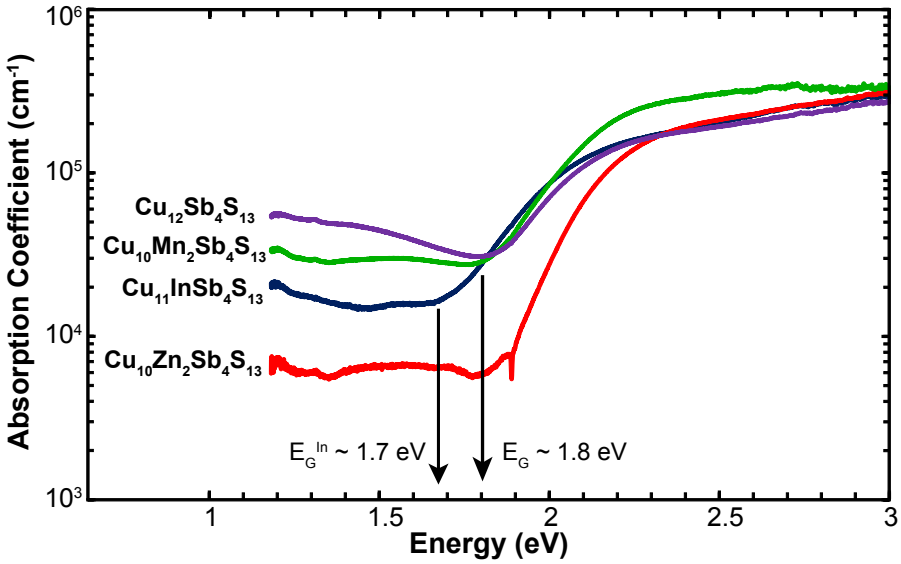


Figure 6.27: Absorption coefficient versus photon energy for $Cu_{12}Sb_4S_{13}$, $Cu_{10}Zn_2Sb_4S_{13}$, $Cu_{10}Mn_2Sb_4S_{13}$ thin films, all of which exhibit a band gap of $E_G \sim 1.8$ eV. The $Cu_{11}InSb_4S_{13}$ thin film, on the other hand exhibits a slightly lower band gap of $E_G \sim 1.7$ eV.

tion, and do not show evidence of free carrier absorption below the band-gap, confirming a reduced hole concentration in comparison to $Cu_{12}Sb_4S_{13}$. Figure 6.27 indicates that the $Cu_{10}Zn_2Sb_4S_{13}$, $Cu_{10}Mn_2Sb_4S_{13}$, and $Cu_{12}Sb_4S_{13}$ thin films all exhibit a band gap $E_G$ = 1.8 eV, while the $Cu_{11}InSb_4S_{13}$ thin film has a slightly reduced band gap $E_G \sim 1.7$ eV. Table 6.6 summarizes the optical and electrical properties of tetrahedrite thin-films. While the hole concentration is reduced in substituted tetrahedrites, the band gap is still larger than the optimal value (1.1 - 1.5 eV) required for a single junction TFSC. However, these higher band gap materials can be utilized in multi-junction tandem TFSCs, or other applications.

### 6.2.3 Band gap tuning in $Cu_{10}Zn_2Sb_4S_{13}$

While $Cu_{10}Zn_2Sb_4S_{13}$ exhibited strong optical absorption with a low sub-band gap absorption and a low hole concentration, the band gap was wider than that desired for a single junction TFSC. Since the band gap decreases going down the anion column of the periodic

| Composition | Band gap [eV] | Resistivity [Ω cm] | Seebeck Coefficient [$\mu$V K$^{-1}$] |
|---|---|---|---|
| $Cu_{12}Sb_4S_{13}$ | 1.83 | 0.001 | 60 |
| $Cu_{10}Mn_2Sb_4S_{13}$ | 1.83 | 9.5 | 180 |
| $Cu_{10}Zn_2Sb_4S_{13}$ | 1.82 | 10 | 180 |
| $Cu_{11}InSb_4S_{13}$ | 1.7 | 4.0 | 120 |

Table 6.6: Measured optical and electrical properties of tetrahedrite thin films.

table, e.g., $E_G^{ZnS}$ (3.7 eV [25]) >$E_G^{ZnSe}$ (2.8 eV [25]) >$E_G^{ZnTe}$ (2.4 eV [25]), replacing S with Se to form $Cu_{10}Zn_2Sb_4Se_{13}$ is expected to provide a suitable band gap for a single junction TFSC absorber. This is also clarified using the SSE scale [147]. The atomic SSE value for Se (-5.9 eV) is lower than S (-6.3 eV), so that the substitution of Se for S is expected to reduce the ionization potential (IP) as well as reduce the band gap. Electron-beam evaporation is used to deposit the following layers: ZnSe/ Cu/ Se/ $Sb_2Se_3$ (25/ 32/ 36/ 75 nm) followed by a post-deposition anneal in an evacuated sealed fused-silica tube at 295 °C for 30 min. The x-ray diffraction patterns for $Cu_{10}Zn_2Sb_4S_{13}$ and $Cu_{10}Zn_2Sb_4Se_{13}$ which are shown in Fig. 6.28, are similar to the other tetrahedrite thin films (e.g., Fig. 6.24) and are closely matched to the $Cu_{12}Sb_4S_{13}$ reference peak.

Figure 6.29 compares the measured absorption coefficient as a function of photon energy for $Cu_{10}Zn_2Sb_4S_{13}$ and $Cu_{10}Zn_2Sb_4Se_{13}$ thin films and shows that the band gap is shifted to a lower energy value of $E_G \sim 1.4$ eV, which is within the desired range of a TFSC absorber. In addition, the $Cu_{10}Zn_2Sb_4Se_{13}$ thin film exhibits exceptionally strong absorption, reaching $\alpha = 3 \times 10^5$ cm$^{-1}$ within $E_G$+0.6 eV. It should be noted that the absorption strength

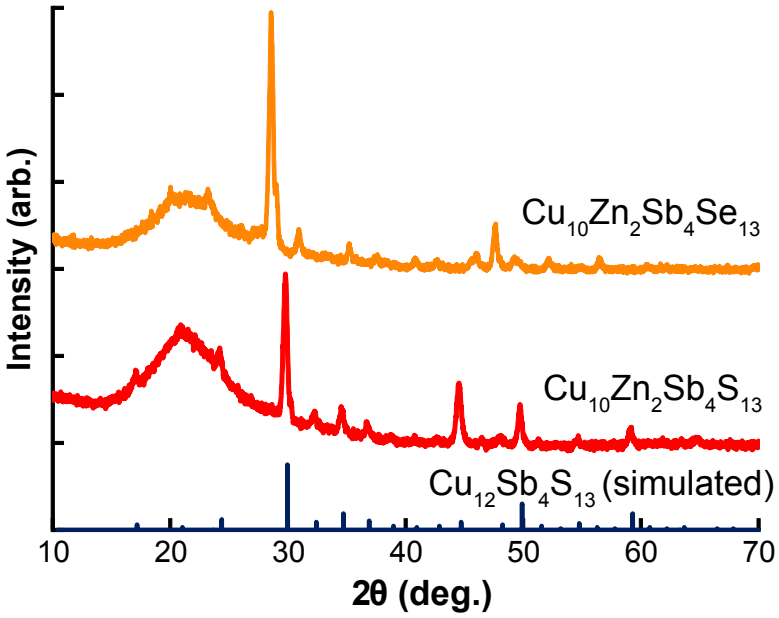


Figure 6.28: X-ray diffraction patterns of a $Cu_{10}Zn_2Sb_4Se_{13}$ and $Cu_{10}Zn_2Sb_4S_{13}$ thin film in comparison to $Cu_{12}Sb_4S_{13}$.

for the $Cu_{10}Zn_2Sb_4Se_{13}$ thin film is stronger than that of current state-of-the-art solar absorber materials, e.g., it is an order of magnitude higher than CdTe. To determine the band gap type, a plot of $\alpha$ v.s. $E^{1/2}$ (direct) and $\alpha$ v.s. $E^2$ (indirect) for a $Cu_{10}Zn_2Sb_4Se_{13}$ thin film is shown in the inset of Fig. 6.29 and indicates that the fundamental band gap in $Cu_{10}Zn_2Sb_4Se_{13}$ is indirect at E = 1.42 eV, while a direct band occurs at E = 1.43 eV. Thus, the fundamental band gap in $Cu_{10}Zn_2Sb_4Se_{13}$ is indirect, although a direct band gap is positioned very close in energy ($\sim$ 0.01 eV).

Electrical characterization of a $Cu_{10}Zn_2Sb_4Se_{13}$ thin film provided a resistivity of $\sim$ 10 $\Omega$ cm, with a Seebeck coefficient S $\sim$ 280 $\mu$V/K. Thin films fabricated via sequential deposition of precursor layers via electron-beam evaporation demonstrated the viability of forming tetrahedrite thin films. However, the absorption coefficient for the $Cu_{10}Zn_2Sb_4Se_{13}$ thin film shown in Fig. 6.29 exhibits rather high sub-band gap absorption ($\alpha \sim 2 \times 10^4$

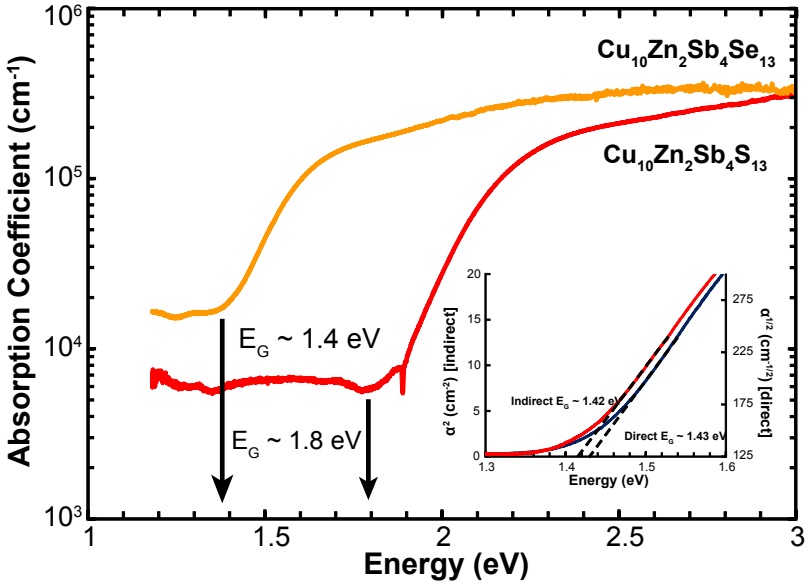


Figure 6.29: Absorption coefficient versus photon energy plot for a $Cu_{10}Zn_2Sb_4S_{13}$ thin film which exhibits a band gap $E_G \sim 1.8$ eV, and for a $Cu_{10}Zn_2Sb_4Se_{13}$ thin film which has a band gap $E_G \sim 1.4$ eV. (inset) Band gap type for plots a $Cu_{10}Zn_2Sb_4Se_{13}$ thin film. An indirect band gap is observed at $E_G \sim 1.42$ eV, while the direct band gap is at $E_G \sim 1.43$ eV.

$cm^{-1}$). This could be due to a non-optimized deposition process. Alternative deposition techniques such as RF magnetron sputtering could be pursued in order to to reduce the level of sub-band gap absorption.

### 6.2.4 $Cu_{10}Zn_2Sb_4Se_{13}$ as a TFSC absorber layer

To demonstrate the photovoltaic capabilities of a $Cu_{10}Zn_2Sb_4Se_{13}$-based TFSC, measured material properties from Table 6.7 and the absorption coefficient plot from Fig. 6.29 are used as inputs to SCAPS. A hole concentration of $N_A = 2 \times 10^{16}$ $cm^{-3}$ is used along with carrier mobilities of $\mu_n$; $\mu_p$ = 50; 14 $cm^2V^{-1}s^{-1}$, respectively. The TFSC device configuration is identical to that used in previous simulations and is shown in the inset of Fig. 6.30 (a). In addition, a minority carrier lifetime ($\tau$) of 1 ns (or $N_T = 10^{14}$ $cm^{-3}$) is used in the simulations, unless mentioned otherwise. A complete list of parameters is listed in Table 6.7. The

| General Device Properties | | | | |
|---|---|---|---|---|
| Parameter | Front Contact | | Back Contact | |
| $\phi_b$ [eV] | $\phi_{bn} = 0.1$ | | $\phi_{bp} = 0.3$ | |
| WF [eV] | 4.1 | | 5.1 | |
| $S_n$ [cm-s$^{-1}$] | $10^7$ | | $10^7$ | |
| $S_p$ [cm-s$^{-1}$] | $10^7$ | | $10^7$ | |
| Reflectivity | 0.1 | | 0.8 | |
| **Layer Properties** | | | | |
| Parameter | $SnO_2$ | CdS | $Cu_{10}Zn_2Sb_4Se_{13}$ | $p^+$-$Cu_{10}Zn_2Sb_4Se_{13}$ |
| W [nm] | 500 | 25 | variable | 100 |
| $\varepsilon/\varepsilon_0$ | 9 | 10 | 8.1 | 8.1 |
| $\mu_n$ [cm$^2$-s$^{-1}$] | 100 | 100 | 50 | 50 |
| $\mu_p$ [cm$^2$-s$^{-1}$] | 25 | 25 | 14 | 14 |
| n (or p) [cm$^{-3}$] | n: $10^{17}$ | n: $10^{17}$ | p: $10^{16}$ | $p^+$: $10^{18}$ |
| $E_G$ [eV] | 3.6 | 2.4 | 1.4 | 1.4 |
| $N_C$ [cm$^{-3}$] | $2.2\times10^{18}$ | $2.2\times10^{18}$ | $8\times10^{17}$ | $8\times10^{17}$ |
| $N_V$ [cm$^{-3}$] | $1.8\times10^{19}$ | $1.8\times10^{19}$ | $1.8\times10^{19}$ | $1.8\times10^{19}$ |
| **Mid-gap Trap State Properties** | | | | |
| Parameter | $SnO_2$ | CdS | $Cu_{10}Zn_2Sb_4Se_{13}$ | $p^+$-$Cu_{10}Zn_2Sb_4Se_{13}$ |
| $N_D$, $N_A$ [cm$^{-3}$] | A: $10^{15}$ | A: $10^{18}$ | D: variable | D: $10^{14}$ |
| $\sigma_n$ [cm$^2$] | $10^{-12}$ | $10^{-15}$ | $10^{-12}$ | $10^{-12}$ |
| $\sigma_p$ [cm$^2$] | $10^{-15}$ | $10^{-12}$ | $10^{-15}$ | $10^{-15}$ |

Table 6.7: Material parameters used for tetrahedrite-based TFSC simulations.

strong onset of absorption in $Cu_{10}Zn_2Sb_4Se_{13}$ along with the absorption coefficient reaching a maximum of $3 \times 10^5$ cm$^{-1}$ at $E_G$ + 0.6 eV suggests that the thickness of the absorber layer can be reduced to less than 1 $\mu$m enabling an ultra-thin drift based TFSC.

To understand the minimum thickness required for a $Cu_{10}Zn_2Sb_4Se_{13}$ TFSC, the simulated variation in device efficiency as a function of absorber layer thickness is shown in Fig. 6.30(a). Efficiencies greater than 20% can be achieved even when the absorber layer thickness is reduced to 300 nm, confirming that a material exhibiting a strong onset coupled with high absorption can indeed provide for an ultra-thin high efficiency TFSC. For thicknesses greater than 500 nm, the efficiency reduces slightly before saturating, since the absorber thickness is greater than the absorption length. As a result, minority carriers electrons have to diffuse towards the edge of the space charge region before getting swept by the built-in field, thereby increasing recombination and decreasing device efficiency. In addition, a minority carrier lifetime of $\tau$ = 1 ns (or $N_T = 10^{14}$ cm$^{-3}$) was used in this simulation, indicating that a TFSC with an efficiency $\eta$ >20% can be achieved without requiring a low-defect material. The thickness requirement for a $Cu_{10}Zn_2Sb_4Se_{13}$ TFSC absorber (300 - 500 nm) is considerably lower than that for a c-Si (20 - 260 $\mu$m [23], [35]), CIGS ($\sim$ 1.5 - 2 $\mu$m [27]) or CdTe (2 - 4 $\mu$m [5]) based solar cell, and is similar to that of an amorphous silicon-based TFSC (300 - 500 nm [41]). However, amorphous silicon is inherently unstable due to the Stabler-Wronski effect [41] as decribed in Ch. 2. As a result, a $Cu_{10}Zn_2Sb_4Se_{13}$ TFSC can have a similar thickness requirement as that of an amorphous silicon-based TFSC, however, with improved performance. Figure. 6.30(b) shows a plot of the simulated quantum efficiency (QE) as a function of $Cu_{10}Zn_2Sb_4Se_{13}$ absorber thickness ($L_A$). The strong absorption coefficient leads to a QE approaching 90% between $\lambda$ = 530 - 770 nm, indica-

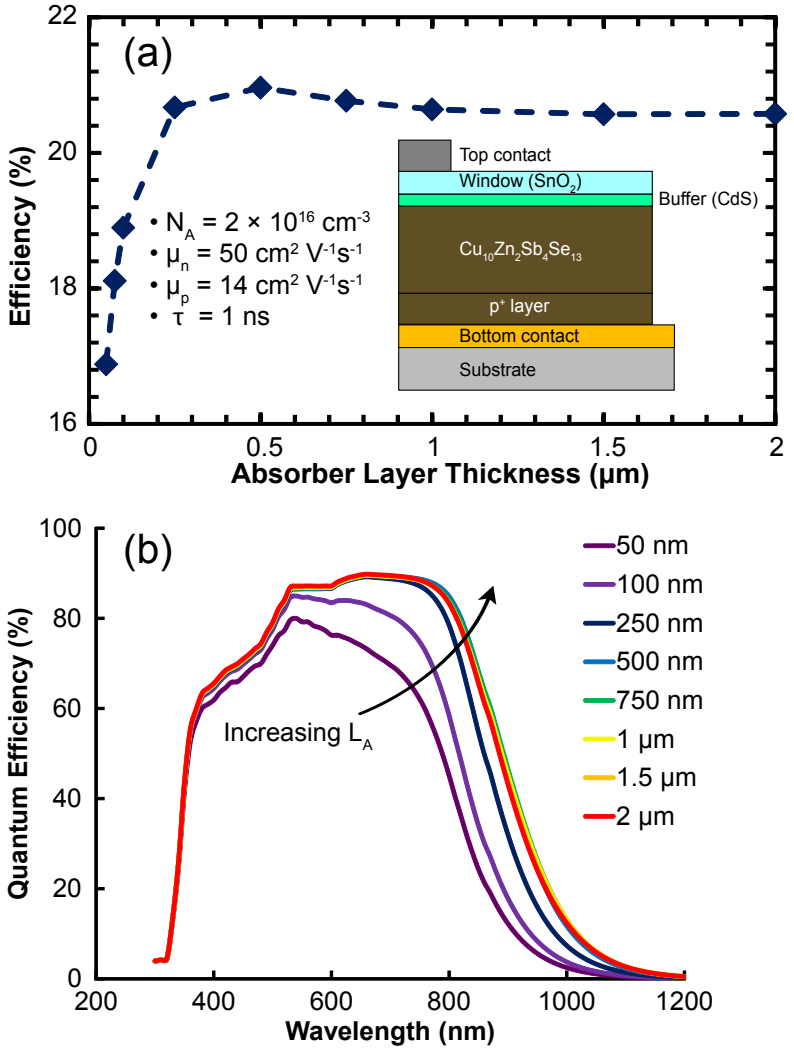


Figure 6.30: (a) Variation in simulated efficiency as a function of $Cu_{10}Zn_2Sb_4Se_{13}$ absorber layer thickness. Efficiencies greater than 20% can be achieved with an absorber layer thickness between 300 - 500 nm. (b) Simulated QE as a function of absorber layer thickness. A maximum of $\sim$ 90% is obtained for $L_A$ = 300 nm, between $\lambda$ = 530 - 770 nm. The QE saturates for $L_A$ greater than 250 nm, and the curves are identical.

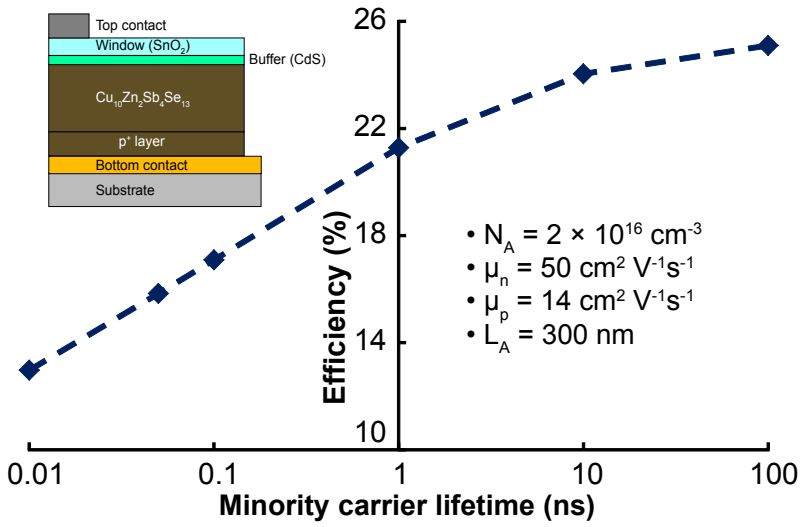


Figure 6.31: Variation in simulated efficiency as a function of minority carrier lifetime in the $Cu_{10}Zn_2Sb_4Se_{13}$ absorber layer.

tive of a strong spectral response. In addition, for $L_A$ greater than 500 nm, the QE curves are identical, indicating that a thickness of 300 - 500 nm is sufficient to fully absorb the solar spectrum. A thickness of 300 nm for the $Cu_{10}Zn_2Sb_4Se_{13}$ absorber layer is used in subsequent simulations.

Figure 6.31 shows the variation in photoconversion efficiency as a function of minority carrier lifetime for a 300 nm thick $Cu_{10}Zn_2Sb_4Se_{13}$ absorber layer. While a lifetime of $\tau$ = 1 ns (or $N_T = 10^{14}$ cm$^{-3}$) provided an efficiency of $\sim$ 21%, increasing the lifetime to $\tau$ = 100 ns (or $N_T = 10^{12}$ cm$^{-3}$) leads to a 25% efficient TFSC. Utilizing additional techniques not considered in this simulation such as light trapping and anti-reflective coatings can potentially improve the efficiency beyond 25%, giving TFSCs a competitive edge compared to silicon solar cells. In addition, Fig. 6.31 indicates that even with a low minority minority carrier lifetime of $\tau$ = 0.01 ns (or $N_T = 10^{16}$ cm$^{-3}$), i.e., a highly defective absorber layer, a 13% efficient TFSC is simulated. This suggests that a drift-based $Cu_{10}Zn_2Sb_4Se_{13}$ TFSC

is more defect tolerant than a comparable diffusion-based TFSC. The strong absorption of $Cu_{10}Zn_2Sb_4Se_{13}$ allows the absorber thickness to be reduced so that it operates as a drift cell, leading to improved defect tolerance.

Since Hall measurements provided inconclusive results for $Cu_{10}Zn_2Sb_4Se_{13}$, assumed carrier mobilities of $Cu_3SbS_4$ ($\mu_n$; $\mu_p = 50$; 14 $cm^2\ V^{-1}\ s^{-1}$) were used in the previous simulation. To understand the variation in performance with lower carrier mobilities, an alternative set of mobilities, $\mu_n$; $\mu_p$ = 10; 1 $cm^2\ V^{-1}\ s^{-1}$ is also simulated. The simulated variation in device efficiency as a function of $Cu_{10}Zn_2Sb_4Se_{13}$ layer thickness ($L_A$) for the lower mobility case, is shown in Fig. 6.32 (a). A maximum of 20% is observed for an absorber layer thickness of 250 nm, beyond which the efficiency reduces slightly before saturating at 19.4% for $L_A > 500$ nm. This lends support to the idea that a material with low carrier mobilities can be used to fabricate a high efficiency TFSC, as long as the absorber layer is sufficiently thin to allow for drift-based operation. Figure 6.32 (b) shows the simulated quantum efficiency as a function of $Cu_{10}Zn_2Sb_4Se_{13}$ absorber layer thickness for the lower mobility case, and indicates that a thickness of 250 nm is sufficient to fully absorb the solar spectrum. For absorber layer thicknesses greater than 250 nm, the QE curves are identical and overlap. Thus, even with lower carrier mobilities, a $Cu_{10}Zn_2Sb_4Se_{13}$ TFSC only requires 250 - 300 nm to provide an efficiency of $\sim$ 20%.

The variation is photoconversion efficiency as a function of minority carrier lifetime for a 300 nm thick $Cu_{10}Zn_2Sb_4Se_{13}$ absorber layer with low carrier mobilities ($\mu_n$; $\mu_p$ = 10; 1 $cm^2\ V^{-1}\ s^{-1}$) is shown in Fig. 6.33. It indicates that with $\tau$ = 1 ns (or $N_T = 10^{14}\ cm^{-3}$), an efficiency $\eta$ = 20% can be obtained, while improving the minority carrier lifetime to $\tau$ = 100 ns (or $N_T = 10^{12}\ cm^{-3}$) can provide for a 25% efficient TFSC. With a low minority

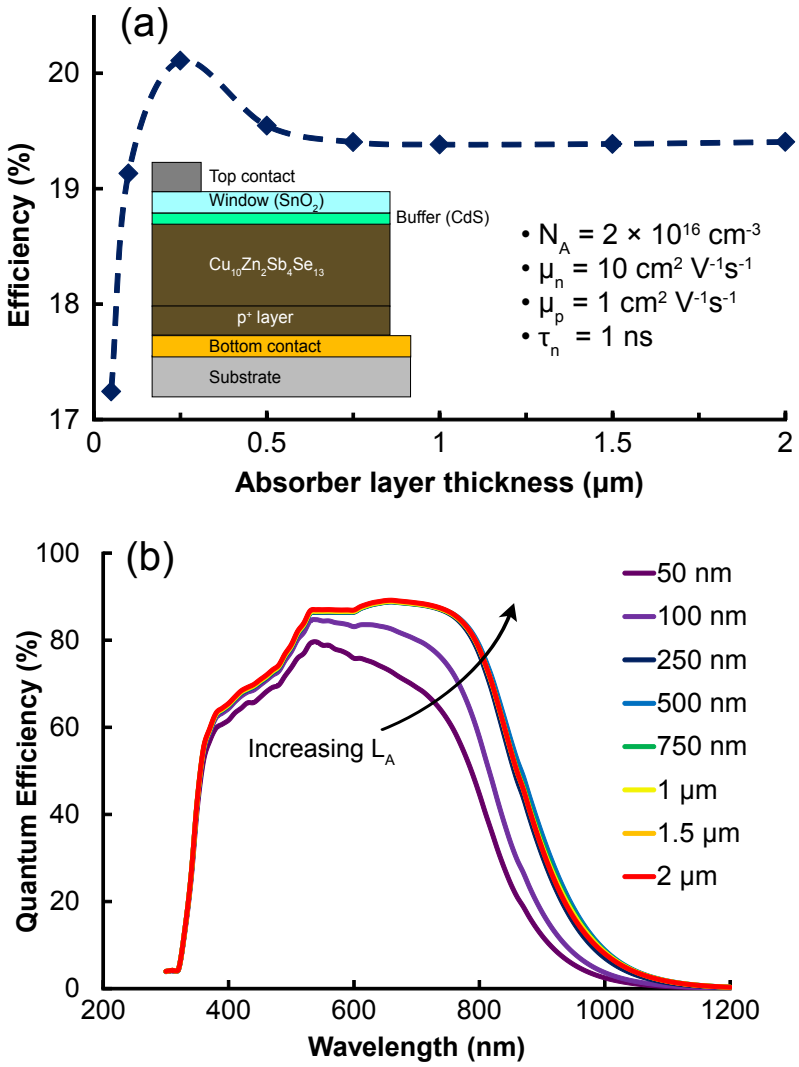


Figure 6.32: (a) Variation in simulated efficiency as a function of $Cu_{10}Zn_2Sb_4Se_{13}$ absorber layer thickness for carrier mobilities, $\mu_n$; $\mu_p$ = 10; 1 $cm^2$ $V^{-1}$ $s^{-1}$. An efficiency of 20% can be achieved with an absorber layer thickness of 250 nm. (b) Simulated QE as a function of absorber layer thickness. A maximum of $\sim$ 90% is obtained for $L_A$ = 250 nm, between $\lambda$ = 530 - 770 nm. The QE saturates for $L_A$ greater than 250 nm, and the curves are identical.

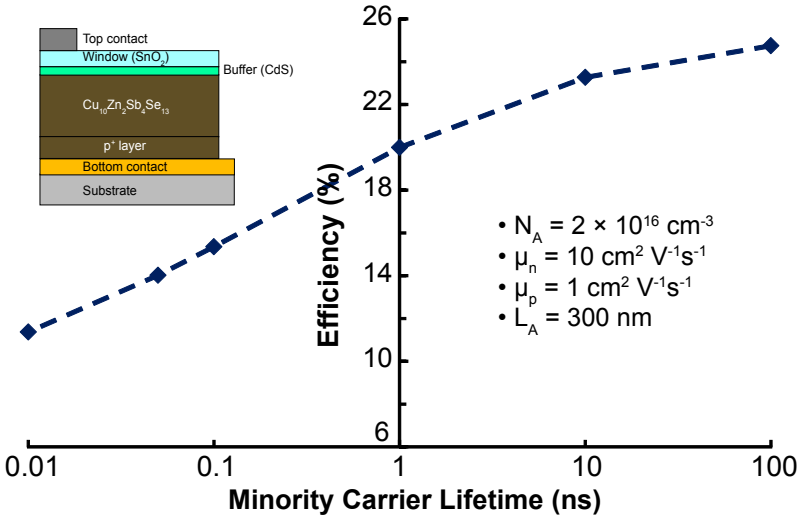


Figure 6.33: Variation in simulated efficiency as a function of minority carrier lifetime in the $Cu_{10}Zn_2Sb_4Se_{13}$ absorber layer.

carrier lifetime of $\tau$ = 0.01 ns (or $N_T = 10^{16}$ cm$^{-3}$), an efficiency of $\eta$ = 11% is simulated. These efficiencies are similar to the high mobility simulations (see Fig. 6.31) confirming the assertion that a strong absorber in a drift-cell configuration is more tolerant in terms of low mobility and low lifetime materials. Table. 6.8 summarizes device simulation results ($\tau$ = 1 ns) for $Cu_3SbS_4$, $CuSbS_2$, and $Cu_{10}Zn_2Sb_4Se_{13}$ in order to highlight the necessary absorber layer properties required to achieve a TFSC with an efficiency $\eta >$15%.

In conclusion, this section described the design and fabrication of new tetrahedrite compounds exhibiting exceptionally strong absorption with an abrupt onset of absorption. Tetrahedrite compounds contain isolated Sb atoms with a $s^2p^0$ low valence electronic configuration. This provides narrow bands near the CBM and VBM, enhancing the total JDOS such that these compounds exhibit strong optical absorption with an abrupt onset near the band gap. $Cu_{10}Zn_2Sb_4Se_{13}$, in particular, has a band gap of $E_G$ = 1.36 eV, with a maximum absorption coefficient value of $3 \times 10^5$ cm$^{-1}$ at $E_G$ + 0.6 eV. TFSC device simulations

| Property | $Cu_3SbS_4$ | $CuSbS_2$ | $Cu_{10}Zn_2Sb_4Se_{13}$ |
|---|---|---|---|
| Band Gap [eV] | 0.9 | 1.4 | 1.36 |
| Thickness [$\mu$m] | 0.5 - 0.75 | 1 - 1.5 | 0.25 - 0.3 |
| Carrier concentration [$cm^{-3}$] | $1 \times 10^{16}$ $cm^{-3}$ | $1 \times 10^{14}$ $cm^{-3}$ | $1 \times 10^{16}$ $cm^{-3}$ |
| Carrier mobility [$cm^2\,V^{-1}\,s^{-1}$] | $\mu_n$ =50; $\mu_p = 14$ | $\mu_n$ =10; $\mu_p = 1$ | $\mu_n$ =50; $\mu_p = 14$ |
| Minority carrier lifetime [ns] | 1 ($N_T = 10^{14}$ $cm^{-3}$) | 1 | 1 |
| Efficiency [%] | 19 | 16 | 21 |

Table 6.8: Required material parameters for a $CuSbS_2$, a $Cu_3SbS_4$, or a $Cu_{10}Zn_2Sb_4Se_{13}$-based TFSC to achieve a simulated efficiency $\eta > 15\%$.

predict photoconversion efficiencies above 20% can be achieved in a TFSC with a 300 nm thick $Cu_{10}Zn_2Sb_4Se_{13}$ absorber layer. Strong absorption coupled with a tunable band gap (1.36 - 1.8 eV) and fabrication temperatures less than 300 °C make the tetrahedrite family of materials especially attractive for TFSC absorber applications. $Cu_{10}Zn_2Sb_4Se_{13}$ is only one example of a large class of possible tetrahedrite compounds. Exploring related materials may provide further opportunities to develop a new generation of high-performance single-junction and tandem TFSCs with ultra-thin absorber layers.

## 6.3 Conclusions

In this chapter, two families of Cu-based absorbers, Cu-V-VI compounds and tetrahedrites are explored as novel solar absorber materials. Using design paradigms aimed at engineering a material to have an enhanced JDOS, $CuSbS_2$ and $Cu_3SbS_4$ thin films were first explored. $CuSbS_2$ is an indirect band gap semiconductor with $E_G$ = 1.4 eV with a low hole

mobility ($\mu_p \sim 1$ cm$^2$ V$^{-1}$ s$^{-1}$). $Cu_3SbS_4$ on the other hand is a direct band gap semiconductor with $E_G$ = 0.9 eV, an absorption coefficient with an abrupt onset of absorption near the band gap, reaching $\alpha = 2 \times 10^5$ cm$^{-1}$ at $E_G$+1.2 eV. Sputtered thin-films exhibited a hole concentration $N_A \sim 10^{17}$ cm$^{-3}$ and a hole mobility $\mu_p \sim 15$ cm$^2$ V$^{-1}$ s$^{-1}$. TFSC device simulations of $Cu_3SbS_4$ indicated that an efficiency of 19% can be achieved with an absorber layer thickness between 500 - 750 nm, assuming a minority carrier lifetime of 1 ns.

$Cu_{12}Sb_4S_{13}$ thin-films exhibited a band gap $E_G$ = 1.8 eV, higher than optimal for a single-junction solar absorber. In spite of the high band gap, the absorption coefficient was measured to be $\alpha = 3 \times 10^5$ cm$^{-1}$ at $E_G$+0.6 eV, which is an order of magnitude higher than that of CdTe. However, $Cu_{12}Sb_4S_{13}$ is a p-type, degenerate ($N_A > 10^{20}$ cm$^{-3}$) semiconductor, which makes it unsuitable for use as a solar absorber. The carrier concentration was then reduced by substituting Zn or Mn, yielding $Cu_{10}Zn_2Sb_4S_{13}$ and $Cu_{10}Mn_2Sb_4S_{13}$. Thin films of these compounds retained strong optical absorption with a band gap $E_G$ = 1.8 eV. However, the carrier concentration was reduced to $N_A \sim 10^{16}$ cm$^{-3}$. Selenium was substituted for sulfur to reduce the band gap to $E_G$ = 1.36 eV in $Cu_{10}Zn_2Sb_4Se_{13}$. TFSC device simulations suggest that efficiencies greater than 20% can be achieved even with the absorber layer thickness is reduced to 300 nm, giving rise to a potential new solar absorber material for high efficiency ultra-thin single junction TFSCs utilizing drift-based transport to effectively extract photogenerated carriers. Only the photovoltaic capability of tetrahedrites as an absorber layer was explored in this study. $Cu_{12}Sb_4S_{13}$, as a p-type, degenerate semiconductor can be utilized as a p-type contact layer to facilitate the formation of a drift-based TFSC and as an ohmic contact layer to other p-type semiconductors. Thin films of tetrahedrite compounds can also be extended to applications beyond solar cells.

# 7. CONCLUSIONS AND RECOMMENDATIONS FOR FUTURE WORK

The objective of this research is to develop next-generation TFSCs utilizing ultra-thin absorbers. The relationship between the absorption strength (absorption coefficient, $\alpha$) and absorber layer material properties including device operation mode is explored first. Improving the absorption strength beyond that of current solar absorbers ($\alpha > 1\times10^5$ cm$^{-1}$) allows for a drift-based TFSC incorporating an ultra-thin absorber ($<1$ $\mu$m). TFSC simulations indicate that the strong built-in drift field aids carrier separation and extraction such that a low-mobility, low minority carrier lifetime (high concentration of mid-gap defects) can still provide a TSFC with high efficiency. The limitations of iron-based absorbers such $FeS_2$ and $Fe_2GeS_4$ are discussed. Copper based absorbers such as $CuSbS_2$, $Cu_3SbS_4$, and tetrahedrite compounds are then explored. $Cu_3SbS_4$ and $Cu_{10}Zn_2Sb_4Se_{13}$ are considered to be promising candidate materials for an ultra-thin drift-based TFSC.

## 7.1 Conclusions

### 7.1.1 TFSC device simulations

Current CdTe and CIGS-based TFSCs utilize thick absorbers (2 - 4 $\mu$m). For efficient carrier extraction in these TFSCs, carrier mobilities and minority carrier lifetime need to be large. This requires a high purity, defect-free absorber layer leading to expensive manufacturing costs. Increasing the absorption strength compared to that of current absorbers not only increases the overall efficiency, but also enables use of an ultra-thin ($<1$ $\mu$m) absorber since less material is required to absorb the full solar spectrum. When the thickness of the absorber is comparable to the depletion width of the TFSC, the device operation mode is close to that of drift, over a wide range of carrier concentrations ($10^{14}$ - $10^{17}$ cm$^{-3}$). The strong built-in

drift field across a thin absorber enhances carrier extraction such that an absorber with low carrier mobilities and a high concentration of mid-gap defects can provide a TFSC with an efficiency >15%.

### 7.1.2 Iron-based absorbers

$FeS_2$ thin films are fabricated using RF magnetron sputtering from an FeS target followed by a post-deposition anneal in the presence of sulfur powder at 550 °C. $FeS_2$ thin films are p-type, and exhibit a high hole concentration ($>10^{20}$ $cm^{-3}$) with a low hole mobility (2 - 3 $cm^2$ $V^{-1}$ $s^{-1}$). Optically, $FeS_2$ thin films have a band gap of $E_G \sim 0.95$ eV (indirect), reaching an absorption of $\alpha = 5 \times 10^5$ $cm^{-1}$ at $E_G$+1.8 eV, but exhibit a rather large sub-band gap absorption. Theoretical calculations indicate that sulfur vacancies easily form at the surface of an $FeS_2$ thin film and sulfur-deficient phases spontaneously form if insufficient sulfur is provided during film growth. While $FeS_2$ exhibits strong optical absorption, the spontaneous decomposition into sulfur-deficient phases is detrimental for solar absorber applications.

To retain the strong optical absorption in $FeS_2$ but prevent decomposition, $Fe_2GeS_4$ (FGS) is identified, and thin films are fabricated using RF magnetron sputtering followed by a post-deposition anneal in $GeS_2$ at 500 °C. Electrical characterization of FGS thin films is inhibited by the strong tendency of the films to react and delaminate from any bottom metal contact during the anneal step. Dynamic SIMS indicates the presence of oxygen uniformly distributed throughout the FGS thin-film, which is mitigated by adding a small amount of zirconium powder in addition to $GeS_2$ during the anneal. FGS thin films exhibit a band gap $E_G$ = 1.45 eV (indirect) with an absorption of $\alpha = 1 \times 10^5$ $cm^{-1}$ at $E_G$+1 eV, indicating a sluggish, non-abrupt onset of absorption. SCAPS simulations indicate that a 13% efficient TFSC can be achieved using a 1 - 1.5 $\mu$m FGS absorber layer with a carrier concentration

$N_A = 2 \times 10^{16}$ cm$^{-3}$, carrier mobilities $\mu_n$ =1; $\mu_p = 0.1$ cm$^2$ V$^{-1}$ s$^{-1}$ and a minority carrier lifetime $\tau$ = 10 ns. The sluggish absorption coefficient, difficulties in achieving a robust bottom contact and a low (13%) simulated efficiency with a rather thick absorber layer (1 - 1.5 $\mu$m), makes FGS an unsuitable candidate for a high performance ultra-thin TFSC application.

### 7.1.3 Copper-based absorbers

Copper-based absorbers within the Cu-V-VI (V = Sb, Bi; VI = S, Se) family such as $CuSbS_2$ and $Cu_3SbS_4$ are explored. These are identified as high absorption materials based on the computed density of states which indicates that a localized Sb-derived conduction band increases the JDOS (refer to Ch. 6). Thin films of $CuSbS_2$ and $Cu_3SbS_4$ are fabricated by sequential deposition of Cu and $Sb_2S_3$ using electron-beam evaporation followed by an anneal at 300 °C in the presence of $CS_2$ gas. $CuSbS_2$ is p-type with a hole concentration $N_A$ = $10^{17}$ cm$^{-3}$ and a hole mobility, $\mu_p$ = 0.1 cm$^2$ V$^{-1}$s$^{-1}$. $CuSbS_2$ exhibits a band gap $E_G$ = 1.4 eV (indirect), but has a non-abrupt onset of absorption near the band gap reaching $\alpha$ = $1 \times 10^5$ cm$^{-1}$ at $E_G$+0.9 eV. $Cu_3SbS_4$ thin films are also p-type with a hole concentration $N_A$ = $10^{18}$ cm$^{-3}$ and a hole mobility, $\mu_p$ = 15 cm$^2$ V$^{-1}$s$^{-1}$. A 2 inch $Cu_3SbS_4$ sputter target purchased from Kurt Lesker provides thin films with a carrier concentration, $N_A \sim 10^{17}$ cm$^{-3}$ and a hole mobility of $\mu_p \sim$ 15 cm$^2$ V$^{-1}$s$^{-1}$. $Cu_3SbS_4$ has a band gap $E_G$ =0.9 eV (direct), and exhibits an abrupt onset of absorption at the band gap, reaching $\alpha$ = $1 \times 10^5$ cm$^{-1}$ at $E_G$+0.6 eV.

SCAPS simulations indicate that a 1 $\mu$m thick $CuSbS_2$ absorber, with a carrier concentration of $2 \times 10^{14}$ cm$^{-3}$, a minority carrier lifetime of 1 ns ($N_T = 10^{14}$ cm$^{-3}$) and carrier mobilities, $\mu_n$, $\mu_p$ = 10, 1 cm$^2$ V$^{-1}$ s$^{-1}$ provides a 16% efficient TFSC. A $Cu_3SbS_4$-based TFSC, on the other hand, only requires an absorber layer between 500 - 750 nm, carrier con-

centration $N_A = 2 \times 10^{16}$ cm$^{-3}$, with a minority carrier lifetime of 1 ns ($N_T = 10^{14}$ cm$^{-3}$), and carrier mobilities of $\mu_n$, $\mu_p$ = 50 and 14 cm$^2$ V$^{-1}$ s$^{-1}$, to provide a 19% efficienct TFSC.

$Cu_{12}Sb_4S_{13}$ is investigated since its calculated DOS is higher compared to that of $CuSbS_2$ and $Cu_3SbS_4$, indicating the potential for strong optical absorption. $Cu_{12}Sb_4S_{13}$ thin films are fabricated via sequential deposition of Cu and $Sb_2S_3$, followed by a post-deposition anneal at 295 °C in the presence of $CS_2$ gas. $Cu_{12}Sb_4S_{13}$ has a band gap $E_G$ =1.8 eV, with a maximum absorption of $\alpha = 3 \times 10^5$ cm$^{-1}$ achieved within $E_G$+1.0 eV. However, these thin films exhibit significant sub-band gap absorption and high carrier concentration ($\sim 10^{20}$ cm$^{-3}$). Divalent $Cu^{2+}$ atoms in $Cu_{12}Sb_4S_{13}$ give rise to a high density of holes in the valence band, resulting in a p-type degenerate semiconductor, making $Cu_{12}Sb_4S_{13}$ unsuitable for a TFSC absorber application. Replacing $Cu^{2+}$ with a transition metal such as Mn or Zn decreases the hole concentration resulting in a non-degenerate semiconductor. The resistivity of a $Cu_{10}Zn_2Sb_4S_{13}$ thin film increases by four orders of magnitude compared to that of $Cu_{12}Sb_4S_{13}$, but the band gap is retained at $E_G$ = 1.8 eV.

Selenium is substituted for sulfur in $Cu_{10}Zn_2Sb_4S_{13}$ to reduce the band gap. Electron-beam evaporation is used to deposit ZnSe/ Cu/ Se/ $Sb_2Se_3$ followed by a post-deposition anneal at 295 °C. The absorption coefficient of $Cu_{10}Zn_2Sb_4Se_{13}$ reaches $\alpha = 3 \times 10^5$ cm$^{-1}$ within $E_G$+0.6 eV, with a band gap $E_G$ = 1.4 eV. SCAPS simulation indicates that a 250 nm $Cu_{10}Zn_2Sb_4Se_{13}$-based TFSC can have an efficiency of up to 21% with a carrier concentration $N_A = 2 \times 10^{16}$ cm$^{-3}$, a minority carrier lifetime of 1 ns ($N_T = 10^{14}$ cm$^{-3}$), and carrier mobilities of $\mu_n$, $\mu_p$ = 50 and 14 cm$^2$ V$^{-1}$ s$^{-1}$, indicating that $Cu_{10}Zn_2Sb_4Se_{13}$ is a promising candidate for high efficiency ultra-thin drift-based single junction TFSCs.

## 7.2 Recommendations for future work

### 7.2.1 TFSC Device Simulation

Simulations undertaken in this study explored the effect of increasing the absorption strength within the context of absorber layer properties and advantages of drift-based operation. It is shown that a drift-based TFSC incorporating a thin-absorber layer can have a range of carrier concentrations, low mobility, and can tolerate a high density of defects. $Cu_3SbS_4$-based TFSCs can be fabricated to validate the assertion that a drift-based TFSC is more tolerant towards defects.

The interfaces between $p^+$-p and p-$n^+$ layers are assumed to be ideal and interface states are not considered here. It would be beneficial to incorporate interface states and simulate properties of a $Cu_3SbS_4$ and a $Cu_{10}Zn_2Sb_4S_{13}$-based TFSC to understand the tolerable density of interface states. Further simulations to suggest routes mitigating the effect of interfaces states can be suggested.

### 7.2.2 Fe-based absorbers

Both $FeS_2$ and FGS are not recommended for further investigation. $FeS_2$ is plagued by spontaneous decomposition resulting in thin-films with a high carrier concentration which cannot be controlled. FGS requires careful oxygen-free process conditions and an appropriate annealing condition such that the FGS thin film does not react with the bottom metal contact. Even if such a process was identified, FGS-based TFSCs are predicted to provide a maximum efficiency of only 13 - 15% when the concentration of defects is minimized.

### 7.2.3 Cu-V-VI based absorbers

While $Cu_3SbS_4$ has a lower optical band gap compared to that of $CuSbS_2$, the strong, abrupt onset of absorption makes it a promising candidate for TFSC development. Sputtered

$Cu_3SbS_4$ thin films (followed by a post-deposition anneal) retained the strong optical absorption and hole mobility, suggesting that sputtering $Cu_3SbS_4$ is a viable option. Zn-doped $Cu_3SbS_4$ (up to 5%) is expected to lower the carrier concentration to $N_A \sim 10^{16}$ $cm^{-3}$ based on bulk synthesis measurements. Thus, Zn-doped $Cu_3SbS_4$ is suggested as a topic for further investigation as a solar absorber.

### 7.2.4 Tetrahedrite-based absorbers

$Cu_{12}Sb_4S_{13}$ is shown to be a p-type degenerate semiconductor which can be used to develop a p-type contact to semiconductors. Within the context of solar absorbers and LEDs, $Cu_{12}Sb_4S_{13}$ can be used as a $p^+$-layer for TFSCs, or as a hole injection layer for ILEDs or OLEDs.

The strong absorption coefficient of $Cu_{10}Zn_2Sb_4Se_{13}$ makes it an ideal candidate to develop ultra-thin TFSCs. Sputtered $Cu_{10}Zn_2Sb_4Se_{13}$ followed by a post-deposition anneal can be used to fabricate TFSCs. Recently, tetrahedrites have been identified as thermoelectric materials. Thermal conductivity measurements on $Cu_{10}Mn_2Sb_4S_{13}$ thin films can be performed to assess the thermoelectric capability. In addition, tetrahedrites can also be explored for IR LED applications.

### 7.2.5 $V_{OC}$ estimation from photoluminescence measurements

In this study, PL measurements were used to estimate the $V_{OC}$ of an FGS thin-film. The extracted $V_{OC}$ was 0.3 V suggesting that further optimization was required. PL measurements on Cu-V-VI compounds and tetrahedrites was not pursued in this study. PL properties of these materials can be studied to see if $V_{OC}$ estimation using PL is a viable technique

to assess absorber layer properties prior to being incorporated into a TFSC. Simultaneously, luminescence properties can also be studied for LED applications.

# BIBLIOGRAPHY


1. L. Yu and A. Zunger, "Identification of potential photovoltaic absorbers based on first-principles spectroscopic screening of materials," *Phys. Rev. Lett.*, vol. 108, pp. 068701–5, 2012.

2. S. Adachi, *Optical Constants of Crystalline and Amorphous Semiconductors: Numerical Data and Graphical Information*. Springer, 1999.

3. A. Ennaoui, S. Fiechter, C. Pettenkofer, N. Alonso-Vante, K. Buker, M. Bronold, C. Hopfner, and H. Tributsch, "Iron disulfide for solar energy conversion," *Solar Energy Materials & Solar Cells*, vol. 29, pp. 289–370, 1993.

4. D. M. Chapin, C. S. Fuller, and G. L. Pearson, "A new silicon p-n junction photocell for converting solar radiation into electrical power," *Journal of Applied Physics*, vol. 25, pp. 676–677, 1954.

5. C. Winneker, "Global market outlook for photovoltaics 2013-2017," tech. rep., European Photovoltaics Industry Association, 2012.

6. M. Meshek, "2012 renewable energy data handbook," tech. rep., Department of Energy, 2013.

7. "Estimated US energy use in 2013," tech. rep., Lawerence Livermore National Laboratory, 2014.

8. A. Luque and S. Hegedus, *Handbook of Photovoltaic Science and Engineering*. Wiley, 2011.

9. P. Würfel, *Physics of Solar Cells: From Principles to New Concepts*. John Wiley & Sons, 2005.

10. J. Nelson, *The Physics of Solar Cells*. Imperial College Press, 2003.

11. G. P. Smestad, "Luminescence and current-voltage characteristics of solar cells and optoelectronic devices," *Solar Energy Materials & Solar Cells*, vol. 25, pp. 51–71, 1992.

12. C. Kittel, *Introduction to Solid State Physics*. Wiley, 1995.

13. E. Merzbacher, *Quantum Mechanics*. Wiley, 1997.

14. M. Fox, *Optical Properties of Solids*. Oxford University Press, USA;, 2010.

15. S. M. Sze and K. K. Ng, *Physics of Semiconductor Devices*. Wiley-Interscience, 2006.

16. M. Lundstrom, *Fundamentals of Carrier Transport*. Cambridge University Press, 2000.

17. P. K. Basu, *Theory of Optical Processes in Semiconductors: Bulk and Microstructures*. Oxford University Press, 1998.

18. G. C. Schatz and M. A. Ratner, *Quantum Mechanics in Chemistry*. Prentice Hall, 1993.

19. P. Yu and M. Cardona, *Fundamentals of Semiconductors: Physics and Materials Properties*. Springer, 1999.

20. K. Seeger, *Semiconductor Physics: An Introduction*. Springer, 1982.

21. P. W. Atkins and D. F. Shriver, *Inorganic Chemistry*. Oxford University Press, 2009.

22. A. S. Marfunin, *Physics of Minerals and Inorganic Materials*. Springer-Verlag, 1979.

23. G. L. Miessler and D. A. Tarr, *Inorganic Chemistry*. Prentice Hall, 2010.

24. G. F. Bassani and G. P. Parravicini, *Electronic states and optical transitions in solids*. Pergamon Press, 1975.

25. J. I. Pankove, *Optical Processes in Semiconductors*. Dover Publications, 1971.

26. T. Tiedje, E. Yablonovitch, G. D. Cody, and B. G. Brooks, "Limiting efficiency of silicon solar cells," *IEEE Transactions on Electron Devices*, vol. 31, pp. 711–716, 1984.

27. J. Poortmans and V. Arkhipov, *Thin Film Solar Cells: Fabrication, Characterization and Applications*. Wiley, 2006.

28. O. Madelung, *Semiconductors: Data Handbook*. Springer, 2004.

29. I. Repins, S. Glynn, J. Duenow, T. Coutts, W. Metzger, and M. Contreras, "Required materials properties for high-efficiency CIGS modules," in *Society of Photographic Instrumentation Engineers (SPIE) Solar Energy + Technology Conference*, 2009.

30. R. Scheer and H.-W. Schock, *Chalcogenide Photovoltaics: Physics, Technologies, and Thin Film Devices*. Wiley-VCH, 2011.

31. D. K. Schroder, *Semiconductor Material and Device Characterization*. Wiley-IEEE Press, 2006.

32. W. Shockley, *Electrons and Holes in Semiconductors*. D. Van Nostrand Company Inc., 1950.

33. J. F. Wager, "ECE 616 class notes." Lecturexx.

34. M. Gloeckler, "Numerical Modeling of CIGS and CdTe Solar Cells: Setting the Baseline," in *Proceedings of 3rd World Conference on Photovoltaic Energy Conversion*, 2003.

35. D. Abou-Ras, T. Kirchartz, and U. Rau, *Advanced Characterization Techniques for Thin Film Solar Cells*. Wiley-VCH, 2011.

36. J. Sites and J. Pan, "Strategies to increase CdTe solar-cell voltage," *Thin Solid Films*, vol. 515, pp. 6099–6102, 2007.

37. T. Kirchartz, *Generalized detailed balance theory of solar cells*. PhD thesis, Rheinisch-Westfaelische Technische Hochschule Aachen, 2009.

38. J. Zhao, A. Wang, M. Green, and F. Ferrazza, "Novel 19.8 % efficient honeycomb textured multicrystalline and 24.4 % monocrystalline silicon solar cells," *Applied Physics Letters*, vol. 73, pp. 1991–1993, 1998.

39. B. Kayes, H. Nie, R. Twist, S. Spruytte, F. Reinhardt, I. Kizilyalli, and G. Higashi, "27.6 % Conversion Efficiency, A New Record for Single-junction Solar Cells Under 1 Sun Illumination," in *Proceedings of the 37th IEEE Photovoltaic Specialists Conference*, 2011.

40. S. Benagli, D. Borrello, E. Vallat-Sauvain, J. Meier, U. Kroll, J. Hötzel, J. Spitznagel, J. Steinhauser, L. Castens, and Y. Djeridane, "High-efficiency amorphous silicon devices on LPCVD-ZnO TCO prepared in industrial KAI-M R&D Reactor," in *24th European Photovoltaic Solar Energy Conference*, 2009.

41. D. A. R. Barkhouse, O. Gunawan, T. Gokmen, T. K. Todorov, and D. B. Mitzi, "Device characteristics of a 10.1 % hydrazine-processed $Cu_2ZnSn(Se,S)_4$ solar cell," *Progress in Photovoltaics: Research and Applications*, vol. 20, pp. 6–11, 2012.

42. M. A. Green, K. Emery, Y. Hishikawa, W. Warta, and E. D. Dunlop, "Solar cell efficiency tables (version 41)," *Progress In Photovoltaics: Research And Applications*, vol. 21, pp. 1–11, 2013.

43. T. Markvart, *Solar Cells: Materials, Manufacture and Operation*. Elsevier Science, 2005.

44. A. V. Shah, *Thin-Film Silicon Solar Cells*. EFPL Press, 2010.

45. M. A. Green, *Solar Cells: Operating Principles, Technology, and System Applications*. Prentice Hall, 1981.

46. F. Meillaud, A. Shah, C. Droz, E. Vallat-Sauvain, and C. Miazza, "Efficiency limits for single-junction and tandem solar cells," *Solar Energy Materials and Solar Cells*, vol. 18-19, pp. 2952–2959, 2006.

47. W. Shockley and H. J. Queisser, "Detailed balance limit of efficiency of pn junction solar cells," *Journal of Applied Physics*, vol. 32, pp. 510–519, 1961.

48. L. I. Berger, *Semiconductor Materials*. CRC Press, 1997.

49. S.-H. Wei and S. B. Zhang, "Chemical trends of defect formation and doping limit in II-VI semiconductors: The case of CdTe," *Physical Review B*, vol. 66, pp. 155211–1–10, 2002.

50. S.-H. Wei, S. B. Zhang, and A. Zunger, "First-principles calculation of band offsets, optical bowings, and defects in CdS, CdSe, CdTe, and their alloys," *Journal of Applied Physics*, vol. 87, pp. 1304–1311, 2000.

51. C. Ferekides, D. Marinskiy, V. Viswanathan, B. Tetali, V. Palekis, P. Selvaraj, and D. Morel, "High effciency CSS CdTe solar cells," *Thin Solid Films*, vol. 361-362, pp. 520–526, 2000.

52. B. Siepchen, C. Drost, B. Spth, V. Krishnakumar, H. Richter, M. Harr, S. Bossert, M. G. K. Hfner, T. Modes, O. Zywitzki, and H. Morgner, "Thin film CdTe solar cells by close spaced sublimation: Recent results from pilot line," *Thin Solid Films*, vol. 535, pp. 224–228, 2012.

53. A. Morales-Acevedo, "Thin film CdS/CdTe solar cells: Research perspectives," *Solar Energy*, vol. 80, p. 675681, 2006.

54. M. Burgelman, J. Verschraegen, S. Degrave, and P. Nollet, "Modeling thin-film pv devices," *Progress In Photovoltaics: Research And Applications*, vol. 12, pp. 143–153, 2004.

55. J. Spies, R. Schafer, J. Wager, P. Hersh, H. Platt, D. Keszler, G. Schneider, R. Kykyneshi, J. Tate, X. Liu, A. D. Compaan, and W. Shafarman, "pin double-heterojunction thin–film solar cell p-layer assessment," *Solar Energy Materials & Solar Cells*, vol. 93, pp. 1296–1308, 2009.

56. H. B. Michaelson, "The work function of the elements and its periodicity," *Journal of Applied Physics*, vol. 48, pp. 4729–4733, 1977.

57. C. Corwine, A. Pudov, M. Gloeckler, S. Demtsu, and J. Sites, "Copper inclusion and migration from the back contact in CdTe solar cells," *Solar Energy Materials & Solar Cells*, vol. 82, pp. 481–489, 2004.

58. J. Fritsche, D. Kraft, A. Thiben, T. Mayer, A. Klein, and W. Jaegermann, "Band energy diagram of CdTe thin film solar cells," *Thin Solid Films*, vol. 403-404, pp. 252–257, 2002.

59. X. Wu, "High-efficiency polycrystalline cdte thin-film solar cells," *Solar Energy*, vol. 77, pp. 803–814, 2004.

60. S. Wagner, J. L. Shay, P. Migliorato, and H. M. Kasper, "$CuInSe_2$/CdS heterojunction photovoltaic detectors," *Applied Physics Letters*, vol. 25, pp. 434–435, 1974.

61. L. L. Kazmerski, F. R. White, and G. K. Morgan, "Thin-film $CuInSe_2$/CdS heterojunction solar cells," *Applied Physics Letters*, vol. 29, pp. 268–269, 1976.

62. K. Mitchell, C. Eberspacher, J. Ermer, and D. Pier, "Single and tandem junction $CuInSe_2$ cell and module technology," in *Conference Record of the Twentieth IEEE Photovoltaic Specialists Conference*, 1988.

63. A. McEvoy, T. Markvart, and L. Castaner, *Practical Handbook of Photovoltaics: Fundamentals and Applications*. Academic Press, 2011.

64. S. B. Zhang, S.-H. Wei, A. Zunger, and H. K. Yoshida, "Defect phyics of $CuInSe_2$ chalcopyrite semiconductor," *Physical Review B*, vol. 57, pp. 9642–9656, 1998.

65. Q. Cao, O. Gunawan, M. Copel, K. B. Reuter, S. J. Chey, V. R. Deline, and D. B. Mitzi, "Defects in $Cu(In,Ga)Se_2$ Chalcopyrite Semiconductors: A Comparative Study of Material Properties, Defect States, and Photovoltaic Performance," *Advanced Energy Materials*, vol. 1, pp. 845–853, 2011.

66. D. Schmid, M. Ruckh, F. Grunwalk, and H. W. Schock, "Chalcopyrite/defect chalcopyrite heterojunctions on the basis of $CuInSe_2$," *Journal of Applied Physics*, vol. 73, pp. 2902–2910, 1993.

67. A. Rockett, D. Liao, J. Heath, J. Cohen, Y. Strzhemechny, L. Brillson, K. Ramanathan, and W. Shafarman, "Near-surface defect distributions in $Cu(In,Ga)Se_2$," *Thin Solid FIlms*, vol. 431-432, pp. 301–306, 2003.

68. Y.-M. Xue, B.-H. Yang, C.-Q. Qu, L. Zhang, C.-M. Xu, and Y. Sun, "Structural and electrical properties of co-evaporated In, Ga rich CIGS thin films," *Optoelectronic Letters*, vol. 4, pp. 437–439, 2008.

69. Y. Cho, D.-W. Kim, S. Ahn, D. Nam, H. Cheong, G. Y. Jeong, J. Gwak, and J. H. Yun, "Recombination in $Cu(In,Ga)Se_2$ thin-film solar cells containing ordered vacancy compound phases," *Thin Solid Films*, 2013.

70. D. R. Linde, ed., *CRC Handbook of Chemistry and Physics*. CRC Press, 2008.

71. A. Romeo, M. Terheggen, D. Abou-Ras, D. L. Btzner, F.-J. Haug, M. Klin, D. Rudmann, and A. N. Tiwari, "Development of thin-film $Cu(In,Ga)Se_2$ and CdTe solar cells," *Progress in Photovoltaics: Research and Applications*, vol. 12, pp. 93–111, 2004.

72. J. Binsma and H. van der Linden, "Preparation of thin $CuInS_2$ films via a two-stage process," *Thin Solid Films*, vol. 97, p. 237243, 1982.

73. V. Probst, F. Karg, J. Rimmasch, W. Riedl, W. Stetter, H. Harms, and O. Eibl, "Advanced stacked elemental layer process for $Cu(In,Ga)Se_2$ thin-film photovoltaic devices," in *Proceedings of the MRS Spring Symposium*, 1996.

74. R. Gay, M. Dietrich, C. Fredric, C. Jensen, K. Knapp, D. Tarrant, and D. Willett, "Efficiency and process improvements in $CuInSe_2$-based modules," in *12th European Photovoltaic Solar Energy Conference*, 1994.

75. M. A. Contreras, B. Egaas, K. Ramanathan, J. Hiltner, A. Swartzlander, F. Hasoon, and R. Noufi, "Progress toward 20% efficiency in Cu(In,Ga)$Se_2$ polycrystalline thin-film solar cells," *Progress in Photovoltaics: Research and Applications*, vol. 7, pp. 311–316, 1999.

76. O. Lundberg, M. Edoff, and L. Stolt, "The effect of Ga-grading in CIGS thin film solar cells," *Thin Solid FIlms*, vol. 480-481, pp. 520–525, 2005.

77. S. R. Kodigala, *Cu($In_{1-x}Ga_xSe_2$) Based Thin Film Solar Cells*. Academic Press, 2010.

78. M. Rusu, S. Sadewasser, T. Glatzel, P. Gashin, A. Simashkevich, and Jäger-Waldau, "Contribution of the ZnSe/$CuGaSe_2$ heterojunction in photovoltaic performances of chalcopyrite-based solar cells," *Thin Solid Films*, vol. 403-404, pp. 344–348, 2002.

79. S. Nishiwaki, N. Kohara, T. Negami, and T. Wada, "$MoSe_2$ layer formation at Cu(In,Ga)$Se_2$/Mo interfaces in high efficiency Cu($In_{1-x}Ga_x$)$Se_2$ solar cells," *Japanese Journal for Applied Physics*, vol. 37, pp. L71 – L73, 1998.

80. M. D. Archer and R. Hill, *Clean Electricity from Photovoltaics*. World Scientific Pub Co Inc, 2001.

81. N. Kohara, S. Nishiwaki, Y. Hashimoto, T. Negami, and T. Wada, "Electrical properties of the Cu(In,Ga)$Se_2$/ $MoSe_2$/Mo structure," *Solar Energy Materials and Solar Cells*, vol. 67, pp. 209–215, 2001.

82. A. Rockett, "The effect of Na in polycrystalline and epitaxial single-crystal $CuIn_{1-x}Ga_xSe_2$," *Thin Solid Films*, vol. 480-481, pp. 2–7, 2005.

83. A. Rockett, "The electronic effects of point defects in Cu($In_xGa_{1-x}$)$Se_2$," *Thin Solid FIlms*, vol. 361-362, pp. 330–337, 2000.

84. M. Powalla and B. Dimmler, "Scaling up issues of CIGS solar cells," *Thin Solid FIlms*, vol. 361-362, pp. 540–546, 2000.

85. D. E. Carlson and C. R. Wronski, "Amorphous silicon solar cell," *Applied Physics Letters*, vol. 28, pp. 671–674, 1976.

86. R. H. Bube, *Photovoltaic Materials*. World Scientific Publishing Company, 1998.

87. A. V. Shah, H. Schade, M. Vanecek, J. Meier, E. Vallat-Sauvain, N. Wyrsch, U. Kroll, C. Droz, and J. Bailat, "Thin-film silicon solar cell technology," *Progress in Photovoltaics: Research and Applications*, vol. 12, pp. 113–142, 2004.

88. J. Tauc, "Optical properties and electronic structure of amorphous Ge and Si," *Materials Research Bulletin*, vol. 3, pp. 37–46, 1968.

89. L. M. Fraas and L. D. Partain, *Solar Cells and Their Applications*. John Wiley & Sons, 2010.

90. R. E. Schropp and M. Zeman, *Amorphous and Microcrystalline Silicon Solar Cells: Modeling, Materials and Device Technology*. Springer, 1998.

91. D. L. Staebler and C. R. Wronski, "Reversible conductivity changes in discharge-produced amorphous Si," *Applied Physics Letters*, vol. 31, pp. 292–294, 1977.

92. J. Emsley, *Nature's Building Blocks: An A-Z Guide to the Elements*. Oxford University Press, 2011.

93. R. Dasbach, G. Willeke, and O. Blenk, "Iron sulfide for photovoltaics," *MRS Bulletin*, vol. 18, pp. 56–60, 1993.

94. C. de las Heras and C. Sanchez, "Characterization of iron pyrite thin films obtained by flash evaporation," *Thin Solid Films*, vol. 199, pp. 259–267, 1991.

95. G. Smestad, A. Ennaoui, S. Fiechter, H. Tributsch, W. Hofmann, M. Birkholz, and W. Kautek, "Photoactive thin film semiconducting iron pyrite prepared by sulfurization of iron oxides," *Solar Energy Materials*, vol. 20, pp. 149–165, 1990.

96. B. Meester, L. Reijnen, A. Goossens, and J. Schoonman, "Synthesis of pyrite ($FeS_2$) Thin Films by Low-Pressure MOCVD," *Chemical Vapor Deposition*, vol. 6, pp. 121–128, 2000.

97. N. Berry, M. Cheng, C. L. Perkins, M. Limpinsel, J. C. Hemminger, and M. Law, "Atmospheric-pressure chemical vapor deposition of iron pyrite thin films," *Advanced Energy Materials*, vol. 2, pp. 1124–1135, 2012.

98. K. Ellmer, D. Lichtenberger, A. Ennaoui, C. Hopfner, S. Fiechter, and H. Tributsch, "Comparison of structural, optical and electrical properties of pyrite ($FeS_2$) layers prepared by MOCVD (normal and low pressure) and reactive magnetron sputtering," in *IEEE PV Specialists conference, IEEE PV Specialists conference*, 1993.

99. M. Jagadeesh and M. S. Seehra, "Electrical resistivity and band gap of marcasite ($FeS_2$)," *Physics Letters A*, vol. 80, pp. 59–61, 1980.

100. G. Willeke, R. Dasbach, B. Sailer, and E. Bucher, "Thin pyrite ($FeS_2$) films prepared by magnetron sputtering," *Thin Solid Films*, vol. 213, pp. 271–276, 1992.

101. K. Büker, N. Alonso-Vante, and H. Tributsch, "Photovoltaic output limitation of n-$FeS_2$ (pyrite) Schottky barriers: A temperature-dependent characterization," *J. Appl. Phys*, vol. 72, pp. 5721–5729, 1992.

102. A. Ennaoui, S. Fiechter, W. Jaegermann, and H. Tributsch, "Photoelectrochemistry of highly quantum efficient single crystalline n-$FeS_2$ (Pyrite)," *J. Electrochem. Soc.*, vol. 133, pp. 97–106, 1986.

103. M. Birkholz, S. Fiechter, A. Hartmann, and H. Tributsch, "Sulfur deficiency in iron pyrite ($FeS_{2-x}$) and its consequences for band-structure models," *Phys. Rev. B*, vol. 43, pp. 11926–11936, 1991.

104. K. Sun, Z. Su, J. Yang, Z. Han, F. Liu, Y. Lai, J. Li, and Y. Liu, "Fabrication of pyrite $FeS_2$ thin films by sulfurizing oxide precursor films deposited via successive ionic layer adsorption and reaction method," *Thin Solid Films*, 2013.

105. B. Chapman, *Glow Discharge Processes: Sputtering and Plasma Etching*. Wiley-Interscience, 1980.

106. M. Ohring, *Material Science of Thin Films*. Academic Press, 2001.

107. D. Smith, *Thin-Film Deposition: Principles and Practice*. McGraw-Hill, 1995.

108. R. D. Mathis, "Thin film evaporation source reference guide," tech. rep.

109. E. Hecht, *Optics*. Addison-Wesley, 2001.

110. R. Azzam and N. Bashara, *Ellipsometry and Polarized Light*. North Holland, 1988.

111. H. Fujiwara, *Spectroscopic Ellipsometry: Principles and Applications*. John Wiley & Sons, 2007.

112. H. Tompkins and E. A. Irene, *Handbook of Ellipsometry*. William Andrew, 2006.

113. *Guide to using WVASE32 - Spectroscopic Ellipsometry Data Acquisition and Analysis Software*.

114. *HALL EFFECT MEASUREMENTS- Lake Shore 7500/9500 Series Hall System Users Manual*.

115. *SCAPS Manual*.

116. X. Gu, X. Yu, and D. Yang, "Efficiency improvement of crystalline silicon solar cells with a back-surface field produced by boron and aluminum co-doping," *Scripta Materialia*, vol. 66, pp. 394–397, 2012.

117. J. G. Fossum, "Physical operation of back-surface-field silicon solar cells," *IEEE Transactions on Electron Devices*, vol. 24, pp. 322–325, 1977.

118. L. Yu, S. Lany, R. Kykyneshi, V. Jieratum, R. Ravichandran, B. Pelatt, E. Altschul, H. A. S. Platt, J. F. Wager, D. A. Keszler, and A. Zunger, "Iron Chalcogenide Photovoltaic Absorbers," *Advanced Energy Materials*, vol. 1, pp. 748–753, 2011.

119. K. Sato, "Reflectivity spectra and optical constants of pyrites ($FeS_2$, $CoS_2$ and $NiS_2$) between 0.2 and 4.4 ev," *J. Phys. Soc. Jpn.*, vol. 53, pp. 1617–1620, 1984.

120. S.-H. Wei, S. B. Zhang, and A. Zunger, "Effects of Na on the electrical and structural properties of $CuInSe_2$," *J. Appl. Phys*, vol. 85, p. 7214, 1999.

121. A. Krishnamoorthy, F. W. Herbert, S. Yip, K. J. V. Vliet, and B. Yildiz, "Electronic states of intrinsic surface and bulk vacancies in $FeS_2$," *Journal of Physics: Condensed Matter*, vol. 25, p. 045004, 2013.

122. H. A. S. Platt, *Copper and iron chalcogenides for efficient solar absorption*. PhD thesis, Oregon State University, 2010.

123. V. Jieratum, *Iron and copper chalcogenides: photovoltaic absorber candidates and $YZrF_7$: a new upconversion host*. PhD thesis, Oregon State University, 2012.

124. I. Barin, *Thermochemical Data of Pure Substances*. VCH Germany, 1995.

125. Y. Wu, C. Wadia, W. Ma, B. Sadtler, and A. P. Alivisatos, "Synthesis and photovoltaic application of copper(I) sulfide nanocrystals," *Nano Letters*, vol. 8, pp. 2551–2555, 2008.

126. J. Bragagnolo, A. M. Barnett, J. Phillips, R. B. Hall, A. Rothwarf, and J. Meakin, "The design and fabrication of thin-film CdS/$Cu_2S$ cells of 9.15-percent conversion efficiency," *IEEE Transactions on Electron Devices*, vol. 27, pp. 645–651, 1980.

127. J. T. R. Dufton, A. Walsh, P. M. Panchmatia, L. M. Peter, D. Colombara, and M. S. Islam, "Structural and electronic properties of $CuSbS_2$ and $CuBiS_2$: potential absorber materials for thin-film solar cells," *Physical Chemistry Chemical Physics*, vol. 14, pp. 7229–7233, 2012.

128. P. Maiello, G. Zoppi, R. W. Miles, N. Pearsall, and I. Forbes, "Chalcogenisation of Cu-Sb metallic precursors into $Cu_3Sb(Se_xS_{1-x})_3$," *Solar Energy Materials and Solar Cells*, vol. 113, pp. 186–194, 2013.

129. E. J. Skoug, J. D. Cain, and D. T. Morelli, "High thermoelectric figure of merit in the $Cu_3SbSe_4$-$Cu_3SbS_4$ solid solution," *Appl. Phys. Lett.*, vol. 98, pp. 261911–1 – 261911–3, 2011.

130. D. Parker and D. J. Singh, "Transport properties of hole-doped $CuBiS_2$," *Physical Review B*, vol. 83, pp. 233206–1 – 233206–4, 2011.

131. M. Kumar and C. Persson, "$Cu_3BiS_3$ as a potential photovoltaic absorber with high optical efficiency," *Appl. Phys. Lett.*, vol. 102, pp. 062109–1 – 062109–4, 2013.

132. N. J. Gerein and J. A. Haber, "$Cu_3BiS_3$, $Cu_3BiS_4$, $Ga_3BiS_3$ and $Cu_5Ga_2BiS_8$ as potential solar absorbers for thin films photovoltaics," in *Conference Record of the Thirty-first IEEE Photovoltaic Specialists Conference*, 2005.

133. D. Colombara, L. Peter, K. Rogers, J. Painter, and S. Roncallo, "Formation of $CuSbS_2$ and $CuSbSe_2$ thin films via chalcogenisation of SbCu metal precursors," *Thin Solid FIlms*, vol. 519, pp. 7438–7443, 2011.

134. L. Yu, R. S. Kokenyesi, D. A. Keszler, and A. Zunger, "Inverse design of high absorption thin-film photovoltaic materials," *Advanced Energy Materials*, vol. 3, pp. 43 – 48, 2013.

135. A. Walsh, D. J. Payne, R. G. Egdell, and G. W. Watson, "Stereochemistry of post-transition metal oxides: revision of the classical lone pair model," *Chemical Society Reviews*, vol. 40, pp. 4445–4463, 2011.

136. D. Tang, J. Yang, F. Liu, Y. Lai, M. Jia, J. Li, and Y. Liu, "One-step electrodeposition and annealing of $CuSbSe_2$ thin films," *Electrochemical and Solid-State Letters*, vol. 15, pp. D11–D13, 2012.

137. W. Monch, *Semiconductor Surfaces and Interfaces*. Springer-Verlag, 1993.

138. J. F. Wager, "Solar cell absorber surfaces from an induced gap states perspective.".

139. J. A. Tossell and D. J. Vaughan, *Theoretical Geochemistry: Applications of Quantum Mechanics in the Earth and Mineral Sciences*. Oxford University Press, 1992.

140. J. W. Miller and J. R. Craig, "Tetrahedrite-tennantite series compositional variation in the cofer deposit, mineral district, virginia," *American*, vol. 68, pp. 227–234, 1983.

141. N. E. Johnson, J. R. Craig, and J. D. Rimstidt, "Compositional trends in tetrahedrite," *Canadian Minerologist*, vol. 24, pp. 358–397, 1986.

142. X. Lu, D. T. Morelli, Y. Xia, F. Zhou, V. Ozolins, H. Chi, X. Zhou, and C. Uher, "High performance thermoelectricity in earth-abundant compounds based on natural mineral tetrahedrites," *Advanced Energy Materials*, vol. 3, pp. 342–348, 2012.

143. X. Fan, E. D. Case, X. Lu, and D. T. Morelli, "Room temperature mechanical properties of natural-mineral-based thermoelectrics," *Journal of Material Science*, vol. 48, pp. 7540–7550, 2013.

144. X. Lu and D. T. Morell, "Natural mineral tetrahedrite as a direct source of thermoelectric materials," *Physical Chemistry Chemical Physics*, vol. 15, pp. 5762–5766, 2013.

145. A. Pfitzner, M. Evain, and V. Petricek, "$Cu_{12}Sb_4S_{13}$: A temperature dependent structure investigation," *Acta Crystallographica Section B*, vol. 53, pp. 337–345, 1997.

146. K. Suekuni, K. Tsuruta, M. Kunii, H. Nishiate, E. Nishibori, S. Maki, M. Ohta, A. Yamamoto, and M. Koyano, "High-performance thermoelectric mineral $Cu_{12-x}Ni_xSb_4S_{13}$ tetrahedrite," *Journal of Applied Physics*, vol. 113, p. 043712, 2013.

147. B. D. Pelatt, R. Ravichandran, J. F. Wager, and D. A. Keszler, "Atomic solid state energy scale," *J. Am. Chem. Soc.*, vol. 133, pp. 16852–16860, 2011.